3D dynamic culture of mesenchymal stem cells under fluid flow

Implications for bone regeneration

Shuntaro Yamada

UNIVERSITY OF BERGEN

3D dynamic culture of mesenchymal stem cells under fluid flow
Implications for bone regeneration

Shuntaro Yamada

Thesis for the degree of Philosophiae Doctor (PhD)
at the University of Bergen

Date of defense: 06.10.2023

Year: 2023

Title: 3D dynamic culture of mesenchymal stem cells under fluid flow

Name: Shuntaro Yamada

Print: Skipnes Kommunikasjon / University of Bergen

Table of Contents

Scientific Environment

The work comprising this thesis was primarily conducted as a part of the activities in the Tissue Engineering research group at the Center of Translational Oral Research (TOR), Department of Clinical Dentistry (IKO), Faculty of Medicine, University of Bergen (UiB), Norway.

Confocal microscopy was conducted at the Molecular Imaging Center (MIC), Department of Biomedicine, Faculty of Medicine, UiB.

Scanning electron microscopy, Fourier-transform infrared spectroscopy, water contact angle measurement, and oxygen plasma activation were performed in collaboration with the Fraunhofer Institute for Silicate Research ISC, Würzburg, Germany.

The work was principally supervised by Prof. Kamal Mustafa, with a co-supervisor, Assoc. Prof. Mohammed Yassin at IKO, UiB. Prof. Jan Hansmann in Fraunhofer Institutes for Silicate Research, Germany, served as an external co-supervisor.

Abstract (English)

The fate and growth of mesenchymal stem cells (MSC) can be altered by biophysical stimuli. In bone, fluid shear stress caused by interstitial fluid flow is considered the primary mechanical stimulus at a cellular level, which drives mechanotransduction to regulate bone formation, homeostasis, and repair. Using this knowledge, attempts have been made to mechanically stimulate bone marrow-derived MSC (BMSC) in culture to improve their osteogenic potential. However, it remains unclear 1) what the optimal dynamic culture condition is to promote osteogenic differentiation of BMSC, 2) how BMSC respond, particularly in a 3D environment, to such a stimulus, and 3) whether fluid stimuli alone are sufficient to induce differentiation.

In the studies included in this thesis, with the prospect of bone tissue engineering, BMSC isolated from Lewis rats cultured on 3D scaffolds were subjected to fluid stimuli using a laminar flow bioreactor to evaluate the biological response of BMSC to fluid stimuli. Specifically, in **Paper I**, 3D scaffolds with highly porous structures were designed and fabricated using polymeric biomaterial, poly(L-lactide-co-trimethylene carbonate). The biocompatibility and osteoconductivity of the scaffolds were evaluated *in vitro* with and without functionalisation by oxygen plasma. Using the 3D scaffolds, a dynamic cell culture platform was established in the bioreactor through thorough optimisation to define experimental variables and operational configurations in **Paper II**. The mechanical regulation of BMSC growth and fate was evaluated in **Paper III** as a proof-of-concept study, showing that the osteogenic differentiation of BMSC was induced solely by fluid stimuli in the bioreactor without the need for osteoinductive supplements. **Paper IV** addressed putative mechanisms behind the mechanically induced osteogenic differentiation and showed that Rho-ROCK-mediated cytoskeletal modulation under fluid flow was required for the growth and differentiation of BMSC.

Taken together, the thesis provides the insight of dynamic cell culture for bone tissue engineering with evidence that fluid stimuli alone can induce osteogenic differentiation of BMSC on 3D scaffolds through cytoskeletal regulations.

Abstract (Norwegian)

Skjebnen og veksten til mesenkymale stamceller (MSC) kan påvirkes av biologiske stimuli. I benvev regnes skjærspenning fra væske forårsaket av interstitiell væskestrøm som den primære mekaniske stimulien på celleplan, som virker som en fremmende stimulus for beinvekst, homeostase og reparasjon. For å forbedre det osteogene potensialet, har det blitt gjort forsøk på å mekanisk stimulere benmargens MSC (BMSC) i kultur ved å bruke denne kunnskapen. Det er imidlertid fortsatt uklart 1) hva som er den optimale dynamiske kulturtilstanden for å fremme osteogen differensiering av BMSC, 2) hvordan BMSC responderer, spesielt i et 3D-miljø, til en slik stimulus, og 3) om stimuli fra væske alene er tilstrekkelig til å indusere differensiering.

I studiene inkludert i avhandlingen, med tanke på bruk av "tissue engineering" for regenereing av benvev, ble BMSC isolert fra Lewis-rotter dyrket på 3D-scaffolds utsatt for væskestimuli ved hjelp av en "laminar flow biorector" for å evaluere deres evne til osteogen differensiering. Spesielt i **Artikkel Ⅰ** ble 3D-scaffolds med svært porøse strukturer designet og produsert ved bruk av et polymert biomaterial, poly(L-lactide-co-trimethylene carbonate), og dets biokompatibilitet og in vitro osteokonduktivitet med og uten funksjonalisering av oksygenplasma ble testet. Ved hjelp av 3D-scaffoldsene ble det etablert en dynamisk cellekulturplattform i bioreaktoren gjennom grundig optimalisering for å definere eksperimentelle variabler og driftskonfigurasjoner i **Artikkel Ⅱ**. Den mekaniske reguleringen av BMSC-vekst og skjebne ble evaluert i **Artikkel Ⅲ** som en "proof of concept"-studie, som viste at den osteogene differensieringen av BMSC utelukkende ble indusert av væskestimuli i bioreaktoren uten behov for osteoinduktive tilskudd. **Artikkel Ⅳ** tok for seg antatte mekanismer bak den mekanisk induserte osteogene differensieringen og viste at Rho-ROCK-mediert cytoskjelettmodulering under væskestrøm var nødvendig for vekst og differensiering av BMSC.

Til sammen gir avhandlingen innsikt i dynamisk cellekultur for "bone tissue engineering" med bevis for at væskestimuli er tilstrekkelig for å indusere osteogen differensiering av BMSC gjennom cytoskjelettreguleringer.

List of Publications

This thesis is based on the following papers and will be referred to according to their Roman numbers:

I. **Yamada S**, Yassin MA, Weigel T, Schmitz T, Hansmann J, Mustafa K. Surface Activation with Oxygen Plasma Promotes Osteogenesis with Enhanced Extracellular Matrix Formation in Three-dimensional Microporous Scaffolds. *Journal of Biomedical Materials Research Part A*. 2021;109(9):1560-1574.

II. **Yamada S**, Yassin MA, Schwarz T, Mustafa K, Hansmann J. Optimization and Validation of a Custom-Designed Perfusion Bioreactor for Bone Tissue Engineering: Flow Assessment and Optimal Culture Environmental Conditions. *Frontiers in Bioengineering and Biotechnology*. 2022;10:811942.

III. **Yamada S**, Yassin MA, Schwarz T, Hansmann J, Mustafa K. Induction of Osteogenic Differentiation of Bone Marrow Stromal Cells on 3D Polyester-based Scaffolds Solely by Subphysiological Fluidic Stimulation in a Laminar Flow Bioreactor. *Journal of Tissue Engineering*. 2021;12:1-17.

IV. **Yamada S**, Yassin MA, Torelli F, Hansmann J, Green JBA, Schwarz T, Mustafa K. Unique Osteogenic Profile of Bone Marrow Stem Cells Stimulated in Perfusion Bioreactor is Rho-ROCK-mediated Contractility Dependent. *Bioengineering & Translational Medicine*. 2023; 8(3),e10509.

The candidate has contributed to the following work during the course of the PhD period, which is not included in this thesis:

I.   **Yamada S**, Lav R, Li J, Tucker AC, Green JBA. Molar Bud-to-Cap Transition is Proliferation Independent. *Journal of Dental Research*. 2019;98(11):1253-1261.

II.   **Yamada S**, Shanbhag S, Mustafa K. Scaffolds in Periodontal Regenerative Treatment. *Dental Clinics of North America*. 2022;66(1):111-130.

III.   Hara K, Hellem E, **Yamada S**, Sariibrahimoglu K, Mølster A, Gjerdet NR, Hellem S, Mustafa K, Yassin MA. Efficacy of Treating Segmental Bone Defects through Endochondral Ossification: 3D Printed Designs and Bone Metabolic Activities. *Materials Today Bio*. 2022;14:100237.

IV.   Kivijärvi T, Goksøyr Ø, Yassin MA, Jain S, **Yamada S**, Morales-López A, Mustafa K, Finne-Wistrand A. Hybrid Material based on Hyaluronan Hydrogels and Poly(l-lactide-co-1,3-trimethylene carbonate) Scaffolds toward a Cell-Instructive Microenvironment with Long-term *In-vivo* Degradability. *Materials Today Bio*. 2022;17:100483.

V.   Al-Sharabi N, Salah S, Shanbhag S, Kampleitner C, Elnour R, **Yamada S**, Birkeland E, Rana N, Tangl S, Gruber R, Mustafa K. Extracellular Vesicles Secreted by Osteogenic-Differentiated Mesenchymal Stem Cells Promote Bone Formation in Rat Calvarial Defect. (Manuscript)

VI.   **Yamada S**, Al-Sharabi N, Torelli F, Angelova A, Fristad I, Mustafa K. Dental Pulp Stem Cell-Derived Conditioned Medium Mitigates Oxidative Stress in Photo-crosslinkable Hydrogels. (Submitted manuscript)

VII. Goksøyr Ø, Yassin MA, **Yamada S**, Rosén A, Suliman S, Mustafa K. Osteogenic Potential of Hyaluronic Acid Hydrogel Modified Poly(L-lactide-co-1,3-trimethylene carbonate) Scaffolds In-vitro and In-vivo. (Manuscript)

VIII. Ali H.R.W., Suliman S, Osman T, Mohamed-Ahmed S, **Yamada S**, Costea DE, Ræder H, Mustafa K. Osteogenic Potential of Xeno-free Mesenchymal Stem Cells Derived from Induced Pluripotent Stem Cells. (Manuscript)

Abbreviations

AF	Alexa Fluor™
ALP/Alpl	Alkaline Phosphatase
ANOVA	Analysis Of Variance
ASC	Adipose-Derived Mesenchymal Stem/Stromal Cells
ATR-FTIR	Attenuated Total Reflectance-Fourier Transform Infrared Spectroscopy
BMP	Bone Morphogenetic Protein
BMSC	Bone Marrow-Derived Mesenchymal Stem/Stromal Cells
CAD	Computer-Aided-Design
CD	Cluster Of Differentiation
CFD	Computational Fluid Dynamics
Col1	Collagen Type 1
Cyr61	Cysteine-rich angiogenic inducer 61
DAPI	4′,6-Diamidino-2-Phenylindole
DEG	Differentially Expressed Genes
DFSC	Dental Follicle Stem Cells
Dmp1	Dentin Matrix Protein 1
DMSO	Dimethyl Sulfoxide
DPSC	Dental Pulp Stem Cells
dsDNA	Double-strand DNA
ECM	Extracellular Matrix
EdU	5-Ethynyl-2′-Deoxyuridine
ELISA	Enzyme-Linked Immunosorbent Assay
FBS	Fetal Bovine Serum
FDA	U.S. Food And Drug Administration
FHI	Fraunhofer Institutes
GRAS	Generally Recognized As Safe
HA	Hydroxyapatite
HFLMMS	High-Frequency Low-Magnitude Mechanical Stimulation
HRP	Horseradish Peroxidase
Lef1	Lymphoid enhancer binding factor 1
MEM	Minimum Essential Medium
MLC	Myosin Light Chain
MLCK	Myosin Light Chain Kinase
MLCP	Myosin Light Chain Phosphatase
MSC	Mesenchymal Stem/Stromal Cells
MYPT1	Myosin Phosphatase Target Subunit 1
NASA	National Aeronautics And Space Administration

NM2A	Non-Muscle Myosin 2A
NM2B	Non-Muscle Myosin 2B
NO	Nitric Oxide
Ocn	Osteocalcin
OM	Osteoinductive Medium
P/S	Penicillin/Streptomycin
PBS	Phosphate Buffered Saline
PC	Principal Component
PCA	Principal Component Analysis
PCL	Polycaprolactone
PCNA	Proliferating Cell Nuclear Antigen
PDLSC	Periodontal Ligament Stem Cells
PFA	Paraformaldehyde
PG	Prostaglandins
PLA	Polylactic Acid
PDGF	Platelet-derived growth factor
PLGA/PLG	Poly(D,L-Lactic-Co-Glycolic Acid)
PLTMC	Poly(Lactide-Co-Trimethylene Carbonate)
pMLC	Phosphorylated Myosin Light Chain
pNPP	P-Nitrophenylphosphate
PPARγ	Peroxisome Proliferator-Activated Receptor Gamma
PTMC	Poly(Trimethylene Carbonate)
Rho	Ras Homolog
ROCK	Rho Associated Coiled Coil Containing Protein Kinase
ROI	Regions Of Interest
RT-qPCR	Reverse Transcription Quantitative Polymerase Chain Reaction
Runx2	Runt-Related Transcription Factor 2
Sca1/Ly6	Stem Cell Antigen-1
SCAP	Stem Cells From Apical Papilla
Sost	Sclerostin
SEM	Scanning Electron Microscopy
SHED	Stem Cells From Exfoliated Deciduous Teeth
Smad	Mothers Against Decapentaplegic
Spp1	Secreted Phosphoprotein 1/Osteopontin
TAZ	Transcriptional Coactivator With Pdz-Binding Motif
UV	Ultraviolet
VEGF	Vascular endothelial growth factor
Wnt	Wingless-Related Integration Site
YAP	Yes-Associated Protein
μCT	Microcomputed Tomography

List of Figures and Tables

1. Introduction

Bone defects are a prevalent pathology that can occur due to various reasons, such as trauma, infection, neoplastic lesions, or osteotomy. Due to the limited spontaneous healing capacity of bone, it often requires extensive surgical interventions to restore its original form and function.

From ancient times to the present day, bone has been one of the tissues most frequently treated by grafting including xenograft, allograft, autograft, and other types of bone substitutes [1]. Since early 1800s when the first autologous bone transplantation was documented by a German surgeon, Phillips von Walter, autologous bone graft has been considered as an effective means of regenerating bone [2]. Autologous bone contains cells, matrices, and growth factors necessary for bone regeneration. These components satisfy osteoconductivity (*i.e.*, ability to support the ingrowth of surrounding bone), osteoinductivity (*i.e.*, ability to induce the osteogenesis of progenitor cells), and osteogenicity (*i.e.*, ability to give rise to osteoblasts). Currently, autologous bone grafts are still considered as the golden standard and annually performed over 2 million times globally [3]. Nevertheless, it is not a panacea. Taking donor-site morbidity for example, nearly 20% of patients may potentially experience minor or major complications after transplantation, which include infection, necrosis, persistent pain, unsightly wound, and sensory paralysis [4,5]. Furthermore, bone resorption after grafting is unavoidable [2,6]. Due to the limitations, great attention has been paid to develop an alternative approach for bone regeneration, namely bone tissue engineering.

1.1 Tissue Engineering Approach for Bone Regeneration

Recent advancement in regenerative medicine is featured by the application of stem cells in combination with scaffolding materials and bioactive molecules, termed "the tissue engineering triad" [7]. By optimal interplay of the triad, bone tissue engineering aims at creating transplantable biofunctional constructs, which are to exhibit osteoconductivity, osteoinductivity, and osteogenicity to orchestrate successful bone regeneration.

1.1.1 Mesenchymal stem/stromal cells for bone tissue engineering

Mesenchymal stem/stromal cells (MSC) are multipotent cells which can be isolated from nearly all adult tissues, such as bone marrow, adipose tissues, dental tissues, skin, liver, lung, pancreas, gastrointestinal tissues, and even brain tissues [8]. Within their niche, MSC interact with surrounding cells to condition the local environment through paracrine signalling, being involved in cell recruitment, vascularisation, and immunomodulation [9–12]. While their lineage commitment *in vivo* is limited to cells of a single germ layer or within the native tissue, MSC can be induced to differentiate into multiple lineages, such as osteoblasts, adipocytes, chondrocytes, neurons, and myocytes, *in vitro* with appropriate chemical, physical, and topographical stimuli [12–14] (Figure 1.1).

As of 2023, over 1,000 clinical trials on locally or systemically administered MSC have been completed or are ongoing globally, according to the database of the U.S. National Library of Medicine. Treated conditions include autoimmune disorders, acute and chronic inflammation, infection, injury, atrophy, and functional disorders in nearly all organs [15,16]. Thus far, no meta-analysis has found a correlation between MSC
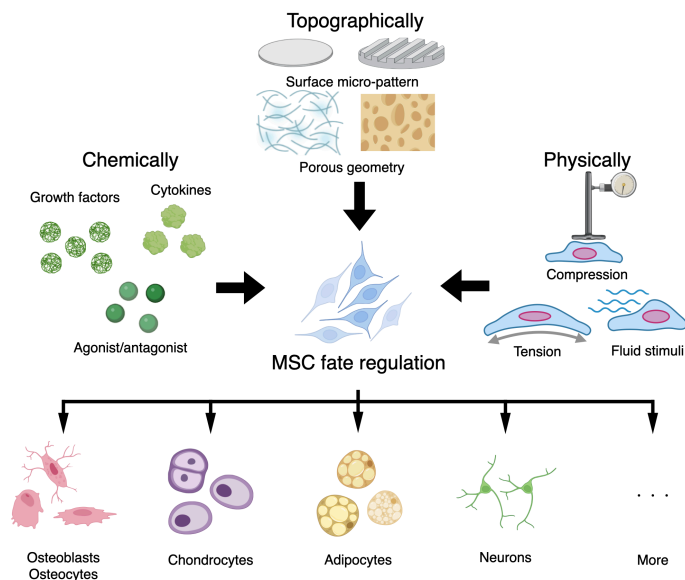
Figure 1.1 MSC fate determination regulated by chemical, physical, and topographical cues

transplantation and serious adverse effects such as multisystem organ failure, malignancy, infection, or death [17–21]. At present, several clinical trials are underway to investigate the use of MSCs for bone regeneration, and preliminary reports suggest improved bone regeneration and vascularisation [22–24].

In tissue engineering, MSC isolated from adult renewable tissues or biological waste are of particular interest due to their accessibility, minimally invasive procedures, low immunogenicity and oncogenicity, and minimum ethical concerns [25–27]. Bone marrow, adipose tissue, and dental tissue are considered attractive sources of MSC for maxillofacial bone reconstruction [28]. In particular, bone marrow-derived MSC (BMSC) have been the most thoroughly explored due to their inherited osteogenic privilege [29]. BMSC, which reside in perivascular niches in the bone marrow stroma, were originally identified as trilineal (*i.e.*, adipogenic, osteogenic, and chondrogenic) mesenchymal precursors, playing an intrinsic role in bone remodelling and repair [12,30,31]. Apart from their differentiation capacity, BMSC secrete a variety of trophic factors, such as insulin-like growth factors, transforming growth factors, vascular endothelial growth factors, fibroblast growth factors, and other signalling molecules, to regulate bone metabolism [32–34]. Despite their prominent characteristics, the downside of using BMSC for cell-therapies is associated with low yield. In healthy individuals, the frequency of BMSC is estimated to be approximately 0.1-1 in 10,000 nucleated cells in bone marrow, and their presence and functionality decreases with age [12,35–39]. Similarly, systemic diseases (*e.g.*, osteoporosis, osteoarthritis), as well as certain medications, are also associated with low yield, and impaired functionality [40,41].

Adipose tissue is considered an alternative source of MSC due to its abundance and accessibility [42]. Isolation of adipose-derived MSC (ASC) can be achieved through a minimally invasive procedure known as liposuction, which is typically performed under local anaesthesia. Not only is the frequency of ASC reportedly 500 to 1,000 times higher than BMSC, but ASC are also more proliferative in culture [43–46]. On the contrary, the osteogenic potential of ASC appears to be inferior to that of BMSC, and the tendency for spontaneous differentiation into adipocytes limits their application for bone regeneration [33].

Bone marrow aspiration and liposuction are routinely performed in clinical settings. However, although the occurrences of major complications and adverse effects are rare, the procedures are still invasive, causing a degree of discomfort for the patients. Dental tissues are gaining popularity as accessible sources of MSC because they can be obtained easily from exfoliated or extracted teeth, which would otherwise be discarded as biological waste. Dental stem cells, namely dental pulp stem cells (DPSC), periodontal ligament stem cells (PDLSC), stem cells from exfoliated deciduous teeth (SHED), stem cells from apical papilla (SCAP), and dental follicle stem cells (DFSC), are highly proliferative in culture and exhibit multilineage differentiation capacity, similar but not identical in potency to that of BMSC and ASC [47,48]. Dental stem cells have a high affinity for differentiation into osteoblasts, and their ability to regenerate bone has been demonstrated in preclinical and clinical studies [49,50]. However, to make the use of dental stem cells a regular part of daily practice, the establishment of a reliable tooth/dental cell banking system for long-term preservation is not to be procrastinated [51–53]. Looking at the current situation, it appears that the regulation lags behind the commercialisation of banking service. Despite some dental cell banks being already in operation in several countries, there is no standardised protocol for sample collection from patients in clinics, transport, cell isolation and expansion, cryopreservation, and characterisation after recovery. The cost of such services varies significantly among providers, and the effectiveness of cell recovery remains uncertain [52]. Therefore, tight partnerships between clinicians, researchers, industries, and regulatory bodies would be necessitated for translating dental stem cells into regenerative medicine.

1.1.2 Synthetic polymers as scaffolding materials for bone tissue engineering

Three-dimensional (3D) scaffolds are an integral component in tissue engineering because they provide structural support for cells to adhere, grow, migrate, and differentiate [54]. The scaffolds are fabricated from biomaterials, referred to as natural or synthetic materials used in medical applications to support, enhance, or replace damaged tissue or a biological function by the National Institute of Biomedical Imaging and Bioengineering and the National Institute of Health, USA. For bone

regeneration, scaffolds need to meet certain criteria: biocompatibility, biodegradability, optimal mechanical and architectural properties, sterilisability, osteoconductivity, and preferably osteoinductivity [55–58]. Within the framework of biomaterials, metals (*e.g.*, titanium, magnesium), ceramics (*e.g.*, calcium phosphate), natural and synthetic polymers, and their composites are often employed in bone tissue engineering [59]. Among the candidates, attention is increasingly being paid to synthetic polymeric biomaterials because of their formability, tunability in mechanical properties and biodegradability, and high tolerance for various functionalisation [60–62].

Synthetic polymers are macromolecules that are synthesised through chemical reactions in a laboratory setting, rather than occurring naturally. These include, but are not limited to, polyesters, polyurethanes, polyamides, and polycarbonates [63]. Compared to natural polymers, synthetic polymers exhibit superior mechanical strength, formability, and predictable *in vivo* degradability, which can be tailored for specific applications by altering chemical composition, crystallinity, and molecular weight [64]. Among the synthetic polymers, aliphatic polyesters, represented by polycaprolactone (PCL) and polylactic acid (PLA), are the most ubiquitously used as scaffolding materials in tissue engineering because both materials are accepted as a "Generally Recognized as Safe (GRAS)" polymer and approved for numerous medical and pharmaceutical applications by the U.S. Food and Drug Administration (FDA) [65–67]. While PCL is retained in a semicrystalline state at room temperature and has a melting temperature at 60 °C, PLA has a grass transition temperature and melting temperature of around 60 °C and 180 °C, respectively [68,69]. PCL's semi-crystalline nature contributes to its unique mechanical properties, such as higher elongation at break and greater ductility, whereas PLA is known for its stiffness and brittleness [70]. This difference in thermomechanical property determines the end-usage. The other aspect to mention is the biodegradability of PCL and PLA. Both polymers primarily undergo slow hydrolytic degradation due to the presence of long hydrophobic aliphatic chains. Complete degradation *in vivo* may take up to 5 years after implantation, depending on the initial crystalline structures, molecular weight, and scaffold architecture [69,71–74]. During hydrolytic degradation in vivo, the ester bonds are cleaved, resulting in the

formation of acidic by-products. For example, PCL generates caproic acid, succinic acid, valeric acid, and butyric acid, while PLA generates lactic acid, before ultimately being decomposed into carbon dioxide and water [75,76]. The acidification potentially elicits a prolonged local inflammatory response, although whether it acts for or against bone regeneration remains debatable [74].

Recently, aliphatic polycarbonate, poly(trimethylene carbonate) (PTMC), which was previously used exclusively for soft tissue engineering, has been introduced in bone tissue engineering. PTMC is an amorphous polymer with a glass transition temperature and melting temperature around -20 ℃ and 38-41 ℃, respectively [77]. Unlike the aliphatic polyesters, PTMC is barely hydrolysed. Instead, it rapidly undergoes enzymic degradation by lipase while yielding glycerol and carbon dioxide but no acidic biproduct [78]. With these unique properties, PTMC is frequently blended with aliphatic polyesters to tune the biodegradability and mechanical properties of polymeric scaffolds. In bone tissue engineering, copolymers of PLA and PTMC, namely poly(lactide-co-trimethylene carbonate) (PLTMC), merits particular attention for their osteoconductivity. When a PLTMC scaffold is transplanted into bone defects, bone formation initiates on the surfaces of the scaffolds and then bone growth extends outward [79]. This trend is not observed in PCL scaffolds, which are often encapsulated by fibrous tissues until bone ingrowth from the surrounding bone reaches the scaffold surfaces. Besides, PLTMC inherits high compatibility with various functionalisation methods from conventional synthetic polymers, which can improve material-cell and material-tissue interactions further [80,81].

1.1.3 Scaffold architecture and fabrication

Porous scaffolds that mimic the architecture of bone matrices offer an effective solution for successful bone regeneration [82]. Not only does a porous structure allow for nutrient transfer and vascularisation, but it also guides MSC fate towards the osteogenic lineage, with a key transcriptional factor for osteogenesis, Runt-related transcription factor 2 (Runx2), being upregulated [83–88]. The porous nature of scaffolds is usually described in terms of porosity, interconnectivity, and pore size.

Porosity, interconnectivity, and pore size are crucial factors governing the permeability of scaffolds, which in turn regulates mass transfer into and out of the scaffold [89]. Additionally, the efficiency of cell infiltration, tissue ingrowth, and vascularisation also depend on the porous characteristics of the scaffold [90,91]. In bone, it has been suggested that, after transplantation, highly porous scaffolds allow more osteoclasts, osteoblasts, and their progenitors to infiltrate into the pores and participate in bone formation, which results in an increase in bone matrix strength [92]. When determining the optimal pore size of bone graft materials, the results of an animal experiment conducted in a canine model, in which porous ceramics of different diameters were transplanted into the femurs, are often referred to [93]. After 4 weeks of transplantation, pores below 75 μm in diameter allowed for a small degree of fibrous tissue infiltration only. Pores between 75 μm and 100 μm were filled with fibrous tissue, but with a minor degree of osteoid. Importantly, the ingrowth of calcified bony tissue was observed only in pores above 100 μm where a greater number of blood vessels had grown into the pores. This *in vivo* study defined the minimum requirement of pore size for bone formation as 100 μm. Subsequent studies that implanted scaffolds with defined pore sizes reported that chondrogenesis preceded ossification in pores with a diameter of 90 μm to 120 μm, whereas direct ossification occurred in pores with a diameter of 350 μm and above [94–96]. In a separate study on ectopic bone formation, a higher degree of ossification was observed in pores ranging from 300 μm to 400 μm, compared to those below 300 μm and above 400 μm [97]. These findings suggest that large pores promote osteogenesis by providing better oxygenation through increased capillary infiltration, whereas small pores may lead to chondrogenesis due to local hypoxia caused by a scarcity of capillaries [98–100]. Porous architecture also influences the stemness and fate determination of MSC. Small pores below 100 μm in diameter are thought to represent a stem cell niche, where the environment maintains the stemness and self-renewal of MSC [101]. Larger pores, on the other hand, mimic vascularised mature matrices, which may facilitate cell differentiation [101]. In analogy to the conventional *in vivo* studies, scaffolds with pore size of larger than 100 μm provide an pro-osteogenic mechanoenvironment to MSC and therefore promote osteogenic differentiation *in vitro* [90]. Additionally, large pore size is advantageous for homogeneous cell distribution and

nutrient supply during cell culture because of improved permeability [102,103]. However, since pore size is negatively correlated with the surface area of the scaffolds, too large pores may attenuate the ability to carry cells and subsequent tissue regeneration [104]. In the context of load-bearing bone regeneration, excessive void spaces within the scaffold can lead to a decrease in mechanical properties, which may be also unfavorable [105,106]. Thus, it is generally accepted that highly porous scaffolds with pore size in the range from 100 μm to 800 μm are preferable for bone tissue engineering, although the optimal internal architecture may vary depending on various factors such as material selection, fabrication method, macrostructure, and the intended therapeutic outcome [90,107,108].

3D porous scaffolds act as an artificial extracellular matrix (ECM), providing mechanical and biochemical support to cells in the vicinity. The incorporation of 3D interconnected porous architectures into scaffolds can be achieved by various fabrication techniques. Electrospinning is a versatile technique widely used to produce nonwoven meshes of polymeric fibres ranging from nano- to micro-scale, by ejecting charged polymer melt or solution under high-voltage electric fields [109]. The resulting products can be designed to resemble the intrinsic architecture of bone ECM, which is predominantly composed of fibrillar collagens ranging in diameter from 1 μm to 5 μm [110,111]. Other representative methods for the fabrication of porous scaffolds include solvent casting/particulate leaching (or simply salt leaching), phase separation, freeze-drying, and gas forming techniques [112]. These methods are used singly or in combination to achieve highly porous structures. The salt leaching method is a simple and effective means of generating highly porous scaffolds. A porogen such as sodium chloride particles is mixed with a polymeric solution in a solvent. After the solvent is completely evaporated, the particles are leached from the construct to create pores [113]. The phase separation technique is based on the application of the thermodynamic properties of polymers [114]. In principle, when polymers are dissolved in a solvent and subjected to certain conditions, they become thermodynamically unstable, leading to the separation of polymer-rich and solvent-rich phases. The solvent-rich phase is then removed through extraction, evaporation, or sublimation, leaving the polymer-rich

phase solidified as the scaffold skeleton. The freeze-drying technique, as the name suggests, begins with freezing an emulsified polymeric solution in a solvent. This causes the crystallisation of the solvent, which then sublimates under a depressurised condition at low temperature. The gas foaming technique, on the other hand, does not require a solvent. Instead, it uses high-pressure CO_2 and occasionally high temperatures for the process. By pressurising and rapidly depressurising, dissolved CO_2 forms the kernels of the gas, which then grow into gas bubbles within the polymeric construct [115]. These conventional methods are proven to effectively generate porous architectures which meet the requirement for bone regeneration. However, a lack of controllability in macrostructure (*i.e.*, overall scaffold geometry) and microstructures (*i.e.*, pore size, pore orientation, pore distribution) is often cited as a drawback [112].

With the growing momentum towards personalised medicine, tailor-made scaffolds are increasingly in demand to meet patient-specific requirements. In recent years, additive manufacturing has emerged in the field of tissue engineering, allowing for the creation of patient-specific scaffolds using computer-aided-design (CAD) software and 3D printing in layers to form complex geometries with internal porous architectures [116]. The latest 3D printers developed for tissue engineering can achieve resolutions as fine as 10 μm, providing greater flexibility and precision in scaffold design compared to the conventional methods [117].

1.2 Mechanical Microenvironment in Bone and Bone Marrow

Since the 19th century when an anatomist, Julius Wolff, hypothesised that bone mass and architecture would adapt in accordance with mechanical stress, it has been accepted both empirically and scientifically that bone is receptive to biophysical stimuli [118]. The principle was incorporated into bone tissue engineering, where the triad concept was revisited and evolved into the "diamond" concept by including mechanical stimuli [119].

Bone growth during adolescence and bone homeostasis during adulthood are governed by physical activities, and routine exercise increases bone mineral density, bone mass, cortical area, and strength, while reducing marrow cavity fat [120,121]. During physical activities, bone and bone marrow are subjected to diverse mechanical stimuli exerted

by muscle contraction, gravitational loading (*i.e.*, compressive and tensile forces), altered hydrostatic pressure, and lymphatic drainage [122,123]. At a cellular level, these stimuli are exerted as, for example, compressive, tensile, and fluid-induced shear forces [124–126]. Osteocytes are principally responsible for mechanosensation and mechanotransduction, transmitting signal molecules to osteoblasts, osteoclasts, and their progenitors through a lacunar-canalicular network to propagate bone remodelling [125,127]. Their progenitors, namely osteoblasts and BMSC, are also mechanoresponsive, adapting their phenotype in response to mechanical stimuli such as substrate deformation, and fluid flow [128].

1.2.1 Mechanical stimuli in bone and bone marrow

Bone is primarily responsible for structural support against loads. Decrease in physical activity as a result of diseases, injury, sedentary lifestyle, microgravity in space, and aging tilts bone remodelling towards resorption, while moderate time-varying loads promote bone accretion [128]. Bone deformation caused by, for example, ground reaction force and muscle contraction can be explained as compressive, tensile, and shear strains [129]. *In vivo* measurement by implanting strain gauges demonstrated that light exercises such as walking or jogging generated peak strain of approximately 200 µε up to 1,000 µε (ε: change in dimension compared to the original dimension) in human tibias [130]. Strenuous activities that fell under infantry training such as uphill and downhill zigzag running recorded a 3-fold increase in strain compared to that during walking, but peak strain was maintained below 2,000 µε regardless of activity type [131]. In 1987, Frost H. M. postulated that balanced bone homeostasis would require functional strain within the range of 300 µε to 1,500 µε [132]. On the contrary, the strain below and above the range, up to 3,000 µε, would lead to bone resorption and bone accretion, respectively [132]. This theory has been well supported to date [133].

Interstitial fluid, which accounts for approximately 20% of body weight, plays a crucial role in transporting nutrients, gases, and waste products to and from cells through extracellular matrix [134]. In comparison to other tissues, interstitial fluid within a lacunar-canalicular network of bone exhibits a higher flow velocity due to the
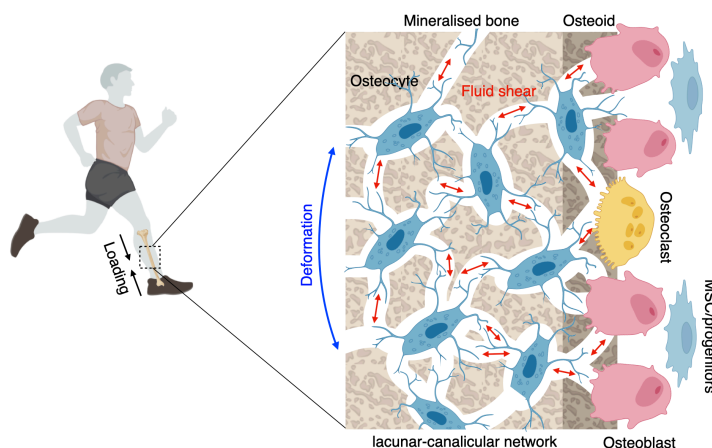
Figure 1.2 Fluid shear stress generated by physical activity in a lacunar-canalicular network
The loading force on a bone is primarily sensed by osteocytes through a change in interstitial fluid flow within the lacunar-canalicular network. This signal is then transduced into biochemical signals and transmitted to neighbouring cells. Adapted from Qin *et al.* (2020) [137].

confinement imposed by the surrounding mineralised tissue [124,135–137] (Figure 1.2). Mechanical loading generates pressure gradients that drive the flow of interstitial fluid from the compressive side of bone to the tensile side [138]. A numerical model estimated that shear stress in a lacunar-canalicular network could reach around 0.8-3 Pa under physiological loading conditions, and similar stress was also predicted on osteoblasts at bone-forming sites [136].

Fluid shear stress is the primary mechanical stimulus in bone marrow, owing to its rich vascular network comprising central venous sinus, nutrient artery, and marrow sinusoids [124]. The magnitude of shear stress in bone marrow is related to its viscosity (*i.e.*, yellow bone marrow or red bone marrow) and trabecular porosity (*i.e.*, healthy bone or osteoporotic bone) [139]. Computational models predicted that high-frequency low-magnitude mechanical stimulation (HFLMMS: 1 g, 30–50 Hz) at an amplitude of 1 g/10 μm would inflict shear stress of approximately 0.1-5 Pa in the bone marrow of long bones and vertebrae [140,141]. An *ex vivo* study using porcine femurs found that compression at a magnitude of 0.07-5 kPa, similar to physiological loading in human, generated shear stress at approximately 1.5-25 Pa in the bone marrow [142].

1.2.2   Mechanosensation and mechanotransduction for bone remodelling

In response to mechanical stimuli, osteocytes, osteoblasts, osteoclasts, and their precursors/progenitors coordinatively orchestrate adaptive changes in bone quantity and quality. Intercellular communication takes place through a lacunar-canalicular network where osteocytes are connected via their dendritic processes, forming a labyrinthine syncytium towards bone surfaces where osteoblasts, osteoclasts, and their precursors/progenitors reside [143]. Biochemical signals are transmitted largely through gap junctions [144].

Osteocytes, which account for over 90% of total bone cells and are approximately 10 times more populous than osteoblasts, act as a command post for mechanosensory and mechanotransduction processes in bone [127,145]. They are able to perceive biophysical signals through their cytoskeletons, dendritic processes, primary cilia, focal adhesions, ion channels, and various surface mechanoreceptors (*e.g.*, integrins) [146]. Upon sensing biophysical stimuli, osteocytes instantaneously release anabolic signals, such as nitric oxide (NO) and prostaglandin (PG) [147,148]. The signals then activate the canonical Wnt signalling pathway, which targets genes including Runx2, to propagate the adaptive changes in bone [147,148]. The role of osteocytes in bone adaptation in response to mechanical stimuli was clearly demonstrated by the conditional targeted ablation of osteocytes in transgenic mice using dentin matrix protein 1 (Dmp1) as a specific osteocyte marker [149]. Osteocyte ablation for a short-term period up to 2 weeks neither affected the population and functionality of osteoblasts nor osteoclasts, nor altered bone mass. Interestingly, osteocyte ablation prevented disuse-induced bone atrophy after 7 days of physical restraint, while it led to significant bone loss with increased osteoclast number and activity in wild-type counterpart. On the contrary, osteocyte deficiency did not inhibit load-induced bone formation, whereas osteoblast deficiency did [149,150]. These results suggest that osteocytes are indispensable for disuse-induced bone atrophy by regulating osteoclast activity, while load-driven bone formation could bypass osteocytes' command.

Not surprisingly, osteoblasts share mechanoreceptive features with their ancestral osteocytes [151,152]. Like osteocytes, osteoblasts immediately produce NO and PG upon mechanical stimulation *in vitro* and activate the canonical Wnt signalling pathway

[147,153]. Nevertheless, the role of osteoblasts in mechanosensation in bone seems limited compared to osteocytes. This is due to their lower frequency and biased distribution on bone surfaces. Given that osteoblasts reside on soft osteoid and newly mineralised bone surfaces, the fluid shear stress exerting on osteoblasts is estimated to be lower than that that experienced by osteocytes in a lacunar-canalicular network [154]. Furthermore, the sensitivity of osteoblasts to mechanical stimuli is reported to be inferior to that of osteocytes [155]. Osteoblasts are therefore considered to be an auxiliary entity in mechanosensation in bone. In fact, a computational model of load-induced trabecular bone remodelling showed that incorporating osteoblast-based surface remodelling had no additional effect on overall bone mass and architecture [156].

1.2.3   BMSC in response to physical activities in body

BMSCs, along with other bone-forming cells, play a supportive role in mechanically induced bone remodelling, despite being relatively rare [157]. In the bone marrow niche, Nestin-positive perivascular stromal cells have been identified as BMSC, which are capable of differentiating into multiple mesenchymal lineages when grown in an adherent culture [158]. These cells can alter their phenotype in response to the mechanical environment.

The *in vivo* response of BMSC to mechanical stimuli has been proven in various rodent models. In general, moderate exercise promotes their growth and osteogenic lineage commitment. For example, training on a treadmill or engaging in climbing exercises has been shown to enhance the colony-forming ability of BMSC, with the expression of anti-apoptosis regulators such as Survivin and B-cell lymphoma-2 upregulated [159–162]. Regarding differentiation, it was shown that BMSC in individuals undergoing long-term training upregulated osteogenic markers, such as Runx2, alkaline phosphatase (ALP), and Osteocalcin (Ocn), but downregulated adipogenic markers, such as Peroxisome proliferator-activated receptor gamma (PPARγ), CCAAT/enhancer binding proteins, and fatty acid binding protein [159,163,164]. Similarly, HFLMMS stimulated BMSC self-renewal and osteogenic differentiation. A study demonstrated HFLMMS applied at 0.2 g, 90 Hz for 15 minutes per day, 5 days per week, for 6 weeks,

increased the number of Stem cell antigen-1 (Sca1/Ly6)-positive stromal cells in bone marrow by approximately 40% [165]. These cells were found to upregulate Runx2 expression significantly but downregulated PPARγ expression. The mechanical regulation of BMSC *in vivo* is a complex process that involves multiple signalling pathways. Among these, the Bone morphogenetic protein (BMP)-Mothers against decapentaplegic (Smad) signalling pathway has been identified as a crucial mediator of the response of BMSC to mechanical stimuli. In trained subjects, BMSC exhibited a significant increase in the phosphorylation of Smad1, which is a key signal transducer for BMP receptors. [164]. However, when a selective inhibitor of the BMP-Smad pathway was locally injected during exercise, the promotive effects of the exercise on BMSC growth and osteogenic differentiation were negated [164]. Additionally, research suggests that the canonical Wnt signalling pathway also participates in *in vivo* fate determination [163].

1.3 Response of MSC to Extrinsic Mechanical Stimuli

It remains unclear whether mechanical stimuli directly regulate BMSC or indirectly via osteocytes. However, BMSC share some of the mechanoreceptive features exhibited by osteocytes, which are retained during *in vitro* culture [152,166]. This has motivated researchers to investigate the responses of BMSC, together with other types of MSC, to various mechanical stimuli, with the aim of stimulating targeted differentiation. Mechanical stimuli that have been studied for their effects on bone cells include fluid shear stress, substrate strain, direct compression, hydrostatic pressure, micro- and hyper-gravity, ultrasound, and electromagnetic field [167–169]. Among these, fluid shear stress has received the most attention due to its proximity to the physiological environment, where it acts as the primary biophysical stimulus for bone cells.

Most evidence on MSC mechanobiology comes from 2D monolayered dynamic cell culture models although cells may respond differently in a 3D environment [170].

1.3.1 Fluid shear stress as a principal biophysical stimulus

Interstitial fluid flowing along the canaliculi has been considered as a major biophysical stimulus to the osteocytes, as well as that flowing along the bone surfaces to the osteoblasts [137]. Likewise, BMSC reside in a mechanically dynamic niche where fluid shear stress can reach levels as high as 25 Pa [142,171]. Simultaneously, the cells are subjected to diverse biophysical stimuli including substrate strains apart from fluid shear stress, which are likely to act in combination rather than independently *in vivo*. The question to be answered is which stimulus triggers mechanotransduction of BMSC towards osteogenesis *in vitro* more effectively.

Besides shear stress, substrate strain is another important biophysical factor. Mechanical loading on bone causes compressive strain on one side of the substrate and tensile strain on the other, resulting in the compression or stretching of cells based on their position. Both fluid flow and substrate stain impose stress on cells and cause cellular deformation, albeit in different manners (Figure 1.3). Fluid flow applies stress on the cell surface and below the unbound cell membrane, whereas substrate strain places stress on the binding side of the cell through the adhesion receptors [172]. That is, cellular deformation, particularly in the innermost part, can be more effectively induced by fluid flow than substrate strain. According to an *in silico* study, the membrane displacement caused by physiological fluid shear stress of 0.6 Pa was estimated to be approximately 7.5 times greater than that by physiological substrate strain of 1,000 με [173]. Interestingly, the study calculated that, in order to induce similar cellular deformation to that by fluid shear stress of 0.6 Pa, substrate strain of approximately 5,000-8,000 με was required. This would far exceed the physiological strain level. The degree of cellular deformation is correlated with anabolic responses to stimuli. Fluid shear stress of 0.4-0.6 Pa instantly increased the production of NO and PGE2 by osteocytes and osteoblasts *in vitro*, but substrate strain did not increase the production
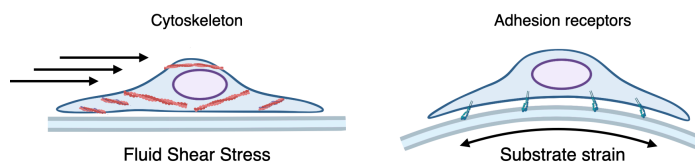
Figure 1.3 The perception of shear stress and substrate strain stimuli by cells
Shear stress is applied to the surface and submembrane region of cells, whereas substrate strain is exerted on the cell-matrix adhesion receptors. Adapted from Mullender *et al.* (2004) [172].

of these biomolecules, or did so only to a negligible extent, even at magnitudes as high as 5,000 με [155,173–176]. Despite some reports claiming that substrate strain within the physiological range could promote osteogenic differentiation, Owan *et al.* demonstrated that the degree of anabolic response was correlated with the increase in flow velocity caused by substrate displacement, rather than the magnitude or rate of strain itself [177]. Since then, tensile and compressive strains with supra-physiological magnitudes of 10,000-100,000 με have been frequently applied in osteoblast as well as MSC culture to induce osteogenic responses [178–182]. This magnitude is close to or exceeds the threshold for bone fracture strain [183].

Fluid shear stress and other biophysical stimuli are inextricably linked and may not be fully distinguishable *in vivo* as well as *in vitro*. However, it would be acceptable to conclude by the results from the conventional studies that fluid shear stress acts as a primary biophysical stimulus to trigger osteogenic responses.

1.3.2 MSC responses to fluid shear stress *in vitro*

Research in bone mechanobiology has revealed the basic responses of osteocytes and osteoblasts to mechanical stimuli. As the promise of stem cell therapy grows, the research focus has shifted to the mechanical control of the growth and fate of MSC since the 2000s [12]. As expected, fluid stimuli have received the most attention. To study MSC responses to fluidic stimuli, dynamic monolayered cell culture (*i.e.*, 2D) models that apply various flow patterns, such as steady, pulsatile, orbital, swirling or oscillatory flow, have often been employed (Table 1.1).

Due to the lack of knowledge about the mechanical sensitivity of MSC, a wide range of stress, varying from sub-millipascal to supraphysiological levels, has been tested. Generally, fluid shear stress at appropriate magnitudes has a supportive effect on the osteogenic potential of MSC. As in osteocytes and osteoblasts, the process of mechanotransduction in MSC begins with rapid production of NO and PGE2, and transient modulation of the canonical Wnt signaling in response to fluid shear stress [184–186]. Subsequently, the cells exhibit osteogenic characteristics, such as upregulation

Table 1.1 Summary of studies (2010–2022) on the effect of fluid shear stress on osteogenic differentiation in monolayer culture models

Species	MSC source	Substrate	Medium	Flow type	Flow condition	Shear stress	Time point	Growth	Upregulated osteogenic genes/PROTEIN	Downregulated osteogenic genes/PROTEIN	ALP activity	Calcium deposition	Other	Ref
Rat	Bone marrow	Glass	OM	Steady	2 hr/day Flow between Day 1 and Day 4	0.4 Pa	Day 4 (PCR) Day 21	NA	COL1, OPN	*runx2, bmp2*	NA	- (day21)	Lamin A ↑ Factin ↑	Guo et al. 2022
					2 hr/day Flow between Day 7 and Day 9	0.4 Pa	Day 10 (PCR) Day 21	NA	*col1* RUNX2, COL1, OCN, OPN	-	↑	↑ (day21)	Lamin A ↑ Factin ↑	
					2 hr/day Flow between Day 14 and Day 17	0.4 Pa	Day 17 (PCR) Day 21	NA	*alp, col1, ocn* RUNX2, COL1, OPN	-	↓ (day21)	↓ (day21)	Lamin A ↑ Factin ↑	
Human	Bone marrow	Well plate	OM	Orbital	6 hr/day	0.3-0.7 Pa	Day 5	-	NA	NA	↑	NA	Notch signalling ↑	Zhao et al. 2022
Mouse	Not specified	Micropatterned well plate	GM	Swirling	1 hr flow-5 hr interval	0.5-0.8 Pa	Day 3	NA	*alp, ocn, col1* ALP, OCN, COL1	-	↑	NA	YAP ↑ Apoptosis ∝ ALP	Jiao et al. 2022
Rat	Bone marrow	Well plate	OM	Oscillatory	1 Hz, 2 hr/day	0.0375 Pa	Day 7	-	*alp, ocn, runx2*	-	↑	NA	INTB1 ↑ FAK-ERK1/2 pathway↑	Jiang et al. 2021
							Day 14		NA	NA	NA	↑		
Human	Bone marrow	Polymer coverslip	GM	Steady	Continuous	10 Pa	Day 1	NA	*dmp1, bmp2, bsp, opn*	-	NA	NA	Hyaluronan synthases ↑	Reiprich et al. 2021
										-				
Rat	Bone marrow	Col-coated glass	OM	Steady	1 h flow-7 hr interval	1 Pa	Day 4	-	*alp, runx2*	-	↑	NA		Dash et al. 2020
					Continuous	0.0001 Pa	Day 4	↑	*alp, runx2*	-	↑	NA		
						1 Pa	Day 4	→	NA	NA	NA	NA		
						0.0001 Pa	Day 4	-	*runx2*	-	↑	↑ (?)		
Equine	Adipose	Well plate	GM	Oscillatory	0.67 Hz, Continuous	0.077 Pa	Day 10	↑	-	-	-	-		Elashry et al. 2019
							Day 21	↑	*alp*	*col1*	↑	-		
		Col-coated glass	OM	Oscillatory	0.67 Hz, Continuous	0.077 Pa	Day 10	↑	*ocn*	*alp*	↑	-		
							Day 21	↑			↑	↑ (?)		
Rat	Bone marrow	Col-coated glass	OM	Steady	3 day OM induction-20 min flow	1 Pa	Day 3	NA	NA	NA	↑	NA		Yue et al. 2019
Mouse	C3H10T1/2	Fibronectin-coated glass	OM	Oscillatory	2 Hz, Continuous	1 Pa	Hour 2	NA	*cox2, runx2, opn*	-	NA	NA	Ca2+ ↑	Stavenschi et al. 2007
					2 Hz, 4 hr/day, Day 1,2,4,5 only	1 Pa	Day 14	NA	COL1	-	NA	NA		
Human	Bone marrow	Fibronectin-coated 1 μm wells	OM	Steady	Continuous	1 Pa	Day 2	NA	RUNX2, OPN, ALP, OCN	-	-	NA	RhoA ↑ Factin↑ CD105↓	Sonam et al. 2016
Rat	Bone marrow	Col-coated glass	GM	Steady	Continuous	1 Pa	Hour 1	NA	NA	NA	↑	NA	Factin ↑ Ca2+ ↑	Lu et al. 2015
Mouse	Bone marrow	Col-coated glass	OM	Steady	40 min flow-10 min interval	1.2 Pa	Hour 3	NA	*sp7, alp, dlx5*	-	NA	NA	RUNX2 - TRPM7-Sp7 pathway ↑	Liu et al. 2015
Human	Alveolar Bone	Well plate	OM	Oscillatory	0.5 Hz, 10 min/day	0.001-0.002 Pa	Day 14	↑ (Day 4)	*runx2, col1, alp,ocn, opn*	-	↑	↑		Lim et al. 2012
					0.5 Hz, 2 hr/day	0.001-0.002 Pa	Day 14	- (DAY4)	*runx2, col1, alp,ocn, opn*	-	-	-		
Human	Bone marrow	Polycarbonate/Glass	GM	Steady	Continuous	2.2 Pa	Day 7	NA	*bmp2, bsp*	-	-	NA		Yourek et al. 2010
			OM	Steady	Continuous	2.2 Pa	Day 7	NA	*opn*	-	-	NA		
Human	Dental Pulp	Polylysine-coated glass	GM	Pulsatile	5 Hz, Continuous	0.6 Pa	Hour 1	NA	NA	NA	NA	NA	NO ↑ PGE2 ↑	Kraft et al. 2010

of osteogenic markers and ALP activity, particularly when cultured in an osteoinductive medium (OM). For example, BMSC flow experiencing fluid shear stress as low as 0.1 mPa upregulated Runx2 mRNA expression, accompanied by enhanced ALP activity, after 4 days of stimulation under steady [187]. Similar observations were reported in both physiological (*i.e.*, 0.5-2 Pa) and supraphysiological (*i.e.*, up to 10 Pa) magnitudes in steady continuous flow models [187–191]. Most studies using steady continuous flow models, albeit the most frequently used, focused, or may have had to focus, on short-term effects on osteogenic responses unless the fluid stimulus was extremely low (*i.e.*, 10 mPa and less). However, short-term changes may be considered transitory. Given that osteogenic differentiation is a sequential process of cellular events, longer observation would be particularly valuable. In fact, despite the induction of osteogenic responses, shear stress of 1 Pa was clearly shown to inhibit cell growth [187]. This observation would be linked to a study analysing cell kinetics under flow, where fluid shear stress arrested the MSC cell cycle at G0/G1 [192]. To balance the promotion of osteogenic responses and cell growth, fluid stimuli should be applied placidly and/or intermittently. Not only does it support cell growth, but intermittent steady flow may exert a robust promoting effect on osteogenic differentiation, both in the short-term and long-term, despite shorter stimulation periods per day compared to continuous flow models [187,193–195]. Alternatively, more physiological-like conditions can be reproduced by oscillatory or pulsatile models. Lim *et al*. reported that the osteogenic gene expression (*e.g.*, Runx2, Col1, Alpl, Ocn, and Spp1) and functionality (*e.g.*, ALP activity and calcium deposition) of MSC significantly increased after 14 days in an oscillatory flow model applied at the magnitude of 0.5 Hz, 1 mPa, only for 10 minutes per day [196]. This suggests that a short-term subtle fluidic stimulus may be sufficient to guide MSC to the osteogenic lineage *in vitro*.

1.3.3 Rho-ROCK dependant cytoskeletal regulation under stress

Cytoskeletal regulation is tightly associated with biophysical stimuli. Upon receiving mechanical cues, various signalling cascades are activated to alter their contractility, morphology, adhesion, and motility to adapt to the environment. The biochemical

mechanisms for regulating the cytoskeleton are highly conserved throughout evolution. Additionally, in regard to MSC in vertebrates, the state of the cytoskeleton reciprocally regulates fate determination. While it is evident that MSC become contracted and rigid as they undergo osteogenic differentiation, high cytoskeletal tension resulting from extrinsic biophysical cues can also promote osteogenic differentiation [197].
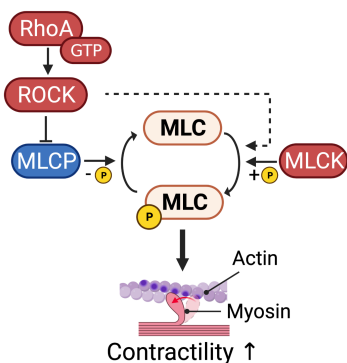
Figure 1.4 Rho-ROCK signalling pathway and cytoskeletal contraction

Among cell mechanosensory systems, the cytoskeleton is the largest mechanoreceptor, which senses cell deformation through the cell membrane [146]. Its contractility, required for cell morphogenesis, motility, cytokinesis, and polarisation, is predominantly regulated by the Rho-ROCK signalling pathway [198] (Figure 1.4). Extrinsic mechanical stimuli activate Rho GTPases via cellular deformation, adhesive receptor activation, and calcium influx, which then activate their effector molecule, Rho-associated protein kinase (ROCK). Subsequently, ROCK phosphorylates Myosin phosphatase target subunit 1 (MYPT1) of Myosin light chain phosphatase (MLCP) to inhibit its enzymatic activity while phosphorylating Myosin light chain (MLC) to trigger cytoskeletal contractility [199]. In addition, the Rho-ROCK signalling pathway also play a role in the formation and maturation of focal adhesions as a downstream target [200]. These morphological events are known to be involved in fate determination of MSC [201].

The osteoinductive effect of fluid stimuli is often observed with dynamic cytoskeletal reorganisation, demonstrated by changes in cell motility, polarity, and morphology [189,190]. Transcriptome analyses of different MSC sources (*i.e.*, BMSC and ASC), exposed to different flow magnitudes ranging from 0.05 Pa to 10 Pa, revealed differentially expressed genes regulating cytoskeletal organisation, cell motility, adhesion, as well as cell-cell and cell-matrix interactions [186,188,202]. The cytoskeletal modulation occurs rapidly and transiently as demonstrated by Kuo *et al.*, showing that

MSC cultured under unidirectional steady flow in a monolayered culture model reoriented their cell alignment parallel to the flow direction within 1 hour [186]. Interestingly, the polymerisation and depolymerisation of filamentous actin was associated with the regulation of the canonical Wnt signalling pathway, which suggests that cytoskeletal reorganisation indeed participates in MSC fate determination [186]. In addition, fluid shear stress at a physiological level has been shown to increase cytoskeletal tension through the activation of the Rho-ROCK signaling pathway in monolayered models [203–205]. This phenomenon is considered an adaptive change that enables the cells to maintain cytoskeletal integrity, motility, and adhesion in the dynamic conditions [204,205]. Although it remains unconclusive how Rho-ROCK mediated contractility is linked to the osteogenic phenotype, several plausible mechanisms have been proposed.

One of the most supported mechanisms is the mediation of Yes-Associated Protein (YAP) and Transcriptional coactivator with PDZ-binding motif (TAZ). YAP and TAZ are transcriptional coregulators, which control cellular plasticity and lineage determination during skeletal development and bone homeostasis directly and indirectly via an interplay with the Wnt signalling pathway [206,207]. They possess the WW domain, which recognises and bind to Pro-Pro-X-Tyr sequence motifs included in the activation domain of Runx2 [208]. Under fluid stimuli, YAP and TAZ are localised in the nuclei, which interact with Runx2 to stimulate Runx2-mediated transcription for osteogenesis [209–211]. The inhibition of ROCK prevented TAZ localisation in nuclei under flow and attenuated fluid shear stress-induced osteogenesis [210]. The ROCK-TAZ axis was also observed in tensile stress-induced osteogenic differentiation [212]. Crosstalk between the Rho-ROCK signalling and YAP in such a context remains unexplored, but the Rho-ROCK-YAP/TAZ-Runx2 signal axis is plausible given their functional analogy. The other probable mechanisms in the Rho-ROCK mediated Runx2 regulation include an interplay with the canonical and non-canonical Wnt signalling and BMP-Smad signalling pathways despite limited evidence [213]. For example, the canonical Wnt signalling pathway is known to be activated under fluidic stimuli in a Rho-ROCK dependent manner [186]. For a better understanding of the interplay between

cytoskeletal regulation and stimulated osteogenesis under fluid flow, further studies on signalling crosstalk are needed, ideally in a 3D platform which mimics the naïve bone-like environment.

1.4 3D Dynamic Cell Culture Platforms for Bone Tissue Engineering

The goal of tissue engineering is to create functional tissue-like constructs that can repair or replace damaged tissues in the body. For bone regeneration, 3D scaffolds are designed to represent a trabecular-like spongy, porous architecture. Compared to monolayered cell culture, scaffolds provide a biomimetic environment where cell-cell and cell-matrix interaction occur in a more physiological manner as *in vivo*. However, one of the main challenges in 3D cell culture is to ensure homogeneity inside the engineered constructs. For example, cellularisation of 3D scaffolds often results in heterogeneous cell distribution due to their low permeability, which prevents the infiltration of cell suspension into the interior [214]. This may cause competition for nutrients locally among the cells during culture. The efficiency of diffusion to the interior positively correlates with the thickness, surface hydrophilicity, and porous characteristics of the scaffold [215]. In addition, the transfer of nutrients, gases, and metabolic by-products in constructs largely relies on passive diffusion in a static condition, where adequate diffusion may only reach a few hundred micrometers from the surface of the scaffolds [215]. As a result, the interior of scaffolds may become an unsuitable environment for cells, hindering their scaling up in size for clinical application [216]. To overcome this challenge, the development of appropriate 3D dynamic cell culture platforms, commonly known as "bioreactors", has been in high demand as a competitive alternative to conventional static culture.

1.4.1   Development concepts of tissue engineering bioreactor systems

Tissue engineering bioreactors refer to devices that provide supportive culture conditions for cells in/on 3D scaffolds by aiding their biological processes [217]. Although bioreactors tend to be regarded as "black boxes" where cell culture is performed by trial and error, their design concepts often lie with the convergence of science and technology across multiple disciplines [218]. Several key development

concepts are commonly implemented when designing bioreactors for tissue engineering.

At a minimum, bioreactors must provide a suitable environment for cell growth, which include maintaining sterility, controlling temperature and humidity, providing appropriate aeration, and supplying necessary nutrients to the cells. To ensure sterility, most bioreactors are developed as closed systems: there is no interface between the inside of the bioreactor and the atmosphere, except for ventilation filters for gas exchange [219]. Furthermore, all components that come into contact with cells and cell culture medium must to be either sterilisable or disposable. To ensure optimal temperature, humidity, and gas concentration, bioreactors need to be either placed in regular CO_2 incubators or integrated with incubator systems. The former design allows for the system to be miniaturised and affordable, while the latter requires relatively complex systems equipped with, for example, heaters, gas ejectors, and humidifiers as well as various sensors for environmental monitoring, and therefore it tends to be larger and expensive, but possibly more versatile [220].

To address the diffusive limitation within the constructs, bioreactors designed for bone tissue engineering often incorporate mechanisms to generate medium movement, such as perfusion or agitation [221]. This is a critical feature in moving from monolayered cell culture to 3D cell culture. The ultimate 3D environment that tissue engineering aims to mimic is the *in vivo* environment where cells are surrounded by ECM. In vascularised tissues *in vivo*, the maximum distance between capillaries is approximately 200 μm, which corresponds to the diffusion limit of nutrients and gasses in the body [222]. The diffusion limit within a porous scaffold with an average pore size of 200 μm is also estimated to be 200-300 μm from the surface in a static condition [215]. Beyond that, cell necrosis may occur in the innermost part of the scaffolds due to a deficiency in nutrients and gasses. This justifies the need of dynamic mechanisms to improve mass transfer into 3D constructs rather than relying on passive diffusion driven by concentration gradient. Moreover, to mimic the *in vivo* biophysically dynamic environment, platforms that generate mechanical stimuli are preferred. These include mechanical

strain, hydraulic pressure, hydrostatic pressure, ultrasound, and electromagnetic field, which have been reported to promote osteogenic differentiation [219].

1.4.2 Flow bioreactor systems for bone tissue engineering

Applying fluid flow is a basic strategy to homogenise the environment and improve mass transfer during cell culture. In recent years, various flow bioreactors have been developed with different features for successful tissue engineering applications. The mainstream flow bioreactors include spinner flask bioreactors, rotating wall vessel bioreactors, and perfusion (laminar flow) bioreactors [219] (Figure. 1.5).
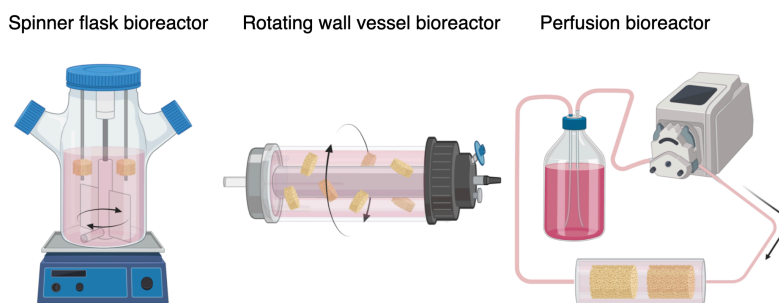
Figure 1.5 Common flow bioreactor systems used in bone tissue engineering

Spinner flask bioreactor is a simple agitation system used in bone tissue engineering. It consists of a glass flask, a filter cap to exchange gas, and an integrated stirrer or a magnetic stirrer placed at the bottom of the flask to generate swirling flow to aid in mass transfer. In the flask, cell-laden constructs are immobilised in needles or sample holders in the flask. It was reported, for example, that the proliferation and distribution of MSC in hydroxyapatite (HA) scaffolds were improved in a spinner flask bioreactor [223]. Noteworthily, in the study, the stimulatory effect on cell proliferation and osteogenic characteristics were more notable in scaffolds with smaller (*i.e.*, 200 μm) and larger pores (*i.e.*, 500 μm), respectively. This may suggest that mass transfer in the scaffolds is more likely to be improved with larger pore sizes, but fluid shear stress exerted on the surfaces can be greater with smaller pore sizes. A major drawback arises from the fact that a current is generated by a stirrer in a spinner flask bioreactor. It is known that the current generates large, nonhomogeneous fluid shear stress which

varies spatiotemporally [224]. Additionally, it produces a transient turbulent flow, which may damage cells [225].

Rotating wall vessel bioreactors were originally developed by the National Aeronautics and Space Administration (NASA) to investigate cell and tissue responses in microgravity environments [226]. Compared to spinner flask bioreactors, rotating wall vessel bioreactors generate uniform and homogeneous flows [225]. In the system, cell-laden samples are placed in a cylindrical chamber which rotates along the long axis. In bone tissue engineering, it has been used mostly for cell cultivation with microcapsules, microbeads, or microspheres. For example, Qiu *et al.* used the system as an effective means of loading cells onto microspheres, showing that BMSC co-cultured with ceramic microspheres in the bioreactor were able to attach and form ECM on the microspheres homogeneously [227]. The benefits of using rotating vessel bioreactors can also be reaped when using cell-laden microspheres. A study showed that, compared to static cell culture, dynamic culture in a rotating wall vessel bioreactor significantly improved matrix mineralisation, ALP activity, and Ocn and Spp1 expression in osteoblasts grown on poly(D,L-lactic-co-glycolic acid) (PLGA) microspheres [228]. However, when macroscale scaffolds are used, the drawback of the system becomes noticeable. In a comparative study, the cell proliferation, ALP activity, and calcium deposition of BMSC on porous PLGA scaffolds with a dimension of 12.7 mm × 6 mm were found to be significantly lower in a rotating wall vessel bioreactor, but higher in a spinner flask bioreactor, compared to static culture [229]. The unfavorable effect was thought to be due to cell damage caused by the collision of the scaffolds with the walls of the bioreactors. Therefore, macroscale scaffolds with high mass may not be suitable in rotating wall vessel bioreactors.

Perfusion bioreactors are systems that are being competitively developed in bone tissue engineering due to their high potential (Table. 1. 2). Compared to the aforementioned systems, perfusion bioreactors generate laminar flows that directly pass through the constructs, as if mimicking blood and interstitial fluid flows. These features allow perfusion bioreactors to greatly overcome limitations on nutrient and gas transport, compared to spinner flask and rotating wall vessel bioreactors where convective forces

Table 1.2 Summary of studies (2010-2022) on the effect of MSC culture in perfusion bioreactors for bone tissue engineering

Species	MSC source	Material	Scaffold	Medium	Flow type	Flow condition	Shear stress range	Time point	Growth	Upregulated osteogenic genes/PROTEIN	Downregulated osteogenic genes/PROTEIN	ALP activity	Calcium deposition	Other	Ref
Human	Bone marrow	Gelatin-Alginate	3D printed	OM	Steady	Contiuous, 7 ml/min	10-100 mPa	21 days	NA	NA	NA	NA	↑		Mainardi w t al. 2022
Human	Adipose	Bio-Oss®	Blocks	GM	Oscillatory	0.00167 Hz, 0.5 ml/min	NA	Hour 1	NA	NA	NA	NA	NA	Cell distribution↑	Engel et al. 2022
Rat	Bone marrow	LTMC	Salt-leached	GM	Steady	8 hr/day, 1.6 ml/min	<13.35 mPa (mean: 0.40 mPa)	Day 21	↓	runx2, sp7, bsp, alp, spp1, ocn, RUNX2, COL1	-	-	↑		Yamada et al. 2022
Human	Bone marrow	Col	Sponge	CM	Steady	3 ml/min overnight followed by 0.3 ml/min	NA	Week 5	NA	NA	NA	NA	↑	Cell distribution↑ Thicker mineralised layer	Pigeot et al. 2021
Human	Adipose	gelatin-βTCP	Form-casting	OM	Steady	Continuous, 1 ml/min	NA	Day 16	NA	runx2, ocn COL1, ALP	-	↑	NA		Nokhbatolfoghahaei et al. 2020
Human	Bone marrow	Chitosan-graphene	Freeze-dried	OM	Steady	1 hr/day, 1mL/min + 1% axial deformation (1 Hz)	Mean: 0.001 mPa	Day 7	↑	NA	NA	NA	↑		Lovecchio et al. 2019
Human	PT-2501	PLA-nHA	Freeze-dried	GM	Steady	1.21 mL/min for 20 hr followed by 0.3 ml/min	NA	Day 21	↑	runx2, sp7, alp, col1, spp1, ocn,	-	NA	↑		Luca et al. 2019
Rabbit	Bone marrow	Col-HA	Freeze-dried	GM/OM	Steady	4 hr/day, 10 ml/min + Mmagnetic field 15 Hz, 1 mT	NA	Day 14	NA	runx2, col1, ocn	-	↑	NA	in vivo bone formation↑ wnt1, tp6, βcatenin↑	Wang et al. 2019
Porcine	Bone marrow	Col-PLA-CaP	Freeze-dried	GM	Steady	Continuous, 0.03 ml/min for 6 hr followed by static culture 1-2 ml/min	NA	Day 7	↑	NA	NA	NA	NA	Cell distribution↑	Sauerova et al. 2019
Human	Adipose	PCL-nHA	Electrospun	OM	Steady	Continuous, 2, 4,5 ml/min	NA	Day 14	↓	runx2	-	↑	↑		Yaghoobi et al. 2019
Rat	Bone marrow	Fibrin	Beads	OM	Steadt	Continuous, 10 ml/min	NA	Day 14	NA	NA	NA	NA	↑	in vivo bone formation↑	Gandhi et al. 2019
Human	Umbilical cord	PLA-PEG	Salt-leached	OM	Steady	Continuous, 3.47 ml/min	NA	Day 21	↑	RUNX2, COL1, OCN	-	↑	↑		Birru et al. 2018
Human	hES	Gelatin-coated PU	Not specified	OM	Steady	Continuous, 3.47 ml/min	NA	Day 10	↑	NA	NA	↑	NA		Birru et al. 2017
Human	Bone marrow	PLG-HA	Salt-leached	OM	Steady	Continuous, 3 ml/min	NA	Day 21	↓	OCN	ibsp	NA	↑	*Compared to culture on orbital shaker	Mitra et al. 2017
Human	Bone marrow	PLCL	Salt-leached	OM	Steady	Continuous, 1.6 mL/min + 1-2% axial deformation (1-2 Hz)	0.125-0.175 mPa	Day 2	NA	spp1, sparc, col1, alp, bmp2	-	NA	NA		Ramani-Mohan et al. 2017
Rat	Bone marrow	PLCL	Salt-leached	Not specified	Oscillatory	0.5 Hz, 10 mL/min + 60 mmHg hydraulic pressure (0.5 Hz)	NA	Day 14	↑	ALP, OCN	-	-	↑		Tang et al. 2017
Human	Bone marrow	Silk fibroin	Salt-leached	OM	Steady	Continuous, 0.2 ml/min	<0.39 mPa	Day 40	↑	NA	NA	→	→		Vetsch et al. 2017
						Continuous, 12 ml/min	<24 mPa	Day 40	↑	NA	NA	↑	→		

Table 1.2 (Continued)

Species	MSC source	Material	Scaffold	Medium	Flow type	Flow condition	Shear stress range	Time point	Growth	Upregulated osteogenic genes/PROTEIN	Downregulated osteogenic genes/PROTEIN	ALP activity	Calcium deposition	Other	Ref
Human	Adipose	Decellularised bone	Granules	OM/GM	Steady	Continuous, 0.6 ml/min	<4 mPa	Day 21	↓	NA	NA	↑	NA		Egger et al. 2017
Human	Bone marrow	Col-Alginate	Casted	OM	Steady	Continuous, 3 ml/min	NA	Day 7/14	NA	bmp2, BMP2	-	NA	NA	*Co-culture with HUVEC	Nguyen et al. 2017
Rat	Bone marrow	Col-HA coated decellularised bone	Block	GM	Oscillatory	0.0167 Hz, 1 ml/min 30 min/day	NA	Day 21	NA	OPN, OCN	-	NA	↑ (1 week)		Chen et al. 2016
Human	hMPC 32F	Gelatin-coated PU	Foam	OM	Steady	2.5 ml/min, 2 hr on Day 3, 5, and 7	NA	Day 8	↓	NA	-	→	NA	*mRNA measured post 1h-perfusion	Filipowska et al. 2016
						2.5 ml/min, 2 hr on Day 5 only	NA		↓	bmp2, runx2	-	→	NA		
						2.5 ml/min, 2 hr on Day 7 only	NA		-	bmp2, runx2	-	-	NA		
						2.5 ml/min, 2 hr on Day 15 only	NA	Day 21	NA	bmp2, runx2, ocn	-	NA	NA		
Human	Bone marrow	PLCL	Salt-leached	OM/GM	Steady	1.6 ml/min for 1 hr followed by 0.8 ml/min for 4×5 min/hr	Mean: 0.076 mPa	Day 7	NA	alp, col1, runx2, spp1 (Day 1) col1, spp1 (Day 7)	-	NA	↑	Cell distribution↑	Kleinhans et al. 2015
Sheep	Bone marrow	CaP-coated Ti Al6V4	Mesh	OM	Steady	Continuous, 0.75 ml/min	NA	Day 14	↑	NA	NA	↑(Day7, 14)	NA		Garcia-Gareta et al. 2014
		HA	Granules	OM	Steady	Continuous, 0.75 ml/min	NA	Day 14	↑	NA	NA	↑(Day4, 7)	NA		
Rat	Bone marrow	glycoaminoglycan	Freeze-dried	OM	Steady	1 ml/min for 1 hr followed by 0.05 ml/min for 7 hr	<0.09 Pa	Day 2	NA	NA	NA	NA	NA	pgf, nox1↑	McCoy et al. 2013
Goat	Bone marrow	Starch-PCL	Melt-spun	OM	Steady	Continuous, 1 ml/min	NA	Day 14/21	↓	NA	NA	↑	NA	Viability ↓ ECM formation↑	Gardel et al. 2013
Human	Bone marrow	Chitosan-alginate	Beads	CM	Steady	Continuous, 1 ml/min	NA	Day 28	NA	NA	NA	NA	NA	Col2↑ Supported chondrogenesis	Forsey et al. 2012
Human	Adipose	Sponceram®	Block	GM	Steady	Continuous, 1 ml/min	Mean: 0.467 mPa	Day 60	-	spp1, ocn	-	NA	↑?		Weyand et al. 2012
Rat	Bone marrow	Polyamide-nHA	Sponge	OM	Steady	Continuous, 2 ml/min	NA	Day 21	↑	OCN	-	↑	NA		Qian et al. 2013
Human	hES (H9)	Decellularised bone	Block	OM	Steady	Continuous, 3.6 ml/min	Mean: 6 mPa	Week 5	↑	OPN	-	↑	↑	in vivo bone formation↑	Marolt et al. 2012
Rat	Bone marrow	PLG	Salt-leached	OM	Steady	Continuous, 3.9 ml/min	26.4 mPa	Day 15	-	opn, OPN	ocn↓	↑?	NA	PGE2↑	Kavlock et al. 2011
					Pulsatile	17 Hz, 3.1-6.1 ml/min (Mean: 3.9 ml/n)	21-42 mPa	Day 15	↓?	opn, OPN	ocn↓	↑?	NA	PGE2↑	
						83 Hz, 3.1-6.1 ml/min (Mean: 3.9 ml/n)	21-42 mPa	Day 15	↓?	opn, OPN	ocn↓	↑?	NA	PGE2↑	
Human	Bone marrow	Pro Osteon® 200μm pores	Block	OM (ViD3)	Steady	Continuous, 0.1 ml/min	NA	Day 21	↓	alp, spp1 (Day 14) opn (Day 21)	runx2, col1, ocn, bsp (Day 14, 21)	↑(Day 7) ↓(Day 14, 21)	NA	No cell growth in dynamic culture with <200 μm pores	Bjerre et al. 2011
		Pro Osteon® 500μm pores	Block	OM (ViD3)	Steady	Continuous, 0.1 ml/min	NA	Day 21	↓	spp1 (Day 14) opn, bmp2 (day 21)	alp, runx2, col1, ocn, bsp (Day 14, 21)	↓(Day7-21)	NA	Rounded morphology↑	
Rat	Bone marrow	RGD modified PLA	Salt-leached	OM	Steady	Continuous, 0.1 and 1 ml/min	NA	Day 8/16	↑(Day8) ↓(Day 16)	NA	NA	↑	↑		Alvarez-Barreto et al. 2010
Human	Bone marrow	Agalose	Casted	CM	Steady	Continuous, 400 μm/s	NA	Week 5	-	NA	NA	NA	NA	GAG↑ Col2↑ Cell distribution↑	Grayson et al. 2010
		Decellularised bone	Block	OM	Steady	Continuous, 400 μm/s	NA	Week 5	NA	COL, BSP	-	NA	NA	Cell distribution ↑	

may not reach the interior of porous scaffolds [229]. This particularly benefits long-term cell culture with low-diffusive scaffolds. In perfusion bioreactors, flow characteristics such as magnitude, duration (*e.g.*, continuous or intermittent), direction (*e.g.*, steady or oscillatory), and frequency (*e.g.*, pulsatile flow) are precisely adjustable [219]. Also, flow characteristics can be described more clearly with less variance, which links to the predictable operation of bioreactors. As a proof of concept, perfusion culture has been shown to promote the osteogenic properties of MSC through fluid shear stress, as well as to improve cell seeding efficiency and cell distribution within porous scaffolds [230–232]. Furthermore, perfusion bioreactors can be used to reduce the use of laboratory animals, as they can reproduce biophysical stimuli close to those *in vivo* [233]. For example, in biomaterial research, it has been suggested that the degradation profile of biomaterials under a perfusion-based dynamic environment is more compatible with that observed *in vivo* than under a static experimental condition [234]. Therefore, the application of perfusion systems allows for long-term cell-matrix interactions to be assessed in a physiologically relevant context without testing it *in vivo*.

1.4.3 Computational fluid dynamics - Modelling and simulation

Computational fluid dynamics (CFD) is a branch of engineering that uses computational algorithms based on mathematical theories to describe the behaviour of fluids under predefined conditions. More than a decade ago, Wendt *et al.* explicitly proposed that optimal experimental parameters in bioreactor-based studies should be determined by correlating experimental data with computational simulation, instead of relying on a trial-and-error approach [232]. Nowadays, CFD is increasingly recognised for its role in bioreactor design, scaffold design, experimental setup, and assessing fluidic impact on cells and scaffolds.

In bioreactor-based tissue engineering, fluid flow impacts cellular behaviours both indirectly through mass transfer and directly through forces generated by the flow. CFD allows researchers to better capture the hydrodynamic environment in any hypothetical setting while minimising trial-and-error attempts in practice. For example, it can be used to explore optimal scaffold designs for bioreactor application by comparing

different architectures with respect to fluid shear distribution and magnitude, mass transfer, and cell and tissue ingrowth [235–239]. With the optimised geometry provided, CFD allows a flow rate to be correlated with local fluid velocity and shear stress so that mass transfer and mechanical stimuli to which the cells are subjected can be estimated. The information would be otherwise obtained through on-site monitoring by directly placing milieu sensor probes within the constructs (*i.e.*, invasive sensing), or indirectly using techniques such as ultrasounds, spectrophotometry, or fluorimetry through the bioreactor walls (*i.e.*, non-invasive sensing) [240]. However, considering the size of tissue engineering scaffolds and the need for a sterile environment, available technology is still inadequate and impractical for monitoring spatiotemporally dependent fluidic behaviours during dynamic cell culture.

For a better understanding of the mechanical impact on cells under flow, fluid shear stress acting on cells can be evaluated by CFD approaches at the level of scaffolds at different resolutions. For the most accurate simulation, a microcomputed tomography (μCT)-based model may be utilised, where scaffold geometry is captured by μCT and reconstructed for simulation in CFD software [241]. This method enables a more precise representation of scaffold geometry, as well as a more realistic flow simulation. In the model, the fluidic interaction with the actual convoluted microarchitecture of the scaffolds can be simulated, allowing for spatiotemporal mapping of fluid shear stress throughout the scaffolds. However, this approach may not always be a feasible solution in reality due to the computational burden and solution time. Prior to computation, CFD meshing, a process of dividing the flow domain into a finite number of small, interconnected mesh elements which are used to solve the mathematical equations that govern fluid flow, is performed. As a scaffold architecture becomes more complex and tortuous, the mesh elements become inevitably finer and more numerous. Therefore, the degree of meshing in the μCT-based model tends to require high computational resources and a long solution time to solve the fluid dynamics [218]. Alternatively, a simplified method by idealising scaffold geometry with average pore size and expedient architectures have been shown to well approximate the fluid dynamics in the original scaffolds [242,243]. In the model, pore size and distribution are assumed to be

homogeneous throughout the scaffold, and as a result, the scaffold geometry can be reproduced by a simple domain with regularly shaped pores [243]. This results in fewer and coarser mesh elements required, reducing the computational demand greatly. Further simplification may be achieved by parameterising the geometry with porosity and permeability and defining it as a porous domain, where fluid flow is described by Darcy's Law [244–246]. These simplified methods suffice to roughly estimate the overall fluidic milieu, but are not suitable for depicting spatiotemporal variations in flow velocity or shear stress within the scaffold because these models do not preserve the microarchitecture [247].

1.5 Rationale for the Thesis

The knowledge gained in the mechanobiology in MSC fate determination has been successfully translated into research for cell-based bone regeneration, as evidenced by the recent surge in the number of perfusion bioreactors developed. Unlike conventional 2D models, 3D dynamic cell culture models aim for long-term culture in prospect of clinical applications.

It has been narrated anecdotally that 3D dynamic cell culture favours the growth and differentiation of MSC. However, when examining previous findings, the knowledge gained on optimal cell culture conditions and biological responses is still fragmented and sometimes contradictory. This complexity may be explained by the many variables involved, including material selection, biochemical and architectural characteristics, cell types, fluid properties, bioreactor-specific factors, and other environmental conditions. Additionally, the difficulty in estimating the hydrodynamic environment also hinders the correlation of fluidic effects to biological phenomena. In a 3D environment, fluid flow can act multiaxially and vary spatiotemporally, creating a more complex and possibly challenging environment for cells compared to a 2D environment, where fluid flow purely exerts shear stress acting uniaxially on cells. Although only a few studies have managed to estimate the magnitude of fluid shear stress during 3D dynamic culture, these studies indicate that flow stimuli below physiological levels are sufficient to induce phenotypic changes in MSC. However, it

remains unclear how MSC perceive the 3D perfusion environment and how this response leads to the modulation of cell growth and osteogenic differentiation. Furthermore, it is ambiguous whether fluidic stimulation alone triggers the differentiation in the absence of chemical osteoinductive agents, or whether what is known as "mechanically induced osteogenic differentiation" is truly equivalent to the conventional osteogenic differentiation induced pharmacologically. Therefore, there is a need for comprehensive analyses of mechanically induced osteogenic differentiation in a defined environment by using a reliable and predictable 3D perfusion bioreactor.

2. Aims and Hypotheses

The overall aim of this work was to establish a 3D dynamic cell culture platform under perfusion and elucidate BMSC responses to fluidic stimuli with respect to their growth and osteogenic properties. The series of the studies were designed and conducted with the hypotheses that subphysiological fluid stimuli would be sufficient to induce osteogenic differentiation of BMSC in 3D dynamic culture, but the mechanically induced osteogenic profile would differ from that induced by osteoinductive supplements.

The specific research objectives corresponding to each study are as follows:

Paper

1. To fabricate and characterise the 3D porous scaffolds of PLTMC with and without plasma surface modification and evaluate their cytocompatibility and *in vitro* osteoconductivity using BMSC in addition to scaffold characterisation for bone tissue engineering.

   I

2. To optimise dynamic culture conditions with the BMSC-laden PLTMC scaffolds and identify environmental variables in a 3D dynamic culture condition using a perfusion bioreactor for bone tissue engineering.

   II

3. To prove the concept that fluid stimuli at a subphysiological level is sufficient to induce the osteogenic differentiation of BMSC using the perfusion bioreactor.

   III

4. To comprehensively examine the effects of fluidic stimuli on the growth and osteogenic differentiation of BMSC in 3D dynamic culture condition, with a particular emphasis on cytoskeletal modulation and the induced osteogenic profile.

   IV

3. Summary of the Study Design

To achieve the objectives, a series of 4 studies were designed (Fig. 3.1).

Paper I addressed the fabrication and characterisation of the 3D porous scaffolds of newly introduced biodegradable copolymers in bone tissue engineering, PLTMC. Surface modification by oxygen plasma was conducted to improve hydrophilicity. On the scaffolds, BMSC were cultured to evaluate the cytocompatibility and *in vitro* osteoconductivity of the scaffolds.

Paper II addressed the optimisation and validation of a 3D dynamic cell culture platform using a perfusion bioreactor system developed for bone tissue engineering. Since "standard culture protocol" does not exist for 3D dynamic culture, environmental factors including medium volume, humidification, air bubble suppression, and optimal flow rate were defined based on cell viability and growth. Furthermore, to correlate mechanical stimuli with biological phenomena, different CFD approaches were compared for better predictive power and practicability.

Paper III was designed to prove the concept of mechanically induced osteogenic differentiation without the osteoinductive supplements using the optimised conditioned. The osteogenic responses of BMSC under flow were evaluated by their gene expression profile, ALP activity, and collagen and mineral deposition on the scaffolds.

Paper IV further investigated mechanically induced osteogenic differentiation. Osteogenic gene expression profile induced mechanically was compared to that induced chemically. Cytoskeletal modulation under flow was evaluated comprehensively by gene and protein expression profiles, enzymatic activity, and cell morphology, and the role of the modulation in mechanically induced osteogenic differentiation was assessed by the pharmacological inhibitors of Rho, ROCK, MLCK, and Myosin II.

Figure 3.1 Schematic illustration of the study design in this thesis
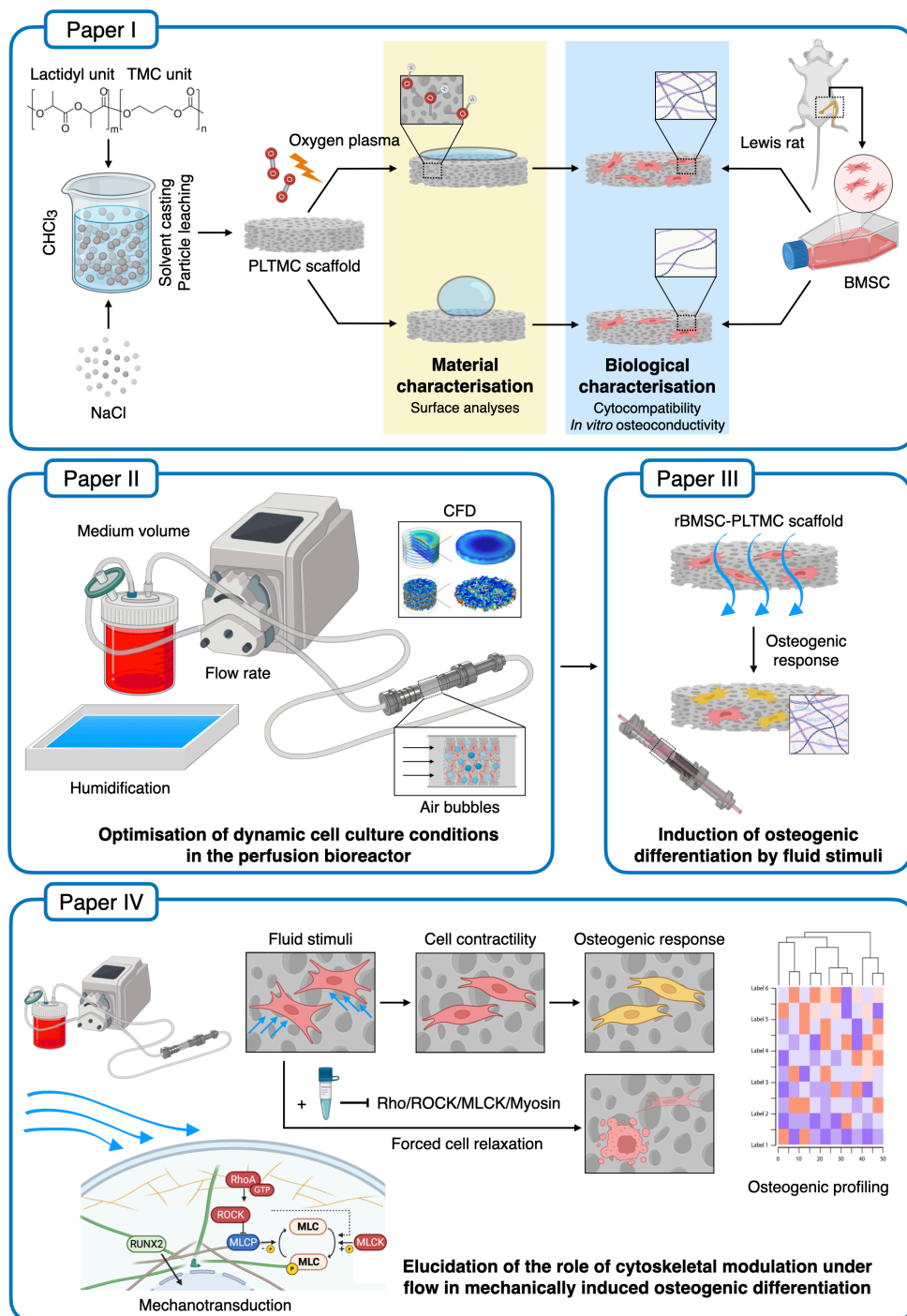
4. Materials and Methods

The methods used in the studies were selected based on their credibility, sensitivity, availability, and reproducibility in line with current golden standards where applicable (*e.g.*, BMSC characterisation by flow cytometry and multilineage differentiation assays). Biological phenomena were evaluated through gene expression at the mRNA and protein levels, which were further confirmed by cellular functionality, such as enzymatic activity, matrix formation, and calcium deposition.

This section selectively focuses on the experimental methodologies that are particularly significant for drawing conclusions in the thesis due to space limitations. Research methods not covered in detail in this section are described in the corresponding paper(s). The methods used in the thesis are listed in the Table 4.1.

Table 4.1 List of methodologies utilised in the thesis

Method	Purpose/Assessment	Paper
PLTMC Scaffold Fabrication and Characterisation		
Solvent casting/Particle leaching	Scaffold fabrication	**I- IV**
Oxygen plasma activation*	Surface modification	**I**
Fourier transform infrared spectroscopy*	Surface chemistry	**I**
Scanning electron microscopy*	Surface topography	**I**
Water contact angle measurement*	Hydrophilicity analysis	**I**
Micro-computed tomography	Topographical analysis	**I-IV**
BMSC Isolation, Expansion and Characterisation		
BMSC isolation from Lewis rats	Cell isolation	**I-IV**
Cryopreservation	Cell preservation	**I-IV**
Cell counting	Growth assessment	**I-IV**
Monolayered culture	Cell expansion	**III**
Pellet culture	Chondrogenic induction	**III**
Micromass culture	Chondrogenic induction	**III**
Flow cytometry	MSC characterisation	**III**
Multi-lineage differentiation	MSC characterisation	**III**
Cytoskeletal staining with Phalloidin	Morphological assessment	**I-IV**
Dynamic Cell Culture in the Perfusion Bioreactor		
Dynamic cell culture	Dynamic cell culture	**II-IV**
***In silico* Modelling**		
CFD simulation	Fluid flow characterisation	**II-IV**
***In vitro* Assessment of Cell Viability and Growth**		
Trypan blue staining	Viability analysis	**II, IV**

Live/Dead staining	Viability analysis	**II**
Crystal violet staining	Cell distribution analysis	**II, IV**
Double-strand DNA quantification	Cell proliferation analysis	**I-IV**
Immunofluorescence (PCNA, Ki67)	Cell proliferation analysis	**I, II**
EdU incorporation assay	Cell proliferation analysis	**IV**

In vitro Assessment of BMSC Osteogenic Differentiation

Alkaline phosphatase activity assay	Enzymatic activity analysis	**I-III**
Alkaline phosphatase staining	Enzymatic activity analysis	**IV**
Alizarin red S staining	Mineralisation analysis	**I-IV**
RT-qPCR (Runx2, Col1a1, Sp7, Alp, Bsp, Ocn, Bmp2)	Quantification of mRNA (Osteogenic markers)	**I-IV**
RT-qPCR (CD44, CD90, CD73)	Quantification of mRNA (Stem cell markers)	**III**
Osteogenic gene expression array (mRNA)	Osteogenic profiling	**IV**
Immunofluorescence (Runx2, COL1)	Protein expression analysis	**I, III, IV**

In vitro Assessment of Cytoskeletal Modulation Under Flow

Cytoskeletal staining with Phalloidin	Morphological assessment	**II-IV**
Immunofluorescence (αTubulin, NM2A, NM2B, pMLC, ROCK1)	Morphological assessment &Phosphorylation analysis	**III, IV**
ROCK activity assay	Enzymatic activity analysis	**III, IV**
RT-qPCR (RhoA, Rock1, Rock2, Mylk)	mRNA expression analysis (Cytoskeletal regulators)	**III, IV**
Cytoskeletal gene expression array (mRNA)	Cytoskeletal profiling	**IV**
Cytoskeleton antibody microarray (Protein)	Cytoskeletal profiling	**IV**

Pharmacological Treatment

Rhosin hydrochloride	Rho GTPase inhibition	**IV**
Y27632 dihydrochloride	ROCK inhibition	**IV**
MLCK inhibitor peptide 18	MLCK inhibition	**IV**
Blebbistatin	Myosin II inhibition	**IV**
Narciclasine	Rho-ROCK activation	**IV**
Calyculin A	MLCP inhibition	**IV**

Bioinformatics

Gene set enrichment analysis	Functional profiling	**IV**
Principle component analysis	Osteogenic profiling	**IV**

Image Acquisition and Quantification

Optical microscopy	Visualisation	**I-IV**
Laser scanning confocal microscopy	Fluorescence visualisation	**I-IV**
Image analysis	Image quantification	**I-IV**

Other methods

Hematoxylin staining	Nucleic acid staining	**III**
Oil Red O staining	Lipid staining	**III**
Alcian Blue staining	GAG staining	**III**
Cryosection	Histology preparation	**III**

* The experiment was conducted by collaborators at FHI, Germany.

4.1 Ethics Statement

The use of animals for the studies was approved by the Norwegian Animal Research Authority (local approval number 20146866) and conducted in compliance with the European Convention for the Protection of Vertebrates used for Scientific Purposes.

4.2 Scaffold Fabrication and Characterisation

4.2.1 Material selection

Synthetic polymers typically exhibit superior mechanical properties and stability compared to their natural counterparts, which make them suitable materials for scaffolding for bone tissue engineering. PLTMC, a recently introduced copolymeric material in tissue engineering, has demonstrated excellent cytocompatibility and reduced chronic inflammation after implantation due to the production of fewer acidic by-products during degradation than polyesters used alone [248]. its lower glass transition temperature provides greater flexibility at room temperature, which facilitates handling and shaping of the material [249]. Therefore, a medical grade copolymer, poly(L-lactide-co-trimethylene carbonate) 70:30 (PLTMC: RESOMER® LT706 S, Evonik, Germany) was selected as a scaffold material for the studies [79,248].

4.2.2 Fabrication of PLTMC 2D discs 3D porous scaffolds (**Paper I-IV**)

For the surface characterisation of PLTMC, 2D flat discs were fabricated by casting dissolved PLTMC in chloroform into glass petri dishes.

For the fabrication of 3D porous scaffolds, a solvent casting/particle leaching technique was used. A gram of PLTMC (dry weight) was dissolved in 10 ml of chloroform and then mixed with 10 grams of sodium chloride particles sieved to a size range of 90 to 600 μm in a glass dish with a10-centimeter diameter (Figure 4.1 A, B). After slow solvent volatilisation, the scaffolds were punched to 10 mm (Paper I) and 12 mm (Paper II-IV) diameters (Figure 4.1 C). This resulted in thicknesses of approximately 0.3 mm and 1.2 mm, respectively. The salt-containing scaffolds were thoroughly washed in water for 3 days to leach the particles.

Prior to cell seeding, the samples were sterilised by 70% ethanol followed by 2 hours of UV irradiation.

Figure 4.1 Fabrication process of PLTMC 3D porous scaffolds
(A, B) PLTMC was dissolved in chloroform and mixed with sodium chloride. After volatilisation, PLTMC scaffolds were punched to a diameter of 10-12 mm. (C) The scaffolds exhibited a highly porous nature after salt leaching.

4.2.3 Surface modification by oxygen plasma irradiation (**Paper I**)

To improve cell-scaffold interaction, the surfaces were modified by oxygen plasma irradiation (100 kHz, 350 W, 0.3 mbar, 12 sccm O_2) for 1, 3, or 5 minutes using a plasma chamber (Pico Plasma System, Diener electronics, Ebhausen, Germany) at FHI, Germany.

4.2.4 Characterisation of surface chemistry, topography, and hydrophilicity (**Paper I**)

The surface chemistry and topography of PLTMC discs and scaffolds were evaluated using attenuated total reflectance-Fourier transform infrared spectroscopy (ATR-FTIR: FT/IR-4100, Jasco, Germany) and scanning electron microscopy (SEM: CrossBeam 340, Zeiss, Germany), respectively, both conducted at FHI, Germany. The FTIR spectra were analysed using the DrawSpectrum 1.7.0. The chemical bonds present in the samples were identified by comparing the characteristic absorption peaks observed in the FTIR spectra with the Infrared Spectroscopy Absorption Table provided by the LibreTexts library (NICE CXone Expert, USA).

Surface hydrophilicity was evaluated by measuring water contact angles on the PLTMC discs by a contact angle goniometer (OCA 15EC, Dataphysics, Filderstadt,

Germany) at FHI, Germany. Additionally, medium droplet retention on the 3D PLTMC scaffolds was assessed.

4.2.5 Scaffold topographical analysis by μCT (**Paper I-IV**)

The scaffolds underwent microcomputed tomography (μCT) scanning using an X-ray tube voltage of 40 kV and a current of 250 μA at a 10 μm spatial resolution (SkyScan 1172, Bruker-MicroCT, Belgium). The CT data was processed, and the porous features of the scaffolds were characterised using Bruker CT-Analyser (CTAn) software for topographical analysis. The representative images were then exported as a .stl file for subsequent in silico analysis (See Section 4.5).

4.3 BMSC Isolation, Expansion, Differentiation, and Characterisation

4.3.1 BMSC isolation and expansion (**Paper I-IV**)

BMSC were isolated from the femurs of Lewis rats. Briefly, the rats were euthanised by carbon dioxide (CO_2) inhalation followed by cervical dislocation. The femurs were washed in PBS, and then the soft tissue attached to the bone was carefully removed. The articular heads were excised to access the marrow cavity, and the femoral bone marrow was then flushed using PBS perfusion. Subsequently, the marrow extracts were minced, plated, and incubated in cell culture flasks containing minimum essential medium (αMEM: 22571, Gibco, USA) supplemented with 2% penicillin/streptomycin (P/S) and 10% fetal bovine serum (FBS) at 37 °C in a 5% CO_2 humidified atmosphere. On the following day, medium was refreshed with a standard growth medium consisting of αMEM with 1% P/S and 10% FBS.

The cells at passage 1-2 were cryopreserved in a freezing medium consisting of 70% αMEM, 20% FBS, and 10% Dimethyl sulfoxide (DMSO) before being slow cooled at a rate of -1 °C per minute in a Mr. Frosty™ container (5100, ThermoFisher, USA). Once the temperature reached -80 °C, the cells were transferred in liquid nitrogen. BMSC at passage 3-5 were used for the experiments.

4.3.2 Multilineage differentiation (**Paper III**)

The multipotency of isolated BMSC was evaluated by assessing their ability to differentiate into osteogenic, adipogenic, and chondrogenic lineages.

For osteogenic differentiation, BMSC were stimulated in an osteogenic medium consisting of the growth medium supplemented with 10 nM dexamethasone (D4902, Merck, USA), 10 mM β-glycerophosphate (G9422, Merck, USA), and 173 μM L-ascorbic acid (A8960, Merck, USA) for 21 days. The osteogenic differentiation was confirmed by Alizarin Red S staining.

For adipogenic differentiation, BMSC were stimulated in an adipogenic medium consisting of the growth medium supplemented with 100 nM Dexamethasone, 10 μg/ml Insulin (I9278, Merck, USA), 0.2 mM Indomethacin (17378, Merck, USA), and 0.5 mM 3-Isobutyl-1-methylxanthine (I5879, Merck, USA) for 14 days. The adipogenic differentiation was confirmed by Oil Red O staining.

For chondrogenic differentiation, pellet culture and micromass culture methods were applied using chondrogenesis-induction medium (CCM000/CCM020, R&D Systems, USA) in accordance with the manufacture's protocol. The chondrogenic differentiation was confirmed by Alcian Blue staining.

4.3.3 MSC characterisation by flow cytometry (**Paper III**)

The expression of putative MSC markers was evaluated by flow cytometry. BMSC were collected in suspension and incubated in blocking buffer consisting of staining buffer (BUF0730, Bio-Rad, USA) with 0.5% bovine serum albumin (BSA: 37525, Thermo Scientific, USA), and 2% FBS for 1 hour at 4 ℃. BMSC were then incubated with primary antibodies for 30 minutes at 4 ℃. Isotype control antibodies were served as negative controls. Subsequently, the cells were centrifuged at 300 rcf for 5 minutes at 4 ℃ and washed in the staining buffer three times. For the cells tagged with unconjugated primary antibodies, secondary antibodies were applied followed by the centrifugation and washing steps. The antibodies used are listed in Table 4.2.

The samples were processed on a BD Accuri C6 flow cytometer (BD Biosciences, USA) and analysed using FlowJo 10 software (BD Biosciences, USA).

Table 4.2 The list of antibodies used for MSC characterisation

Target	Isotype	Conjugate	Ref. No	Manufacturer	Dilution
Primary antibody (Host species: mouse unless specified)					
CD44H	IgG2aκ	-	203901	BioLegend	1:100
CD73	IgG1κ	-	551123	BD Pharmingen	1:100
CD90	IgG1κ	PE	551401	BD Pharmingen	1:100
Sca1*	Polyclonal	-	AB4336	Merck	1:500
CD34	IgG2aκ	FITC	11034182	eBioscience	1:100
CD45	IgG1κ	PE	202207	BioLegend	1:100
CD79	IgG1κ	PE	12079241	eBioscience	1:100
Stro1	IgMλ	-	14668882	Invitrogen	1:100
Isotype control antibodies (Host species: mouse)					
	IgG1κ	-	554121	BD Pharmingen	1:100
	IgG1κ	PE	400111	BioLegend	1:100
	IgM	-	14475282	Invitrogen	1:100
	IgG2aκ	-	401501	BioLegend	1:100
	IgG2aκ	FITC	400207	BioLegend	1:100
Secondary antibody (Host species: goat)					
Mouse IgG		AF 488	A11001	Invitrogen	1:500
Rat IgG		AF 488	A11008	Invitrogen	1:500
Mouse IgM		AF 647	A21238	Invitrogen	1:500

Host species: Mouse *Host species: Rat, AF: Alexa Fluor™

4.4 Dynamic Cell Culture in the Perfusion Bioreactor

4.4.1 Perfusion bioreactor system and its configuration (**Paper II-IV**)

The perfusion bioreactor used in the studies was designed and developed at FHI, Germany, for the automated production of bone tissue engineering constructs, based on a previously introduced generic modular bioreactor platform [220]. It consists of an integrated incubator system and monitor control units where interlinked analog-to-digital and digital-to-digital communication are allowed (Fig. 4.2 A, B).

The incubator system is equipped with environmental sensors (*e.g.*, CO_2, O_2, pH, pressure, and temperature), a heating pad, a gas ejector, fans, and peristaltic pumps to
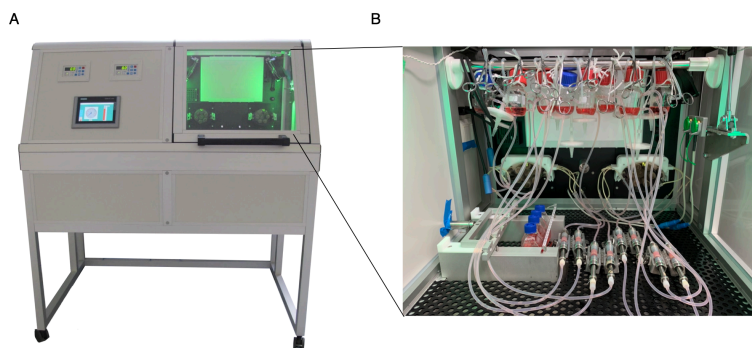
Figure 4.2 Perfusion bioreactor system used in the studies
(A) The perfusion (laminar flow) bioreactor developed at FHI was utilised in the studies. (B) A representative experimental setting for 3D dynamic cell culture.

ensure an optimal and stable culture environment. Medium reservoirs and culture chambers, where the scaffolds were placed, were connected by silicon tubes which were attached to the peristaltic pumps responsible for perfusing the culture medium at given flow rates.

The monitor control human-machine interface displays the environmental factors measured by the sensors on the attached monitor and allows for adjustments where necessary. The fluid pattern can also be precisely tuned, with options for continuous or intermittent flow, unidirectional or bidirectional flow, steady or oscillatory or pulsating flow at any frequency and magnitude.

4.4.2 Dynamic cell culture using the perfusion bioreactor (**Paper II-IV**)

Before commencing dynamic cell culture, the basic environmental parameters, such as medium volume, humidification, and air bubble suppression measures, were empirically optimised in **Paper II** by comparing different culture conditions.

To mechanically stimulate BMSC, cell-laden PLTMC scaffolds were placed in the sample chambers, in which different flow patterns were applied (Table 4.3). In summary, **Paper II** disclosed optimal dynamic culture conditions obtained by exploring various flow rates and stimulation durations with a particular focus on cell viability and growth, as well as their osteogenic responses. **Paper III** adopted 2

promising flow conditions, namely steady intermittent flow at 0.8 ml/minute and 1.6 ml/minute for 8 hours a day, to investigate BMSC growth and osteogenic differentiation. **Paper IV** explored the role of cytoskeletal modulation in mechanically induced osteogenic responses under steady intermittent flow at 1.0 ml/minute.

In the incubator system, atmosphere was maintained at 37 °C with 5% CO_2. The growth medium (*i.e.*, without the osteoinductive supplements) was used unless otherwise mentioned.

Table 4.3 The list of flow patterns applied in the studies

Flow rate	Duration per day	Flow type	Paper
0.8 ml/minute	8 hours	Steady	**II, III**
	24 hours	Steady	**II,**
1.0 ml/minute	8 hours	Steady	**IV**
1.6 ml/minute	8 hours	Steady	**II, III**
	24 hours	Steady	**II**
3.2 ml/minute	8 hours	Steady	**II**

4.5 *In silico* Modelling for CFD simulation

4.5.1 General methodology and theories for *in silico* modelling (**Paper II-IV**)

The CFD simulation was performed using COMSOL Multiphysics version 5.6-6.0 (COMSOL AB, Sweden). In brief, the geometry of the sample chamber was computationally reproduced where a scaffold domain was placed. The scaffold domain was modelled by simplified geometry or μCT geometry approach as described in the section 4.5.2-3. Once the geometry was modelled, it was meshed into fine tetrahedral elements for computation (Fig. 4.3).

In the model, the mechanical properties (*i.e.*, dynamic viscosity and density) of a fluid domain were assumed to be comparable to water at 37 °C. No slip boundary condition was prescribed on solid walls. At the inlet of the sample chamber, 0.8 ml/minute, 1.0 ml/minute, 1.6 ml/minute, or 3.2 ml/minute was prescribed according to the experimental conditions specified in the previous section. At the outlet, a static
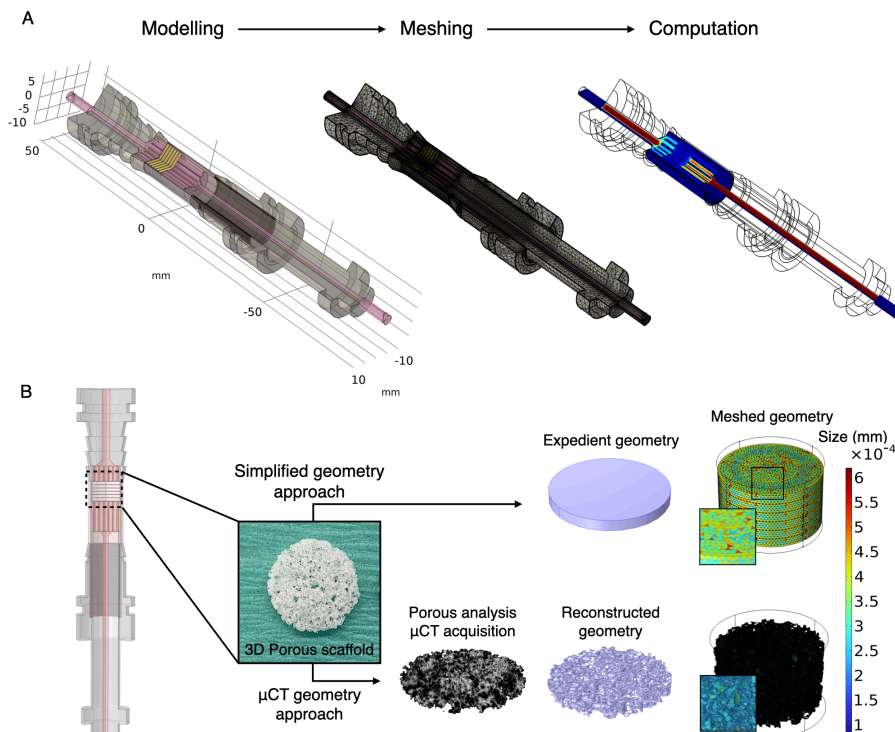
Figure 4.3 General workflow of CFD simulation using simplified and μCT geometry approaches

(A) The workflow for in silico modeling and simulation. (B) The estimation of fluid shear stress on the scaffold surface was performed using both expedient and μCT geometry approaches. The μCT geometry approach resulted in significantly finer mesh elements, increasing the computational burden for solving the model.

pressure, $P_0 = 0$ was prescribed. In paper **IV**, a pressure drop over the scaffolds was initially calculated using a simplified model based on the previously proposed "multiscale CFD approach" for more accurate simulation [250]. A static pressure of 8.6 Pa was defined as a boundary condition at the surface of the scaffold nearest to the outlet.

The fluid domain was defined as incompressible Newtonian fluid flow, which is governed by the Navier-Stokes equation and the continuity equation and as follows:

$$\rho(u.\nabla)u = \nabla.[-pI + K] + F \qquad \text{---(i)}$$

$$\rho \nabla.u = 0 \qquad \text{---(ii)}$$

where ρ is the fluid density, u is the fluid velocity, ∇ is the nabla operator, p is the pressure, I is the identity tensor, K is the stress tensor, and F is the body force per unit volume. The stress tensor, K is described as:

$$K = \mu(\nabla u + (\nabla u)^T) \qquad\qquad \text{---(iii)}$$

where μ is the dynamic viscosity of the fluid and $(\nabla u)^T$ represents the transpose of the velocity gradient tensor. The equation (i) is the Navier-Stokes equation for an incompressible fluid, which describes the motion of a fluid under the combined effects of pressure, viscosity and body forces. The equation (ii) is the continuity equation for an incompressible fluid, stating that the divergence of velocity is zero and therefore, mass is conserved in the flow. The equation (iii) is the stress tensor equation, stating that the stress on a fluid is related to the rate of deformation tensor in the case of a Newtonian fluid.

Fluid shear stress at a boundary of a fluid in motion was described by the stress tensor equation as follows:

$$\tau = \mu \frac{\partial u}{\partial n}$$

where τ is the shear stress at the boundary and $\frac{\partial u}{\partial n}$ is the rate of change of fluid velocity normal to the boundary.

4.5.2 Scaffold modelling - simplified geometry approach (**Paper II, III**)

The scaffold domain was modelled as a simple cylindrical column parameterised with porosity and permeability obtained from the µCT analysis. Fluid flow in the porous domain was defined as the Darcy model, described by the Navier-Stokes equations for fluid flow in a porous medium and the Darcy-Brinkman equation.

$$\frac{1}{\varepsilon_p}\rho(u.\,\nabla)u\frac{1}{\varepsilon_p} = \nabla.\left[-pI + K - \left(\mu\kappa^{-1} + \frac{Q_m}{\varepsilon_p^2}\right)u + F\right. \qquad \text{---(iv)}$$

$$\rho\,\nabla.u = Q_m \qquad\qquad \text{---(v)}$$

$$K = \mu\frac{1}{\varepsilon_p}(\nabla u + (\nabla u)^T) - \frac{2}{3}\mu(\nabla.u)I \qquad\qquad \text{---(vi)}$$

Where ε_p is the porosity, κ is the permeability, and Q_m is the mass flow rate. The equation (iv) is a modified form of the Navier-Stokes equation, which accounts for the effects of porosity and permeability on fluid flow. The equation (v) the continuity equation for fluid flow in a porous medium. It states that the rate of change of fluid density within the medium is equal to the mass flow rate into or out of the medium (*i.e.*, Gauss law). The equation (vi) is the Darcy-Brinkman equation, which describes the relationship between the fluid velocity and the permeability of the porous medium.

4.5.3 Scaffold modelling - µCT geometry approach (**Paper II-IV**)

The scaffold domain was generated by using the µCT geometry. In brief, the geometry obtained from µCT scanning was exported as a *.stl* file. Scanning defects including self-intersections, paper-thin regions, narrow edges, and holes were repaired in MeshLab version 2021.05 [251], Blender version 2.92 (Blender Institute, Netherland), and Rhino 7 (Robert McNeel & Associates, USA). The repaired geometry was then imported into the COMSOL Multiphysics as a solid object for computation.

A partially segmented scaffold geometry was used as a representative to reduce the computational burden in Paper **III**, whereas the fluid dynamics was simulated using the complete scaffold geometry in Paper **II** and **IV**.

4.6 Reverse Transcription Quantitative Polymerase Chain Reaction (**Paper I-IV**)

For the quantification of mRNA expression level, reverse transcription quantitative polymerase chain reaction (RT-qPCR) was conducted. Total RNA from samples was extracted using the Maxwell® 16 Cell LEV Total RNA Purification Kit (AS1280, Promega, USA), following the instructions provided by the manufacturer. Reverse transcription was performed using a High-Capacity cDNA Reverse Transcription Kit (4368814, Applied Biosystems, USA) on a SimpliAmp Thermal Cycler (A24811, Applied Biosystems, USA). The quantitative PCR was conducted on a StepOne real-time PCR system (4453320, Applied Biosystems, USA) using the TaqMan Fast Universal PCR Master Mix (4366073, Applied Biosystems, USA) and TaqMan gene

expression assays/arrays (4331182/4351372/4413256/4413255, Applied Biosystems, USA), which included target primers and probes. The thermal cycles for DNA amplification involved 1 cycle at 95 ℃ for 20 seconds, followed by 40 cycles at 95 ℃ for 1 second and 60 ℃ for 20 seconds. The relative quantification of mRNA level was determined by the ΔΔCt method after normalisation to housekeeping gene(s) [252]. The set of genes evaluated is provided in the corresponding paper.

4.7 Viability and Growth Assessment

4.7.1   Quantification of double-strand DNA (**Paper II-IV**)

The amount of double strand DNA (dsDNA) is roughly associated with the number of cells in the samples. Therefore, dsDNA was quantified to evaluate cell proliferation. Samples were collected in a 300 μl aqueous solution of 0.1% Triton X-100 and subjected to a freeze-and-thaw cycle three times to lyse the cells. The detection of dsDNA in the lysate was performed by using Quant-iT™ PicoGreen™ dsDNA Assay Kit (P7589, Thermo Fisher Scientific, USA) in accordance with the manufacturer's protocol. The fluorescence was measured at Ex/Em = 480/520 nm using a microplate reader (VLBL00D0; ThermoFisher Scientific, Finland).

4.7.2   Immunofluorescence of proliferation markers (**Paper I-III**)

To assess a cell proliferative state, the expression of proliferating cell nuclear antigen (PCNA) and Ki67 antigen was evaluated by immunofluorescence.

Samples were fixed in 4% paraformaldehyde (PFA) for 15 minutes at room temperature. For PCNA staining, a heat induced antigen retrieval process was carried out by treating the samples in 10 mM sodium citrate (pH 6.0) at a temperature of 95 ℃ for 20 minutes. Subsequently, the samples were permeabilised in 0.1% Triton X-100 in PBS for 15 minutes and incubated in blocking solution consisting of 10-20% normal goat serum and 0.1% Triton X-100 or Tween-20 in PBS for 1 hour at room temperature. The samples were then incubated overnight with primary antibodies. For non-conjugated primary antibodies, secondary antibodies were applied subsequently. The primary and secondary antibodies used in the studies are listed in the Table. 4.4. The

counterstaining of nuclei and filamentous actin (F-actin) was simultaneously conducted during the secondary incubation using 4′,6-diamidino-2-phenylindole (DAPI: 1:2500-5000; 62247, Thermo Scientific, USA) and Alexa Fluor™ 488 Phalloidin (1:500; A12379, Invitrogen, USA), respectively.

The samples were visualised using a laser scanning confocal microscopy (TCS SP8 STED 3X, Leica, Germany). The ratios of PCNA and Ki67 positive cells were quantified by the "Analyze Particles" function in Fiji/ImageJ after binarisation of the fluorescent nuclei [253].

Table 4.4   The antibodies used for immunofluorescence of proliferation markers

Primary antibody		Secondary antibody			
Target Dilution	Manufacturer Ref. No	Target Dilution	Conjugate	Manufacturer Ref. No	Paper
PCNA 1:100-200	Santa Cruz Biotechnology sc-56	Mouse 1:500	AF635	Invitrogen A31575	**I, III**
Ki67 1:50	Invitrogen 50569882	Conjugated with eFlour™ 660			**II**
AF: Alexa Fluor™					

4.7.3   EdU incorporation assay (**Paper IV**)

5-ethynyl-2'-deoxyuridine (EdU) is a thymidine analogue that is incorporated into the DNA of proliferating cells during the S-phase of cell cycle.

To quantify the number of proliferating cells during a specific period, BMSC were incubated with 30 μM EdU in the growth medium for 24 hours under both static and dynamic conditions at 37 ℃ with 5% CO_2. Subsequently, the samples were fixed in ice-cold methanol for 5 minutes at -20 ℃. The detection of incorporated EdU into DNA was then carried out using a click chemistry reaction with the Click-iT™ EdU Cell Proliferation Kit (C10337, Invitrogen, USA) following the manufacturer's protocol. The nuclei were counterstained with Hoechst 33342 (1:1000: H3570, Invitrogen, USA).

Fluorescent images were acquired using the confocal microscope. For quantification, the EdU and Hoechst-labelled nuclei were segmented and counted using the StarDist plugin in Fiji/ImageJ [254].

4.8 Osteogenic Functionality Assessment

4.8.1 Immunofluorescence of osteogenic markers (**Paper I-IV**)

Samples for Runx2 staining and COL1 staining were fixed in 4% PFA for 15 minutes at room temperature and in ice-cold methanol for 5-10 minutes at -20 ℃, respectively. After permeabilisation and blocking as described previously, the samples were incubated with the primary antibodies followed by incubation with secondary antibodies as listed in Table 4.5. The counterstaining of nuclei with DAPI was performed simultaneously during the secondary incubation. Images were acquired using the confocal microscope and analysed in Fiji/ImageJ.

Table 4.5 The antibodies used for immunofluorescence of osteogenic markers

Primary antibody		Secondary antibody				
Target Dilution	Manufacturer Ref. No	Target Dilution	Conjugate	Manufacturer Ref. No	Paper
Runx2 1:250	Abcam ab23981	Rabbit 1:250	AF568	Invitrogen A11011	**I**
Runx2 1:250	Abcam ab192256	Rabbit 1:250	AF568	Invitrogen A11011	**III**
COL1 1:1000	Abcam ab90395	Mouse 1:250-500	AF635	Invitrogen A31575	**I, III**
COL1 1:500	Invitrogen MA1-26771	Mouse 1:500	AF635	Invitrogen A31575	**IV**
AF: Alexa Fluor™						

4.8.2 Alkaline phosphatase activity assay (**Paper I-III**)

Samples were collected in a 300 μl aqueous solution of 0.1% Triton X-100 and subjected to a freeze-and-thaw cycle three times to obtain cell lysate. In the lysate, an equal volume of p-Nitrophenylphosphate (pNPP, 20-106; Merck, USA) was added and incubated at room temperature so that ALP catalysed the hydrolysis of pNPP.

Absorbance was measured at 405 nm on the microplate reader. ALP activity was normalised to the dsDNA quantity.

4.8.3   Alkaline phosphatase staining (**Paper IV**)

Samples were fixed in 4% PFA for 2 minutes at room temperature. Immediately afterwards, the samples were incubated with BCIP®/NBT solution (B5655, Merck, USA) for 30 minutes at room temperature. For quantification, the cells were destained by overnight incubation in 100 mM cetylpyridium chloride at room temperature. The absorbance was measured at 540 nm using the microplate reader.

4.8.4   Alizarin red S staining (**Paper I-IV**)

Samples were fixed in 4% paraformaldehyde (PFA) for 40 minutes and washed three times with Milli-Q® water. Calcium deposition was evaluated by staining with 0.1% Alizarin Red S (A5533, Merck, USA) for 20 minutes, followed by thorough washing with Milli-Q® water. For quantification, the dye was extracted in 100 mM cetylpyridium chloride at room temperature. Absorbance was measured at 540 nm using the microplate reader.

4.9 Assessment of Cytoskeletal Modulation Under Flow

4.9.1   Immunofluorescence of cytoskeleton and its regulators (**Paper III-IV**)

Samples were fixed in 4% PFA for 15 minutes at room temperature. For the detection of phosphorylated protein, fixation was undertaken in the presence of a protease and phosphatase inhibitor cocktail (1:10; ab201119, Abcam, UK). After permeabilisation and blocking as described previously, the samples were incubated with primary antibodies followed by incubation with secondary antibodies as listed in Table 4.6. The counterstaining with DAPI and Alexa Fluor™ 488 Phalloidin was performed simultaneously during the secondary incubation.

Images were acquired using the confocal microscope and analysed in Fiji/ImageJ. For morphometric analysis, fluorescent nuclei were segmented by the StarDist plugin in Fiji/ImageJ. Regions of interests (ROIs) were automatically drawn around each nucleus

during the process. The aspect ratio of the ROIs was then measured using the shape descriptors module within Fiji/ImageJ.

Table 4.6 The antibodies used for immunofluorescence of cytoskeleton and its regulators

Primary antibody		Secondary antibody			
Target Dilution	Manufacturer Ref. No	Target Dilution	Conjugate	Manufacturer Ref. No	Paper
αTubulin 1:250	Invitrogen 62204	Rabbit 1:500	AF635	Invitrogen A31575	**III**
ROCK1 1:250	GeneTex GTX113266	Rabbit 1:500	AF568	Invitrogen A11011	**III**
NM2A 1:200	BioLegend 909801	Rabbit 1:500	AF546	Invitrogen A11010	**IV**
NM2B 1:200	GeneTex GTX634160	Mouse 1:500	AF635	Invitrogen A31575	**IV**
pMLC2 1:250	Invitrogen MA5-15163	Mouse 1:500	AF635	Invitrogen A31575	**IV**

AF: Alexa Fluor™

4.9.2 Cytoskeleton antibody microarray (**Paper IV**)

To understand cytoskeletal regulation under flow, an ELISA-based antibody microarray was utilised. The Cytoskeleton Array kit (PCP141, Full Moon BioSystem, USA) was used for sample analysis following the manufacturer's instructions for preparation and detection.

In short, samples, which were cultured under static and dynamic conditions for 3 days, were corrected, and proteins extraction was performed by vigorous vortexing with lysis beads in the extraction buffer. Due to low protein yield, the cell lysates from three separate experiments were combined. The protein samples were labelled with biotin dissolved in dimethylformamide in a labelling buffer. The biotinylated samples were then incubated with the antibody microarray slides and detected with Cy3-Streptavidin solution. The slides were scanned using a GenePix® Microarray Scanner (Molecular Devices, USA), and the data was analysed using GenePix® ProMicroarray Image Analysis Software.

4.9.3 ROCK activity assay (**Paper IV**)

The enzymatic activity of ROCK was quantified using the ROCK Activity Assay Kit (ab211175, Abcam, USA), in accordance with the manufacturer's protocol. Cell lysates were obtained in Mammalian Cell Lysis Buffer (ab179835, Abcam, USA) in the presence of the protease and phosphatase inhibitor cocktail. The cell lysates were then added to wells where myosin phosphatase target subunit 1 (MYPT1) was coated. The kinase reaction was initiated by adding 10 mM Dithiothreitol and 2 mM Adenosine triphosphate. The wells were then incubated for 60 minutes at room temperature to allow the enzyme to phosphorylate MYPT1. After the kinase reaction, the wells were incubated with anti-phospho-MYPT1 (Thr696) for 60 minutes at room temperature. This was followed by incubation with a horseradish peroxidase (HRP)-conjugated secondary antibody for 60 minutes at room temperature. The optical density of the HRP substrate was measured at 450 nm using the microplate reader.

4.10 Pharmacological Treatment

4.10.1 Inhibition of cytoskeletal contractility (**Paper IV**)

To elucidate the role of cytoskeletal contractility under flow in mechanically induced osteogenic differentiation, inhibitors of Rho GTPases (*e.g.*, RhoA), ROCK, MLCK, and non-muscle myosin II were applied to prevent cell contraction and instead trigger relaxation (Figure 4.4). The working concentrations of the inhibitors were preliminarily determined as the minimal concentration required for
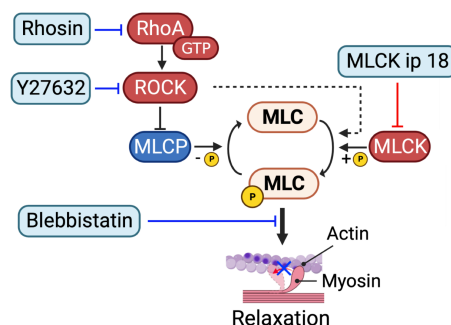
Figure 4.4 Pharmacological inhibition of Rho-ROCK signalling pathway and cytoskeletal contractility

effective inhibition of the target without compromising cell viability and growth (Table 4.7). With these concentrations, the BMSC culture under static and dynamic conditions were maintained for up to 14 days, with the media containing the inhibitors being refreshed every second day.

Table 4.7 Inhibitors of cytoskeletal contractility used in the studies

Inhibitor (Referred as)	Target	Working concentration	Manufacturer Ref. No
Rhosin hydrochloride (Rhosin)	Rho GTPases	20 μM	Biotechne 5003
Y27632 dihydrochloride (Y27632)	ROCK1/2	10 μM	Biotechne 1254
MLCK inhibitor peptide 18 (MLCK ip 18)	MLCK	1 μM	MedChemExpress HY-P1029
(±)-Blebbistatin (Blebbistatin)	Non muscle myosin II	10 μM	Merck 203390

4.11   Bioinformatics and statistics

4.11.1 Gene set enrichment analysis (**Paper IV**)

With differentially expressed genes (DEGs) identified statistically, gene set enrichment analysis was conducted to evaluate functional enrichment using R package gprofiler2, and Cytoscape 3.9.1 with referral to the STRING 11.5, UniProt, and Reactome pathway databases.

4.11.2 Principal component analysis (**Paper IV**)

Principal component analysis (PCA) is a technique used to reduce the dimensionality of a data set by identifying patterns in the data and projecting it onto a new set of axes. To perform PCA, the $\log_2$(fold-change) values of gene expression data was first centred and then the covariance matrix was calculated using a R package, pcaMethods, under Bioconductor 3.16 [255]. The eigenvectors of the covariance matrix were then used to transform the data onto a set of principal components (PCs). PC1 and PC2 were displayed as the x and y-axis, respectively, to visualise expression patterns.

4.11.3 Data comparison and visualisation (**Paper I- IV**)

Statistical analyses and data visualisation were performed by using SPSS Statistics 24-25 (IBM, USA), R 3.4-4.2, and Prism 9 (Dotmatics, USA).

For pairwise comparisons, Student's t-test was utilised. For multiple comparisons, data were analysed using a one-way or two-way analysis of variance (ANOVA) followed by a post-hoc test (as specified in the following section). The criterion for statistical significance was set at a p-value of less than 0.05. The data are presented as mean ± s.e.m. unless mentioned otherwise.

5. Main Results and Discussion

5.1 BMSC Characterisation and Multilineage Differentiation (Paper I-IV)

The use of inbred animal-derived primary cells offers an advantage as it provides a homogeneous population, unlike human primary cells that often exhibit donor variations. Therefore, BMSC isolated from inbred Lewis rats were used throughout the studies.

The isolated cells exhibited fibroblastic morphologies on a plastic surface with a colonogenic characteristics (Figure 5.1 A). Under certain inductive stimuli, the cells were capable of undergoing osteogenic, adipogenic, and chondrogenic differentiation (Figure 5.1 B).

Flow cytometry analysis revealed that BMSC exclusively expressed putative MSC markers for rats, namely CD44H, CD73, CD90, and Sca1/Ly6, while not expressing
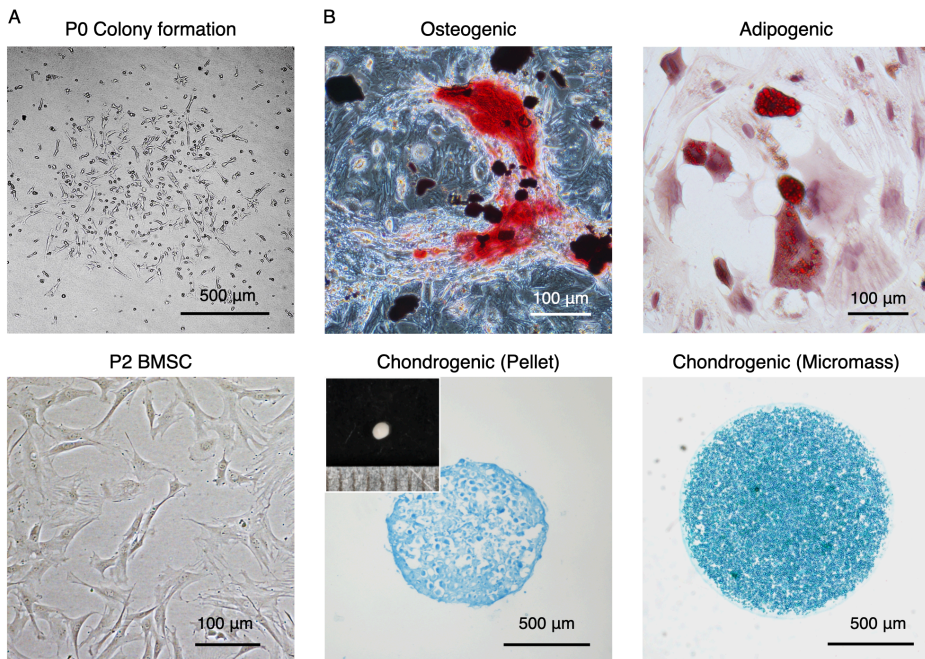
Figure 5.1 Cell morphology and multipotency of BMSC isolated from Lewis rats
(A) Colonogenicity and morphology of BMSC on a plastic surface. (B) Multi-lineage differentiation of rat BMSC into osteoblasts, adipocytes, and chondrocytes in a pellet culture and micromass culture.

negative markers, CD34, CD45, and CD79. This expression profile well aligns with previous reports on rat-derived MSC [256,257]. Stro1-expressing cells accounted for 4.1% of the population. Although Stro1 is commonly referred to as a MSC marker, a histological study refuted this by demonstrating that less than 1% of nucleated bone marrow cells in rat expressed Stro1 *in vivo*, but it was rather expressed in the endothelium [258].

Taken together, the cells used in the studies exhibited a characteristic MSC phenotype and multipotency, which are functionally analogous to human BMSC [12].
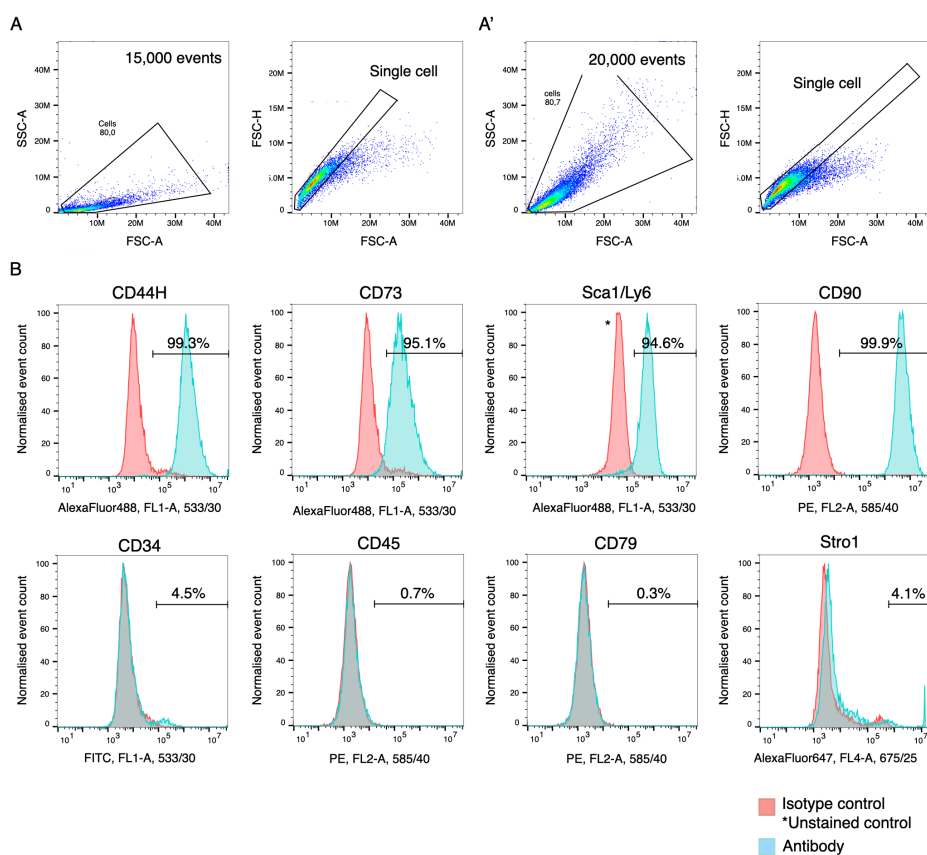
Figure 5.2 BMSC characterisation by flow cytometry
(A, A') Gating strategies for surface marker characterisation using unfixed cells, and for an intracellular marker (*i.e.*, Sca1/Ly6) using fixed cells in ice-cold methanol, respectively. (B) Expression profile of positive and negative MSC markers as well as Stro1 for BMSC used in the studies.

5.2 PLTMC as a Promising Scaffolding Material for Bone Tissue Engineering

5.2.1 PLTMC possessed preferable properties to support biocompatibility **(Paper I)**

PLTMC has been recently introduced as a promising biomaterial for tissue engineering applications due to its biocompatibility, biodegradability, formability, and tunable mechanical properties. To gain insights into the suitability of the biomaterial for bone tissue engineering, surface characterisation was conducted on naive PLTMC and plasma-treated PLTMC. The main focus was on hydrophilicity/hydrophobicity, with contact angle and surface chemistry evaluated both before and after plasma surface modification. The contact angle measurement showed that naive PLTMC had a contact angle of approximately 70°, and the hydrophilicity was further improved by plasma irradiation, reducing the angle by 10-20°. The improved wettability was maintained for a period of two weeks, especially when exposed to oxygen plasma irradiation for at least 3 minutes (Figure 5.3A, B). Based on the measurement, PLTMC can be classified as a hydrophilic material since it was lower than 90° [259]. The contact angle of PLTMC was compatible or lower than conventional aliphatic polyesters, such as PCL and PLA
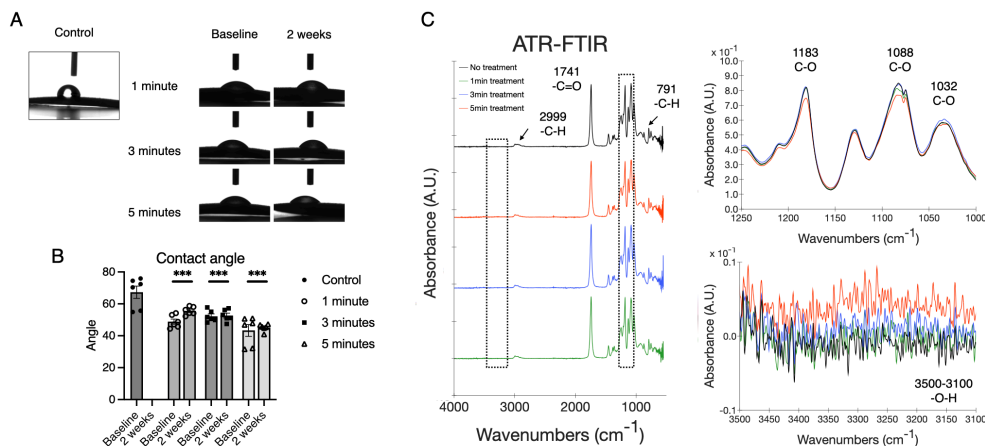
Figure 5.3 Surface hydrophilicity of PLTMC before and after plasma surface modification

(A, B) Water contact angle measurement immediately after plasma irradiation and 2 weeks after treatment. Plasma exposure was conducted for 1, 3, and 5 minutes. (C) Surface chemistry evaluated by ATR-FTIR showed that the improved wettability was mostly attributed to the addition of an -OH functional group. ***$p < 0.001$ (Dunnett's test/Comparison of samples immediately after plasma irradiation).

[260–263]. It has been suggested that the optimal contact angle for osteoblasts and MSC is approximately 50 – 85°, and therefore the surface hydrophilicity of PLTMC indeed well fits the application for bone tissue engineering [73,264,265]. ATR-FTIR analysis measuring wavenumbers in the range between 500 and 4000 cm^{-1} showed minor changes before and after plasma irradiation. In particular, an increase in absorption between 3500 and 3100 cm^{-1}, which corresponds to a hydroxyl (-OH) group, in the plasma treated groups suggested the addition of hydrophilic functional groups on the surface, which may have contributed to the improved wettability.

Designing a porous geometry with appropriate size of pores assures mass transfer within the scaffold while providing architectural cues to the cells attached. In the studies, a solvent casting/particle leaching technique was used to fabricate PLTMC scaffolds with a trabecular-like porous architecture. By optimising the formulation of the components, highly interconnected porous scaffolds, evaluated by μCT, with a porosity of approximately 90% were achieved (Table. 5.1). Most of the pores were identified as open pores, which were interconnecting and therefore thought to facilitate nutrient exchange within the scaffold.

Table 5.1 Architectural properties of PLTMC scaffolds

	Average ($N = 5$)	S.D.
Thickness (mm)	1.22	0.084
Surface area (cm^2)		
- φ 10 mm	2.17	0.069
- φ 12 mm	3.12	0.099
Density (kg/m^3)	129.60	9.81
Porogen diameter (μm)	90-600	-
Porosity (%)	91.71	3.44
Open pores (%)	91.71	3.44
Close pores (%)	0.00031	0.00048

The use of synthetic polymers as scaffolding materials is often hindered by their inherent "hydrophobic" nature, which is amplified in the form of porous scaffolds. The high porosity of the scaffold results in a high air content, which impedes the infiltration of cell suspension during cell seeding [266]. Although PLTMC was considered
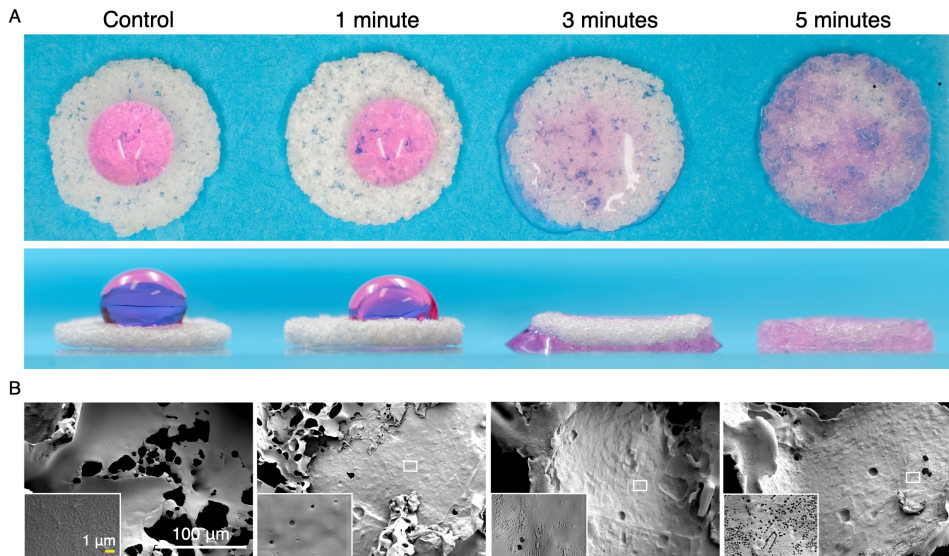
Figure 5.4 The hydrophobicity and surface topography of PLTMC scaffolds before and after plasma surface modification

(A) The medium retention on the scaffold surface due to the porous nature of PLTMC was disturbed by plasma surface modification. In particular, plasma irradiation for 3 minutes and longer improved medium infiltration significantly. (B) SEM images showing topographical changes after plasma irradiation.

"hydrophilic" by definition, the fabricated PLTMC scaffolds indeed exhibited a hydrophobic nature (Figure 5.4 A). When a droplet of culture medium was placed on the surface of the PLTMC scaffold, it remained on the surface and did not infiltrate into the scaffold when it was dry. This issue was effectively solved by the irradiation of oxygen plasma to the scaffolds for a duration of longer than 3 minutes. SEM analysis showed the presence of submicron-level craters on the scaffold surfaces after plasma irradiation, which would have contributed to the observed improvement in wettability (Figure 5.4 B).

Due to the improvement of medium infiltration, cell seeding efficiency increased by approximately 20% in the plasma-treated scaffolds, resulting in higher dsDNA yield in the early phase of cell culture by day 3 ($p = 0.011$) (Figure 5.5 A). Nevertheless, the yield of dsDNA from the untreated scaffolds had become comparable by day 7 to that from the treated counterpart, with over 70% of the cells found to be proliferative in both groups (Figure 5.5 B, C).
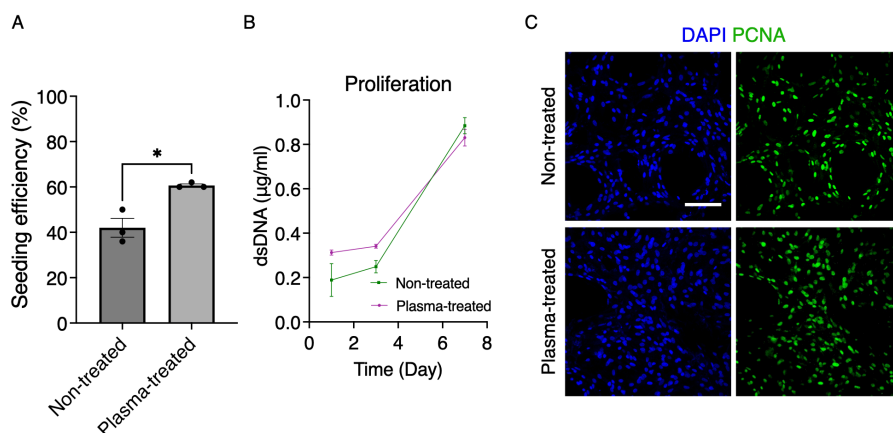
Figure 5.5 Cell adhesion and growth on the plasma-treated and non-treated PLTMC scaffolds

For the plasma treated group, oxygen plasma was irradiated for 3 minutes. (A) Cell seeding efficiency was improved by approximately 20% by plasma surface modification. (B) dsDNA quantification shows that cell proliferation was supported by the PLTMC scaffolds. (C) Immunofluorescence of PCNA shows highly proliferative BMSC on the scaffolds. The proliferation of BMSC was not influenced by the surface modification. Scale = 100 μm. *$p < 0.05$ (Student's t-test)

5.2.2 PLTMC scaffolds exhibited *in vitro* osteoconductivity **(Paper I)**

To evaluate the *in vitro* osteoconductivity of PLTMC scaffolds, the gene expression of osteogenic markers, ECM secretion, and mineralisation were assessed. When cultured in the osteogenic medium, BMSCs upregulated Runx2 expression on PLTMC scaffolds, with slight enhancement observed on day 7 on the plasma-treated scaffolds. (Figure 5.6 A). Importantly, Runx2 was localised in the nuclei during the early phase of differentiation, indicating that it acted as a transcription factor for osteogenesis (Figure 5.6 B). BMSC secreted COL1 on the PLTMC scaffolds, which was promoted by the surface modification. On day 21, it covered approximately 50% of the surfaces of both untreated and treated scaffolds, with no significant difference (Figure 5.6 C, D). The matrix was subsequently calcified as demonstrated by the presence of mineralised nodules visualised through Alizarin Red S staining, indicating that the PLTMC scaffolds supported a series of osteogenic differentiation (Figure 5.6 E, F). The study concluded that plasma surface modification accelerated the initiation and maturation of osteogenic responses, possibly due to improved cell seeding efficiency
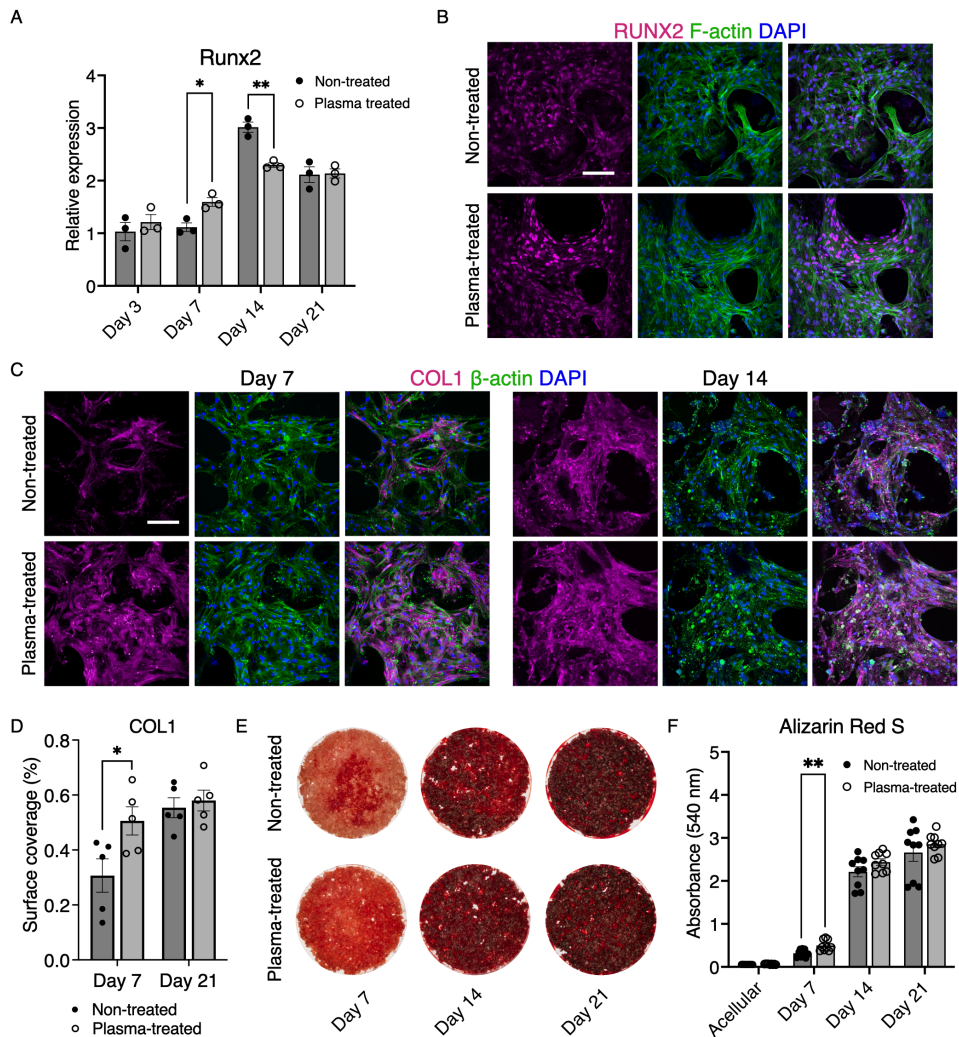
Figure 5.6 BMSC Osteogenic differentiation on the PLTMC scaffolds
(A) mRNA expression level of Runx2 measured by RT-qPCR. (B) Immunofluorescence of Runx2 showing its nuclear localisation. (C) Immunofluorescence of COL1 and (D) quantification. (E) Alizarin Red S staining of the scaffolds and (F) quantification. Scale = 100 μm. $*p < 0.05$, $**p < 0.01$ (Student's t-test).

and distribution. However, the effect of surface modification on long-term osteogenic differentiation appeared to be marginal.

In short, the fabricated PLTMC scaffolds possessed a favourable architecture for bone tissue engineering, supporting cell growth and osteogenic differentiation even without functionalisation.

5.3 Optimisation of Dynamic Cell Culture Conditions in the Bioreactor

5.3.1 Basic environmental factors impacted general cell health in dynamic culture (**Paper II**)

Dynamic cell culture using bioreactor systems often deviates from conventional cell culture in experimental conditions, not only in terms of mechanical stimuli applied during the culture but also in terms of other basic cell culture parameters such as medium volume, temperature, humidity, and pressure. The control of conditions in dynamic cell culture can vary depending on the specific system being used, making it essential to optimise these conditions in order to ensure stable and reproducible cell culture operations.

First, the optimal medium volume was determined by comparing different cell-to-medium ratios (Figure 5.7 A). In a monolayered culture condition, the minimum medium volume recommended by the manufacturer, which corresponded to 0.04 μl/cell (based on the initial cell number), supported cell viability and growth, but the limited nutrient supply to the cells resulted in slower growth compared to cells grown in larger volumes of medium (*i.e.*, 0.08 μl/cell and 0.16 μl/cell) (Figure 5.7 B, C). However, when using the porous scaffolds, the difference in cell growth was marginal,
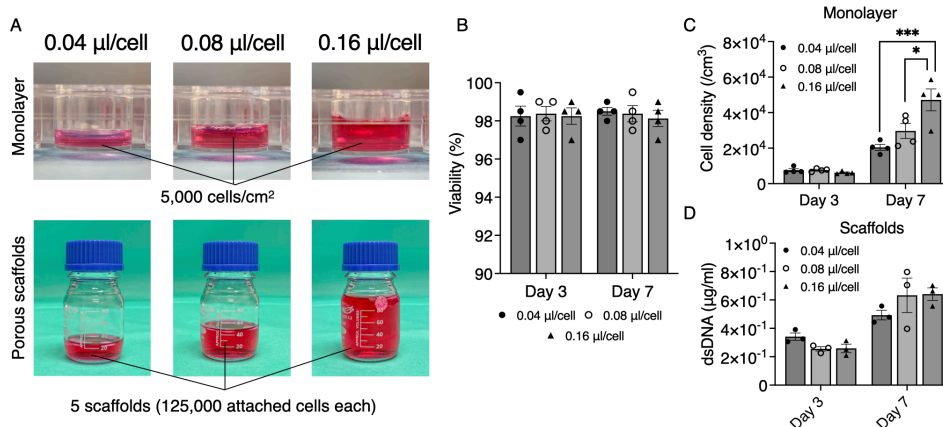
Figure 5.7 Optimisation of medium volume required for 3D cell culture
(A) Experimental conditions testing 3 cell-to-medium ratios. (B) Viability of BMSC culturing with different medium volumes. (C, D) The effect of medium volume on BMSC proliferation under the monolayered and 3D cell culture conditions. *$p < 0.05$, ***$p < 0.001$ (Bonferroni test).

likely due to the larger available surface areas and cell growth pattern on the scaffolds. This suggested that the medium volume at 0.04 μl/cell, which corresponded to 25 ml in the system, was sufficient (Figure 5.7 D). Therefore, based on the findings and consideration on cost-effectiveness, 25 ml of culture medium was considered optimum for dynamic cell culture in the present system.
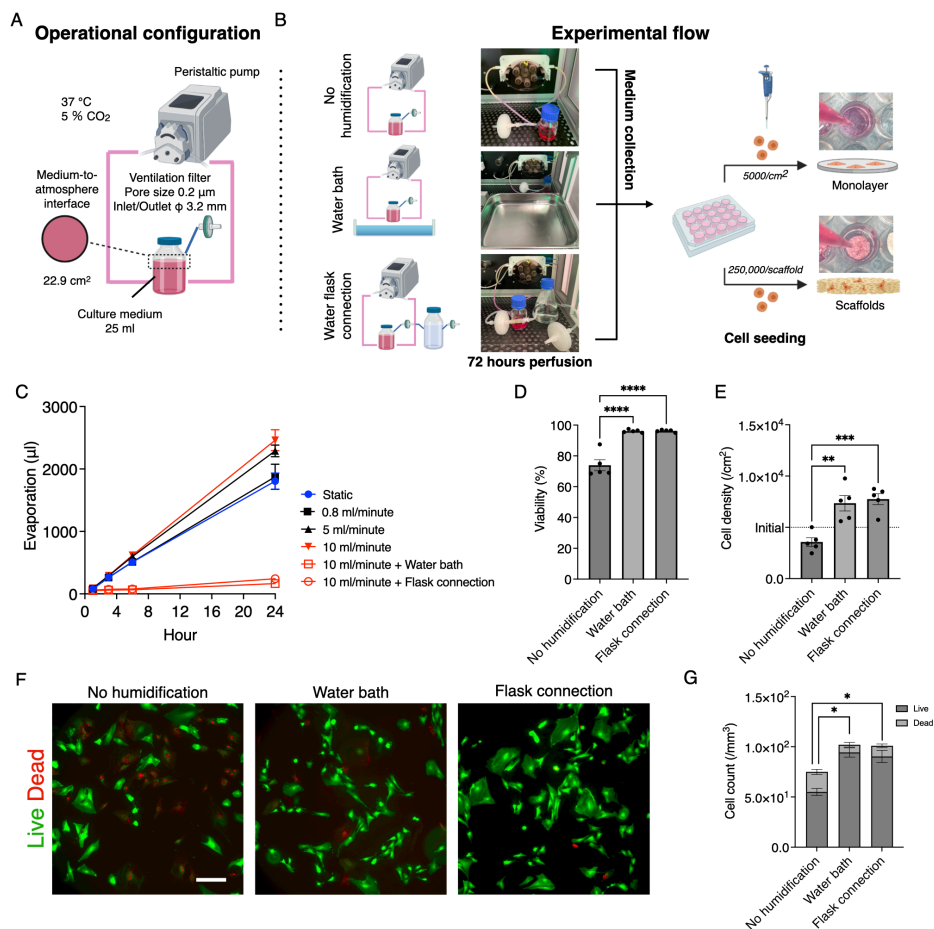
Figure 5.8 Humidification strategy for dynamic cell culture
(A) Schematic illustration of operational configuration. (B) Illustration of humidification strategies and experimental flow. Growth medium was perfused for 72 hours with/without humidification and subsequently used for cell culture. (C) The effect of humidification on a degree of medium loss. Evaporation occurred in a velocity dependent manner, which was prevented by the humidification means. (D, E) The viability and cell growth of monolayered BMSC cultured in the previously perfused medium with/without humidification. (F, G) Live/Dead staining of BMSC on the porous scaffolds cultured in the perfused medium with/without humidification. Scale bar = 100 μm. $*p < 0.05$, $**p < 0.01$, $***p < 0.001$, $****p < 0.0001$ (Bonferroni test).

Maintaining high humidity in an incubator is an essential aspect to preserve osmotic balance in the culture medium [267,268]. However, traditional humidification methods used in cell culture incubators, such as open water bath or steam injection, may not be always suitable for complex bioreactor systems because these methods may cause machine malfunction or damage to electrical components. Therefore, effective humidification strategies were explored in the present bioreactor by assessing medium quality under perfusion (Figure 5.8 A, B). When humidification was not provided, the medium was subjected to aggressive evaporation through the ventilation filter at a rate as high as 10% over 24 hours. Notably, the rate of evaporation from perfused medium was observed to be higher than medium placed statically, and it increased in a velocity-dependant manner (Figure 5.8 C). The quality of the medium was therefore deteriorated by condensation, which affected cell viability and growth (Figure 5.8 D-G). The placement of a water bath in the bioreactor effectively prevented evaporation, as did connecting an additional water flask to the ventilation filter, although the water bath caused bedewing on the incubator surface. The medium, which was humidified during perfusion even at 10 ml/minute for 72 hours, supported cell viability and growth effectively. Although the former approach may not be favoured in complex bioreactor systems, the later approach may provide a simple solution for humidification in perfusion bioreactor systems.

The other critical consideration for dynamic cell culture is the prevention of air bubbles during perfusion. Fluid flow through scaffolds can be impeded by bubbles trapped within the pores, which can negatively affect cell growth [269]. Air bubbles can arise due to varying pressure conditions that induce outgassing. In perfusion bioreactors used for bone tissue engineering, fluid agitation, the presence of serum proteins, and the microporous and hydrophobic nature of polymeric scaffolds can all contribute to the generation of air bubbles [270,271]. With no exception, it was also the obstacle in the present bioreactor system (Figure 5.9 A-D). To avoid this, various techniques can be used, such as increasing the flow rate, using degassing units, or modifying the surface properties of the scaffold [246]. In the study, hydrostatic pressure was applied to increase the solubility of gases as described by Henry's law, in order to minimise the
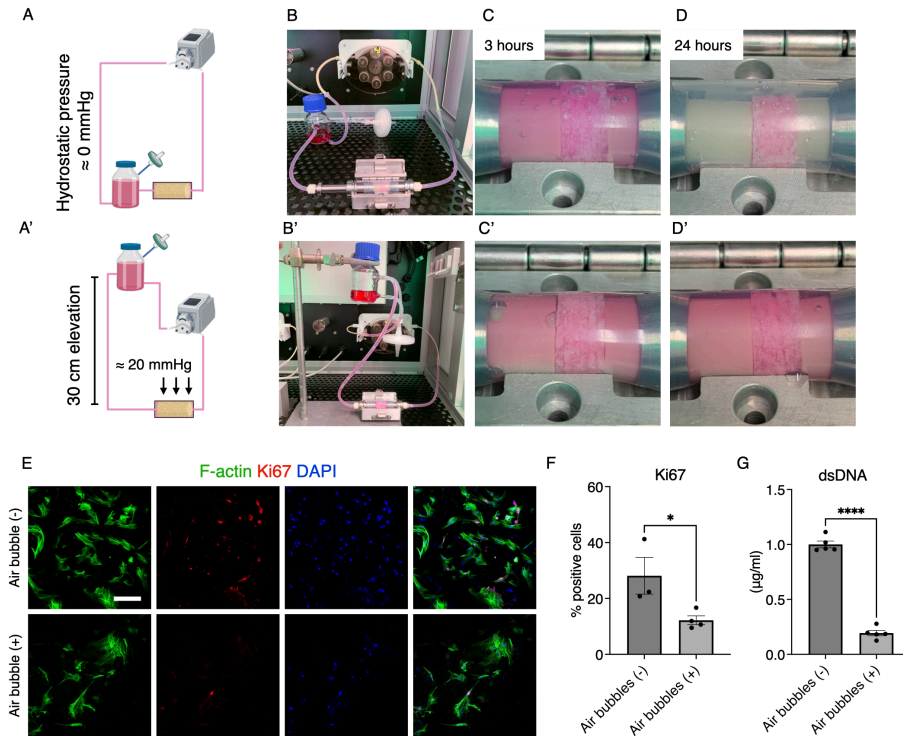
Figure 5.9 Air bubble formation in the perfusion bioreactor
(A-D, A'-D') Air bubble formation in the perfusion bioreactor and preventative measure by applying hydrostatic pressure. (E, F) Immunofluorescence of Ki67 showing less proliferative cells in the presence of air bubbles. (G) Quantification of dsDNA showing the negative impact of air bubbles on cell growth. Scale bar = 100 μm. *$p < 0.05$, ****$p < 0.0001$ (Student's t-test).

accumulation of air bubbles in the sample chambers (Figure 5.9 A'-D'). Under atmospheric pressure, air bubbles accumulated, resulting in a decreased proliferative status of the cells, as shown by a reduction in Ki67 expression and dsDNA yield (Figure 5.9 E-G). The accumulation of air bubbles was effectively suppressed simply by elevating the medium reservoir by 30 cm, which corresponded to hydrostatic pressure of approximately 20 mmHg (equivalent to 2.7 kPa). The required pressure for a given setup should depend on various experimental factors, such as material selection, scaffold architecture, flow patterns, and fluid paths. It is well established that static pressure can favourably influence the fate determination of BMSC towards osteogenesis and chondrogenesis, especially when high magnitudes of pressure (*e.g.*, 100 kPa) are applied intermittently [272]. Limited evidence exists regarding the effect of

continuous application of pressure at lower magnitudes on their fate determination, and it remains unclear if 2.7 kPa was significant. However, it would be assumed that applying hydrostatic pressure for air bubble suppression may favourably influence cell differentiation towards an osteogenic lineage.

5.3.2 Cell survival and growth depended on the intensity and duration of fluid stimuli (**Paper II**)

Following to the optimisation of the basic environmental factors, optimal flow rates were explored (Figure 5.10 A). In contrast to 2D perfusion experiments where MSC were reported to tolerate fluid shear stress of 1 Pa and above, MSC in a 3D environment seem more sensitive and vulnerable, and even physiological levels of shear stress may
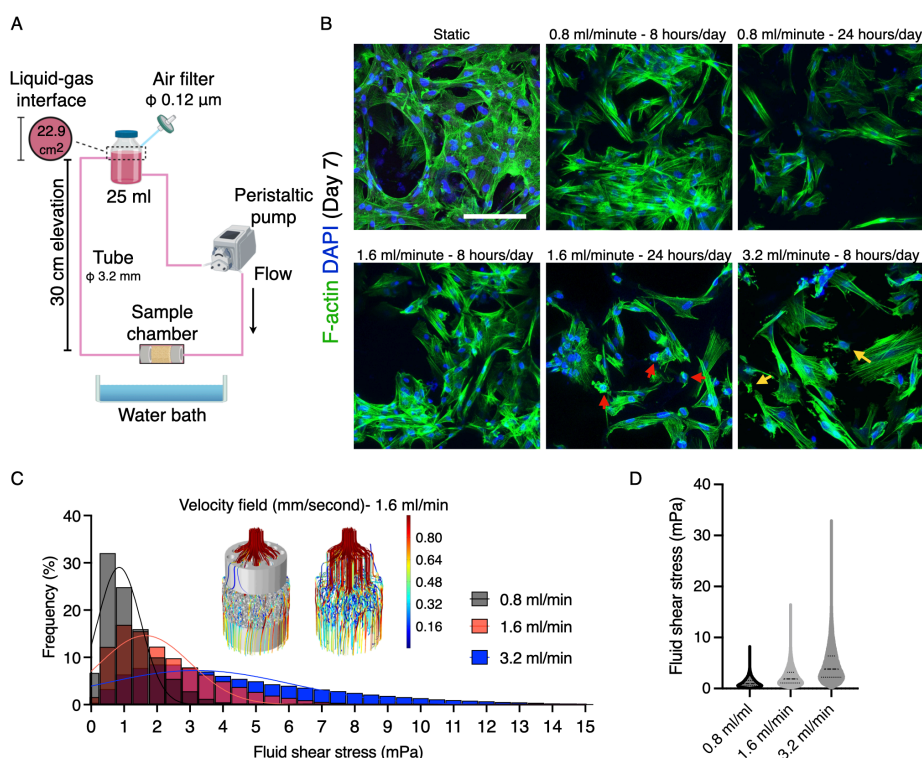
Figure 5.10 The evaluation of flow rate on cell viability and growth
(A) Experimental configuration to optimise flow rate. (B) Cytoskeletal staining of BMSC under fluid flow at different flow rates. (C, D) Frequency distribution of fluid shear stress and spatial flow velocity field estimated by CFD simulation using the μCT geometry. Shear stress was measured at a surface level (approximately 1.1 million elements of the geometry). Scale bar = 100 μm.

have a damaging effect [221]. Therefore, subphysiological levels of fluid flow were tested, which included 0.8 ml/minute, 1.6 ml/minute, and 3.2 ml/minute in the system. In addition, flow durations of 8 hours and 24 hours per day were tested. Under the dynamic conditions, BMSC exhibited a contracted morphology with dense filamentous actin (Figure 5.10 B). However, As the intensity and duration of flow stimuli increased, adverse effects on cell viability and growth were observed. In particular, flow stimuli for 24 hours per day inhibited cell growth even at the lowest tested flow rate of 0.8 ml/minute and induced an apoptotic response at 1.6 ml/minute. The flow rate of 3.2 ml/minute caused cell fragmentation due to excessive fluid shear. CFD simulation estimated that the flow rates of 0.8 ml/minute, 1.6 ml/minute, and 3.2 ml/minute exerted mean fluid shear stresses of 0.88 mPa, 1.76 mPa, and 3.51 mPa, respectively, despite heterogeneity among the scaffolds (Figure 5.10 C, D).

Based on the findings, flow rates between 0.8 ml/minute and 1.6 ml/minute (*i.e.,* shear stress range between 0.88 mPa and 1.76 mPa) and duration of 8 hours per day were considered optimal in the system and, therefore, applied in the subsequent studies to evaluate the fluidic effect on osteogenic differentiation.

5.4 Mechanical Induction of Osteogenic Differentiation by Fluid Stimuli

5.4.1   Fluid stimuli suppressed cell growth (**Paper III**)

Using the optimised conditions, the role of fluid stimuli in the growth and fate determination of BMSC was further evaluated in the perfusion bioreactor. Immunofluorescence of PCNA demonstrated that fluidic stimuli significantly reduced cell proliferation, reducing PCNA positive cells by approximately 40-50% at the given flow rates (Figure 5.11 A-C). Especially, the flow rate of 1.6 ml/minute prevented BMSC from increasing their number over the period of 21 days. The findings of studies investigating the effects of perfusion culture on cell proliferation are often contradictory: some studies reported improved cell proliferation, while others reported no significant difference or even suppressed growth [219]. This could be explained by the differences in inherent mass transport efficiency within the scaffolds used in each study. Specifically, dense scaffolds with low permeability pose a challenge for the

transport of essential nutrients and gasses to the cells residing within scaffold interiors. In such cases, a perfused environment can provide the much-needed fluid flow to facilitate transport and prevent cellular starvation. In the present studies, the highly interconnected porous scaffolds with over 90% porosity were designed, which supported the growth of BMSC even in the static environment. Therefore, it could be assumed that improved mass transfer by flow impacted cell growth minimally in the present setup. On contrary, previous studies have reported that continuous exposure to fluid shear stress arrests the cell cycle of MSC and osteoblasts at the G0 or G1 phase, which well supports the present observation [192,273].
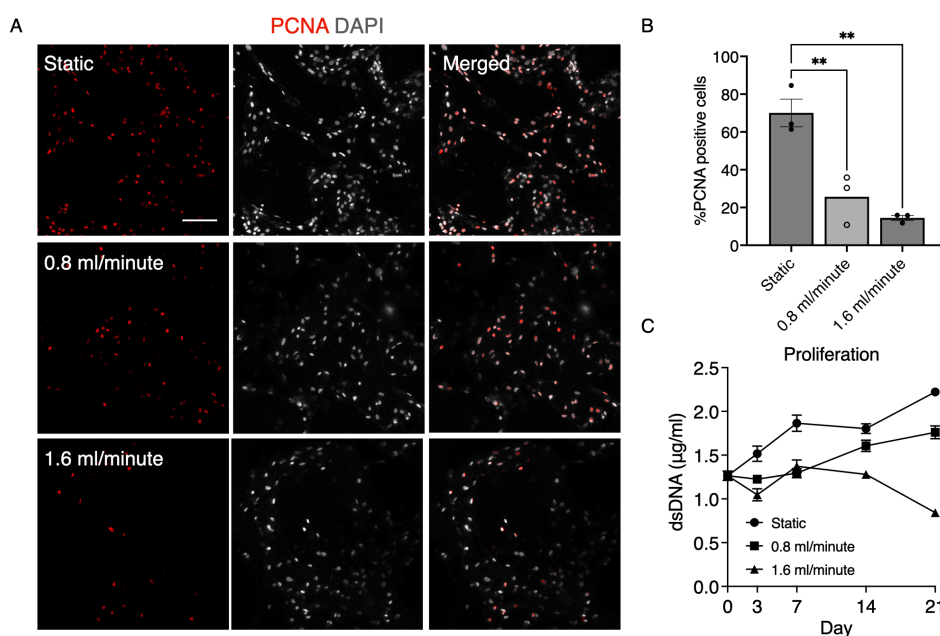
Figure 5.11 Cell proliferation under fluid stimuli
(A) Immunofluorescence of PCNA under the static and dynamic conditions for 7 days. (B) Quantification of PCNA positive cells. (C) Quantification of dsDNA over the period of 21 days under the static and dynamic conditions, showing delayed proliferation in a velocity-dependent manner. Scale bar = 100 μm. **$p < 0.01$ (Bonferroni test).

5.4.2 Osteogenic differentiation was induced solely by fluid stimuli (**Paper III**)

The evidence from conventional bone mechanobiology implies that 3D dynamic culture may trigger osteogenic differentiation even without the need for osteoinductive
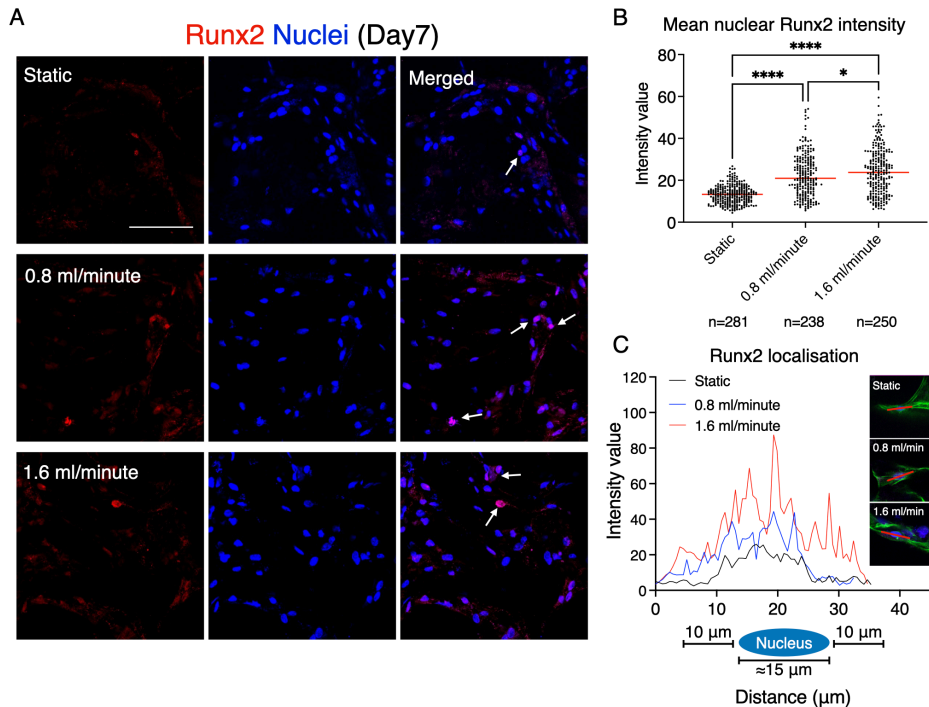
Figure 5.12 Runx2 expression prolife of BMSC under dynamic culture
(A) Immunofluorescence of Runx2, showing the upregulation and nuclear localisation in the dynamic cell culture conditions. (B) Quantification of mean Runx2 expression in the nuclei, showing approximately 9% and 14% of BMSC localised Runx2 in the nuclei under the dynamic conditions at flow rates of 0.8 ml/minutes and 1.6 ml/minutes, respectively. (C) Runx2 expression profile in a representative cell, showing that the nuclear localisation increased in a velocity-dependent manner. Scale bar = 100 μm. $*p < 0.05$, $****p < 0.0001$ (Bonferroni test).

supplementation, as observed in the 2D models. Therefore, the osteogenic responses of BMSC were evaluated using the perfusion bioreactor.

To validate the concept, BMSC were subjected to perfusion at flow rates of 0.8 ml/minutes and 1.6 ml/minutes. After 7 days of dynamic culture, approximately 9% and 14% of BMSC cultured under perfusion at 0.8 ml/minute and 1.6 ml/minute, respectively, localised Runx2 in their nuclei (Figure 5.12 A, B). Furthermore, the intensity of Runx2 expression was dependent on flow velocity within the tested magnitudes (Figure 5.12 C). These findings indicate that fluid stimuli indeed trigger the initiation of osteogenic differentiation by allowing Runx2 to act as a transcription factor in the nuclei.
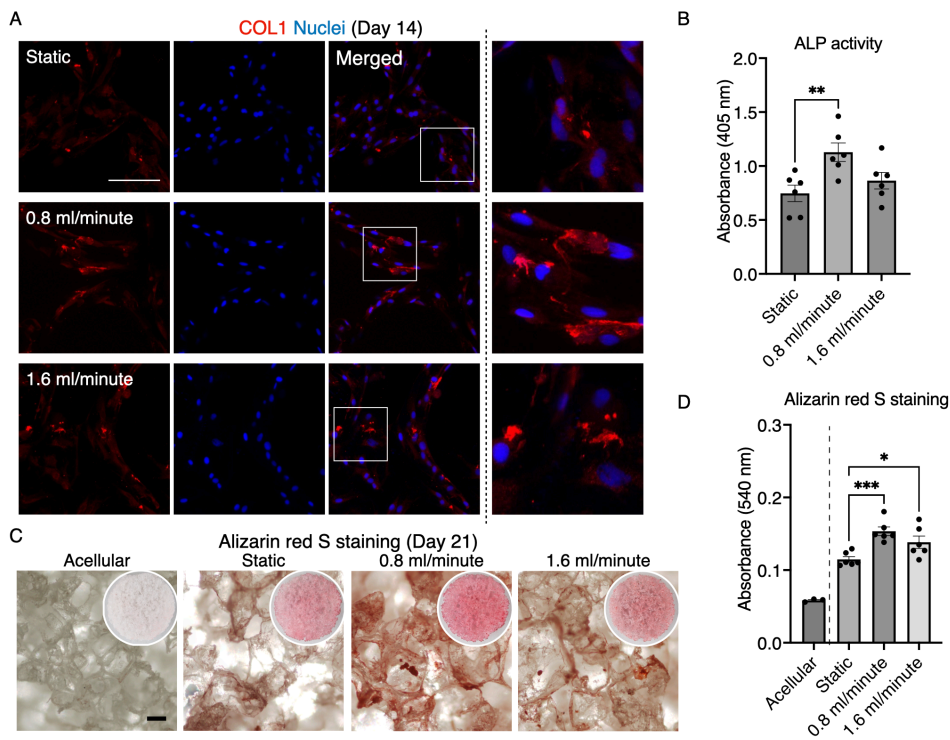
Figure 5.13 Osteogenic differentiation solely induced by fluid stimuli in the perfusion bioreactor

(A) Immunofluorescence of COL1 after 14 days of the dynamic conditions. (B) ALP activity on day 14 normalised to dsDNA. (C, D) Alizarin red S staining, showing the deposition of calcium nodules on the scaffolds after 21 days of dynamic culture. Scale bar = 100 μm. $*p < 0.05$, $**p < 0.01$, $***p < 0.001$ (Bonferroni test).

The osteogenicity of BMSC was further evaluated by measuring their functionality, namely collagen formation, ALP activity, and mineral deposition. After 14 days of dynamic culture, BMSC secreted COL1 at a higher level than those in the static condition, and ALP activity was also upregulated, particularly when subjected to flow at 0.8 ml/minute (Figure 5.13 A, B). After 21 days, BMSC showed slight but definite mineralisation even in the absence of osteoinductive supplements (Figure 5.13 C, D).

The osteogenic functionality of BMSC, as demonstrated by COL1 secretion and mineralisation, was found to be inferior under fluid flow conditions compared to those cultured in the osteogenic medium (as seen in Figure 5.6). The osteogenic supplements consist of dexamethasone, ascorbic acid, and β-glycerophosphate. Dexamethasone is
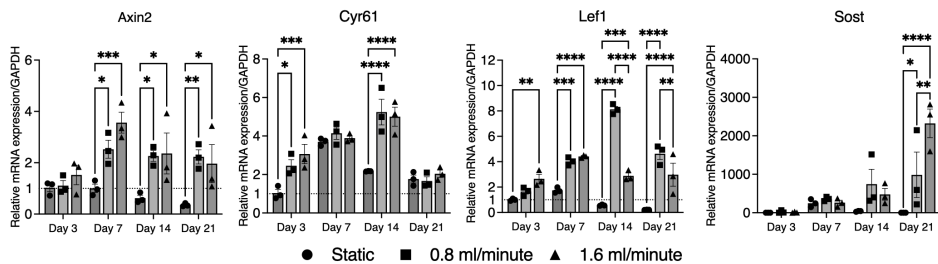
Figure 5.14 The gene expression of Wnt target genes and its regulator under fluidic stimuli
RT-qPCR analysis of the Wnt target genes (*i.e.*, Axin2, Cyr61, Lef1) and a regulator (*i.e.*, Sost) expressed by BMSC under the dynamic conditions over the period of 21 days. *$p < 0.05$, **$p < 0.01$, *** $p < 0.001$, ****$p < 0.0001$ (Bonferroni test).

known to trigger osteogenic differentiation by upregulating Runx2 expression through the activation of TAZ, Mitogen-activated protein kinase phosphatase 1, and canonical Wnt signalling pathway [274]. In fact, In the experiment, a direct transcriptional target of canonical Wnt signalling, Axin2, as well as Cysteine-rich angiogenic inducer 61 (Cyr61) and Lymphoid enhancer binding factor 1 (Lef1), were significantly upregulated under fluid stimuli together with a Wnt negative feedback regulator, Sclerostin (Sost), which is also known as an osteocyte marker (Figure 5.14). This suggests that the fluid stimuli effectively activate the canonical Wnt signalling pathway. Therefore, such mechanical stimuli could be a viable alternative to dexamethasone in the induction of osteogenic differentiation. Ascorbic acid is essential for collagen formation as it acts as a cofactor for prolyl and lysyl hydroxylase enzymes during collagen post-translational modification. The growth medium used in the studies (*i.e.*, αMEM) contained ascorbic acid as a basic component, and therefore BMSC were able to secrete COL1 to a lesser degree compared to the cells with additional supplementation of ascorbic acid. β-glycerophosphate acts as a source of inorganic phosphate for HA formation [274]. The insufficient supply of phosphate in the growth medium may be the reason for the limited amount of mineralisation induced by fluid stimuli.

5.4.3 Mechanically induced osteogenic profile differed from the chemically induced differentiation (**Paper IV**)

To investigate further on mechanically induced osteogenic responses, the expression of genes involved in osteogenesis altered by fluid stimuli (*i.e.*, flow rate of 1.0 ml/minute generating shear stress at mean and median of 1.56 mPa and 1.29 mPa, respectively) was profiled and compared to the expression pattern resulting from pharmacologically induced osteogenic differentiation by OM.

Using the gene expression array, the expression levels of 85 markers were evaluated. The results showed that while the degree of upregulation in mechanically stimulated
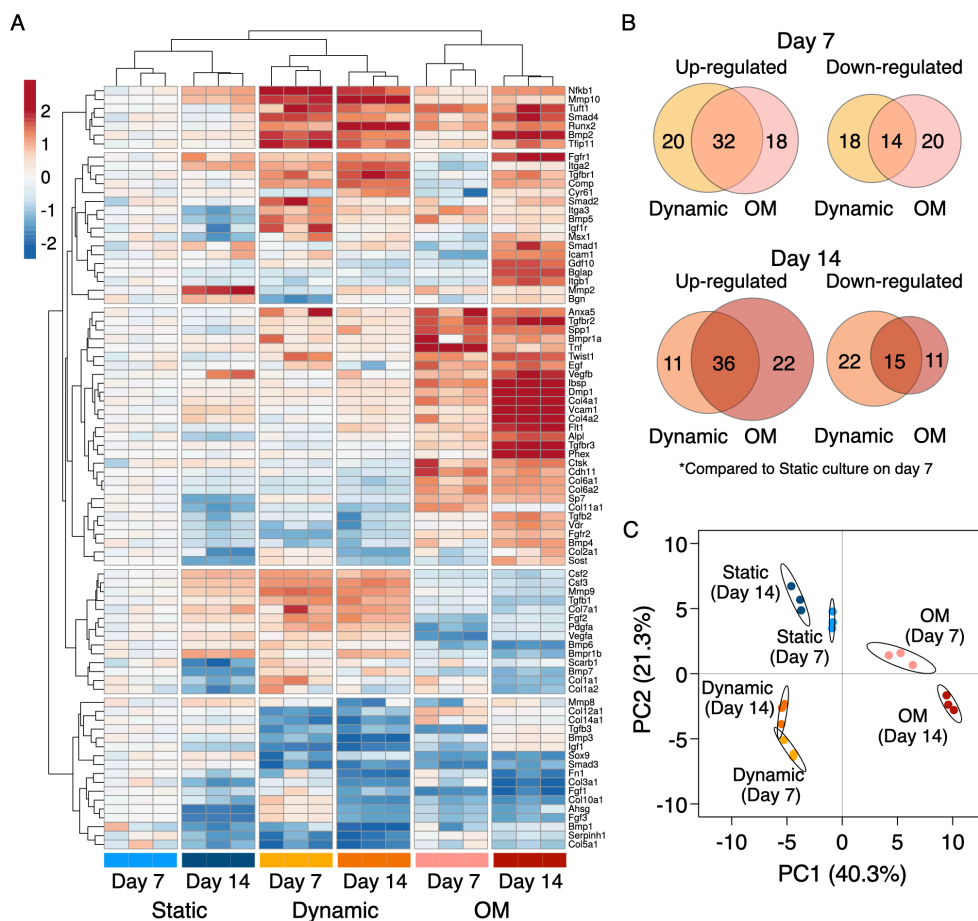
Figure 5.15 Osteogenic profiling by gene expression array
(A) Heatmap of differentially expressed genes (DEGs) involved in osteogenic differentiation. (B) Venn diagrams of upregulated and downregulated genes in BMSC stimulated mechanically and chemically. (C) Principal component (PC) analysis of osteogenic gene expression profile. Prediction ellipses are such that a new observation from the same group will fall inside the ellipse with probability 0.95.

BMSC was lower than those cultured in OM, BMSC under the fluid stimuli upregulated certain markers, which numbered 52 and 47 on day 7 and day 14, respectively (Figure 5.15 A, B). The upregulated markers on day 14 included conventional osteogenic markers, such as Runx2, Dmp1 (4.38-fold, $p = 0.0012$), Alpl (1.21-fold, $p = 0.038$), Spp1 (3.28-fold, $p = 0.0025$), and Ibsp (5.15-fold, $p = 0.0021$). In addition, transforming growth factor-β superfamily and its transducer (TGFβ: Tgfb1, Tgfb2; BMP: Bmp2, Bmp5, Bmp6, Bmp7; Smad2, Smad4), fibroblast growth factors (FGF: Fgf1, Fgf2, Fgf3), and colony-stimulating factors (CSF: Csfs: Csf2, Csf3) were found to be upregulated under the fluid stimuli. Distinctively, BMSC under the fluid stimuli, but not the cells cultured in OM, upregulated genes encoding bone ECM components (*e.g.*, Col1a1, Col1a2, Col2a1, Col4a1, Col7a1, Col10a1) and matrix metalloproteinases (*e.g.*, Mmp9, 61.62-fold, $p = 0.00010$; Mmp10, 149.66-fold, $p = 0.0069$) simultaneously, suggesting the presence of dynamic ECM remodelling under fluid flow. PCA revealed that the osteogenic profile of mechanically stimulated BMSC certainly differed from that induced by the osteogenic medium despite the similarity of their resulting functionality (Figure 5.15 C).

To better understand the underlying mechanisms of mechanosensation and mechanotransduction in relation to osteogenic responses, further investigation was conducted by hypothesising that cytoskeletal adaptation to the fluid stimuli was associated with fate determination.

5.5 Role of Rho-ROCK-mediated Cytoskeletal Contractility in Growth and Differentiation under Flow

5.5.1 Fluid stimuli altered cytoskeletal regulators and adhesion molecules (**Paper IV**)

First, cytoskeletal modulation under fluid flow was assessed comprehensively at a mRNA expression level. The gene expression array demonstrated that 82 out of 155 tested genes encoding cytoskeletal regulators and adhesion molecules were significantly upregulated in the dynamic condition (Figure 5.16 A). The gene set enrichment analysis predicted the functional enrichment of Rho GTPases, which was
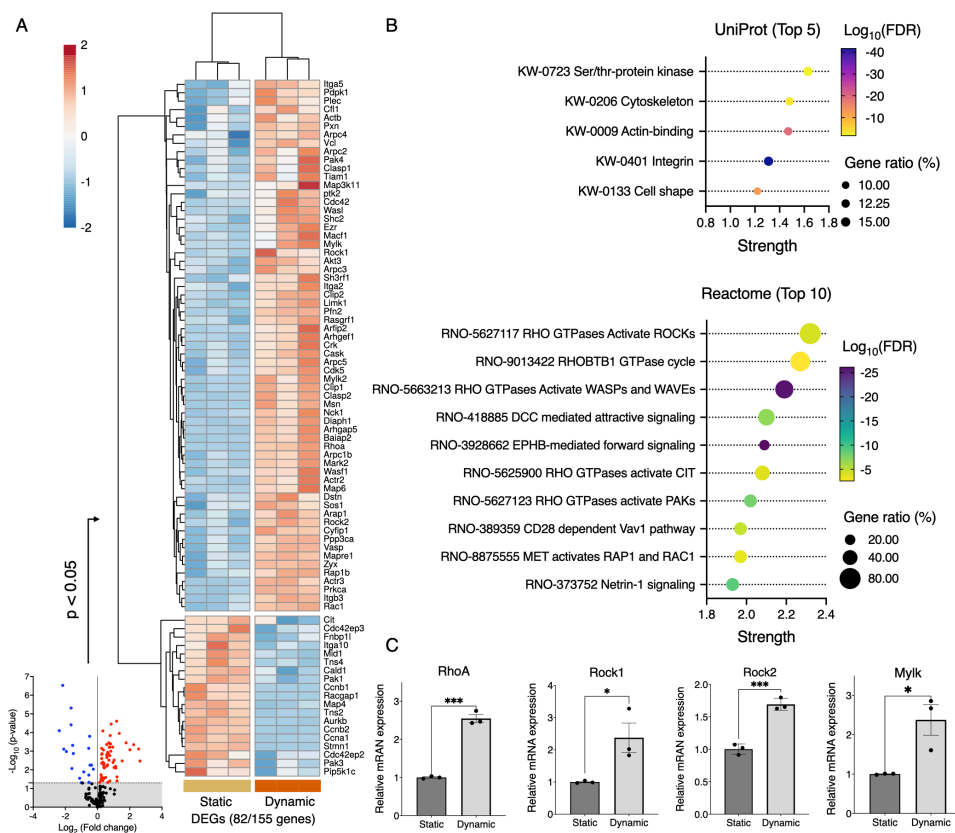
Figure 5.16 Gene expression array and gene set enrichment analysis
(A) Gene expression array evaluating 155 genes encoding cytoskeletal regulators and adhesion molecules. Only DEGs (82 markers, $p < 0.05$) were displayed in the heatmap. (B) Gene set enrichment analysis of DEGs using UniProt and Reactome pathway databases. (C) mRNA expression levels of RhoA and its downstream targets quantified by RT-qPCR. $*p < 0.05$, $***p < 0.001$ (Student's t-test).

verified by RT-qPCR, showing the upregulation of RhoA and its downstream targets, namely Rock1, Rock2, and Mylk (Figure 5.16 B, C). Immunofluorescence demonstrated that BMSC subjected to the fluid stimuli exhibited more elongated morphology with an increase in phosphorylation of MLC and thicker filamentous actin, which was accompanied by the enhanced enzymatic activity of ROCK (Figure 5.17 A, B). This resulted in more elongated morphology under the fluid stimuli as shown by an increase in the aspect ratio of the nuclei [275] (Figure 5.17 C). These results indicate that even considerably low level of fluid stimuli, such as shear stress of 1-2 mPa in the present 3D model, are sufficient to trigger cytoskeletal modulation mediated by Rho-
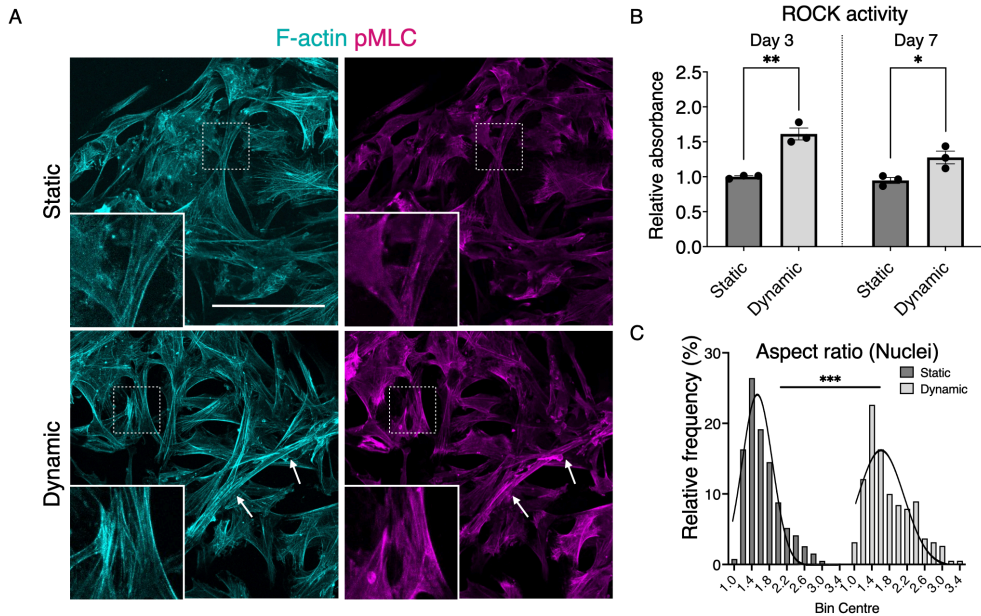
Figure 5.17 Enhanced cell contractility and ROCK activity under fluid flow
(A) Immunofluorescence of pMLC co-stained with filamentous actin (F-actin). Arrows indicate sites where enriched F-actin and pMLC were co-localised. (B) The enzymatic activity of ROCK. (C) Cell morphometrical analysis using nuclear aspect ratio, showing more elongated cell nuclei under fluid flow. The fitted distribution lines were generated by Gaussian distribution equation. Scale bar = 100 μm. *$p < 0.05$, **$p < 0.01$, ***$p < 0.001$ (B: Student's t-test, C: Mann-Whitney U test).

ROCK signalling pathways, as previously reported in 2D monolayer models with shear stress of 1-3 Pa [203–205].

5.5.2   Cytoskeletal contraction was required for cell growth under flow (**Paper IV**)

To investigate the role of cytoskeletal contractility in the growth and fate determination of BMSC under the dynamic condition, inhibitors, namely Rhosin, Y27632, MLCK ip 18, and Blebbistatin, which target RhoA, ROCK1/2, MLCK, and Myosin II, respectively, were prescribed.

In the static condition, these inhibitors at the optimal concentration did not affect cell proliferation as evidenced by EdU incorporation and dsDNA quantification (Figure 5. 18 A-C). As demonstrated in the previous section, BMSC under fluid flow showed decreased proliferation, but they were still able to continue to increase their number.
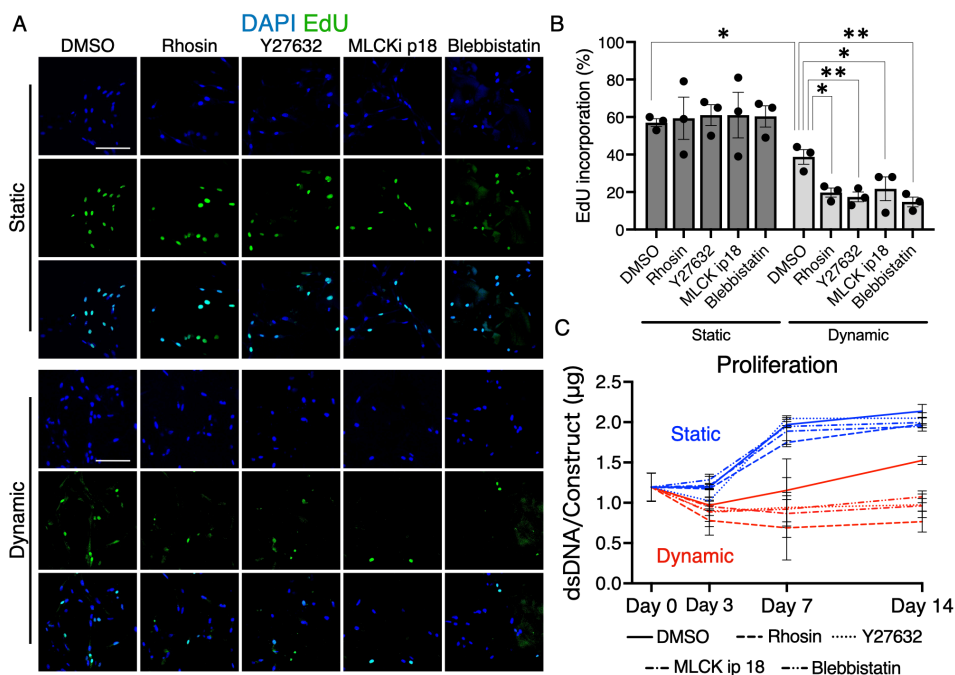
Figure 5.18 Effects of the inhibition of Rho-ROCK-mediated cytoskeletal contraction on cell proliferation in the static and dynamic conditions.
(A, B) EdU incorporation for 24 hours in the presence of the Rho, ROCK, MLCK, and Myosin II inhibitors. (C) Cell proliferation in the presence of the inhibitors measured by dsDNA quantification. Scale bar = 100 μm. $*p < 0.05$, $**p < 0.01$ (Student's t-test for comparison between the static and dynamic conditions, Dunnett's test for multiple comparisons).

However, when the inhibitors were applied in the dynamic condition, their cell cycle was notably stagnated, which resulted in almost no population gain over the period of 14 days. This observation indicates that cell contractility is necessary to maintain their proliferative status in the dynamic condition despite cell contraction may be associated with decreased proliferation (Data included in the supplementary in Paper IV, showing the pharmacological activation of Rho and cell contraction inhibited cell growth).

5.5.3   Cytoskeletal contraction was required for mechanically induced osteogenic differentiation under flow (**Paper IV**)

Finally, the role of cytoskeletal contractility in the mechanically induced osteogenic differentiation was investigated. Notably, the inhibitors used in the study fully nullified
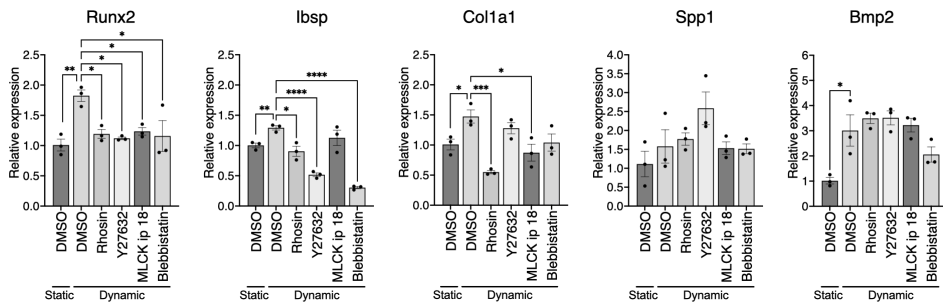
Figure 5.19 mRNA expression level of putative osteogenic markers under the fluid stimuli in the presence of the inhibitors against Rho-ROCK-mediated cytoskeletal contraction
For the comparison between the static and dynamic condition, Student's t-test was performed. For multiple comparisons, Dunnett's test was performed to compare the treated samples by the inhibitors with the DMSO control. $*p < 0.05$, $* p < 0.01$, $***p < 0.001$, $****p < 0.0001$ (Student's t-test for comparison between the static and dynamic conditions; Dunnett's test for multiple comparisons within the dynamic condition).

the upregulation of Runx2 that was induced mechanically (Figure 5.19). Additionally, the upregulation of other osteogenic markers, including Bsp and Col1a1, was also significantly mitigated by the inhibitors. The extent of suppression appeared to vary depending on the markers evaluated, and the inhibitors did not affect the expression of Spp1 and Bmp2 significantly. This observation suggests that Rho-ROCK-mediated cytoskeletal contractility may not solely trigger the mechanically induced osteogenic responses, but rather it appears to be a multifactorial phenomenon. In fact, previous studies reported that ERK/MAPK signalling, P38 signalling, TGFβ signalling, Hedgehog signalling, Notch signalling, and Wnt signalling pathways were also modulated in MSC as well as osteoblasts and osteocytes under various fluid stimuli [191,276–279]. The activation of these pathways were shown to play a regulatory role in osteogenic differentiation, which may bypass Rho-ROCK-mediated cytoskeletal modulation [280]. However, provided that Runx2 is the key transcriptional factor for osteogenesis, the data suggest the activation of Rho-ROCK signalling and cell contractility by the fluid stimuli are indispensable to initiate the differentiation cascade.

The osteogenic functionality was further evaluated by their functionality, including collagen secretion, ALP activity, and mineralisation in the presence of the inhibitors under the fluid stimuli. Similar to the gene expression pattern, COL1 secretion and ALP activity enhanced by the fluidic stimuli were negated by the inhibitors (Figure

5.20 A-D). For the mineralisation assay, β-glycerophosphate was supplemented. Adding the phosphate source allowed BMSC stimulated by fluid flow to mineralise the scaffolds extensively, whereases the supplementation was not sufficient to induce osteogenic differentiation in the static condition (Figure 5.20 E, F). The inhibitors suppressed the mineralisation, particularly when the actomyosin contraction was directly inhibited by blebbistatin.

Despite the observation that Rho-ROCK-mediated cell contractility was necessary for the unique osteogenic responses induced by the fluid stimuli, whether the signalling is sufficient to induce the differentiation remains unexplored. It is certain that cell
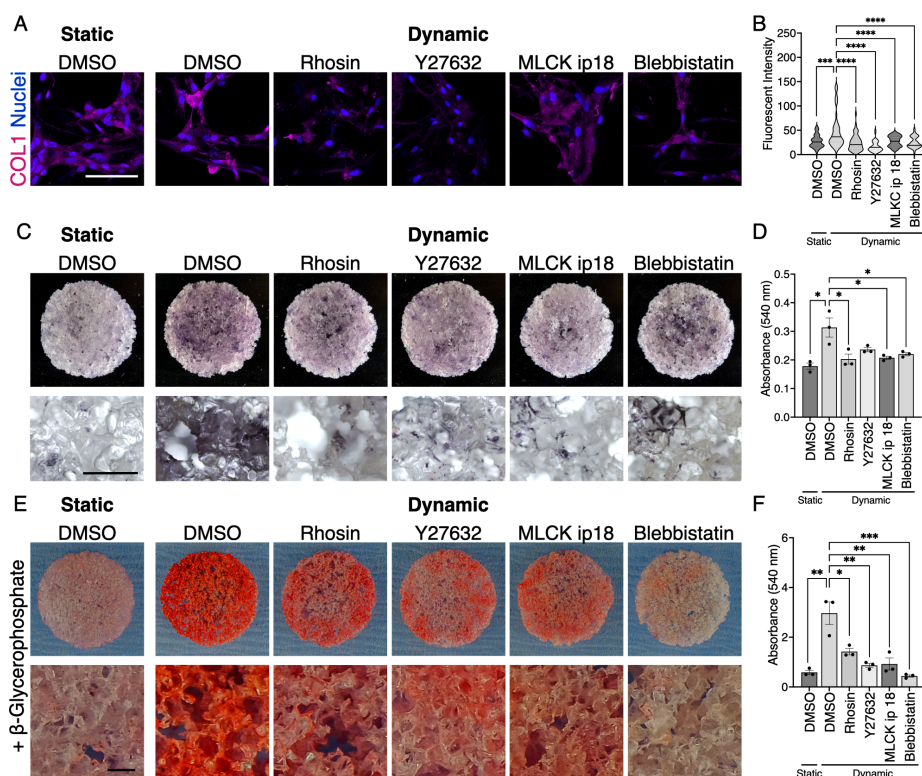
Figure 5.20 Effects of the inhibition of Rho-ROCK-mediated cytoskeletal contractility on mechanically induced osteogenic differentiation in the dynamic condition
(A, B) Immunofluorescence of COL1 and quantification. (C, D) ALP staining and quantification. (E, F) Alizarin red Staining and quantification. For the experiment, β-glycerophosphate was supplemented as a source of inorganic phosphate for mineralisation. Scale bar = 100 μm. *$p < 0.05$, **$p < 0.01$, ***$p < 0.001$, ****$p < 0.0001$ (Student's t-test for comparison between the static and dynamic conditions; Dunnett's test for multiple comparisons within the dynamic condition).

contraction and osteogenic differentiation are highly compatible phenomena [197]. In paper IV, it was shown that the forced cell contraction by Rho activation or MLCP inhibition altered osteogenic gene expression and ALP activity, suggesting an involvement of cell contraction in MSC fate determination towards the osteogenic lineage. It would be reasonable to assume that multiple signalling pathways coordinately regulate mechanically induced fate determination. Further studies are needed to elucidate whether the activation of Rho-ROCK signalling pathway or cell contraction alone can trigger the differentiation.

6. Conclusions

In the present thesis, a series of studies were conducted from a tissue engineering perspective, starting from scaffold fabrication to the optimisation of dynamic culture conditions, the proof-of-concept study for mechanical stimulation for osteogenic differentiation, and the analyses of causality between fluidic stimulation and biological phenomena. From the studies, the following conclusions were drawn:

1. PLTMC possesses superb cytocompatibility and *in vitro* osteoconductivity with BMSC, which supports the survival, growth, and osteogenic differentiation of BMSC for the long term. Its favourable flexibility, formability, and tunability allowed for the fabrication of highly porous scaffolds for bone tissue engineering, which can be applied in a perfusion system.

2. The implementation of dynamic cell culture necessitates not only the optimisation of flow rate, but also careful attention to other environmental factors. These parameters can exert a significant influence on the growth and differentiation of BMSC. Although a successful implementation of a bioreactor for dynamic cell culture requires careful consideration from both mechanical engineering and biological perspectives, once achieved, it can result in highly promising biological readouts.

3. Fluid stimuli are sufficient to induce the osteogenic differentiation of BMSC in the absence of the osteoinductive supplements. Notably, the mechanically induced osteogenic profile differs from the chemically induced counterpart, despite the resemblance of their osteogenic functionality, which is represented by an increase in collagen secretion, ALP activity, and mineralisation.

4. Dynamic cell culture stimulates the Rho-ROCK-mediated cytoskeletal contractility of BMSC in addition to the activation of other cytoskeletal regulators and adhesion molecules. These responses were induced by the extremely low levels of fluid stimuli in the 3D system compared to those previously reported in 2D models. The cytoskeletal adaptation to the dynamic environment is necessary for cell survival and mechanically induced osteogenic differentiation.

7. Limitations and Future Perspectives

In the studies, BMSC isolated from Lewis rats were used to minimise donor variation and improve consistency through the studies. With the cell type, the range of flow rate between 0.8 ml/minute and 1.6 ml/minute, which exerted mean fluid shear stresses of 0.88 mPa and 1.76 mPa in the setup, respectively, was considered optimal for long-term culture in the context of bone tissue engineering. However, the optimised parameters may not be universally transferable to the other experimental conditions. For example, optimal flow patterns may vary depending on a range of factors, such as cell types, donor species, tissue origin, donor age, gender, and nutritional status [281]. Particularly, donor variation between human individuals should not be underestimated. Indeed, responses to fluid shear stress have been shown to vary significantly among different donors [282]. Moreover, while mechanically induced osteogenic responses were observed in αMEM with FBS in the present studies, the optimal selection of culture medium has yet to be thoroughly explored. In particular, there is a growing trend towards opposition to the utilisation of substances derived from animals in the manufacture of cell products. Hence, identification of a suitable and ideally serum-free medium needs to be addressed. Therefore, further optimisation and validation will be required before the technology can be confidently translated into a clinical setting.

In addition, despite the conclusive findings that fluid stimuli can trigger osteogenic differentiation, whether this is significant clinically has not been elucidated yet. To prove that the mechanically stimulated BMSC contribute to better bone regeneration, *in vivo* preclinical experiments are required. For clinical translation, the size of the cell-laden construct will be larger than what was used in the present studies, and therefore, the importance of perfusion bioreactors will further increase as they provide robust fluid flow to improve mass transfer into the interior of the scaffolds. However, the thickness of a scaffold to be adequately nourished *in vivo* is thought to be limited to a few millimeters [283]. This implies that, in an *in vivo* environment where robust flow such as that generated by bioreactors may not be present, engineered constructs may experience a deficiency in nutrient and gas supply after implantation, potentially leading to treatment failure. Therefore, for scaling up, consideration of vascularising

the constructs would be required. To date, various strategies have been employed to create vascularised construct, mostly by co-culturing endothelial cells and MSC [284,285]. Since perfusion culture facilitates the formation of a vascular network in engineered constructs, it can be a logical strategy to attempt to stimulate the osteogenic properties of BMSC and pre-vascularisation simultaneously [286–288]. Furthermore, the functionalisation of scaffolds by, for example, loading growth factors, may offer additional benefits to stimulate capillary formation by regulating microenvironment after implantation. Possible candidates include pro-angiogenic factors, such as FGFs, vascular endothelial growth factors (VEGFs), platelet-derived growth factors (PDGFs), and TGFβ, and inflammatory regulators, such as interleukins and CSFs, which may contribute to the successful integration of the engineered constructs to the implanted sites [289].

Finally, there are also several regulatory challenges that must be overcome in order to bring engineered constructs from bioreactors to patients. MSC for cell therapies are treated as advanced therapy medicinal products (ATMP), and therefore, the production process for tissue engineering constructs is strictly regulated by Current Good Manufacturing Practice (cGMP). With no exception, cells manipulated in bioreactor systems are subject to strict regulatory oversight. Additionally, bioreactor systems for cell production fit the category of class 1 medical device (according to EU MDR for the EU, FDA for the USA), and therefore, they must satisfy regional regulations through general safety and performance tests and clinical evaluation. However, as an emerging technology, there is a lack of consensual standard with respect to, for example, device designs, safety assessment, cell production process, and methods to evaluate produced constructs [217]. The bioreactor prototypes introduced to date have been developed under different concepts. In addition, attempts to automate cell culture are underway to reduce operator dependency and improve production efficiency [290]. In other words, the environment surrounding machinery-based tissue engineering is becoming more and more complex. Standardisation of the emerging technology may be achieved through anticipatory consensus standards, as a society of nanotechnology previously proposed and managed to agree, among academics, clinicians, industry, and

regulatory bodies [291]. The degree of standardisation is debatable, but it will facilitate the commercialisation and clinical translation of the technology.

8. References

1. Donati, D., Zolezzi, C., Tomba, P. & Viganò, A. Bone grafting: historical and conceptual review, starting with an old manuscript by Vittorio Putti. *Acta Orthop.* **78**, 19–25 (2007).

2. Grant, G. A. *et al.* Failure of autologous bone—assisted cranioplasty following decompressive craniectomy in children and adolescents. *J. Neurosurg. Pediatr.* **100**, 163–168 (2004).

3. Schmidt, A. H. Autologous bone graft: Is it still the gold standard? *Injury* **52**, S18–S22 (2021).

4. Younger, E. M. & Chapman, M. W. Morbidity at Bone Graft Donor Sites. *J. Orthop. Trauma* **3**, 192–195 (1989).

5. Dimitriou, R., Mataliotakis, G. I., Angoules, A. G., Kanakaris, N. K. & Giannoudis, P. V. Complications following autologous bone graft harvesting from the iliac crest and using the RIA: A systematic review. *Injury* **42**, S3–S15 (2011).

6. Fourcade, C., Lesclous, P. & Guiol, J. Assignment of autogenous bone grafts for reconstruction of the alveolar ridge before implant placement. *J. Oral Med. Oral Surg.* **25**, 1 (2019).

7. Murphy, C., O'Brien, F., Little, D. & Schindeler, A. Cell-scaffold interactions in the bone tissue engineering triad. *Eur. Cells Mater.* **26**, 120–132 (2013).

8. da Silva Meirelles, L., Chagastelles, P. C. & Nardi, N. B. Mesenchymal stem cells reside in virtually all post-natal organs and tissues. *J. Cell Sci.* **119**, 2204–13 (2006).

9. Liang, X., Ding, Y., Zhang, Y., Tse, H.-F. & Lian, Q. Paracrine Mechanisms of Mesenchymal Stem Cell-Based Therapy: Current Status and Perspectives. *Cell Transplant.* **23**, 1045–1059 (2014).

10. Maacha, S. *et al.* Paracrine Mechanisms of Mesenchymal Stromal Cells in Angiogenesis. *Stem Cells Int.* **2020**, 1–12 (2020).

11. Gao, F. *et al.* Mesenchymal stem cells and immunomodulation: current status and future prospects. *Cell Death Dis.* **7**, e2062–e2062 (2016).

12. Pittenger, M. F. *et al.* Multilineage Potential of Adult Human Mesenchymal Stem Cells. *Science.* **284**, 143–147 (1999).

13. Sanchez-Ramos, J. *et al.* Adult Bone Marrow Stromal Cells Differentiate into Neural Cells in Vitro. *Exp. Neurol.* **164**, 247–256 (2000).

14. Herzog, E. L., Chai, L. & Krause, D. S. Plasticity of marrow-derived stem cells. *Blood* **102**, 3483–3493 (2003).

15. Squillaro, T., Peluso, G. & Galderisi, U. Clinical Trials with Mesenchymal Stem Cells: An Update. *Cell Transplant.* **25**, 829–848 (2016).

16. Han, Y. *et al.* The secretion profile of mesenchymal stem cells and potential applications in treating human diseases. *Signal Transduct. Target. Ther.* **7**, 92 (2022).

17. Lalu, M. M. *et al.* Safety of Cell Therapy with Mesenchymal Stromal Cells (SafeCell): A Systematic Review and Meta-Analysis of Clinical Trials. *PLoS One* **7**, e47559 (2012).

18. Wang, Y., Yi, H. & Song, Y. The safety of MSC therapy over the past 15 years: a meta-analysis. *Stem Cell Res. Ther.* **12**, 545 (2021).

19. Yim, H., Jeong, H., Cho, Y., Jeong, S. & Oh, I. Safety of Mesenchymal Stem Cell Therapy: A Systematic Review and Meta-Analysis. *Cytotherapy* **18**, S132 (2016).

20. Kvistad, C. E. *et al.* Safety and Clinical Efficacy of Mesenchymal Stem Cell Treatment in Traumatic Spinal Cord Injury, Multiple Sclerosis and Ischemic Stroke - A Systematic Review and Meta-Analysis. *Front. Neurol.* **13**, 891514 (2022).

21. Barkholt, L. *et al.* Risk of tumorigenicity in mesenchymal stromal cell-based therapies - Bridging scientific observations and regulatory viewpoints. *Cytotherapy* **15**, 753–759 (2013).

22. Kraus, K. H. & Kirker-Head, C. Mesenchymal stem cells and bone regeneration. *Vet. Surg.* **35**, 232–42 (2006).

23. Rodríguez-Fuentes, D. E. *et al.* Mesenchymal Stem Cells Current Clinical Applications: A Systematic Review. *Arch. Med. Res.* **52**, 93–101 (2021).

24. Gjerde, C. *et al.* Cell therapy induced regeneration of severely atrophied mandibular bone in a clinical trial. *Stem Cell Res. Ther.* **9**, 213 (2018).

25. Schu, S. *et al.* Immunogenicity of allogeneic mesenchymal stem cells. *J. Cell. Mol. Med.* **16**, 2094–2103 (2012).

26. Volarevic, V. *et al.* Ethical and Safety Issues of Stem Cell-Based Therapy. *Int. J. Med. Sci.* **15**, 36–45 (2018).

27. Orbay, H., Tobita, M. & Mizuno, H. Mesenchymal Stem Cells Isolated from Adipose and Other Tissues: Basic Biological Properties and Clinical Applications. *Stem Cells Int.* **2012**, 1–9 (2012).

28. Costela-Ruiz, V. J. *et al.* Different Sources of Mesenchymal Stem Cells for Tissue Regeneration: A Guide to Identifying the Most Favorable One in Orthopedics and Dentistry Applications. *Int. J. Mol. Sci.* **23**, 6356 (2022).

29. Infante, A. & Rodríguez, C. I. Osteogenesis and aging: lessons from mesenchymal stem cells. *Stem Cell Res. Ther.* **9**, 244 (2018).

30. Castillo, A. B. & Jacobs, C. R. Mesenchymal Stem Cell Mechanobiology. *Curr. Osteoporos. Rep.* **8**, 98–104 (2010).

31. Pontikoglou, C., Deschaseaux, F., Sensebé, L. & Papadaki, H. A. Bone Marrow Mesenchymal Stem Cells: Biological Properties and Their Role in Hematopoiesis and Hematopoietic Stem Cell Transplantation. *Stem Cell Rev. Reports* **7**, 569–589 (2011).

32. Arjmand, B. *et al.* Prospect of Stem Cell Therapy and Regenerative Medicine in Osteoporosis. *Front. Endocrinol. (Lausanne).* **11**, 430 (2020).

33. Oryan, A., Kamali, A., Moshiri, A. & Baghaban Eslaminejad, M. Role of Mesenchymal Stem Cells in Bone Regenerative Medicine: What Is the Evidence? *Cells. Tissues. Organs* **204**, 59–83 (2017).

34. Aasebø, E. *et al.* Proteomic Comparison of Bone Marrow Derived Osteoblasts and Mesenchymal Stem Cells. *Int. J. Mol. Sci.* **22**, 5665 (2021).

35. Stenderup, K., Justesen, J., Clausen, C. & Kassem, M. Aging is associated with decreased maximal life span and accelerated senescence of bone marrow stromal cells. *Bone* **33**, 919–926 (2003).

36. Mueller, S. M. & Glowacki, J. Age-related decline in the osteogenic potential of human bone marrow cells cultured in three-dimensional collagen sponges. *J. Cell. Biochem.* **82**, 583–590 (2001).

37. Friedenstein, A. J., Chailakhjan, R. K. & Lalykina, K. S. The development of fibroblast colonies in monolayer cultures of guinea-pig bone marrow and spleen cells. *Cell Tissue Kinet.* **3**, 393–403 (1970).

38. Castro-Malaspina, H. *et al.* Characterization of human bone marrow fibroblast colony-forming cells (CFU-F) and their progeny. *Blood* **56**, 289–301 (1980).

39. Wexler, S. A. *et al.* Adult bone marrow is a rich source of human mesenchymal 'stem' cells but umbilical cord and mobilized adult blood are not. *Br. J. Haematol.* **121**, 368–374 (2003).

40. Kastrinaki, M.-C. *et al.* Functional, molecular and proteomic characterisation of bone marrow mesenchymal stem cells in rheumatoid arthritis. *Ann. Rheum. Dis.* **67**, 741–749 (2008).

41. Kiernan, J., Davies, J. E. & Stanford, W. L. Concise Review: Musculoskeletal Stem Cells to Treat Age-Related Osteoporosis. *Stem Cells Transl. Med.* **6**, 1930–1939 (2017).

42. Catalano, E. *et al.* Adipose-derived adult stem cells: available technologies for potential clinical regenerative applications in dentistry. *Crit. Rev. Biomed. Eng.* **41**, 483–93 (2013).

43. Varma, M. J. O. *et al.* Phenotypical and Functional Characterization of Freshly Isolated Adipose Tissue-Derived Stem Cells. *Stem Cells Dev.* **16**, 91–104 (2007).

44. Astori, G. *et al.* 'In vitro' and multicolor phenotypic characterization of cell subpopulations identified in fresh human adipose tissue stromal vascular fraction and in the derived mesenchymal stem cells. *J. Transl. Med.* **5**, 55 (2007).

45. Fraser, J. K., Wulur, I., Alfonso, Z. & Hedrick, M. H. Fat tissue: an underappreciated source of stem cells for biotechnology. *Trends Biotechnol.* **24**, 150–154 (2006).

46. Mohamed-Ahmed, S. *et al.* Adipose-derived and bone marrow mesenchymal stem cells: a donor-matched comparison. *Stem Cell Res. Ther.* **9**, 168 (2018).

47. Egusa, H., Sonoyama, W., Nishimura, M., Atsuta, I. & Akiyama, K. Stem cells in dentistry - Part I: Stem cell sources. *J. Prosthodont. Res.* **56**, 151–165 (2012).

48. Huang, G. T.-J. T.-J., Gronthos, S. & Shi, S. Mesenchymal stem cells derived from dental tissues vs. those from other sources: their biology and role in regenerative medicine. *J. Dent. Res.* **88**, 792–806 (2009).

49. Zheng, C., Chen, J., Liu, S. & Jin, Y. Stem cell-based bone and dental regeneration: a view of microenvironmental modulation. *Int. J. Oral Sci.* **11**, 23 (2019).

50. Yamada, Y., Nakamura-Yamada, S., Konoki, R. & Baba, S. Promising advances in clinical trials of dental tissue-derived cell-based regenerative medicine. *Stem Cell Res. Ther.* **11**, 175 (2020).

51. Chalisserry, E. P., Nam, S. Y., Park, S. H. & Anil, S. Therapeutic potential of dental stem cells. *J. Tissue Eng.* **8**, 204173141770253 (2017).

52. Zeitlin, B. D. Banking on teeth – Stem cells and the dental office. *Biomed. J.* **43**, 124–133 (2020).

53. Huang, Y.-H., Yang, J.-C., Wang, C.-W. & Lee, S.-Y. Dental Stem Cells and Tooth Banking for Regenerative Medicine. *J. Exp. Clin. Med.* **2**, 111–117 (2010).

54. Garg, T., Singh, O., Arora, S. & Murthy, R. S. R. Scaffold: A Novel Carrier for Cell and Drug Delivery. *Crit. Rev. Ther. Drug Carr. Syst.* **29**, 1–63 (2012).

55. Place, E. S., George, J. H., Williams, C. K. & Stevens, M. M. Synthetic polymer scaffolds for tissue engineering. *Chem. Soc. Rev.* **38**, 1139 (2009).

56. Chan, B. P. & Leong, K. W. Scaffolding in tissue engineering: general approaches and tissue-specific considerations. *Eur. Spine J.* **17**, 467–479 (2008).

57. Requicha, J. F. *et al.* Design and characterization of a biodegradable double-layer scaffold aimed at periodontal tissue-engineering applications. *J. Tissue Eng. Regen. Med.* **10**, 392–403 (2016).

58. Ghassemi, T. *et al.* Current Concepts in Scaffolding for Bone Tissue Engineering. *Arch. bone Jt. Surg.* **6**, 90–99 (2018).

59. Wu, S., Liu, X., Yeung, K. W. K., Liu, C. & Yang, X. Biomimetic porous scaffolds for bone tissue engineering. *Mater. Sci. Eng. R Reports* **80**, 1–36 (2014).

60. Kohane, D. S. & Langer, R. Polymeric Biomaterials in Tissue Engineering. *Pediatr. Res.* **63**, 487–491 (2008).

61. Arifin, N., Sudin, I., Ngadiman, N. H. A. & Ishak, M. S. A. A Comprehensive Review of Biopolymer Fabrication in Additive Manufacturing Processing for 3D-Tissue-Engineering Scaffolds. *Polymers (Basel).* **14**, 115 (2022).

62. Weigel, T., Schinkel, G. & Lendlein, A. Design and preparation of polymeric scaffolds for tissue engineering. *Expert Rev. Med. Devices* **3**, 835–851 (2006).

63. Vroman, I. & Tighzert, L. Biodegradable polymers. *Materials (Basel).* **2**, 307–344 (2009).

64. Donnaloja, F., Jacchetti, E., Soncini, M. & Raimondi, M. T. Natural and Synthetic Polymers for Bone Scaffolds Optimization. *Polymers (Basel).* **12**, 905 (2020).

65. Singhvi, M. S., Zinjarde, S. S. & Gokhale, D. V. Polylactic acid: synthesis and biomedical applications. *J. Appl. Microbiol.* **127**, 1612–1626 (2019).

66. Conn, R. E. *et al.* Safety assessment of polylactide (PLA) for use as a food-contact polymer. *Food Chem. Toxicol.* **33**, 273–283 (1995).

67. Woodruff, M. A. & Hutmacher, D. W. The return of a forgotten polymer—Polycaprolactone in the 21st century. *Prog. Polym. Sci.* **35**, 1217–1256 (2010).

68. Farah, S., Anderson, D. G. & Langer, R. Physical and mechanical properties of PLA, and their functions in widespread applications — A comprehensive review. *Adv. Drug Deliv. Rev.* **107**, 367–392 (2016).

69. Chen, C.-C., Chueh, J.-Y., Tseng, H., Huang, H.-M. & Lee, S.-Y. Preparation and characterization of biodegradable PLA polymeric blends. *Biomaterials* **24**, 1167–1173 (2003).

70. Patrício, T., Domingos, M., Gloria, A. & Bártolo, P. Characterisation of PCL and PCL/PLA Scaffolds for Tissue Engineering. *Procedia CIRP* **5**, 110–114 (2013).

71. Feng, P. *et al.* Degradation mechanisms and acceleration strategies of poly (lactic acid) scaffold for bone regeneration. *Mater. Des.* **210**, 110066 (2021).

72. Sun, H., Mei, L., Song, C., Cui, X. & Wang, P. The in vivo degradation, absorption and excretion of PCL-based implant. *Biomaterials* **27**, 1735–1740 (2006).

73. Dwivedi, R. *et al.* Polycaprolactone as biomaterial for bone scaffolds: Review of literature. *J. Oral Biol. Craniofacial Res.* **10**, 381–388 (2020).

74. Böstman, O. & Pihlajamäki, H. Clinical biocompatibility of biodegradable orthopaedic implants for internal fixation: a review. *Biomaterials* **21**, 2615–2621 (2000).

75. da Silva, D. *et al.* Biocompatibility, biodegradation and excretion of polylactic acid (PLA) in medical implants and theranostic systems. *Chem. Eng. J.* **340**, 9–14 (2018).

76. Bliley, J. M. & Marra, K. G. Polymeric Biomaterials as Tissue Scaffolds. in *Stem Cell Biology and Tissue Engineering in Dental Sciences* 149–161 (Elsevier, 2015). doi:10.1016/B978-0-12-397157-9.00013-8

77. Brossier, T., Volpi, G., Lapinte, V. & Blanquer, S. Synthesis of Poly(Trimethylene Carbonate) from Amine Group Initiation: Role of Urethane Bonds in the Crystallinity. *Polymers (Basel).* **13**, 280 (2021).

78. Yang, L., Li, J., Li, M. & Gu, Z. The in vitro and in vivo degradation of cross-linked poly(trimethylene carbonate)-based networks. *Polymers (Basel).* **8**, (2016).

79. Hassan, M. N. *et al.* Contact osteogenesis by biodegradable 3D-printed poly(lactide-co-trimethylene carbonate). *Biomater. Res.* **26**, 55 (2022).

80. Kivijärvi, T. *et al.* Hybrid material based on hyaluronan hydrogels and poly(l-lactide-co-1,3-trimethylene carbonate) scaffolds toward a cell-instructive microenvironment with long-term in vivo degradability. *Mater. Today Bio* **17**, 100483 (2022).

81. Jain, S. *et al.* Engineering 3D degradable, pliable scaffolds toward adipose tissue regeneration; optimized printability, simulations and surface modification. *J. Tissue Eng.* **11**, 204173142095431 (2020).

82. Lee, S. *et al.* Potential Bone Replacement Materials Prepared by Two Methods. *MRS Proc.* **1418**, mrsf11-1418-mm06-02 (2012).

83. Jeong, Y. Y. *et al.* Comparison of 2- and 3-Dimensional Cultured Periodontal Ligament Stem Cells; a Pilot Study. *Appl. Sci.* **11**, 1083 (2021).

84. Lund, A. W., Bush, J. A., Plopper, G. E. & Stegemann, J. P. Osteogenic differentiation of mesenchymal stem cells in defined protein beads. *J. Biomed. Mater. Res. Part B Appl. Biomater.* **87B**, 213–221 (2008).

85. Lund, A. W., Stegemann, J. P. & Plopper, G. E. Mesenchymal Stem Cells Sense Three Dimensional Type I Collagen through Discoidin Domain Receptor 1. *Open Stem Cell J.* **1**, 40–53 (2009).

86. Han, S. *et al.* The Three-Dimensional Collagen Scaffold Improves the Stemness of Rat Bone Marrow Mesenchymal Stem Cells. *J. Genet. Genomics* **39**, 633–641 (2012).

87. Yamaguchi, Y., Ohno, J., Sato, A., Kido, H. & Fukushima, T. Mesenchymal stem cell spheroids exhibit enhanced in-vitro and in-vivo osteoregenerative potential. *BMC Biotechnol.* **14**, 105 (2014).

88. Baraniak, P. R. & McDevitt, T. C. Scaffold-free culture of mesenchymal stem cell spheroids in suspension preserves multilineage potential. *Cell Tissue Res.* **347**, 701–711 (2012).

89. Dias, M. R., Fernandes, P. R., Guedes, J. M. & Hollister, S. J. Permeability analysis of scaffolds for bone tissue engineering. *J. Biomech.* **45**, 938–944 (2012).

90. Karageorgiou, V. & Kaplan, D. Porosity of 3D biomaterial scaffolds and osteogenesis. *Biomaterials* **26**, 5474–5491 (2005).

91. Somo, S. I. *et al.* Pore Interconnectivity Influences Growth Factor-Mediated Vascularization in Sphere-Templated Hydrogels. *Tissue Eng. Part C Methods* **21**, 773–785 (2015).

92. Amini, A. R., Adams, D. J., Laurencin, C. T. & Nukavarapu, S. P. Optimally Porous and Biomechanically Compatible Scaffolds for Large-Area Bone Regeneration. *Tissue Eng. Part A* **18**, 1376–1388 (2012).

93. Hulbert, S. F. *et al.* Potential of ceramic materials as permanently implantable skeletal prostheses. *J. Biomed. Mater. Res.* **4**, 433–456 (1970).

94. Jin, Q.-M. *et al.* Effects of geometry of hydroxyapatite as a cell substratum in BMP-induced ectopic bone formation. *J. Biomed. Mater. Res.* **51**, 491–499 (2000).

95. Kuboki, Y., Jin, Q. & Takita, H. Geometry of Carriers Controlling Phenotypic Expression in BMP-Induced Osteogenesis and Chondrogenesis. *J. Bone Jt. Surgery-American Vol.* **83**, S1-105-S1-115 (2001).

96. Kuboki, Y., Jin, Q., Kikuchi, M., Mamood, J. & Takita, H. Geometry of Artificial ECM: Sizes of Pores Controlling Phenotype Expression in BMP-Induced Osteogenesis and Chondrogenesis. *Connect. Tissue Res.* **43**, 529–534 (2002).

97. Tsuruga, E., Takita, H., Itoh, H., Wakisaka, Y. & Kuboki, Y. Pore Size of Porous Hydroxyapatite as the Cell-Substratum Controls BMP-Induced Osteogenesis. *J. Biochem.* **121**, 317–324 (1997).

98. Filipowska, J., Tomaszewski, K. A., Niedźwiedzki, Ł., Walocha, J. A. & Niedźwiedzki, T. The role of vasculature in bone development, regeneration and proper systemic functioning. *Angiogenesis* **20**, 291–302 (2017).

99. Al Hadi, H., Smerdon, G. R. & Fox, S. W. Hyperbaric oxygen therapy accelerates osteoblast differentiation and promotes bone formation. *J. Dent.* **43**, 382–388 (2015).

100. Lafont, J. E. Lack of oxygen in articular cartilage: consequences for chondrocyte biology. *Int. J. Exp. Pathol.* **91**, 99–106 (2010).

101. Swanson, W. B. *et al.* Macropore design of tissue engineering scaffolds regulates mesenchymal stem cell differentiation fate. *Biomaterials* **272**, 120769 (2021).

102. O'Brien, F. J. *et al.* The effect of pore size on permeability and cell attachment in collagen scaffolds for tissue engineering. *Technol. Heal. Care* **15**, 3–17 (2007).

103. Huri, P. Y., Arda Ozilgen, B., Hutton, D. L. & Grayson, W. L. Scaffold pore size modulates in vitro osteogenesis of human adipose-derived stem/stromal cells. *Biomed. Mater.* **9**, 045003 (2014).

104. O'Brien, F. J., Harley, B. A., Yannas, I. V. & Gibson, L. J. The effect of pore size on cell adhesion in collagen-GAG scaffolds. *Biomaterials* **26**, 433–441 (2005).

105. Torres-Sanchez, C. *et al.* The effect of pore size and porosity on mechanical properties and biological response of porous titanium scaffolds. *Mater. Sci. Eng. C* **77**, 219–228 (2017).

106. Wang, C. *et al.* Effect of Pore Size on the Physicochemical Properties and Osteogenesis of Ti6Al4V Porous Scaffolds with Bionic Structure. *ACS Omega* **5**, 28684–28692 (2020).

107. Loh, Q. L. & Choong, C. Three-Dimensional Scaffolds for Tissue Engineering Applications: Role of Porosity and Pore Size. *Tissue Eng. Part B Rev.* **19**, 485–502 (2013).

108. Nazarov, R., Jin, H.-J. & Kaplan, D. L. Porous 3-D Scaffolds from Regenerated Silk Fibroin. *Biomacromolecules* **5**, 718–726 (2004).

109. Jun, I., Han, H.-S., Edwards, J. & Jeon, H. Electrospun Fibrous Scaffolds for Tissue Engineering: Viewpoints on Architecture and Fabrication. *Int. J. Mol. Sci.* **19**, 745 (2018).

110. Mouw, J. K., Ou, G. & Weaver, V. M. Extracellular matrix assembly: a multiscale deconstruction. *Nat. Rev. Mol. Cell Biol.* **15**, 771–785 (2014).

111. Nair, A. K., Gautieri, A., Chang, S.-W. & Buehler, M. J. Molecular mechanics of mineralized collagen fibrils in bone. *Nat. Commun.* **4**, 1724 (2013).

112. Turnbull, G. *et al.* 3D bioactive composite scaffolds for bone tissue engineering. *Bioact. Mater.* **3**, 278–314 (2018).

113. Mikos, A. G. *et al.* Preparation and characterization of poly(l-lactic acid) foams. *Polymer (Guildf).* **35**, 1068–1077 (1994).

114. Zeinali, R., del Valle, L. J., Torras, J. & Puiggalí, J. Recent Progress on Biodegradable Tissue Engineering Scaffolds Prepared by Thermally-Induced Phase Separation (TIPS). *Int. J. Mol. Sci.* **22**, 3504 (2021).

115. Dehghani, F. & Annabi, N. Engineering porous scaffolds using gas-based techniques. *Curr. Opin. Biotechnol.* **22**, 661–666 (2011).

116. Bose, S., Vahabzadeh, S. & Bandyopadhyay, A. Bone tissue engineering using 3D printing. *Mater. Today* **16**, 496–504 (2013).

117. Liu, F. & Wang, X. Synthetic Polymers for Organ 3D Printing. *Polymers (Basel).* **12**, 1765 (2020).

118. Avrunin, A. S. & Tses, E. A. The birth of a new scientific field — biomechanics of the skeleton. Julius Wolff and his work 'Das Gesetz der Transformation der Knochen'. *Hist. Med.* **3**, (2016).

119. Giannoudis, P. V., Einhorn, T. A. & Marsh, D. Fracture healing: The diamond concept. *Injury* **38**, S3–S6 (2007).

120. Kohrt, W. M., Bloomfield, S. A., Little, K. D., Nelson, M. E. & Yingling, V. R. Physical Activity and Bone Health. *Med. Sci. Sport. Exerc.* **36**, 1985–1996 (2004).

121. Daly, R. M. & Bass, S. L. Lifetime sport and leisure activity participation is associated with greater bone size, quality and strength in older men. *Osteoporos. Int.* **17**, 1258–1267 (2006).

122. Wittkowske, C., Reilly, G. C., Lacroix, D. & Perrault, C. M. In Vitro Bone Cell Models: Impact of Fluid Shear Stress on Bone Formation. *Front. Bioeng. Biotechnol.* **4**, 719–728 (2016).

123. Wang, L., You, X., Zhang, L., Zhang, C. & Zou, W. Mechanical regulation of bone remodeling. *Bone Res.* **10**, 16 (2022).

124. Cowin, S. C. & Cardoso, L. Blood and interstitial flow in the hierarchical pore space architecture of bone tissue. *J. Biomech.* **48**, 842–854 (2015).

125. Robling, A. G., Castillo, A. B. & Turner, C. H. Biomechanical and molecular regulation of bone remodeling. *Annu. Rev. Biomed. Eng.* **8**, 455–498 (2006).

126. Jacobs, C. R., Temiyasathit, S. & Castillo, A. B. Osteocyte Mechanobiology and Pericellular Mechanics. *Annu. Rev. Biomed. Eng.* **12**, 369–400 (2010).

127. Bonewald, L. F. The amazing osteocyte. *J. Bone Miner. Res.* **26**, 229–238 (2011).

128. Ozcivici, E. *et al.* Mechanical signals as anabolic agents in bone. *Nat. Rev. Rheumatol.* **6**, 50–59 (2010).

129. Yang, P. F., Brüggemann, G.-P. & Rittweger, J. What do we currently know from in vivo bone strain measurements in humans? *J. Musculoskelet. Neuronal Interact.* **11**, 8–20 (2011).

130. Milgrom, C. *et al.* The Effect of Shoe Gear on Human Tibial Strains Recorded During Dynamic Loading: A Pilot Study. *Foot Ankle Int.* **17**, 667–671 (1996).

131. Burr, D. B. *et al.* In vivo measurement of human tibial strains during vigorous activity. *Bone* **18**, 405–410 (1996).

132. Frost, H. M. Bone ?mass? and the ?mechanostat?: A proposal. *Anat. Rec.* **219**, 1–9 (1987).

133. Frost, H. M. Bone's mechanostat: A 2003 update. *Anat. Rec.* **275A**, 1081–1101 (2003).

134. Khonsary, S. Guyton and Hall: Textbook of Medical Physiology. *Surg. Neurol. Int.* **8**, 275 (2017).

135. Knothe Tate, M. L., Steck, R., Forwood, M. R. & Niederer, P. In vivo demonstration of load-induced fluid flow in the rat tibia and its potential implications for processes associated with functional adaptation. *J. Exp. Biol.* **203**, 2737–2745 (2000).

136. Weinbaum, S., Cowin, S. C. & Zeng, Y. A model for the excitation of osteocytes by mechanical loading-induced bone fluid shear stresses. *J. Biomech.* **27**, 339–360 (1994).

137. Qin, L., Liu, W., Cao, H. & Xiao, G. Molecular mechanosensors in osteocytes. *Bone Res.* **8**, 23 (2020).

138. Duncan, R. L. & Turner, C. H. Mechanotransduction and the functional response of bone to mechanical strain. *Calcif. Tissue Int.* **57**, 344–358 (1995).

139. Gurkan, U. A. & Akkus, O. The Mechanical Environment of Bone Marrow: A Review. *Ann. Biomed. Eng.* **36**, 1978–1991 (2008).

140. Coughlin, T. R. & Niebur, G. L. Fluid shear stress in trabecular bone marrow due to low-magnitude high-frequency vibration. *J. Biomech.* **45**, 2222–9 (2012).

141. Dickerson, D. A., Sander, E. A. & Nauman, E. A. Modeling the mechanical consequences of vibratory loading in the vertebral body: microscale effects. *Biomech. Model. Mechanobiol.* **7**, 191–202 (2008).

142. Metzger, T. A., Schwaner, S. A., LaNeve, A. J., Kreipke, T. C. & Niebur, G. L. Pressure and shear stress in trabecular bone marrow during whole bone loading. *J. Biomech.* **48**, 3035–43 (2015).

143. Cowin, S. C. Mechanosensation and fluid transport in living bone. *J. Musculoskelet. Neuronal Interact.* **2**, 256–60 (2002).

144. Donahue, H. . Gap junctions and biophysical regulation of bone cell differentiation. *Bone* **26**, 417–422 (2000).

145. Manolagas, S. C. Birth and Death of Bone Cells: Basic Regulatory Mechanisms and Implications for the Pathogenesis and Treatment of Osteoporosis. *Endocr. Rev.* **21**, 115–137 (2000).

146. Klein-Nulend, J., Bakker, A. D., Bacabac, R. G., Vatsa, A. & Weinbaum, S. Mechanosensation and transduction in osteocytes. *Bone* **54**, 182–190 (2013).

147. Bakker, A. D., Soejima, K., Klein-Nulend, J. & Burger, E. H. The production of nitric oxide and prostaglandin E2 by primary bone cells is shear stress dependent. *J. Biomech.* **34**, 671–677 (2001).

148. Robling, A. G. *et al.* Mechanical Stimulation of Bone in Vivo Reduces Osteocyte Expression of Sost/Sclerostin. *J. Biol. Chem.* **283**, 5866–5875 (2008).

149. Tatsumi, S. *et al.* Targeted Ablation of Osteocytes Induces Osteoporosis with Defective Mechanotransduction. *Cell Metab.* **5**, 464–475 (2007).

150. Grimston, S. K., Brodt, M. D., Silva, M. J. & Civitelli, R. Attenuated Response to In Vivo Mechanical Loading in Mice With Conditional Osteoblast Ablation of the Connexin43 Gene (Gja1). *J. Bone Miner. Res.* **23**, 879–886 (2008).

151. Cowin, S. C., Moss-Salentijn, L. & Moss, M. L. Candidates for the Mechanosensory System in Bone. *J. Biomech. Eng.* **113**, 191–197 (1991).

152. Hoey, D. A., Chen, J. C. & Jacobs, C. R. The primary cilium as a novel extracellular sensor in bone. *Front. Endocrinol. (Lausanne).* **3**, 75 (2012).

153. Marie, P. J. & Marie, P. J. Osteoblast Biology and Mechanosensing. in *Mechanosensing Biology* 105–126 (Springer Japan, 2011). doi:10.1007/978-4-431-89757-6_8

154. Bonewald, L. F. & Johnson, M. L. Osteocytes, mechanosensing and Wnt signaling. *Bone* **42**, 606–615 (2008).

155. Klein-Nulend, J. *et al.* Sensitivity of osteocytes to biomechanical stress in vitro. *FASEB J.* **9**, 441–445 (1995).

156. Mullender, M. G. & Huiskes, R. Osteocytes and bone lining cells: Which are the best candidates for mechano-sensors in cancellous bone? *Bone* **20**, 527–532 (1997).

157. Hassan, M. N. F. Bin *et al.* Large-Scale Expansion of Human Mesenchymal Stem Cells. *Stem Cells Int.* **2020**, 1–17 (2020).

158. Méndez-Ferrer, S. *et al.* Mesenchymal and haematopoietic stem cells form a unique bone marrow niche. *Nature* **466**, (2010).

159. Marędziak, M., Śmieszek, A., Chrząstek, K., Basinska, K. & Marycz, K. Physical Activity Increases the Total Number of Bone-Marrow-Derived Mesenchymal Stem Cells, Enhances Their Osteogenic Potential, and Inhibits Their Adipogenic Properties. *Stem Cells Int.* **2015**, 1–11 (2015).

160. Baker, J. M., De Lisio, M. & Parise, G. Endurance exercise training promotes medullary hematopoiesis. *FASEB J.* **25**, 4348–4357 (2011).

161. Menuki, K. *et al.* Climbing exercise enhances osteoblast differentiation and inhibits adipogenic differentiation with high expression of PTH/PTHrP receptor in bone marrow cells. *Bone* **43**, 613–620 (2008).

162. Zhang, Y.-X. *et al.* Treadmill exercise enhances therapeutic potency of transplanted bone mesenchymal stem cells in cerebral ischemic rats via anti-apoptotic effects. *BMC Neurosci.* **16**, 56 (2015).

163. Liu, S. *et al.* Intensity-dependent effect of treadmill running on differentiation of rat bone marrow stromal cells. *Mol. Med. Rep.* **17**, 7746–7756 (2018).

164. Zhang, L. *et al.* Medium-Intensity Treadmill Exercise Exerts Beneficial Effects on Bone Modeling Through Bone Marrow Mesenchymal Stromal Cells. *Front. cell Dev. Biol.* **8**, 600639 (2020).

165. Luu, Y. K. *et al.* Mechanical Stimulation of Mesenchymal Stem Cell Proliferation and Differentiation Promotes Osteogenesis While Preventing Dietary-Induced Obesity. *J. Bone Miner. Res.* **24**, 50–61 (2009).

166. Steward, A. J. & Kelly, D. J. Mechanical regulation of mesenchymal stem cell differentiation. *J. Anat.* **227**, 717–731 (2015).

167. Meng, R. *et al.* Human mesenchymal stem cells are sensitive to abnormal gravity and exhibit classic apoptotic features. *Acta Biochim. Biophys. Sin. (Shanghai).* **43**, 133–142 (2011).

168. Marycz, K., Kornicka, K. & Röcken, M. Static Magnetic Field (SMF) as a Regulator of Stem Cell Fate – New Perspectives in Regenerative Medicine Arising from an Underestimated Tool. *Stem Cell Rev. Reports* **14**, 785–792 (2018).

169. Delaine-Smith, R. M. & Reilly, G. C. Mesenchymal stem cell responses to mechanical stimuli. *Muscles. Ligaments Tendons J.* **2**, 169–80 (2012).

170. Jansen, K. A. *et al.* A guide to mechanobiology: Where biology and physics meet. *Biochim. Biophys. Acta - Mol. Cell Res.* **1853**, 3043–3052 (2015).

171. Curtis, K. J., Coughlin, T. R., Varsanik, M. A. & Niebur, G. L. Shear Stress in Bone Marrow has a Dose Dependent Effect on cFos Gene Expression in In Situ Culture. *Cell. Mol. Bioeng.* **12**, 559–568 (2019).

172. Mullender, M. *et al.* Mechanotransduction of bone cellsin vitro: Mechanobiology of bone tissue. *Med. Biol. Eng. Comput.* **42**, 14–21 (2004).

173. Mcgarry, J. G., Klein-Nulend, J., Mullender, M. G. & Prendergast, P. J. A comparison of strain and fluid shear stress in stimulating bone cell responses—a computational and experimental study. *FASEB J.* **19**, 1–22 (2005).

174. Smalt, R., Mitchell, F. T., Howard, R. L. & Chambers, T. J. Induction of NO and prostaglandin E2 in osteoblasts by wall-shear stress but not mechanical strain. *Am. J. Physiol. - Endocrinol. Metab.* **273**, (1997).

175. Fermor, B. *et al.* Primary Human Osteoblast Proliferation and Prostaglandin E2 Release in Response to Mechanical Strain In Vitro. *Bone* **22**, 637–643 (1998).

176. Zaman, G. *et al.* Mechanical Strain Stimulates Nitric Oxide Production by Rapid Activation of Endothelial Nitric Oxide Synthase in Osteocytes. *J. Bone Miner. Res.* **14**, 1123–1131 (1999).

177. Owan, I. *et al.* Mechanotransduction in bone: osteoblasts are more responsive to fluid forces than mechanical strain. *Am. J. Physiol. Physiol.* **273**, C810–C815 (1997).

178. You, J. *et al.* Substrate Deformation Levels Associated With Routine Physical Activity Are Less Stimulatory to Bone Cells Relative to Loading-Induced Oscillatory Fluid Flow. *J. Biomech. Eng.* **122**, 387–393 (2000).

179. Charoenpanich, A. *et al.* Cyclic Tensile Strain Enhances Osteogenesis and Angiogenesis in Mesenchymal Stem Cells from Osteoporotic Donors. *Tissue Eng. Part A* **20**, 67–78 (2014).

180. Rath, B., Nam, J., Knobloch, T. J., Lannutti, J. J. & Agarwal, S. Compressive forces induce osteogenic gene expression in calvarial osteoblasts. *J. Biomech.* **41**, 1095–1103 (2008).

181. Koike, M., Shimokawa, H., Kanno, Z., Ohya, K. & Soma, K. Effects of mechanical strain on proliferation and differentiation of bone marrow stromal cell line ST2. *J. Bone Miner. Metab.* **23**, 219–225 (2005).

182. Kanno, T. *et al.* Tensile mechanical strain up-regulates Runx2 and osteogenic factor expression in human periosteal cells: Implications for distraction osteogenesis. *J. Oral Maxillofac. Surg.* **63**, 499–504 (2005).

183. Turunen, M. J. *et al.* Sub-trabecular strain evolution in human trabecular bone. *Sci. Rep.* **10**, 13788 (2020).

184. Becquart, P. *et al.* Human mesenchymal stem cell responses to hydrostatic pressure and shear stress. *Eur. Cell. Mater.* **31**, 160–73 (2016).

185. Kraft, D. C. E. *et al.* Mechanosensitivity of dental pulp stem cells is related to their osteogenic maturity. *Eur. J. Oral Sci.* **118**, 29–38 (2010).

186. Kuo, Y.-C. *et al.* Oscillatory Shear Stress Mediates Directional Reorganization of Actin Cytoskeleton and Alters Differentiation Propensity of Mesenchymal Stem Cells. *Stem Cells* **33**, 429–442 (2015).

187. Dash, S. K., Sharma, V., Verma, R. S. & Das, S. K. Low intermittent flow promotes rat mesenchymal stem cell differentiation in logarithmic fluid shear device. *Biomicrofluidics* **14**, 054107 (2020).

188. Reiprich, S., Akova, E., Aszódi, A. & Schönitzer, V. Hyaluronan Synthases' Expression and Activity Are Induced by Fluid Shear Stress in Bone Marrow-Derived Mesenchymal Stem Cells. *Int. J. Mol. Sci.* **22**, 3123 (2021).

189. Sonam, S., Sathe, S. R., Yim, E. K. F., Sheetz, M. P. & Lim, C. T. Cell contractility arising from topography and shear flow determines human mesenchymal stem cell fate. *Sci. Rep.* **6**, 20415 (2016).

190. Lu, J. *et al.* The Lineage Specification of Mesenchymal Stem Cells Is Directed by the Rate of Fluid Shear Stress. *J. Cell. Physiol.* **231**, 1752–1760 (2016).

191. Yourek, G., McCormick, S. M., Mao, J. J. & Reilly, G. C. Shear stress induces osteogenic differentiation of human mesenchymal stem cells. *Regen. Med.* **5**, 713–24 (2010).

192. Luo, W. *et al.* Laminar shear stress delivers cell cycle arrest and anti-apoptosis to mesenchymal stem cells. *Acta Biochim. Biophys. Sin. (Shanghai).* **43**, 210–6 (2011).

193. Kreke, M. R., Sharp, L. A., Woo Lee, Y. & Goldstein, A. S. Effect of Intermittent Shear Stress on Mechanotransductive Signaling and Osteoblastic Differentiation of Bone Marrow Stromal Cells. *Tissue Eng. Part A* **14**, 529–537 (2008).

194. Kreke, M. R. & Goldstein, A. S. Hydrodynamic Shear Stimulates Osteocalcin Expression But Not Proliferation of Bone Marrow Stromal Cells. *Tissue Eng.* **10**, 780–788 (2004).

195. Kreke, M., Huckle, W. & Goldstein, A. Fluid flow stimulates expression of osteopontin and bone sialoprotein by bone marrow stromal cells in a temporally dependent manner. *Bone* **36**, 1047–1055 (2005).

196. Lim, K.-T. *et al.* Enhanced Osteogenesis of Human Alveolar Bone-Derived Mesenchymal Stem Cells for Tooth Tissue Engineering Using Fluid Shear Stress in a Rocking Culture Method. *Tissue Eng. Part C Methods* **19**, 128–145 (2013).

197. Titushkin, I. & Cho, M. Modulation of Cellular Mechanics during Osteogenic Differentiation of Human Mesenchymal Stem Cells. *Biophys. J.* **93**, 3693–3702 (2007).

198. Amano, M., Nakayama, M. & Kaibuchi, K. Rho-kinase/ROCK: A key regulator of the cytoskeleton and cell polarity. *Cytoskeleton* **67**, 545–554 (2010).

199. Totsukawa, G. *et al.* Distinct Roles of Rock (Rho-Kinase) and Mlck in Spatial Regulation of Mlc Phosphorylation for Assembly of Stress Fibers and Focal Adhesions in 3t3 Fibroblasts. *J. Cell Biol.* **150**, 797–806 (2000).

200. Goetsch, K. P., Snyman, C., Myburgh, K. H. & Niesler, C. U. ROCK-2 Is Associated With Focal Adhesion Maturation During Myoblast Migration. *J. Cell. Biochem.* **115**, 1299–1307 (2014).

201. Hyväri, L. *et al.* Focal Adhesion Kinase and ROCK Signaling Are Switch-Like Regulators of Human Adipose Stem Cell Differentiation towards Osteogenic and Adipogenic Lineages. *Stem Cells Int.* **2018**, 1–13 (2018).

202. Chen, W.-T. *et al.* Alteration of mesenchymal stem cells polarity by laminar shear stimulation promoting β-catenin nuclear localization. *Biomaterials* **190–191**, 1–10 (2019).

203. Arnsdorf, E. J., Tummala, P., Kwon, R. Y. & Jacobs, C. R. Mechanically induced osteogenic differentiation – the role of RhoA, ROCKII and cytoskeletal dynamics. *J. Cell Sci.* **122**, 546–553 (2009).

204. Zheng, W. *et al.* Fluid flow stress induced contraction and re-spread of mesenchymal stem cells: a microfluidic study. *Integr. Biol.* **4**, 1102 (2012).

205. Riehl, B. D., Lee, J. S. oo., Ha, L. & Lim, J. Y. u. Fluid-flow-induced mesenchymal stem cell migration: role of focal adhesion kinase and RhoA kinase sensors. *J. R. Soc. Interface* **12**, 20141351 (2015).

206. Yang, C., Tibbitt, M. W., Basta, L. & Anseth, K. S. Mechanical memory and dosing influence stem cell fate. *Nat. Mater.* **13**, 645–652 (2014).

207. Park, H. W. *et al.* Alternative Wnt Signaling Activates YAP/TAZ. *Cell* **162**, 780–794 (2015).

208. Hong, J.-H. *et al.* TAZ, a Transcriptional Modulator of Mesenchymal Stem Cell Differentiation. *Science (80-.).* **309**, 1074–1078 (2005).

209. Coughlin, T. R. *et al.* The Effect of Fluid Flow Shear Stress and Substrate Stiffness on Yes-Associated Protein (YAP) Activity and Osteogenesis in Murine Osteosarcoma Cells. *Cancers (Basel).* **13**, 3128 (2021).

210. Kim, K. M. *et al.* Shear stress induced by an interstitial level of slow flow increases the osteogenic differentiation of mesenchymal stem cells through TAZ activation. *PLoS One* **9**, e92427 (2014).

211. Zhong, W. *et al.* Mesenchymal Stem Cell and Chondrocyte Fates in a Multishear Microdevice Are Regulated by Yes-Associated Protein. *Stem Cells Dev.* **22**, 2083–2093 (2013).

212. Li, W. *et al.* ROCK-TAZ signaling axis regulates mechanical tension-induced osteogenic differentiation of rat cranial sagittal suture mesenchymal stem cells. *J. Cell. Physiol.* **235**, 5972–5984 (2020).

213. Strzelecka-Kiliszek, A. *et al.* Functions of Rho family of small GTPases and Rho-associated coiled-coil kinases in bone cells during differentiation and mineralization. *Biochim. Biophys. Acta - Gen. Subj.* **1861**, 1009–1023 (2017).

214. Danti, S. *et al.* Growing Bone Tissue-Engineered Niches with Graded Osteogenicity: An In Vitro Method for Biomimetic Construct Assembly. *Tissue Eng. Part C Methods* **19**, 911–924 (2013).

215. Botchwey, E. A., Dupree, M. A., Pollack, S. R., Levine, E. M. & Laurencin, C. T. Tissue engineered bone: Measurement of nutrient transport in three-dimensional matrices. *J. Biomed. Mater. Res.* **67A**, 357–367 (2003).

216. Rouwkema, J., Koopman, B. F. J. M., Blitterswijk, C. A. Van, Dhert, W. J. A. & Malda, J. Supply of Nutrients to Cells in Engineered Tissues. *Biotechnol. Genet. Eng. Rev.* **26**, 163–178 (2009).

217. Hansmann, J., Groeber, F., Kahlig, A., Kleinhans, C. & Walles, H. Bioreactors in tissue engineering-principles, applications and commercial constraints. *Biotechnol. J.* **8**, 298–307 (2013).

218. Singh, H. & Hutmacher, D. W. Bioreactor Studies and Computational Fluid Dynamics. in *Advances in Biochemical Engineering/Biotechnology* **112**, 231–249 (2009).

219. Rauh, J., Milan, F., Günther, K.-P. & Stiehler, M. Bioreactor systems for bone tissue engineering. *Tissue Eng. Part B. Rev.* **17**, 263–80 (2011).

220. Schuerlein, S. *et al.* A versatile modular bioreactor platform for Tissue Engineering. *Biotechnol. J.* **12**, 1600326 (2017).

221. Gaspar, D. A., Gomide, V. & Monteiro, F. J. The role of perfusion bioreactors in bone tissue engineering. *Biomatter* **2**, 167–75 (2012).

222. Novosel, E. C., Kleinhans, C. & Kluger, P. J. Vascularization is the key challenge in tissue engineering. *Advanced Drug Delivery Reviews* **63**, (2011).

223. Mygind, T. *et al.* Mesenchymal stem cell ingrowth and differentiation on coralline hydroxyapatite scaffolds. *Biomaterials* **28**, 1036–1047 (2007).

224. Berry, J. D. *et al.* Characterisation of stresses on microcarriers in a stirred bioreactor. *Appl. Math. Model.* **40**, 6787–6804 (2016).

225. Ghasemian, M. *et al.* Hydrodynamic characterization within a spinner flask and a rotary wall vessel for stem cell culture. *Biochem. Eng. J.* **157**, 107533 (2020).

226. Schwarz, R. P., Goodwin, T. J. & Wolf, D. A. Cell culture for three-dimensional modeling in rotating-wall vessels: An application of simulated microgravity. *J. Tissue Cult. Methods* **14**, 51–57 (1992).

227. Qiu, Q.-Q., Ducheyne, P. & Ayyaswamy, P. S. Fabrication, characterization and evaluation of bioceramic hollow microspheres used as microcarriers for 3-D bone tissue formation in rotating bioreactors. *Biomaterials* **20**, 989–1001 (1999).

228. Yu, X., Botchwey, E. A., Levine, E. M., Pollack, S. R. & Laurencin, C. T. Bioreactor-based bone tissue engineering: The influence of dynamic flow on osteoblast phenotypic expression and matrix mineralization. *Proc. Natl. Acad. Sci.* **101**, 11203–11208 (2004).

229. Sikavitsas, V. I., Bancroft, G. N. & Mikos, A. G. Formation of three-dimensional cell/polymer constructs for bone tissue engineering in a spinner flask and a rotating wall vessel bioreactor. *J. Biomed. Mater. Res.* **62**, 136–148 (2002).

230. Ramírez-Rodríguez, G. B. *et al.* Biomimetic Mineralization Promotes Viability and Differentiation of Human Mesenchymal Stem Cells in a Perfusion Bioreactor. *Int. J. Mol. Sci.* **22**, 1447 (2021).

231. Yamada, S., Yassin, M. A., Schwarz, T., Hansmann, J. & Mustafa, K. Induction of osteogenic differentiation of bone marrow stromal cells on 3D polyester-based scaffolds solely by subphysiological fluidic stimulation in a laminar flow bioreactor. *J. Tissue Eng.* **12**, 20417314211019376 (2021).

232. Pigeot, S. *et al.* Orthotopic Bone Formation by Streamlined Engineering and Devitalization of Human Hypertrophic Cartilage. *Int. J. Mol. Sci.* **21**, 7233 (2020).

233. Liebsch, M. *et al.* Alternatives to animal testing: current status and future perspectives. *Arch. Toxicol.* **85**, 841–858 (2011).

234. Koo, Y. *et al.* The Effects of Static and Dynamic Loading on Biodegradable Magnesium Pins In Vitro and In Vivo. *Sci. Rep.* **7**, 14710 (2017).

235. Ali, D., Ozalp, M., Blanquer, S. B. G. & Onel, S. Permeability and fluid flow-induced wall shear stress in bone scaffolds with TPMS and lattice architectures: A CFD analysis. *Eur. J. Mech. - B/Fluids* **79**, 376–385 (2020).

236. Liu, L. *et al.* Architectural design of Ti6Al4V scaffold controls the osteogenic volume and application area of the scaffold. *J. Mater. Res. Technol.* **9**, 15849–15861 (2020).

237. Malvè, M., Bergstrom, D. J. & Chen, X. B. Modeling the flow and mass transport in a mechanically stimulated parametric porous scaffold under fluid-structure interaction approach. *Int. Commun. Heat Mass Transf.* **96**, 53–60 (2018).

238. Maes, F., Van Ransbeeck, P., Van Oosterwyck, H. & Verdonck, P. Modeling fluid flow through irregular scaffolds for perfusion bioreactors. *Biotechnol. Bioeng.* **103**, 621–630 (2009).

239. Mehrian, M., Lambrechts, T., Papantoniou, I. & Geris, L. Computational Modeling of Human Mesenchymal Stromal Cell Proliferation and Extra-Cellular Matrix Production in 3D Porous Scaffolds in a Perfusion Bioreactor: The Effect of Growth Factors. *Front. Bioeng. Biotechnol.* **8**, 376 (2020).

240. Rolfe, P. Sensing in tissue bioreactors. *Meas. Sci. Technol.* **17**, 578–583 (2006).

241. Zermatten, E. *et al.* Micro-Computed Tomography Based Computational Fluid Dynamics for the Determination of Shear Stresses in Scaffolds Within a Perfusion Bioreactor. *Ann. Biomed. Eng.* **42**, 1085–1094 (2014).

242. Boschetti, F., Raimondi, M. T., Migliavacca, F. & Dubini, G. Prediction of the micro-fluid dynamic environment imposed to three-dimensional engineered cell systems in bioreactors. *J. Biomech.* **39**, 418–425 (2006).

243. Cioffi, M., Boschetti, F., Raimondi, M. T. & Dubini, G. Modeling evaluation of the fluid-dynamic microenvironment in tissue-engineered constructs: A micro-CT based model. *Biotechnol. Bioeng.* **93**, 500–510 (2006).

244. Ramani-Mohan, R. K. *et al.* Deformation strain is the main physical driver for skeletal precursors to undergo osteogenesis in earlier stages of osteogenic cell maturation. *J. Tissue Eng. Regen. Med.* **12**, e1474–e1479 (2018).

245. Egger, D. *et al.* Development and characterization of a parallelizable perfusion bioreactor for 3D cell culture. *Bioengineering* **4**, (2017).

246. Yamada, S., Yassin, M. A., Schwarz, T., Mustafa, K. & Hansmann, J. Optimization and Validation of a Custom-Designed Perfusion Bioreactor for Bone Tissue Engineering: Flow Assessment and Optimal Culture Environmental Conditions. *Front. Bioeng. Biotechnol.* **10**, 811942 (2022).

247. Wendt, D., Riboldi, S. A., Cioffi, M. & Martin, I. Bioreactors in Tissue Engineering: Scientific Challenges and Clinical Perspectives. in *Advances in Biochemical Engineering/Biotechnology* **112**, 1–27 (2009).

248. Fukushima, K. Poly(trimethylene carbonate)-based polymers engineered for biodegradable functional biomaterials. *Biomaterials Science* (2016). doi:10.1039/c5bm00123d

249. Sartoneva, R. *et al.* Comparison of Poly(l-lactide-co-ε-caprolactone) and Poly(trimethylene carbonate) Membranes for Urethral Regeneration: An In Vitro and In Vivo Study. *Tissue Eng. Part A* **24**, 117–127 (2018).

250. Zhao, F., Melke, J., Ito, K., van Rietbergen, B. & Hofmann, S. A multiscale computational fluid dynamics approach to simulate the micro-fluidic environment within a tissue engineering scaffold with highly irregular pore geometry. *Biomech. Model. Mechanobiol.* **18**, 1965–1977 (2019).

251. Cignoni, P. *et al.* MeshLab: An open-source mesh processing tool. in *6th Eurographics Italian Chapter Conference 2008 - Proceedings* (2008).

252. Livak, K. J. & Schmittgen, T. D. Analysis of relative gene expression data using real-time quantitative PCR and the 2(-Delta Delta C(T)) Method. *Methods* **25**, 402–8 (2001).

253. Schindelin, J. *et al.* Fiji: An open source platform for biological image analysis. *Nat. Methods* **9**, 676–682 (2012).

254. Schmidt, U., Weigert, M., Broaddus, C. & Myers, G. Cell Detection with Star-Convex Polygons. in *Lecture Notes in Computer Science (including subseries Lecture Notes in Artificial Intelligence and Lecture Notes in Bioinformatics)* **11071 LNCS**, 265–273 (2018).

255. Stacklies, W., Redestig, H., Scholz, M., Walther, D. & Selbig, J. pcaMethods a bioconductor package providing PCA methods for incomplete data. *Bioinformatics* **23**, 1164–1167 (2007).

256. Ridzuan, N., Al Abbar, A., Yip, W. K., Maqbool, M. & Ramasamy, R. Characterization and Expression of Senescence Marker in Prolonged Passages of Rat Bone Marrow-Derived Mesenchymal Stem Cells. *Stem Cells Int.* **2016**, 1–14 (2016).

257. Woodbury, D., Schwarz, E. J., Prockop, D. J. & Black, I. B. Adult rat and human bone marrow stromal cells differentiate into neurons. *J. Neurosci. Res.* **61**, 364–370 (2000).

258. Lin, G. *et al.* Tissue Distribution of Mesenchymal Stem Cell Marker Stro-1. *Stem Cells Dev.* **20**, 1747–1752 (2011).

259. Law, K.-Y. Definitions for Hydrophilicity, Hydrophobicity, and Superhydrophobicity: Getting the Basics Right. *J. Phys. Chem. Lett.* **5**, 686–688 (2014).

260. Zhou, Q. *et al.* Alkali-Mediated Miscibility of Gelatin/Polycaprolactone for Electrospinning Homogeneous Composite Nanofibers for Tissue Scaffolding. *Macromol. Biosci.* **17**, 1700268 (2017).

261. Xu, S. *et al.* Selective laser sintering fabrication of nano-hydroxyapatite/poly-&epsilon;-caprolactone scaffolds for bone tissue engineering applications. *Int. J. Nanomedicine* **8**, 4197 (2013).

262. Narayanan, G., Shen, J., Boy, R., Gupta, B. & Tonelli, A. Aliphatic Polyester Nanofibers Functionalized with Cyclodextrins and Cyclodextrin-Guest Inclusion Complexes. *Polymers (Basel).* **10**, 428 (2018).

263. Tümer, E. H., Erbil, H. Y. & Akdoğan, N. Wetting of Superhydrophobic Polylactic Acid Micropillared Patterns. *Langmuir* **38**, 10052–10064 (2022).

264. Menzies, K. L. & Jones, L. The Impact of Contact Angle on the Biocompatibility of Biomaterials. *Optom. Vis. Sci.* **87**, 387–399 (2010).

265. Schugens, C., Maquet, V., Grandfils, C., Jerome, R. & Teyssie, P. Biodegradable and macroporous polylactide implants for cell transplantation: 1. Preparation of macroporous polylactide supports by solid-liquid phase separation. *Polymer (Guildf).* **37**, 1027–1038 (1996).

266. Yassin, M. A. *et al.* Surfactant tuning of hydrophilicity of porous degradable copolymer scaffolds promotes cellular proliferation and enhances bone formation. *J. Biomed. Mater. Res. Part A* **104**, 2049–2059 (2016).

267. Triaud, F. *et al.* Evaluation of Automated Cell Culture Incubators. *JALA J. Assoc. Lab. Autom.* **8**, 82–86 (2003).

268. Chi, H.-J. *et al.* Effect of evaporation-induced osmotic changes in culture media in a dry-type incubator on clinical outcomes in in vitro fertilization-embryo transfer cycles. *Clin. Exp. Reprod. Med.* **47**, 284–292 (2020).

269. Walls, P. L. L. *et al.* Quantifying the potential for bursting bubbles to damage suspended cells. *Sci. Rep.* **7**, 15102 (2017).

270. Lee, J., Kentish, S. & Ashokkumar, M. Effect of surfactants on the rate of growth of an air bubble by rectified diffusion. *J. Phys. Chem. B* **109**, 14595–8 (2005).

271. Kang, J. H., Kim, Y. C. & Park, J.-K. Analysis of pressure-driven air bubble elimination in a microfluidic device. *Lab Chip* **8**, 176–178 (2008).

272. Zhao, Y. Y.-H. H. *et al.* Hydrostatic pressure promotes the proliferation and osteogenic/chondrogenic differentiation of mesenchymal stem cells: The roles of RhoA and Rac1. *Stem Cell Res.* **14**, 283–96 (2015).

273. Yu, L. *et al.* Fluid shear stress induces osteoblast differentiation and arrests the cell cycle at the G0 phase via the ERK1/2 pathway. *Mol. Med. Rep.* **16**, 8699–8708 (2017).

274. Langenbach, F. & Handschel, J. Effects of dexamethasone, ascorbic acid and β-glycerophosphate on the osteogenic differentiation of stem cells in vitro. *Stem Cell Res. Ther.* **4**, 117 (2013).

275. Chen, B., Co, C. & Ho, C.-C. Cell shape dependent regulation of nuclear morphology. *Biomaterials* **67**, 129–136 (2015).

276. Monteiro, D. A. *et al.* Fluid shear stress generates a unique signaling response by activating multiple TGFβ family type I receptors in osteocytes. *FASEB J.* **35**, e21263 (2021).

277. Zhao, Y. *et al.* Notch signaling and fluid shear stress in regulating osteogenic differentiation. *Front. Bioeng. Biotechnol.* **10**, 1–14 (2022).

278. Lau, K.-H. W., Kapur, S., Kesavan, C. & Baylink, D. J. Up-regulation of the Wnt, Estrogen Receptor, Insulin-like Growth Factor-I, and Bone Morphogenetic Protein Pathways in C57BL/6J Osteoblasts as Opposed to C3H/HeJ Osteoblasts in Part Contributes to the Differential Anabolic Response to Fluid Shear. *J. Biol. Chem.* **281**, 9576–9588 (2006).

279. Johnson, G. P., Fair, S. & Hoey, D. A. Primary cilium-mediated MSC mechanotransduction is dependent on Gpr161 regulation of hedgehog signalling. *Bone* **145**, 115846 (2021).

280. James, A. W. Review of Signaling Pathways Governing MSC Osteogenic and Adipogenic Differentiation. *Scientifica (Cairo).* **2013**, 1–17 (2013).

281. Siegel, G. *et al.* Phenotype, donor age and gender affect function of human bone marrow-derived mesenchymal stromal cells. *BMC Med.* **11**, 146 (2013).

282. Zhang, H., Kay, A., Forsyth, N. R., Liu, K.-K. & El Haj, A. J. Gene expression of single human mesenchymal stem cell in response to fluid shear. *J. Tissue Eng.* **3**, 204173141245198 (2012).

283. Griffith, C. K. *et al.* Diffusion Limits of an in Vitro Thick Prevascularized Tissue. *Tissue Eng.* **11**, 257–266 (2005).

284. Baldwin, J. *et al.* In vitro pre-vascularisation of tissue-engineered constructs A co-culture perspective. *Vasc. Cell* **6**, 13 (2014).

285. Rouwkema, J., Westerweel, P. E., de Boer, J., Verhaar, M. C. & van Blitterswijk, C. A. The Use of Endothelial Progenitor Cells for Prevascularized Bone Tissue Engineering. *Tissue Eng. Part A* **15**, 2015–2027 (2009).

286. Lovett, M., Lee, K., Edwards, A. & Kaplan, D. L. Vascularization strategies for tissue engineering. *Tissue Engineering - Part B: Reviews* **15**, 353–370 (2009).

287. Harvestine, J. N. *et al.* Osteogenic preconditioning in perfusion bioreactors improves vascularization and bone formation by human bone marrow aspirates. *Sci. Adv.* **6**, eaay2387 (2020).

288. Watson, E. & Mikos, A. G. Advances in In Vitro and In Vivo Bioreactor-Based Bone Generation for Craniofacial Tissue Engineering. *BME Front.* **4**, 1–14 (2023).

289. De Witte, T.-M., Fratila-Apachitei, L. E., Zadpoor, A. A. & Peppas, N. A. Bone tissue engineering via growth factor delivery: from scaffolds to complex matrices. *Regen. Biomater.* **5**, 197–211 (2018).

290. Doulgkeroglou, M.-N. *et al.* Automation, Monitoring, and Standardization of Cell Product Manufacturing. *Front. Bioeng. Biotechnol.* **8**, 811 (2020).

291. Rashba, E. & Gamota, D. Anticipatory standards and the commercialization of nanotechnology. *Journal of Nanoparticle Research* **5**, 401–407 (2003).

9. Original Papers

Paper I

Surface Activation with Oxygen Plasma Promotes Osteogenesis with Enhanced Extracellular Matrix Formation in Three-dimensional Microporous Scaffolds

S. Yamada, MA. Yassin, T. Weigel, T. Schmitz, J. Hansmann, K. Mustafa

I

ORIGINAL ARTICLE

Surface activation with oxygen plasma promotes osteogenesis with enhanced extracellular matrix formation in three-dimensional microporous scaffolds

Shuntaro Yamada[1] | Mohammed A. Yassin[1] | Tobias Weigel[2,3] |
Tobias Schmitz[2] | Jan Hansmann[2,3,4] | Kamal Mustafa[1]

[1]Department of Clinical Dentistry, Faculty of Medicine, University of Bergen, Bergen, Norway

[2]Chair of Tissue Engineering and Regenerative Medicine (TERM), University Hospital Würzburg, Würzburg, Germany

[3]Translational Center Regenerative Therapies, Fraunhofer Institute for Silicate Research (ISC), Würzburg, Germany

[4]Department Electrical Engineering, University for Applied Sciences Würzburg/Schweinfurt, Schweinfurt, Germany

Correspondence
Kamal Mustafa, Department of Clinical Dentistry, Faculty of Medicine, University of Bergen, Bergen, Norway.
Email: kamal.mustafa@uib.no

Funding information
Trond Mohn Foundation, Grant/Award Number: BFS2018TMT10

Abstract

Various types of synthetic polyesters have been developed as biomaterials for tissue engineering. These materials commonly possess biodegradability, biocompatibility, and formability, which are preferable properties for bone regeneration. The major challenge of using synthetic polyesters is the result of low cell affinity due to their hydrophobic nature, which hinders efficient cell seeding and active cell dynamics. To improve wettability, plasma treatment is widely used in industry. Here, we performed surface activation with oxygen plasma to hydrophobic copolymers, poly(L-lactide-co-trimethylene carbonate), which were shaped in 2D films and 3D microporous scaffolds, and then we evaluated the resulting surface properties and the cellular responses of rat bone marrow stem cells (rBMSC) to the material. Using scanning electron microscopy and Fourier-transform infrared spectroscopy, we demonstrated that short-term plasma treatment increased nanotopographical surface roughness and wettability with minimal change in surface chemistry. On treated surfaces, initial cell adhesion and elongation were significantly promoted, and seeding efficiency was improved. In an osteoinductive environment, rBMSC on plasma-treated scaffolds exhibited accelerated osteogenic differentiation with osteogenic markers including RUNX2, osterix, bone sialoprotein, and osteocalcin upregulated, and a greater amount of collagen matrix and mineral deposition were found. This study shows the utility of plasma surface activation for polymeric scaffolds in bone tissue engineering.

KEYWORDS
biomaterials, bone tissue engineering, lactide-TMC, mesenchymal stem cells, osteogenic differentiation, plasma activation

1 | INTRODUCTION

Calcified bone is a highly committed tissue where spontaneous healing and regeneration are severely limited after damage. This is a major challenge for modern medicine because complications related to bone are frequent as results of trauma, infection, and carcinoma. Current therapeutic approaches to patients with critical-sized bony defects include autologous, allogeneic and xenogeneic bone transplantation, the implantation of bioinert materials (e.g., titanium implants) and the use of synthetic biomaterial as bone substitutes, but

none of the treatments can achieve complete bone regeneration and functional recovery.[1,2] Meanwhile, a tissue engineering approach has been shown to be an alternative and promising means, which aims to regenerate functional tissues in combination with biomaterials, progenitor cells, and soluble factors.[3] This allows reducing therapeutic invasion to the patients, and it is theoretically applicable to defects in any size and shape. Biodegradable aliphatic polyesters have been developed as scaffolding materials in bone tissue engineering. Poly(ʟ-lactide-co-trimethylene carbonate) (lactide-TMC) has been shown to be biocompatible to a greater or lesser degree depending on composition, allowing cellular events on the surface.[4-7]

For bone regeneration, biomaterials are preferably manufactured three-dimensionally with high porosity and interconnectivity to replicate bony structures in vivo.[8] However, the use of aliphatic polymers as three-dimensional (3D) microporous scaffolds is problematic because of their hydrophobic nature. Lactide-TMC, which is known to be more hydrophilic than first generation polyester biopolymers such as polylactic acid (PLA) and poly(ε-caprolactones) (PCL), is still not the exception.[6,9,10] Starting with cell seeding on the scaffolds, hydrophobicity hampers the infiltration of cell suspension into the micropores, which results in low seeding efficiency and inhomogeneous cell distribution.[11] This also causes the alteration of the "cell niche", leading to changes in paracrine signaling distance, cell-to-cell interaction and competitive nutrient supply.[12-16] Since the initial inhomogeneity persists, it may also mask or exaggerate cellular reactions to the environment. Therefore, various methods have been suggested as a means of surface modification such as chemical coating, alkaline hydrolysis, and plasma activation.[17]

Plasma activation is a surface modification procedure, which is widely used to hydrophilize material surfaces industrially. The effect is known to be attributed to the composition of polar functional groups (i.e., —OH, —COOH, —NH$_2$, —SO$_2$) on the materials and modification of nanotopography by etching and sputtering.[18] In regenerative medicine of bone tissue including orthoperiodic surgery and dentistry, the technique has been applied to promote faster healing and improve osteointegration of implanted devices, that is, titanium implant.[19] Recently, the application field has widened to the field of tissue engineering, and plasma activation of biodegradable aliphatic polyesters in combination with cells has become a focus of research. The effects of plasma activation using several different plasma sources (i.e., oxygen, nitrogen, argon, carbon dioxide, ammonia, and air plasma) has been tested using different cell types including vascular smooth muscle cells, umbilical endothelial cells, mammary epithelial cells, retinal pigment epithelial cells, keratinocytes, chondrocytes, osteoblasts, and fibroblast.[17,18] Based on these findings, it was recognized that appropriate plasma activation of polymeric scaffolds enhanced cellular adhesion by promoting the elongation of cell tentacles and proliferation although cells might behave differently depending on the type of cells and materials.[18,20] Osteoblastic cells, MC3T3-E1, responded to the plasma treated surface by upregulating their mRNA expression of alkaline phosphatase, osterix, runt-related transcription factor 2 (RUNX2), and osteocalcin.[21] This promotion of osteogenic property is suggested as a consequence of increased protein absorption on plasma-treated surfaces.[22] For multipotent cells, however, the effects of surface modification should not be restricted to proliferation and adhesion because physical surface properties are the key determinants of cell fate.[15,23] Indeed, several studies have suggested the change in nanotopography/hydrophilicity of the surfaces is responded by the alternation of multiple signaling pathways which are known to regulate cell fate. This includes αvβ1 integrin signaling pathway,[24,25] Rho/Rock signaling pathway,[26] AP-1 signaling pathway[23] and canonical and non-canonical Wnt signaling pathways.[27,28] To date, comprehensive responses of multipotent cells on plasma-activated aliphatic polymers have not been well elucidated.

Thus, our aim was first to improve seeding efficiency by modifying the surface properties of 3D lactide-TMC scaffolds with oxygen plasma, and then, to explore the behaviors of rat bone marrow-derived stem cells (rBMSC) towards osteogenic differentiation. Here, we demonstrate that surface activation with oxygen plasma of two-dimensional (2D) films and 3D microporous scaffolds increased wettability mainly by roughening the surfaces nanoscopically. This consequently led to a notable improvement of seeding efficiency and allowed rBMSC to attach, elongate, and establish cell-to-cell interaction from an early phase of their growth. We further showed that it accelerated proliferative activity, extracellular matrix formation, and mineralization, with upregulation of lineage-specific markers for osteogenic differentiation. This study comprehensively evaluated adhesion, proliferation, and osteogenic differentiation of rBMSC in 3D microporous scaffolds treated with oxygen plasma for bone tissue engineering.

2 | MATERIALS AND METHODS

2.1 | Materials

The medical grade synthetic biomaterial lactide-TMC was purchased (RESOMER® LT706 S, Evonik) and used as a scaffold material as follows for this study.

2.2 | Methods

2.2.1 | Fabrication of 2D flat films and 3D microporous scaffolds of lactide-TMC

For 2D flat film preparation, lactide-TMC polymer was dissolved in chloroform and poured into glass petri dishes. After chloroform was completely evaporated, 10 mm diameter samples were punched out. For 3D microporous scaffold preparation, samples were prepared by a salt leaching technique.[29] Lactide-TMC polymer was dissolved in chloroform and then mixed with sodium chloride particles with a size range of 90–600 μm. After the complete evaporation of chloroform, scaffolds were prepared with a 10 mm diameter and 1.2 mm thickness. Subsequently, the scaffolds were thoroughly washed with distilled water to remove sodium chloride. Macro- and microstructures of the scaffolds and their topographical properties were evaluated by microCT (μCT) (see Figure A1 and Table 1, respectively).

TABLE 1 The morphological characteristics of 3D microporous scaffolds used in the study

	Average ($n = 5$)	SD
Weight (g)	0.012	0.0016
Thickness (mm)	1.22	0.084
Volume (mm^3)	95.82	6.57
Density (kg/m^3)	129.60	9.81
Porosity (%)	91.71	3.44
Open pores (%)	91.71	3.44
Close pores (%)	0.00031	0.00048

2.2.2 | Oxygen plasma activation and pre-treatment before cell seeding

The 2D flat films and 3D scaffolds were treated in a plasma chamber (Pico Plasma System, Diener electronics, Ebhausen, Germany) with oxygen plasma for 1, 3, or 5 min respectively, using a 100 kHz generator operated at a plasma process power of 350 W and pure oxygen gas (0.3 mbar, 12 sccm O_2).

For cell culture experiments, the treated-samples were placed in wells of low-adherent 48-well plates (10861–560; VWR International) and washed in 70% ethanol followed by through wash in PBS in sterile environment. The samples were then sterilized by ultraviolet (UV) radiation for 2 hr. The samples were then washed with PBS twice and pre-incubated in minimum of essential medium (αMEM) overnight before seeding.

2.2.3 | Fourier transform infrared spectroscopy (ATR-FTIR)

The ATR-FTIR spectra were recorded using an FT-IR-4100 instrument (Jasco, Gross-Umstadt, Germany). Each sample was measured by 128 scans and a resolution of 0.5 cm^{-1} in the range between 500 and 4000 cm^{-1}.

2.2.4 | Scanning electron microscopy

The samples were analyzed by scanning electron microscopy (SEM) using a high-resolution SEM (Zeiss CB 340, Oberkochen, Germany). Before SEM analysis, the samples were coated with a 2 nm coating of platinum in a sputter coater (EM ACE600, Leica, Vienna, Austria).

2.2.5 | Contact angle measurement and 3D hydrophilic assessment

Surface wettability of the 2D flat films was determined with a contact angle measuring device (OCA 15EC, Dataphysics, Filderstadt,

Germany) using 3 μl of ultrapure water dripped onto the surface. The experiment was performed on three different samples for each condition (0, 1, 3, 5 min of plasma treatment). In order to evaluate the treatment's stability over time, the measurements were repeated on fresh samples 2 weeks after the plasma process.

For wettability evaluation of the 3D microporous scaffolds, the measurement took place 2 weeks after the plasma activation. 50 μl αMEM was dropped on each scaffold. Photographic images were captured after 60 s.

2.2.6 | Cell culture and seeding

The study was approved by the Norwegian Animal Research Authority and performed according to the European Convention for the Protection of Vertebrates used for Scientific Purposes (local approval number 20146866). Bone marrow stem cells were isolated from the femurs of Lewis rats (rBMSC) as previously described[30] and maintained in αMEM supplemented with 10% fetal bovine serum (FBS) and 1% penicillin–streptomycin at 37°C in 5% CO_2 humidified atmosphere. Cells from passage 3–4 were used for the study. When the cells reached approximately 80% confluence, the cells were trypsinized, and 10,000 and 100,000 cells were seeded on the lactide-TMC films and the microporous scaffolds in the 48 well plates, respectively. After seeding, the well plates were stirred at 800 rpm for 30 s to homogenize cell distribution. Flat films were collected 24 hr after seeding. For the evaluation of osteogenesis of rBMSC, the 3D microporous scaffolds that were treated with oxygen plasma for 3 min were transferred into osteoinductive medium, αMEM supplemented with 200 nM dexamethasone, 10 mM glycerophosphate and 0.05 mM ascorbic acid on the following day (day 0) and evaluated on days 1, 3, 7, 14, and 21. The experimental timeline is shown in Figure A2.

2.2.7 | Evaluation of seeding efficiency and viability

3D microporous scaffolds were used for the evaluation of seeding efficiency. Three hours after seeding, non-adherent cells and cells attached on wells, not scaffolds, were collected and stained with 0.4% Trypan blue solution (T10282; Invitrogen). The number of cells and viability was counted using a Countess Automated Cell Counter (A27977; Invitrogen). Seeding efficiency was calculated as follows:

$$\text{Seeding efficiency}\,(\%) = 1 - \frac{\text{Cells left in a well} + \text{Non adherent cells}}{\text{Cells seeded on a scaffold}}$$

2.2.8 | Immunofluorescence and image analyses

2D film samples and 3D microporous scaffolds for immunofluorescence were collected 3, 6, and 24 hr after seeding and day 3, 7, 14, and 21, respectively. Samples for F-actin, RUNX2, and PCNA staining were fixed in 4% paraformaldehyde for 15 min at room

temperature, and samples for Col1 and β-Actin staining were fixed in cold methanol for 10 min. For PCNA staining only, antigen retrieval was performed with 10 mM sodium citrate (pH 6) at 95°C for 20 min. The samples were then permeabilized in 0.1% Triton X-100 in PBS (PBST) for 10 min three times and blocked with 10% goat serum in PBST for 1 hr at room temperature followed by incubation with primary antibodies at 4°C overnight. Primary antibodies used were as follows: anti-collagen I antibody (1:1000, ab90395; Abcam, UK), anti-Runx2 antibody (1:250, ab23981; Abcam, UK), anti-β-Actin antibody (1:100, PA1-183; Thermo Fisher Scientific), anti-PCNA antibody (1:200, sc-56; Santa Cruz). After washes in PBS 6 times (10 min each), the samples were incubated for 1 hr at room temperature with species-specific secondary antibodies conjugated to AlexaFluor 488/568/635 (1:250, A11008/A11011/A31575; Life Technology). Nuclei and F-actin (for RUNX2 staining only) were counterstained with 4′,6-diamidino-2-phenylindole (DAPI; 1:5000, 62,247; Thermo Fisher Scientific) and Alexa Fluor 488 Phalloidin (1:500, A12379; Invitrogen), respectively. Specimens were washed six times (10 min each) with PBST and mounted on confocal dishes in PBS. Stack images with a z-step size of 0.8 μm were acquired by a confocal microscope (TCS SP8; Leica, Germany) with a water immersion 25× objective. Images were obtained by the same acquisition setting, and each channel was separately obtained by a sequential scan function to perform quantitative analyses. Images were processed in Fiji/ImageJ for quantification.[31]

2.2.9 | Double-strand DNA quantification

Samples were collected on days 1, 3, 7, 14, and 21 and immersed in PBST following a wash with PBS. Freezing–thawing cycle at −80°C was repeated twice to collect cytolysate from the samples. Double strand DNA (dsDNA) was quantified by using Quant-iT™ PicoGreen™ dsDNA Assay Kit (P7589; Invitrogen) according to the manufactures

TABLE 2 Primers used for RT-qPCR gene expression analysis

Gene	Symbol	Cat. No.
Glyceraldehyde-3-phosphate dehydrogenase	GAPDH	Rn01749022_g1
Runt-related transcription factor 2	RUNX2	Rn01512298_m1
Collagen, type I, alpha 1	Col1A1	Rn01463848_m1
Alkaline phosphatase	ALP	Rn01516028_m1
Bone sialoprotein	BSP	Rn00561414_m1
Sp7 transcription factor	Sp7 (Osterix)	Rn01761789_m1
Bone gamma-carboxyglutamate protein	Bglap (Osteocalcin: OCN)	Rn00566386_g1
Thy-1	Thy1 (CD90)	Rn00562048_m1
Ecto-5′-nucleotidase	Nt5e (CD73)	Rn00665212_m1
CD44	CD44	Rn00681157_m1

protocol. Fluorescence intensity was measured with an excitation wavelength of 480 nm and emission wavelength of 520 nm using Varioskan™ LUX multimode microplate reader (VLBL00D0; Thermo Fisher Scientific, Finland).

2.2.10 | Total RNA extraction and reverse transcription polymerase chain reaction

Samples for RT-qPCR were collected on days 3, 7, 14, and 21. RNA extraction was performed using a Maxwell® 16 Cell LEV Total RNA Purification Kit (AS1280; Promega) in accordance with protocol provided by the supplier. Reverse transcription was then performed with the High Capacity cDNA Reverse Transcription Kit (4,368,814; Applied Biosystems). RT-qPCR was performed on StepOne™ Real-Time PCR System with T TaqMan™ Gene Expression Assay (4,453,320, Applied Biosystems). Primers used are given in Table 2. The amplification was performed as follow: initial denaturation at 95°C for 20 s, followed by 40 cycles of 95°C for 1 s and 60°C for 20 s. Each sample was assessed in triplicate. Specificity of the reaction was assessed by amplification curve, and the relative expression of the genes was calculated using the $2^{-\Delta\Delta CT}$ method following to normalization to a housekeeping gene GAPDH.[32]

2.2.11 | Alkaline phosphatase activity assay

Samples were collected on days 1, 3, 7, 14, and 21. Cytolysate was collected by freezing–thawing cycle at −80°C, equal volume of P-nitrophenyl phosphate (pNPP, 20–106; Sigma-Aldrich, Germany) was added in each sample. Absorbance was measured at 405 nm using a Varioskan™ LUX multimode microplate reader (VLBL00D0; Thermo Fisher Scientific, Finland).

2.2.12 | Alizarin red S staining and quantification

Samples taken on days 1, 3, 7, 14, and 21 were fixed in 4% PFA for 40 min and washed three times with Milli-Q® water. The samples were then incubated with 0.1% Alizarin Red S for 20 min followed by thorough wash with Milli-Q® water. For quantification, the dye was extracted with 100 mM cetylpyridium chloride overnight. Absorbance of the extract was measured at 540 nm using a Varioskan™ LUX multimode microplate reader (VLBL00D0; Thermo Fisher Scientific, Finland).

2.2.13 | Statistics

All statistical analyses were conducted with SPSS 24.0 (IBM). For the comparison of 1, 3, and 5 min-treated groups to the control, one-way ANOVA followed by Dunnett post hoc test was performed. Pairwise comparison was performed by Student's t test. For RT-qPCR, logarithmic value of $2^{-\Delta\Delta CT}$ was calculated to normalize to the endogenous

FIGURE 1   Surface characterization before and after plasma activation with oxygen of 2D films of lactide-TMC. (a,b) Water contact angle measurement before, immediately after and 2 weeks after plasma activation for 1, 3, and 5 min. Values are presented as mean ± *SD*. *p < .05, **p < .01, ***p < .001. (c) Scanning electron microscopy images of plasma-treated 2D films. Scale bar: white = 10 μm, yellow = 1 μm. (d) Offset ATR-FTIR spectrum of plasma-treated films. (e) Super-positioned ATR-FTIR spectrum between 1250 and 1000 cm^{-1} indicating an ether group (—C—O) and (f) 3500 and 3100 cm^{-1} indicating an alcohol group (—O—H)

control and evaluated by Student's *t* test. p < .05 was considered statistically significant.

3 | RESULTS

3.1 | Plasma activation with oxygen plasma hydrophilized lactide-TMC by roughening the surfaces nanotopographically with a slight increase in an alcohol group

Lactide-TMC films were plasma-treated for 1, 3, and 5 min, and the contact angle was significantly reduced by approximately 20–25° in all groups (p < .001). The effect was maintained for at least 2 weeks except for one treated for 1 min in which the recurrence was observed (p = .006) (Figure 1(a,b)). SEM revealed that the surfaces were spotted in plasma-treated groups, and the level of nano-roughness was correlated with the dosage of oxygen plasma (Figure 1

(c)). Surface chemistry was evaluated by ATR-FTIR spectra, showing that there was a minimum change in chemical composition before and after the treatment. Characteristic peaks were observed at 2999, 1741, 1183–1032, and 791 cm^{-1}, which are assigned to —C—H, —C=O, —C—O, and —C—H, respectively. These peaks were almost identical among the groups except for the 5 min-treated samples in which the intensity of —C—O decreased (Figure 1(d,e)). In the range between 3500 and 3100 cm^{-1}, which is assigned to —O—H group, the absorbance slightly increased in the plasma-treated groups in a dose-dependent manner (Figure 1(f)).

3.2 | Plasma-treated surfaces promote initial adhesion, elongation, and proliferation of rBMSC

To access the initial cellular adhesion, elongation and proliferation, rBMSC were seeded on flat films treated with oxygen plasma. After 3–6 hr of seeding, cells attached on plasma-treated films exhibited
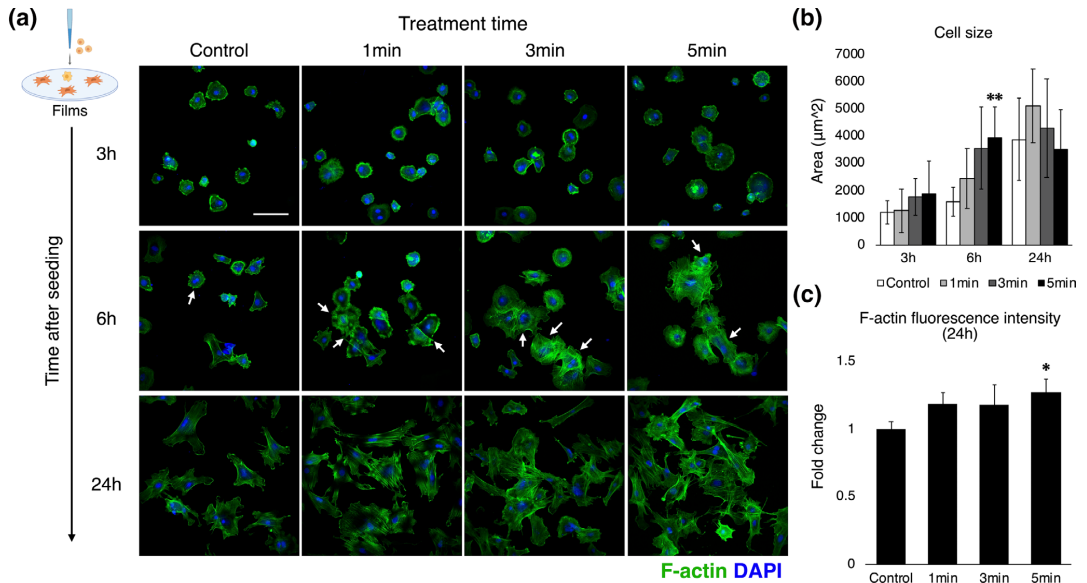
FIGURE 2 Initial cell adhesion, elongation, and proliferation on the plasma-treated 2D films. (a) Confocal images of bone marrow stem cells stained for F-actin and nuclei after 3, 6, and 24 hr of cell seeding on plasma-treated films. Arrows indicate cells undergoing cell divisions. (b) the image quantification of cell size and (c) F-actin fluorescence intensity measured at 24 hr of seeding. Values are presented as mean ± SD. Scale bar = 100 μm. $^*p < .05$, $^{**}p < .01$

more extended morphology than on the control despite the heterogeneous cell population causing large variation in the morphological quantification. Notably, active cellular proliferation and elongation were clearly observed on plasma-treated films at 6 hr, which resulted in the formation of complex cell-to-cell interaction. This also led to the stagnation or reduction in cell size in the 3 and 5 min-treated groups at 24 hr because of high cell density. On the other hand, cells on the control surface were less elongated, remaining isolated over the time (Figure 2(a,b)). There was a tendency for an increase in F-actin intensity in longer plasma-treated groups, indicating enhanced actin polymerization on the plasma-treated surfaces ($p = .026$ between the control and the 5 min-treated group) (Figure 2(c)).

3.3 | Improvement of hydrophilicity and seeding efficiency on 3D LTMC scaffolds

3D microporous scaffolds were treated with oxygen plasma for 1, 3, and 5 min to improve surface hydrophilicity without altering macro/micro-structure of the scaffolds. After the drop of αMEM, the medium almost immediately soaked into the scaffolds treated for more than 3 min while the droplet maintained an elliptical shape on the control and 1 min-treated scaffolds (Figure 3(a)). As with the 2D films, the surfaces were roughened with the texture of nanoscopic spots by oxygen plasma, which was limited superficially in submicron scale (Figure 3 (b)). Consistent with wettability, cell seeding efficiency was

significantly improved in the groups treated for 3 and 5 min compared to the control ($p = .027$ and .016, respectively) (Figure 3(c)). It is noteworthy that, due to the low absorbency, medium was distributed unevenly within the control scaffolds. However, prolonged plasma treatment negatively correlated with cell viability for the cells that remained on the wells, particularly in the 5 min-treated group ($p = .006$) (Figure 3(d)).

3.4 | Increase in cellular proliferation on plasma-treated scaffolds

rBMSC were seeded on control and plasma-treated scaffolds for 3 min, and cellular proliferation was evaluated on days 1, 3, 7, 14, and 21 after seeding. The quantification of dsDNA shows statistical significance between the control and plasma-treated scaffolds on day 1 ($p = .049$) and day 3 ($p = .007$), and proliferative activity reached the highest level in both groups around day 7. Subsequently, suppression of proliferation was observed in both groups. While the control group showed a gradual decrease by day 21, proliferative activity of cells on the plasma-treated scaffolds had already nadired on day 14 ($p = .0014$) (Figure 4(a)). To assess cell cycle status, samples were stained with anti-PCNA antibody. After seeding, the majority of cells in both groups expressed PCNA, indicating the cells were proliferative. Cells highly expressing PCNA (PCNA[High+] cells) accounted for the majority of cells by day 7, but
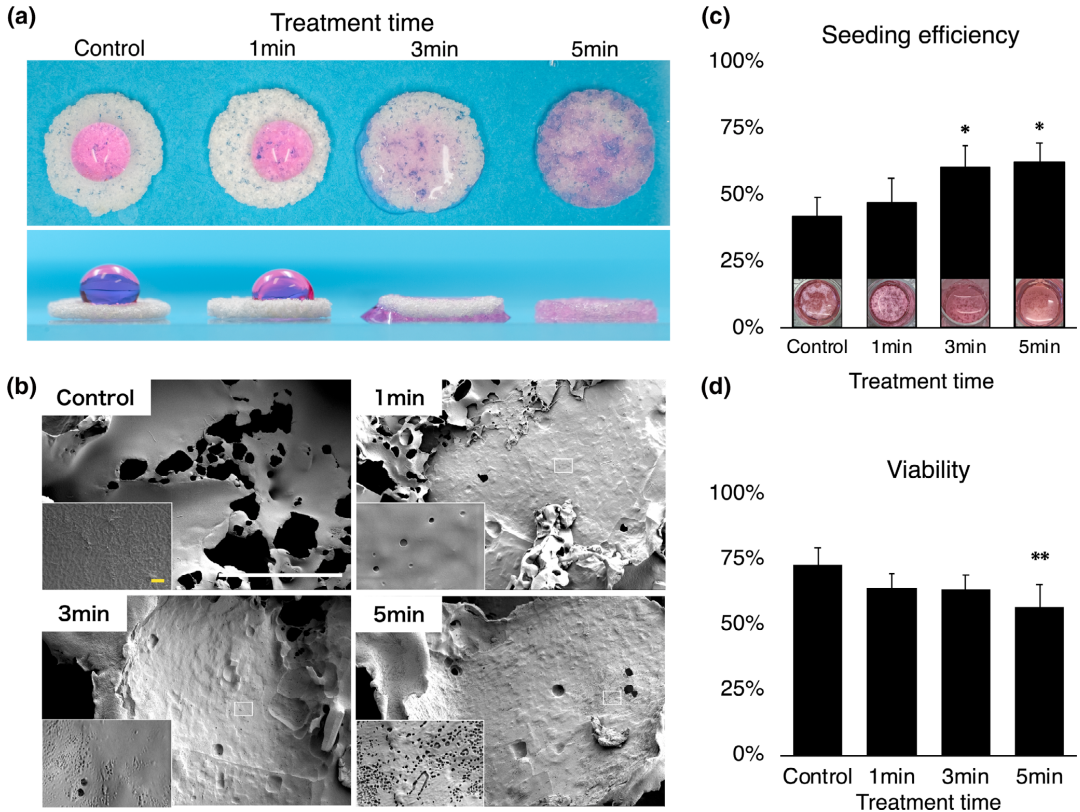
FIGURE 3 Characterization of surface topography and measurement of seeding efficiency with 3D microporous lactide-TMC scaffolds after plasma activation with oxygen plasma. (a) Photographical images of medium droplets on microporous scaffolds treated with oxygen plasma for 1, 3, and 5 min. The images were taken at 60 s of a drop of 50 μl α-MEM. (b) Scanning electron microscopy images of plasma-treated 3D microporous scaffolds. The magnified parts were marked with white boxes. Scale bar: white = 100 μm, yellow = 1 μm. (c) Seeding efficiency with the representative appearance of the scaffolds in wells and (d) cell viability measured after 1 hr of seeding. Values are presented as mean ± *SD*. *$p < .05$, **$p < .01$

PCNA expression was downregulated afterwards, and cells weakly expressing PCNA (PCNA^{low+} cells) became the majority on day14 and 21 (Figure 4(b)). Quantification shows that approximately 70% of the cells expressed PCNA by day14 in both groups, slightly higher in the plasma-treated group, after which proliferation was significantly down regulated (Figure 4(c)).

3.5 | Promotion of osteogenic differentiation on plasma-treated scaffolds

To evaluate osteogenic differentiation, mRNA expression of osteogenic markers, RUNX2, Col1A1, bone sialoprotein (BSP), osterix, ALP, and OCN was measured (Figure 5(a)). A key transcription factor and early osteogenic marker, RUNX2, remained upregulated by day 14 in both groups. The cells on plasma-treated scaffolds showed significant upregulation of RUNX2 on day 7 ($p = .015$) compared with rBMSC on control scaffolds. The peak was observed on day 14 in the control group while the RUNX2 level was stable from day 14 to day 21 in the plasma-treated group. The expression of an early osteogenic marker, Col1A1, was significantly upregulated as early as day 3 in the plasma-treated group ($p = .042$), which was the highest throughout the experimental period. The peak of ColA1 expression in the control group was observed on day 7 ($p = .0044$). Another osteogenic marker, ALP, displayed continuous upregulation over time in both groups. However, regarding the comparison between groups, the regulatory pattern was time-dependant and did not show a clear pattern. The expression of osterix, an osteogenic marker related to the maturation process of pre-osteoblasts, increased continuously over time in both groups. Notably, the plasma-treated group consistently showed higher expression compared with the control (day 7 $p = .006$, day 21 $p = .008$). Similarly, BSP was significantly upregulated on day 3 and day 21 in the plasma-treated group (day 3 $p = .00089$, day 21 $p = .028$).[33] A late osteogenic marker, OCN, clearly indicated that the
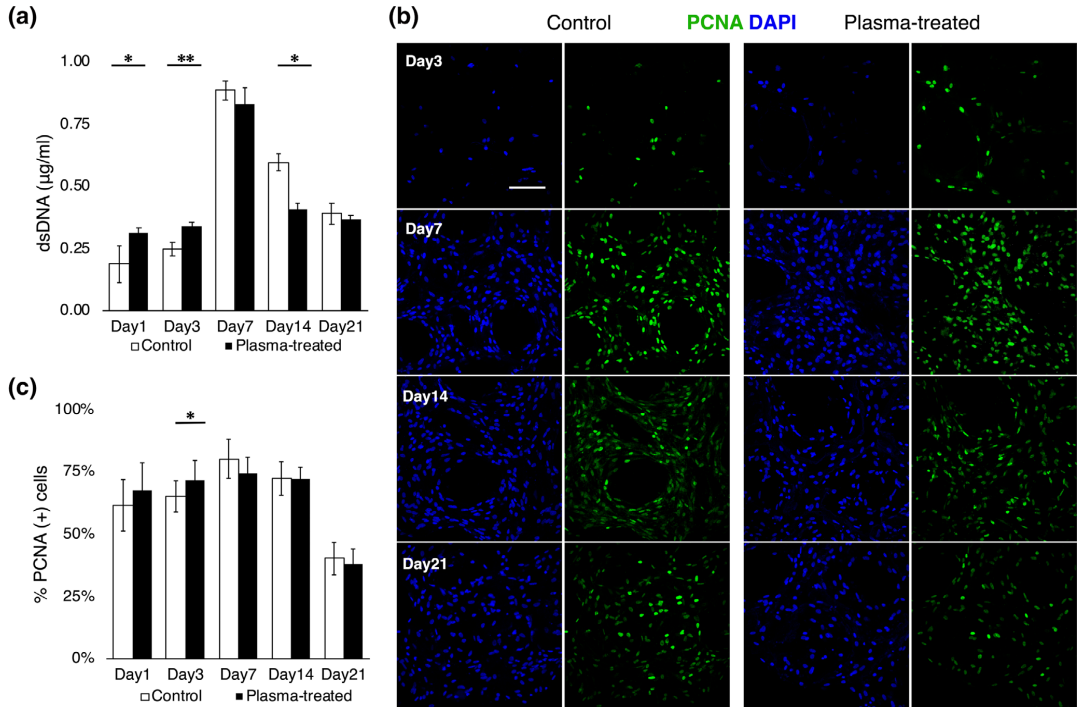
FIGURE 4 Proliferative activity and cell cycle of bone marrow stem cells on the 3D plasma-treated scaffolds for 3 min. (a) The quantification of dsDNA of bone marrow stem cells on day 1, 3, 7, 14, and 21 after seeding. (b) Immunofluorescence images for PCNA on day 3, 7, 14, and 21 after seeding. Scale bar = 100 μm. (c) The image quantification of the ratio of PCNA positive cells. Values are presented as mean ± *SD*. *$p < .05$, **$p < .01$

expression was enhanced in the late stage, particularly in the plasma-treated group, and a significant difference between the groups was observed on day 14 ($p = .047$) and day 21 ($p = .020$). To evaluate the general property as MSC, putative markers for rat MSC, CD44, CD73, and CD90, were measured.[34] These were expressed consistently with a small fluctuation throughout the experimental period, following a comparable tendency in both groups (Figure 5(b)).

Immunofluorescence showed that RUNX was highly expressed throughout the experiment in both groups (Figure 5(c)). The nuclear accumulation of RUNX2 was found mainly on day 7 and day 14, and the expression was diffused to cytoplasm on day 21. This indicates that the early RUNX2 expression acted as a transcription factor for osteogenic differentiation. Notably, the groups of cells with RUNX2 highly expressed in nuclei were focally found on day 7 only in the plasma-treated group.

3.6 | Accelerated differentiation confirmed by the increased level of collagen matrix formation

To evaluate the formation of extracellular matrix, samples were stained with anti-collagen I antibody which specifically reacts with non-denaturing 3D helical structure of native collagen type I (Col1).

Consistent with the early expression of osteogenic markers, collagen formation was significantly accelerated on plasma-treated scaffolds (Figure 6(a)). While the Col1 formation gradually increased over time in the control group, the remarkable Col1 formation was observed as early as 7 days post-osteoinduction in the plasma-treated group. Quantification of surface coverage by Col1 shows that it reached approximately 50% on day 7 in the plasma-treated group, which was 20% higher than the control ($p = .037$) (Figure 6(b)). On day 21, the control group caught up to the plasma-treated group. Col1 intensity was slightly higher in the plasma-treated group on day 7 and day 21, suggesting the formation of a dense Col1 layer, but it was not statistically significant (Figure 6(c)).

3.7 | Enhanced mineralization on plasma-treated scaffolds

To assess mineralization as a consequence of osteogenic differentiation, ALP activity and calcium deposition were evaluated. ALP activity was continuously upregulated by day 14 in both groups (Figure 7(a)). Although the upregulation of ALP activity in the plasma-treated group was found on day 1 and day 3, the increase ratio over time was lower. Alizarin red S quantification showed the promotion of mineralization

(a)

(b)

(c)

Control   RUNX2 F-actin DAPI   Plasma-treated
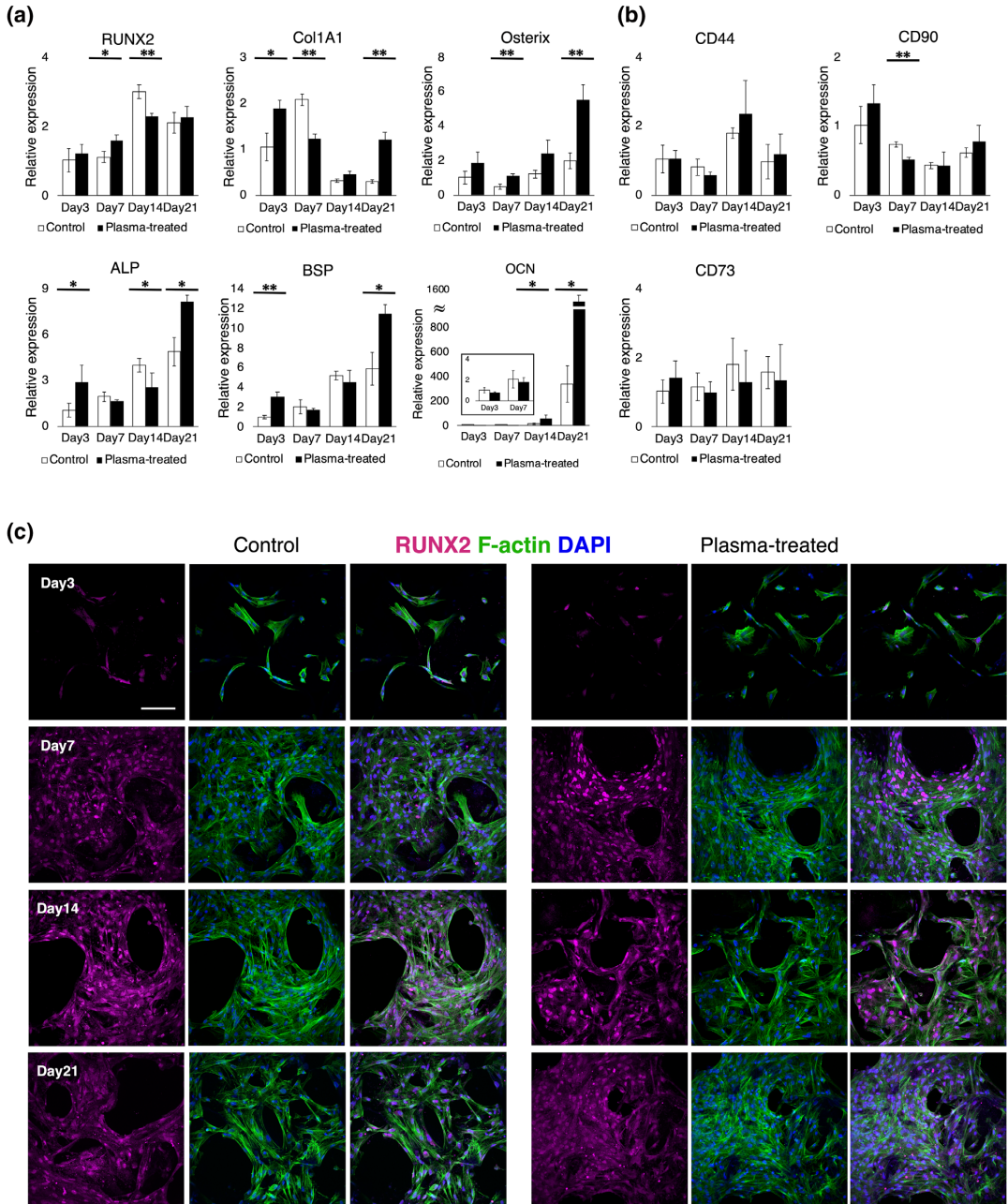
FIGURE 5   Evaluation of osteogenic differentiation of bone marrow stem cells on the 3D plasma-treated scaffolds for 3 min. (a,b) mRNA expression of osteogenic differentiation markers and a putative mesenchymal stem cell marker on day 3, 7, 14, and 21 after seeding on the 3D plasma-treated scaffolds. Relative mRNA levels were normalized to GAPDH. Values are presented as mean ± 95% confidence interval. *$p < .05$, **$p < .01$, ***$p < .001$ (c) immunofluorescence images for RUNX2. Scale bar = 100 μm

in the plasma-treated group (Figure 7(b,c)). Interestingly, calcium deposition in the control was not as homogeneous as their counterpart on day 7, demonstrating the heterogeneity of cell distribution.

Quantification confirmed the greater production of calcium by cells on plasma-treated scaffolds, particularly on day 3 ($p = .031$) and day 7 ($p = .003$) (Figure 7(d)).
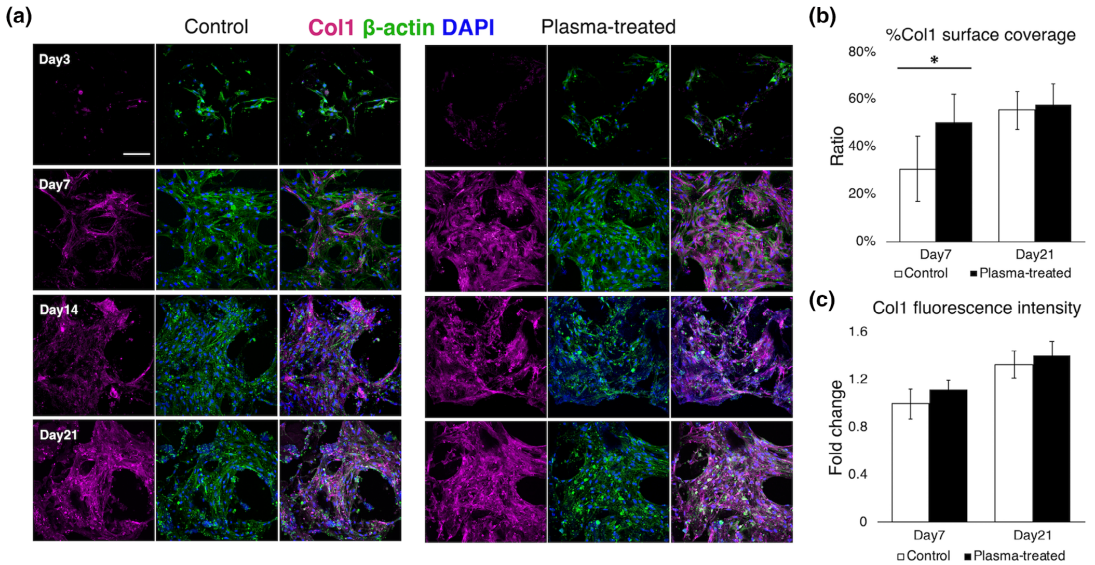
FIGURE 6 Collagen type 1 formation by bone marrow stem cells on the 3D plasma-treated scaffolds for 3 min. (a) Immunofluorescence images for collagen type 1 on day 3, 7, 14, and 21 after seeding. Scale bar = 100 μm. The quantifications of (b) surface coverage rate and (c) fluorescence intensity of collagen type 1 on day 7 and day 21 after seeding. Values are presented as mean ± *SD*. **p* < .05
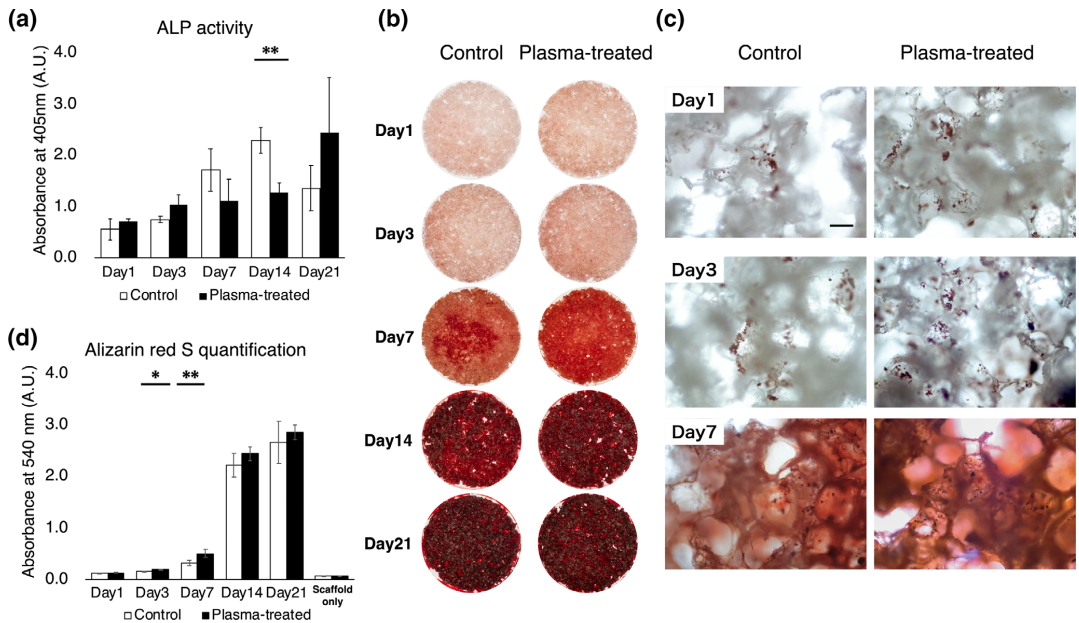
FIGURE 7 Alkaline phosphatase (ALP) activity of bone marrow stem cells and mineralization on the 3D plasma-treated scaffolds for 3 min. (a) ALP activity of bone marrow stem cells on the 3D plasma-treated scaffolds on day 1, 3, 7, 14, and 21 after seeding. (b) Macroscopic and (c) microscopic images of the 3D plasma-treated scaffolds stained with Alizarin Red S. Scale bar = 100 μm (d) The quantification of Alizarin red S staining. Values are presented as mean ± *SEM*. **p* < .05, ***p* < .01

4 | DISCUSSION

Biodegradable aliphatic polymers such as PLA, PCL, and lactide-TMC, have been tested for various applications in biomedicine and shown to possess decent properties for bone tissue engineering, that is, they are biocompatible and biodegradable and have appropriate mechanical strength as a graft material. They also have good moldability, which allows one to form the materials in arbitrary shapes with high porosity by freeze-drying, salt leaching, gas foaming and 3D printing techniques.[35] In this study, we have selected Lactide-TMC as a scaffold material because Lactide-TMC has higher flexibility than conventional aliphatic polymers such as PLA and PCL, which facilitates handling, fabrication and shaping of the scaffolds.[36] Further, the material is known to possess a unique degradation property. During degradation, the material produces less acidic by-products because of its component, trimethylene carbonate, causing less local inflammation at the implanted sites.[37] However, the hydrophobicity of aliphatic polymers including Lactide-TMC is a common obstacle regardless of the type of applications, hindering efficient cell adhesion and growth, and therefore, a surface modification is preferred.[38]

Plasma as an ionized gas was first described in 1927 by the Nobel laureate Irving Langmuir. Since then, surface treatment by plasma activation has been extensively studied. The first application of plasma for surface modification of biodegradable aliphatic polymers was in 1997, which applied vacuum oxygen and nitrogen plasma to PLA fabrics.[39] Afterward, the treatment has been tested with a variety of cell types, and high biocompatibility has been verified. It is currently applied to biomaterials and biomedical devices approved for clinical implantation.[40] There are several advantages to surface activation of biomaterials with oxygen plasma beyond biocompatibility. Typically, surface oxidation for hydrophilization occurs only within a depth of 5–50 nm from the surface, indicating that plasma activation does not alter the bulk properties of the materials.[41,42] Therefore, the materials can maintain their mechanical properties such as strength, flexibility, formability, stability/degradability while the surfaces are modified to be more bioactive.[18] Further, the fact that oxygen gas is abundant equates to high availability and low cost, which is critical for clinical application.

Our structural and chemical characterization of plasma-treated lactide-TMC is consistent with previous studies using other types of biopolymers. Since wettability is closely influenced by surface chemistry and topography, we have performed SEM and ATR-FTIR together with contact angle measurement. We showed that plasma activation for as short as 1 min significantly increased surface roughness while the addition of functional groups was limited, indicating that changes in surface properties of lactide-TMC after short-term oxygen plasma treatment was mainly due to a mechanical etching effect by bombardment of oxygen molecules rather than chemical modification. We also performed atomic force microscopy (AFM), but we could not obtain reliable data because of extremely rough and inhomogeneous surfaces after the treatment (data not shown). The induced hydrophilicity lasted for at least 2 weeks, which would adapt readily to clinical settings.

Optimal cell adhesion and elongation can only be achieved when the surface wettability is appropriate, which may vary depending on the type of cells as well as materials.[43] Therefore, we first compared cell kinetics on 1, 3, and 5 min-treated surfaces of lactide-TMC with the control surface. On the plasma treated surfaces, initial cell adhesion and elongation of rBMSC were greatly enhanced within 24 hr of seeding in a dose-dependent manner. Moreover, we observed an increase in F-actin intensity on plasma-treated surfaces. The density of F-actin is known to be associated with the strength of cell adhesion as well as the generation of physical forces to change cell morphology and to migrate.[44-46] Recent morphological analyses using adipose-derived MSC revealed the detailed mechanism of accelerated initial cell adhesion on plasma-treated polystyrene surfaces. The cells on plasma-treated surfaces by ammonia, carbon dioxide, and acrylic acid plasma exhibited more filopodia-like and lamellipodial-like protrusions after only 1 hr of adhesion.[20] A promising mechanism for enhancing adhesion was suggested by Griffin et al. They functionalized nanocomposite polymer, POSS-PCU, using different types of plasma gas and showed an increase in total protein absorption to the surface following incubation with serum. This included cell adhesion serum proteins such as fibronectin and vitronectin, suggesting that the surface was modified to be more bioactive.[47] These results together confirm that hydrophilized polymeric surfaces by plasma activation activates cell kinetics.

Further evaluation was conducted with 3D microporous scaffolds as it is crucial to evaluate cell fate in a 3D environment similar to that in vivo. As wettability increased, the seeding efficiency was improved. This was attributed to the high infiltration of cells. The efficiency of cell seeding is a key factor for clinical application because it is directly linked to time and cost of treatment.[48] However, we also showed that the group treated for 5 min had significantly decreased cellular viability, implying that prolonged treatment may affect cell health. Similar findings were reported previously, showing that excessive plasma treatment led to low viability of osteoblast precursors and significantly disrupted cell adhesion.[27] One possible reason could be due to reactive oxygen species (ROS) that are bound to the surface, causing cell senescence and apoptosis,[49-53] and/or simply wettability inappropriate for osteoprogenitors.[54] Therefore, we used 3 min-treated samples for further studies because this increased seeding efficiency equivalent to that seen after 5 min treatment without the risk of compromising cell viability.

Stem cell fate is firmly governed by surface physical properties such as surface roughness, polarity and wettability, which together control the gene expression of uncommitted cells.[55,56] Therefore, we evaluated osteogenesis in an osteoinductive environment. Firstly, the proliferative activity of rBMSC was assessed as it reflects not only cell growth but also osteogenic maturation. The quantification of dsDNA indicates that rBMSC increased their proliferative activity before reaching confluence. Then, the proliferation was suppressed because of tight cell-to-cell contact, which is a prerequisite for osteogenic maturation.[48,57] This process was significantly accelerated in the plasma-treated group. Immunofluorescence of PCNA further demonstrated active cell cycle in both groups by day 7 but the expression gradually

decreased afterwards. Although statistical analysis showed no significance, the intensity as well as the ratio of PCNA+ cells in the plasma-treated group were higher on day 1 and day 3 and lower on day 7 and later. The magnitude of PCNA expression is related to the cell cycle. Cells highly express PCNA during S/G2/M phases and weakly during G1 phase, but cells which do not undergo cell cycle (i.e., G0 phase) do not express PCNA.[58,59] Therefore, our results suggest that the proliferative activity of rBMSC in 3D plasma-treated scaffolds was initially promoted as it was with 2D surfaces, and they commenced their maturation process slightly earlier than the cells on the control surfaces.

RUNX2 is a key transcription factor that plays a major role in driving osteogenic differentiation of precursor cells. In murine osteogenic cells, an initial increase in RUNX2 expression is involved in the induction of differentiation although continuous upregulation is observed.[60,61] We showed that RUNX2 expression was significantly upregulated in mRNA and protein levels in the plasma-treated group on day 7 compared with the control, and the mRNA expression had plateaued by day 14 when the control group showed the highest expression. This indicates that plasma-treated scaffolds accelerated the induction of osteogenic differentiation. Interestingly, despite high mRNA expression, RUNX2 protein accumulated in nuclei was clearly observed only on day 7 and day 14, suggesting there is a discordance between transcription and translation in murine RUNX2. Osterix is the other key osteogenic transcription factor and the downstream target of RUNX2, which is necessary to transform osteogenic precursors into mature osteoblasts.[62] We showed that mRNA expression of osterix was continuously upregulated over the period of differentiation, and that expression was significantly higher in the plasma-treated group throughout the experimental period. The maturation process was confirmed by the expression of BSP and OCN as mature osteoblast markers.[33] Both expression levels were significantly upregulated on day 21 in the plasma-treated group. These findings are consistent with a previous report using an osteoblastic cell line on plasma-treated chitosan scaffolds.[43] However, we were unable to show a clear separation of ALP expression and its activity pattern between the groups. A possible mechanism of increased expression in the late phase, based on previous findings, is that the release of plasma membrane vesicles is a part of a controlled apoptosis process, which is necessary for tissue-specific maturation.[63-65] This was also demonstrated with osteoblastic cells in which the release of ALP from osteoblastic cells undergoing apoptosis was involved in mineralisation.[66] Additionally, ALP is involved in numerous biological processes, and it is expressed in all of living cells.[67] Collagen type 1 is the main extracellular matrix in bone. RT-qPCR showed that Col1A1a expression was significantly higher in the plasma-treated group on day 3, but the trend was reversed on day 7. This is supported by immunofluorescence showing that the formation of collagen type 1 was established as early as on day 7 on the plasma-treated scaffolds. Apart from the increase in collagen formation activity of rBMSC, previous studies have found that wettability itself alters the assembly pattern of collagen fibers, which further activates cell-matrix interaction via integrinα1 and α2

heterodimers.[68,69] This suggests not only that modified surface properties enhance collagen formation by the cells but also that collagen matrix formed on the treated surface further enhance cell activity. Finally, the promotion of osteogenic differentiation was confirmed by alizarin red S staining, showing more calcium deposition in the plasma-treated group, particularly on day 3 and day 7. It is noteworthy that non-uniformity of staining was observed in the control. This is probably ascribed to inhomogeneous cell seeding because of hydrophobicity of the untreated material. Although it appears the control group caught up with the plasma-treated group on day 21 in terms of mineralization and collagen formation, this is probably due to supersaturation of the formed substances. Thus, the promotion of osteogenic differentiation may persist longer than 21 days.

In this study, we have chosen oxygen plasma mainly because of high availability and cost-effectiveness. Additionally, it can also hydroxylate and etch the polymer surfaces, which is ideal for the purpose of hydrophilisation.[48,70] However, different types of plasma cause diverse surface chemistry and topography, leading to different biological effects.[71] It has been reported that plasma activation with argon gas but not oxygen gas promoted chondrogenic and osteogenic differentiation of rat adipose-derived stem cells.[72] Hence, the ideal plasma gas and dosage should be optimized for each cell type, species and therapeutic target tissue.

5 | CONCLUSION

In this work, the surface of flat films and 3D microporous scaffolds of the aliphatic polymer lactide-TMC was modified by oxygen plasma for different treatment times (i.e., 1, 3, and 5 min). After treatment, nanotopographical roughness of lactide-TMC significantly increased, resulting in improved wettability. Importantly, the effect persisted at least for 2 weeks after treatment, which may potentially facilitate the translation of plasma-treated polymeric scaffolds to the clinical setting. We found that initial cell adhesion and elongation of rBMSC on plasma-treated surfaces were significantly promoted compared to the control. Also, a higher seeding efficiency was achieved when scaffolds were treated for more than 3 min. However, prolonged treatment was associated with lower cell viability, and therefore, 3 min-treatment was considered optimal for the evaluation of osteogenesis of rBMSC. We showed that cell growth and osteogenic differentiation were significantly promoted in the plasma-treated group, resulting in the promotion of extracellular matrix formation and mineral deposition. Surface activation with oxygen plasma is a promising strategy for bone tissue engineering as it is an accessible technique that can modify surface properties suitable for cell growth and osteogenic differentiation without compromising the bulk properties.

CONFLICT OF INTEREST

The authors declare no potential conflict of interest.

DATA AVAILABILITY STATEMENT

The data that support the findings of this study are available from the corresponding author upon reasonable request.

ORCID

Shuntaro Yamada https://orcid.org/0000-0003-0282-5498

REFERENCES

1. Campana V, Milano G, Pagano E, et al. Bone substitutes in orthopaedic surgery: from basic science to clinical practice. *J Mater Sci Mater Med*. 2014;25:2445-2461.
2. Roddy E, DeBaun MR, Daoud-Gray A, Yang YP, Gardner MJ. Treatment of critical-sized bone defects: clinical and tissue engineering perspectives. *Eur J Orthop Surg Traumatol*. 2018;28:351-362.
3. Amini AR, Laurencin CT, Nukavarapu SP. Bone tissue engineering: recent advances and challenges. *Crit Rev Biomed Eng*. 2012;40: 363-408.
4. Fuoco T, Mathisen T, Finne-Wistrand A. Poly(l-lactide) and poly(l-lactide-co-trimethylene carbonate) melt-spun fibers- structure–processing–properties relationship. *Biomacromolecules*. 2019;20: 1346-1361.
5. Guo GK, Lu ZQ, Zhang Y, Li SM. In vivo study on the histocompatibility and degradation behavior of biodegradable. *Acta Biochim Biophys Hung*. 2011;43:433.
6. Messias AD, Martins KF, Motta AC, Duek EA, Synthesis d R. Characterization, and osteoblastic cell culture of poly(L-co-D,L-lactide-co-trimethylene carbonate) scaffolds. *Int J Biomater*. 2014;2014:1-7.
7. Ji L-J, Lai K-L, He B, et al. Study on poly(l-lactide-co-trimethylene carbonate): synthesis and cell compatibility of electrospun film. *Biomed Mater*. 2010;5:045009.
8. Hassan MN, Yassin MA, Suliman S, Lie SA, Gjengedal H, Mustafa K. The bone regeneration capacity of 3D-printed templates in calvarial defect models: a systematic review and meta-analysis. *Acta Biomater*. 2019;91:1-23.
9. Sisson AL, Ekinci D, Lendlein A. The contemporary role of ε-caprolactone chemistry to create advanced polymer architectures. *Polymer*. 2013;54:4333-4350.
10. Jamshidian M, Tehrany EA, Imran M, Jacquot M, Desobry S. Polylactic acid: production, applications, nanocomposites, and release studies. *Compr Rev Food Sci Food Saf*. 2010;9:552-571.
11. Jeon H, Lee H, Kim GA. Surface-modified poly(ε-caprolactone) scaffold comprising variable nanosized surface-roughness using a plasma treatment. *Tissue Eng Part C Method*. 2014;20:951-963.
12. Kim K, Dean D, Mikos AG, Fisher JP. Effect of initial cell seeding density on early osteogenic signal expression of rat bone marrow stromal cells cultured on cross-linked poly(propylene fumarate) disks. *Biomacromolecules*. 2009;10:1810-1817.
13. Francis K, Palsson BO. Effective intercellular communication distances are determined by the relative time constants for cytochemokine secretion and diffusion (cell signalingbioreactor designtissue engineering). 1997;94:12258.
14. Mauck RL, Wang CCB, Oswald ES, Ateshian GA, Hung CT. The role of cell seeding density and nutrient supply for articular cartilage tissue engineering with deformational loading. *Osteoarthritis Cartilage*. 2003; 11:879-890.
15. Lane SW, Williams DA, Watt FM. Modulating the stem cell niche for tissue regeneration. *Nat Biotechnol*. 2014;32:795-803.
16. Schofield R. The relationship between the spleen colony-forming cell and the haemopoietic stem cell. *Blood Cells*. 1978;4(1-2):7-25.

17. Recek N, Resnik M, Motaln H, et al. Cell adhesion on polycaprolactone modified by plasma treatment. *Int J Polym Sci*. 2016; 2016:1-9.
18. Jacobs T, Morent R, De Geyter N, Dubruel P, Leys C. Plasma surface modification of biomedical polymers: influence on cell-material interaction. *Plasma Chem Plasma Process*. 2012;32:1039-1073.
19. Qiu Z-Y, Chen C, Wang X-M, Lee I-S. Advances in the surface modification techniques of bone-related implants for last 10 years. *Regen Biomater*. 2014;1:67-79.
20. Kleinhans C, Schmohl L, Barz J, Kluger PJ. Low-pressure plasma activation enables enhanced adipose-derived stem cell adhesion. *J Biomed Mater Res - Part B Appl Biomater*. 2020;108(4):1527-1535.
21. Li Y, Kim JH, Choi EH, Han I. Promotion of osteogenic differentiation by non-thermal biocompatible plasma treated chitosan scaffold. *Sci Rep*. 2019;9:3712.
22. Barradas AMC, Lachmann K, Hlawacek G, et al. Surface modifications by gas plasma control osteogenic differentiation of MC3T3-E1 cells. *Acta Biomater*. 2012;8:2969-2977.
23. Trappmann B, Gautrot JE, Connelly JT, et al. Extracellular-matrix tethering regulates stem cell fate. *Nat Mater Nature*. 2012;11:642-649.
24. Park JH, Wasilewski CE, Almodovar N, et al. The responses to surface wettability gradients induced by chitosan nanofilms on microtextured titanium mediated by specific integrin receptors. *Biomaterials*. 2012; 33:7386-7393.
25. Hao L, Fu X, Li T, et al. Surface chemistry from wettability and charge for the control of mesenchymal stem cell fate through self-assembled monolayers. *Colloids Surf B Biointerfaces*. 2016;148:549-556.
26. Zhang T, Lin S, Shao X, et al. Effect of matrix stiffness on osteoblast functionalization. *Cell Prolif*. 2017;50:e12338.
27. Olivares-Navarrete R, Hyzy SL, Hutton DL, et al. Role of non-canonical Wnt signaling in osteoblast maturation on microstructured titanium surfaces. *Acta Biomater*. 2011;7:2740-2750.
28. Galli C, Piemontese M, Lumetti S, Manfredi E, MacAluso GM, Passeri G. The importance of WNT pathways for bone metabolism and their regulation by implant topography. *Eur Cell Mater*. 2012;24:46-59.
29. Odelius K, Plikk P, Albertsson A-C. Elastomeric hydrolyzable porous scaffolds: copolymers of aliphatic polyesters and a polyether-ester. *Biomacromolecules*. 2005;6:2718-2725.
30. Yassin MA, Leknes KN, Pedersen TO, et al. Cell seeding density is a critical determinant for copolymer scaffolds-induced bone regeneration. *J Biomed Mater Res Part A*. 2015;103:3649-3658.
31. Schindelin J, Arganda-Carreras I, Frise E, et al. Fiji: an open source platform for biological image analysis. *Nat Methods*. 2012;9:676-682.
32. Livak KJ, Schmittgen TD. Analysis of relative gene expression data using real-time quantitative PCR and the 2(-Delta Delta C[T]) method. *Methods*. 2001;25:402-408.
33. Miron RJ, Zhang YF. Osteoinduction: a review of old concepts with new standards. *J Dent Res*. 2012;91:736-744.
34. Suto EG, Mabuchi Y, Suzuki N, et al. Prospectively isolated mesenchymal stem/stromal cells are enriched in the CD73+ population and exhibit efficacy after transplantation. *Sci Rep*. 2017;7(4838):1-10.
35. Pina S, Ribeiro VP, Marques CF, et al. Scaffolding strategies for tissue engineering and regenerative medicine applications. *Materials*. 2019; 12:1824.
36. Sartoneva R, Nordback PH, Haimi S, et al. Comparison of poly(l-lactide-co-ε-caprolactone) and poly(trimethylene carbonate) membranes for urethral regeneration: an in vitro and in vivo study. *Tissue Eng Part A*. 2018;24(1-2):117-127.
37. Fukushima K. Poly(trimethylene carbonate)-based polymers engineered for biodegradable functional biomaterials. *Biomater Sci*. 2016;4(1): 9-24.
38. Yassin MA, Leknes KN, Sun Y, Lie SA, Finne-Wistrand A, Mustafa K. Surfactant tuning of hydrophilicity of porous degradable copolymer scaffolds promotes cellular proliferation and enhances bone formation. *J Biomed Mater Res Part A*. 2016;104:2049-2059.

39. Hirotsu T, Masuda T, Matumura Y, Takahashi M. Surface effects of plasma treatments on some biodegradable polymers. *J Photopolym Sci Technol*. 1997;10:123-128.

40. Bose S, Robertson SF, Bandyopadhyay A. Surface modification of bio-materials and biomedical devices using additive manufacturing. *Acta Biomater*. 2018;66:6-22.

41. Altuncu E, Üstel F, Esen SG, Karayel E. Infuence of oxygen and nitro-gen plasma treatment on polypropyleme (PP) bumper surface. *J Achiev Mater Manuf Eng*. 2016;77:18.

42. Lin W-C, Mohd Razali N. Temporary wettability tuning of PCL/PDMS micro pattern using the plasma treatments. *Materials*. 2019;12:644.

43. Dowling DP, Miller IS, Ardhaoui M, Gallagher WM. Effect of surface wettability and topography on the adhesion of osteosarcoma cells on plasma-modified polystyrene. *J Biomater Appl*. 2011;26:327-347.

44. Gardel ML, Schneider IC, Aratyn-Schaus Y, Waterman CM. Mechani-cal integration of actin and adhesion dynamics in cell migration. *Annu Rev Cell Dev Biol*. 2010;26:315-333.

45. Kwon S, Yang W, Moon D, Kim KS. Biomarkers to quantify cell migra-tion characteristics. *Cancer Cell Int BioMed Central*. 2020;20:1.

46. Dogterom M, Koenderink GH. Actin-microtubule crosstalk in cell biol-ogy. *Nat Rev Mol Cell Biol*. 2019;20:38-54.

47. Griffin MF, Ibrahim A, Seifalian AM, Butler PEM, Kalaskar DM, Ferretti P. Chemical group-dependent plasma polymerisation prefer-entially directs adipose stem cell differentiation towards osteogenic or chondrogenic lineages. *Acta Biomater*. 2017;50:450-461.

48. Hettle R, Corbett M, Hinde S, et al. The assessment and appraisal of regenerative medicines and cell therapy products: an exploration of methods for review, economic evaluation and appraisal. *Health Technol Assess*. 2017;21:1-204.

49. Jha N, Ryu JJ, Choi EH, Kaushik NK. Generation and role of reactive oxygen and nitrogen species induced by plasma, lasers, chemical agents, and other systems in dentistry. *Oxid Med Cell Longev*. 2017; 2017:1-13.

50. Arndt S, Wacker E, Li Y-F, et al. Cold atmospheric plasma, a new strat-egy to induce senescence in melanoma cells. *Exp Dermatol*. 2013;22: 284-289.

51. Weiss M, Gümbel D, Hanschmann E-M, et al. Cold atmospheric plasma treatment induces anti-proliferative effects in prostate cancer cells by redox and apoptotic signaling pathways. *PLoS One*. 2015;10: e0130350.

52. Xia J, Zeng W, Xia Y, et al. Cold atmospheric plasma induces apoptosis of melanoma cells via sestrin2-mediated nitric oxide synthase signaling. *J Biophotonics*. 2019;12:e201800046.

53. Turrini E, Laurita R, Stancampiano A, et al. Cold atmospheric plasma induces apoptosis and oxidative stress pathway regulation in T-lymphoblastoid leukemia cells. *Oxid Med Cell Longev*. 2017;2017:1-13.

54. Hao L, Yang H, Du C, et al. Directing the fate of human and mouse mes-enchymal stem cells by hydroxyl–methyl mixed self-assembled mono-layers with varying wettability. *J Mater Chem B*. 2014;2:4794-4801.

55. Oehr C. Plasma surface modification of polymers for biomedical use. *Nucl Instru Method Phys Res Sec B Beam Interact Mater Atoms*. 2003; 208:40.

56. Ferrari M, Cirisano F, Morán MC. Mammalian cell behavior on hydrophobic substrates: influence of surface properties. *Colloids Interf*. 2019;3:48.

57. Abo-Aziza FAM, Az A. The impact of confluence on bone marrow mesenchymal stem (BMMSC) proliferation and osteogenic differenti-ation. *Int J Hematol Stem Cell Res*. 2017;11:121.

58. Zerjatke T, Gak IA, Kirova D, et al. Quantitative cell cycle analysis based on an endogenous all-in-one reporter for cell tracking and clas-sification. *Cell Rep*. 2017;19:1953-1966.

59. Schönenberger F, Deutzmann A, Ferrando-May E, Merhof D. Discrim-ination of cell cycle phases in PCNA-immunolabeled cells. *BMC Bioin-formatics*. 2015;16:180.

60. Liu B, Lu Y, Wang Y, Ge L, Zhai N, Han J. A protocol for isolation and identification and comparative characterization of primary osteoblasts from mouse and rat calvaria. *Cell Tissue Bank*. 2019;20:173-182.

61. Hassumi JS, Mulinari-Santos G, Fabris AL d S, et al. Alveolar bone healing in rats: micro-CT, immunohistochemical and molecular analy-sis. *J Appl Oral Sci*. 2018;26:e20170326.

62. Hojo H, Ohba S, He X, Lai LP, McMahon AP. Sp7/osterix is restricted to bone-forming vertebrates where it acts as a dlx co-factor in osteo-blast specification. *Dev Cell*. 2016;37:238-253.

63. Huppertz B, Frank HG, Kaufmann P. The apoptosis cascade-morphological and immunohistochemical methods for its visualiza-tion. *Anat Embryol*. 1999;200:1-18.

64. Mills JC, Stone NL, Pittman RN. Extranuclear Apoptosis. *J Cell Biol*. 1999;146:703-708.

65. Johansson A-C, Appelqvist H, Nilsson C, Kågedal K, Roberg K, Öllinger K. Regulation of apoptosis-associated lysosomal membrane permeabilization. *Apoptosis*. 2010;15:527-540.

66. Farley JR, Stilt-Coffing B. Apoptosis may determine the release of skeletal alkaline phosphatase activity from human osteoblast-line cells. *Calcif Tissue Int*. 2001;68:43-52.

67. Štefková K, Procházková J, Pacherník J. Alkaline phosphatase in stem cells. *Stem Cells Int*. 2015;1:2015.

68. Coelho NM, González-García C, Planell JA, Salmerón-Sánchez M, Altankov G. Different assembly of type IV collagen on hydrophilic and hydrophobic substrata alters endothelial cells interaction. *Eur Cell Mater*. 2010;19:262-272.

69. Coelho NM, González-García C, Salmerón-Sánchez M, Altankov G. Arrangement of type IV collagen on NH2 and COOH functionalized surfaces. *Biotechnol Bioeng*. 2011;108:3009-3018.

70. Yamamoto M, Matsumae T, Kurashima Y, et al. Comparison of argon and oxygen plasma treatments for ambient room-temperature wafer-scale au–au bonding using ultrathin au films. *Micromachines*. 2019;10:119.

71. Griffin M, Palgrave R, Baldovino-Medrano V, Butler P, Kalaskar D. Argon plasma improves the tissue integration and angiogenesis of subcutaneous implants by modifying surface chemistry and topogra-phy. *Int J Nanomedicine*. 2018;13:6123-6141.

72. Griffin MF, Ibrahim A, Seifalian AM, Butler PEM, Kalaskar DM, Ferretti P. Argon plasma modification promotes adipose derived stem cells osteogenic and chondrogenic differentiation on nanocomposite polyurethane scaffolds; implications for skeletal tissue engineering. *Mater Sci Eng C*. 2019;105:110085.

APPENDIX
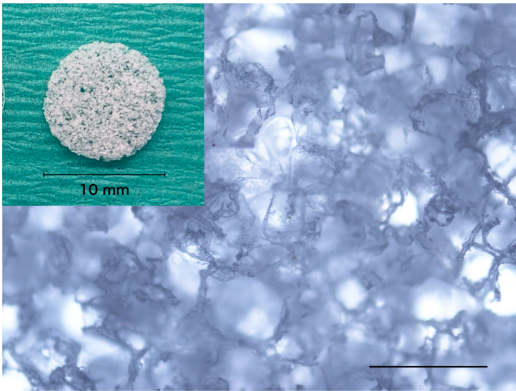
FIGURE A1 Macro- and microscopic image of lactide-TMC microporous scaffolds used in the study. Scale bar = 500 μm (microscopic image)
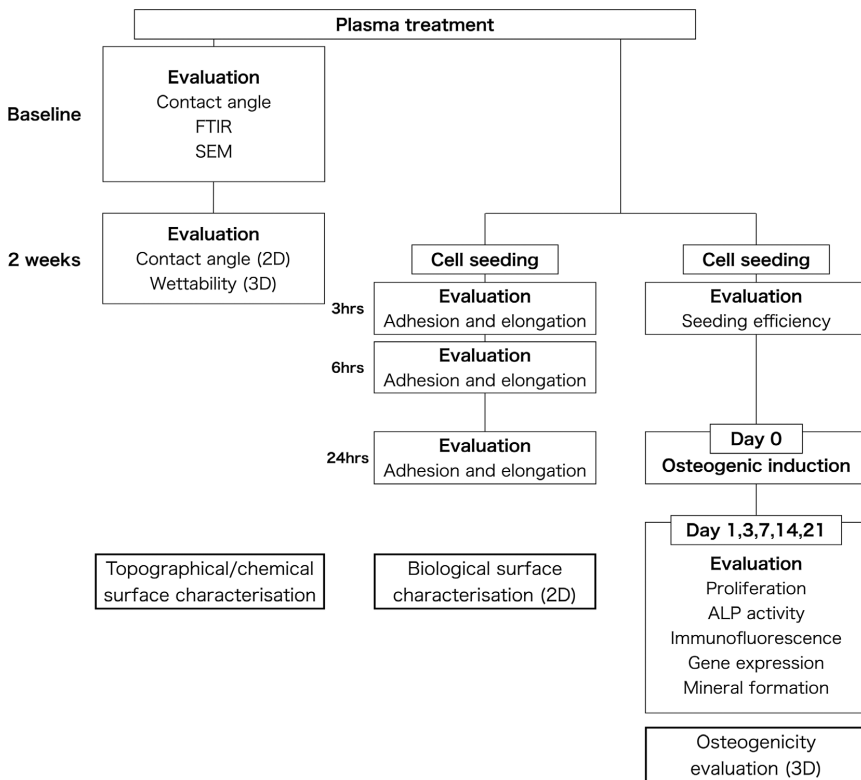
FIGURE A2 Experimental flow and timeline

Paper II

Optimization and Validation of a Custom-Designed Perfusion Bioreactor for
Bone Tissue Engineering:
Flow Assessment and Optimal Culture Environmental Conditions

S. Yamada, MA. Yassin, T. Schwarz, K. Mustafa, J. Hansmann

II

Optimization and Validation of a Custom-Designed Perfusion Bioreactor for Bone Tissue Engineering: Flow Assessment and Optimal Culture Environmental Conditions

Shuntaro Yamada[1]*, Mohammed A. Yassin[1], Thomas Schwarz[2], Kamal Mustafa[1] and Jan Hansmann[2,3,4]*

[1]Centre of Translational Oral Research, Tissue Engineering Group, Department of Clinical Dentistry, University of Bergen, Bergen, Norway, [2]Translational Centre Regenerative Therapies, Fraunhofer Institute for Silicate Research ISC, Würzburg, Germany, [3]Chair of Tissue Engineering and Regenerative Medicine, University Hospital Würzburg, Würzburg, Germany, [4]Department Electrical Engineering, University of Applied Sciences Würzburg-Schweinfurt, Würzburg, Germany

Various perfusion bioreactor systems have been designed to improve cell culture with three-dimensional porous scaffolds, and there is some evidence that fluid force improves the osteogenic commitment of the progenitors. However, because of the unique design concept and operational configuration of each study, the experimental setups of perfusion bioreactor systems are not always compatible with other systems. To reconcile results from different systems, the thorough optimization and validation of experimental configuration are required in each system. In this study, optimal experimental conditions for a perfusion bioreactor were explored in three steps. First, an *in silico* modeling was performed using a scaffold geometry obtained by microCT and an expedient geometry parameterized with porosity and permeability to assess the accuracy of calculated fluid shear stress and computational time. Then, environmental factors for cell culture were optimized, including the volume of the medium, bubble suppression, and medium evaporation. Further, by combining the findings, it was possible to determine the optimal flow rate at which cell growth was supported while osteogenic differentiation was triggered. Here, we demonstrated that fluid shear stress up to 15 mPa was sufficient to induce osteogenesis, but cell growth was severely impacted by the volume of perfused medium, the presence of air bubbles, and medium evaporation, all of which are common concerns in perfusion bioreactor systems. This study emphasizes the necessity of optimization of experimental variables, which may often be underreported or overlooked, and indicates steps which can be taken to address issues common to perfusion bioreactors for bone tissue engineering.

Keywords: perfusion, bioreactor, dynamic cell culture, bone tissue engineering, regenerative medicine, mesenchymal stem cell, shear stress

INTRODUCTION

Critical sized bony defects have only a limited capacity for spontaneous healing. Repair requires extensive surgical intervention using autografts, allografts, xenografts or alloplastic materials (Roddy et al., 2018). However, none of the conventional clinical approaches has achieved the complete repair of native anatomy and function. Tissue engineering approaches, where multipotent cells are combined with scaffold biomaterials to regenerate bone, first emerged in the mid-1980s. Since then, there have been numerous *in vitro* and *in vivo* studies and by 2020, around 150 clinical trials of cell-based bone regenerative therapies had been registered by the U.S. National Library of Medicine (Amini et al., 2012). Mesenchymal stem/stromal cells (MCS) are among the most widely used sources for bone regeneration. MSC are abundantly available from various mesenchymal tissues such as bone marrow, adipose tissue, umbilical cord, and dental tissues (Marquez-Curtis et al., 2015). For scaffolding, three-dimensional (3D) porous scaffolds are preferred, as they mimic the structure of cancellous bone, stimulating MSC towards the osteogenic lineage (Zhang et al., 2018).

A major disadvantage of 3D scaffolds is the low passive diffusion-based mass transport of nutrients and gases, which leads to uneven cell growth within the scaffolds (Rouwkema et al., 2009). To overcome this disparity, various perfusion bioreactor systems have been developed specifically for bone regeneration (Rauh et al., 2011; Yeatts et al., 2013). Perfusion bioreactors provide uniform nutrient supply within the scaffolds while removing waste products, improving cell wellbeing (Rauh et al., 2011). Furthermore, attempts have been made to induce/promote osteogenesis by controlling the mechanical stimulus exerted by fluid flow (Gaspar et al., 2012). In fact, in recent years an increasing number of studies have reported the positive effect of fluid flow on MSC growth and osteogenesis. However, inconsistent results owing to system variation impede a clear understanding of biological responses to the stimuli. This is not only because experimental configuration such as bioreactor design and flow characteristics varies significantly among systems, but also because 3D dynamic cell culture involves various technical challenges which are not encountered in conventional cell culture protocols (Mandenius and Mandenius, 2016). Consequently, each system is to be operated under specific conditions. This is determined by a series of optimization steps: estimation of the magnitude of mechanical stimuli, conditioning of the culture environment and determination of the optimal flow rate for osteogenic differentiation. Nevertheless, environmental conditions applied in dynamic systems seem to be underreported. Indeed, a general caution has recently been issued, noting that a majority of cell culture studies omitted to monitor, control, or report environmental factors such as temperature, gas concentration and medium conditions (Klein et al., 2021).

The first step would be to estimate a promising flow rate by evaluating mechanical stimuli exerted by fluid flow. In the case where a porous geometry is assumed to be isotropic throughout the scaffold, shear stress can be corelated by the Kozeny-Carman

equation (Arramon and Nauman, 2001; Daish et al., 2017). However, the equation requires an empirical constant which depends on the geometry of pores, and it may not be suitable for anisotropic and multiphasic porous scaffolds (Truscello et al., 2012). The estimation of fluidics can be alternatively performed by *in silico* modeling, where the flow of culture medium is computationally reproduced in accordance with imported geometry and assigned parameters. In bone tissue engineering, using a scaffold with highly irregular pore geometry and distribution, the high computational cost is a barrier to precise simulation (Zhao et al., 2019). Ideally, a full scaffold geometry acquired by microcomputed tomography (microCT) should be used, but it may not always be feasible because of high computational demand (Jungreuthmayer et al., 2009; Acosta Santamaría et al., 2013). Alternatively, simplified geometry with porous parameters may be employed as a porous medium domain, despite lack of consensus as to its accuracy and predictive power (Campos Marin and Lacroix, 2015). The next step would be to optimize the culture environment. Optimization and validation of each environmental factor are required for successful operation. In conventional culture this may not be given close attention. For example, a perfusion bioreactor often requires a large volume of culture medium to establish continuous flow. The optimal amount depends on the number of vital cells on the scaffolds, and deficiency or excess may cause inhibition of cell growth and paracrine signaling (Schreivogel et al., 2019). Other environmental factors such as temperature, humidity, and static pressure alter MSC behavior, and this needs to be considered in designing systems. A stand-alone bioreactor, namely a bioreactor designed not to be used in a conventional incubator, often consists of complex electric appliances such as various sensors, heating system, gas ejectors, electric outlets and conductors in addition to pump systems (Schuerlein et al., 2017). The installation of these appliances is essential to condition the atmosphere, but highly humid environment is likely to be incompatible with such electrical systems (Rauh et al., 2011; Lane et al., 2014). A major technical challenge is the suppression of air bubble formation, which disturbs fluid flow and damages cells (Sobolewski et al., 2012; Walls et al., 2017; Walsh et al., 2017). Fluidic systems for bone tissue engineering tend to fulfil conditions for bubble formation: highly porous geometry, hydrophobic biomaterials, surfactant in the culture medium, and medium agitation (Sung and Shuler, 2009; Piola et al., 2013; Yu et al., 2017a; Yamada et al., 2021a). All these factors influence cell behavior, and therefore represent uncertainties if not addressed and correctly controlled. Once optimization is completed, the effect of fluid flow on cell behavior may be tested.

The successful operation of perfusion bioreactors for tissue engineering depends largely on the identification and validation of proper culture conditions. Unfortunately, despite an increasing number of studies on 3D dynamic cell culture in bone tissue engineering, comparison of study results is difficult, because each bioreactor system is operated with a unique experimental configuration. Nevertheless, most experimental issues which arise are common to all perfusion bioreactors.

To date, the literature in this field reveals the need for thorough optimization of experimental variables in a perfusion bioreactor. There is also a need to identify and address specific challenges which may arise in using a perfusion bioreactor for 3D dynamic culture. It is important that methods developed to address these issues are readily transferable for application in different bioreactors and can thus serve as general guidelines for designing and setting up flow bioreactor systems. The aim of this study was therefore to identify and optimize experimental variables in a laminar flow bioreactor with an integrated incubation system, by exploring basic cell culture conditions which can be adjusted towards stable dynamic cell culture. The study covers validation of the method applied to estimate fluid effects, the optimization of environmental factors such as medium volume, humidity control, air bubble suppression, and the identification of optimal flow rate. The study was based on rat bone marrow-derived mesenchymal stem/stromal cells (rBMSC), seeded onto 3D polymeric scaffolds for osteogenic differentiation.

MATERIALS AND METHODS

rBMSC Isolation and Expansion
The study was approved by the Norwegian Animal Research Authority (local approval number 20146866) and conducted in compliance with the European Convention for the Protection of Vertebrates used for Scientific Purposes.

rBMSC were isolated as previously described (Yassin et al., 2015). rBMSC from the femurs of Lewis rats were maintained in growth medium consisting of alpha minimum essential medium (α-MEM: 22571-020, Gibco™, United States) supplemented with 1% penicillin and streptomycin (SV30010, HyClone, United States) and 10% fetal bovine serum (FBS: 10270-106, Gibco™, United States) at 37°C in 5% CO_2 humidified atmosphere. The characterization of rBMSC including the expression of putative MSC markers and the ability of multi-lineage differentiation was previously described (Yamada et al., 2021a). rBMSC from the third to fifth passages were used in the study.

3D Porous Scaffold Preparation and Cell Seeding
3D microporous scaffolds (diameter 12 mm, thickness 1.2 mm) were produced by a solvent casting technique as previously described (Odelius et al., 2005; Yamada et al., 2021b). Briefly, a solution of Poly (L-lactide-co-trimethylene carbonate) (LTMC) (RESOMER. LT706 S, Evonik) in chloroform was mixed with sodium chloride (NaCl) particles with a diameter of 90–600 μM in Petri dishes and left with the lids on to allow gradual evaporation of the chloroform. After complete evaporation, the dried constructs were punched into 12 mm pieces and washed thoroughly in distilled water to remove the remaining NaCl particles. The scaffolds were then placed in 48-well plates and exposed to ultraviolet radiation for 2 h, following to washing with 70% ethanol for sterilization. Prior to cell seeding, the scaffolds were pre-wetted in the growth medium for 24 h.

250,000 rBMSC were seeded per scaffold and incubated for 72 h before being transferred into the culture chamber of the bioreactor.

MicroCT Scanning and Structural Analysis of the Porous Scaffolds
The microstructure of the scaffolds was scanned by microcomputed tomography (microCT) using a voltage of 40 kV and a current of 250 mA at 10 μm spatial resolution (SkyScan 1172: Bruker-MicroCT, Kontich, Belgium). The acquired geometry was exported in .stl file for further in silico modeling.

Configuration of the Laminar Flow Bioreactor
The laminar flow bioreactor was developed in the Fraunhofer Institute for Silicate Research. It comprises peristaltic pumps and an integrated incubator system, including a heating pad, electric fans, hydropressure sensors, a CO_2 sensor, and a temperature sensor (Figure 1A). The standard components for dynamic cell culture under perfusion are demonstrated in Figure 1B. The culture chamber, made of stainless steel, was designed to accommodate 3D scaffolds with a maximum diameter of 12 mm. The following sections present the experimental design in detail, including descriptions of specific settings (i.e., tubing, position of medium reservoir, scaffold placement). The perfusion experiment was conducted at 37°C in 5% CO_2 atmosphere.

In silico Modeling for Fluid Dynamics Simulation
In order to make the microCT data applicable in the simulation, a reference geometry was segmented from the .stl file, and a hypothetical whole-scaffold geometry was then reconstructed computationally, by assuming that the segmented geometry represented the microstructure of the scaffold. Precisely, the one fourth of the scanned geometry was repaired and then mirrored to reconstruct a disk-shaped geometry due to a substantial computational burden. Scanning defects such as self-intersections, paper-thin regions, too-narrow edges (i.e., edges smaller than defined minimum element size as mentioned below), and holes were repaired using computer-aided design (CAD) software, MeshLab ver. 2021.05 (Cignoni et al., 2008), Blender ver. 2.92 (Blender, 2021), and Rhino 7 (Robert McNeel & Associates, United States). In silico modeling was undertaken in the COMSOL Multiphysics version 5.6 (COMSOL AB, Sweden). Briefly, a simplified geometry was designed with a cylindrical disc with a diameter of 12 mm, which was defined as a porous domain. For the porous domain, porosity was measured by microCT analysis, and permeability was obtained as described previously by measuring pressure drop over cylindrical scaffolds and applying the Darcy's law (Ramani-Mohan et al., 2018). The microCT geometry was imported as a solid object. A domain comprising a stack of six scaffolds was then placed in a cylindrical
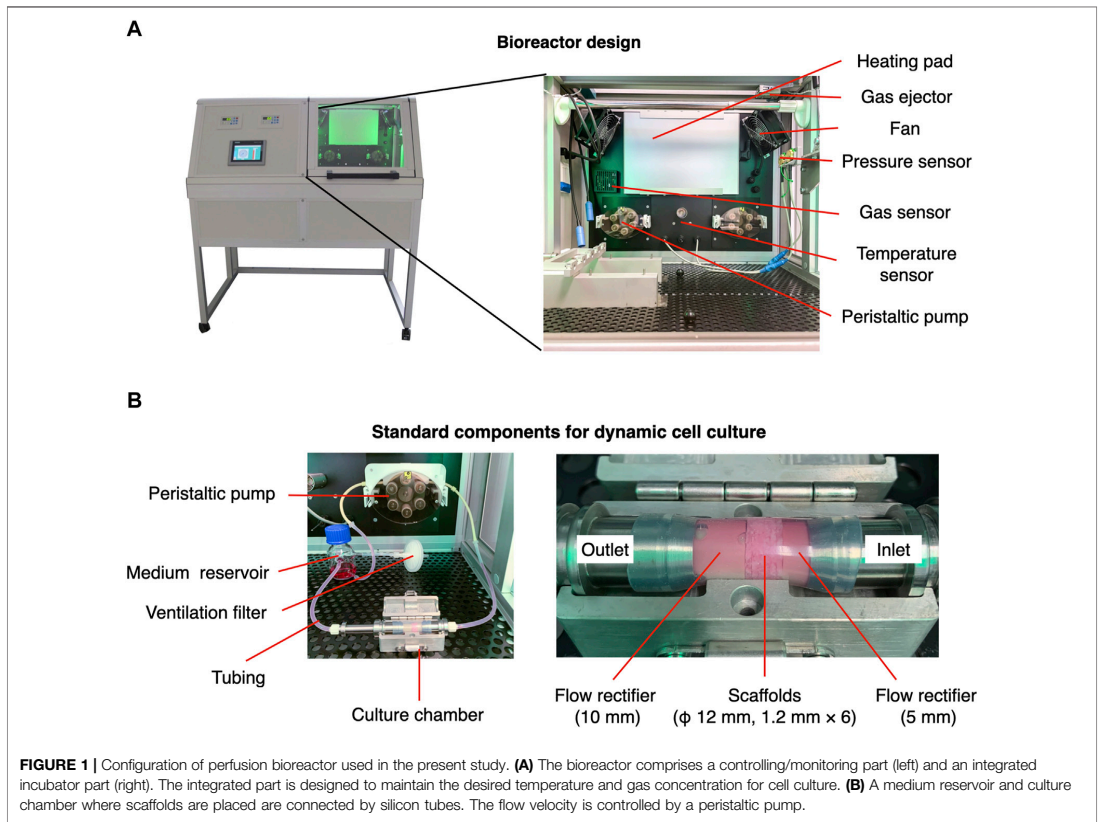
FIGURE 1 | Configuration of perfusion bioreactor used in the present study. **(A)** The bioreactor comprises a controlling/monitoring part (left) and an integrated incubator part (right). The integrated part is designed to maintain the desired temperature and gas concentration for cell culture. **(B)** A medium reservoir and culture chamber where scaffolds are placed are connected by silicon tubes. The flow velocity is controlled by a peristaltic pump.

fluid path with a diameter of 12.5 mm, where fully developed flow at either 0.8, 1.6, or 3.2 ml/min was prescribed. It was assumed that fluid flow within scaffolds could be laminar flow because of extremely low flow velocity. Assigned fluid was defined as incompressible Newtonian fluid with the viscosity of water at 37°C (i.e., 0.6913 mPa·s) and density 997 kg/m³. Non-slip boundary conditions were enforced at the solid walls. For computation, the geometries were then meshed into linier tetrahedron elements using a physics-controlled mesh module with prescribed mesh resolution "Finer" where the maximum element size, minimum element size, maximum element growth rate, curvature factor, and resolution of narrow regions were defined as 0.429 mm, 0.0464 mm, 1.1, 0.4, 0.9, respectively. Finally, computation was performed by the stationary solver.

A laminar flow was defined by the Navier-Stokes equation as follows:

$$\rho\,(u.\nabla)u = \nabla.[-pI + K] + F$$
$$\rho\,\nabla.u = 0$$
$$K = \mu\left(\nabla u + (\nabla u)^T\right)$$

where ρ, u, I, p, μ, and F, denote fluid density, fluid velocity, identity vector, pressure, dynamic viscosity, and volume force. For the porous domain used in the simplified geometry, the Darcy flow model was used with Darcy-Brinkman equation as follows:

$$\frac{1}{\varepsilon_P}\rho\,(u2.\nabla)u\,\frac{1}{\varepsilon_P} = \nabla.\left[-pI + K\right] - \left(\mu\kappa^{-1} + \frac{Q_m}{\varepsilon_P^2}\right)u + F$$
$$\rho\,\nabla.u = Qm$$
$$K = \mu\frac{1}{\varepsilon_P}\left(\nabla u + (\nabla u)^T\right) - \frac{2}{3}\mu\frac{1}{\varepsilon_P}(\nabla.u)I$$
$$F = 0,\; Qm = 0$$

where ε_p, κ, and Qm denote porosity, permeability, and mass souse. The effect of gravity was not included for simplification. It was modeled by assuming zero mass source and zero volume force due to low fluid viscosity and Reynolds number below 1 (data not shown). Shear stress τ was then computed as previously described using the equation (Egger et al., 2017):

$$\tau = \mu\frac{\partial\mu}{\partial n}$$

where n indicates the x-, y-, and z-direction. Shear stress was presented using volume and surface area in the simplified and in the microCT approach, respectively.

Quantification of Double Strand DNA

Samples were collected in 0.1% Triton X-100, and the cell lysate was obtained by three freeze-thaw cycles. Double strand DNA (dsDNA) was quantified using Quant-iT™ PicoGreen™ dsDNA Assay Kit (P7589, Thermo Fisher Scientific, United States) in accordance with the manufacturer's protocol. The fluorescence intensity was measured at Ex/Em = 480/520 nm using a microplate reader (VLBL00D0, ThermoFisher Scientific, Finland).

Quantification of Alkaline Phosphatase Activity

The cell lysate, which was obtained by freeze-thaw cycles, was incubated with P-nitrophenyl phosphate (20-106, Sigma-Aldrich, Germany) for 15 min at room temperature. Absorbance was measured at 405 nm using the microplate reader. ALP activity was normalized by the amount of dsDNA in the samples.

Immunofluorescent Staining and Confocal Microscopy

Samples were fixed in 4% paraformaldehyde (PFA) for 15 min at room temperature and permeabilize in 0.1% Triton X-100 in PBS (PBSTx) for 15 min at room temperature. Nonspecific binding was blocked with 20% goat serum (G6767, Sigma, United States) in 0.1% Tween-20 in PBS (PBSTw) for 60 min at room temperature. The samples were then incubated with anti-Ki67 monoclonal antibody conjugated with eFluor 660 (50-5698-82, Thermo Fisher Scientific, United States) overnight at 4˚C. Filamentous actin (F-actin) and nuclei were counterstained with Phalloidin Alexa Fluor 488 (1:250; A12379, Thermo Fisher Scientific, United States) and $4',6$-diamidino-2-phenylindole (DAPI, 1:5000; 62247, Thermo Fisher Scientific, United States) for 60 min at room temperature, followed by washing five times, for 5 min each, with PBSTw. The samples were mounted in ProLong™ Gold antifade reagent (P36939; Thermo Fisher Scientific, United States). Z-Stack images were acquired by confocal microscopy (TCS SP8; Leica, Germany) and the multichannel images were processed with Fiji/ImageJ (Schindelin et al., 2012). All images in the study were presented as maximum projection z-stack images of 100 μm thickness.

Live/Dead Staining

For Live/Dead staining, a Live/Dead Cell Viability Kit was used in accordance with the manufacturer's protocol. Briefly, the samples were washed with Dulbecco's phosphate-buffered saline (DPBS; 14190-144, Gibco™, United States) 3 times and incubated with 2 μM calcein AM and 4 μM Ethidium homodimer-1 for 30 min at room temperature. The samples were then visualized by confocal microscopy.

Reverse Transcription Quantitative Polymerase Chain Reaction

Samples for gene expression assay were snap-frozen in liquid nitrogen and stored at −80˚C. Total RNA was extracted using a Maxwell® 16 Cell LEV Total RNA Purification Kit (AS1280; Promega, United States) in accordance with the manufacturer's protocol. Reverse transcription was then undertaken using a High-Capacity cDNA reverse Transcription Kit (4368814; Applied Biosystems, United States). RT-qPCR was performed with the StepOne™ real-time PCR system (4376357, Applied Biosystems, United States) with TaqMan™ Gene Expression Assay (4331182, Thermo Fisher Scientific, United States). The primers used were Runt-related transcription factor 2 (RUNX2, Rn01512298_m1, Thermo Fisher Scientific, United States), Osterix (Rn01761789 m1, Thermo Fisher Scientific, United States), and Glyceraldehyde-3-phosphate dehydrogenase (GAPDH, Rn01749022 g, Thermo Fisher Scientific, United States). The amplification was performed as follows: initial denaturation at 95˚C for 20 s followed by 40 cycles at 95˚C for 1 s and 60˚C for 20 s. Relative gene expression was calculated by the ΔΔCt method, normalized by the endogenous control, GAPDH (Livak and Schmittgen, 2001). The data are presented as a mean value ± standard error (s.e.m) of three replicates.

Alizarin Red S Staining and Quantification

Samples were fixed in 4% PFA for 40 min and washed three times in Milli-Q® water. The samples were then incubated with 0.1% Alizarin Red S staining (A5533; Sigma-Aldrich, United States) for 20 min at room temperature, followed by thorough washing with Milli-Q® water. For quantification, the dye was extracted in 100 mM cetylpyridium chloride overnight at room temperature. Absorbance was measured at 540 nm using the microplate reader.

Evaluation of the Effect of Growth Medium Volume on Cell Growth

To evaluate the effect of medium volume on cell growth on a 2D mono-surface and the 3D porous scaffolds, cell growth was evaluated in different volumes of growth medium. For 2D experiments, rBMSC were seeded into wells of 12-well plates at the standard initial seeding density of 5,000 cells/cm². For testing, the cells were separated into three different groups, according to the volume of growth medium: 0.76 ml, the lowest limit of the manufacturer's recommendation, 1.52 ml, and 3.04 ml, which corresponded to 0.04 μl/cell, 0.08 μl/cells, and 0.16 μl/cells, respectively, at the time of seeding. After 3 and 7 days of incubation at 37˚C in 5% CO_2 humidified atmosphere, the cells were trypsinised, stained with 0.4% Trypan Blue (T10282, Thermo Fisher Scientific, United States), and analyzed by the Countess 2 Automated Cell Counter (Thermo Fisher Scientifics, United States). Likewise, the optimal ratio of cell-to-medium volumes was evaluated on the 3D scaffolds where 250,000 cells were seeded.

According to a previous report, the seeding efficiency was estimated to be 50% (Yamada et al., 2021b), and therefore, 125,000 cells were considered to have attached to the scaffold initially. Five scaffolds, corresponding to 625,000 cells, were then incubated with the growth medium at medium-to-cell ratios of either 0.04 μl/cell (i.e., 25 ml), 0.08 μl/cell (i.e., 50 ml), or 0.16 μl/cell (i.e., 100 ml) at 37°C in 5% CO_2 humidified atmosphere. The medium was refreshed every 72 h. Cell growth was analyzed on days 3 and 7 by quantification of dsDNA.

Evaluation of the Effect of Humidification on Cell Growth and Viability

To measure medium evaporation during perfusion in the bioreactor, 25 ml of the growth medium was perfused at 0.8 ml/min, 5 ml/min and 10 ml/min at 37°C in 5% CO_2 environment. During perfusion, the ventilation filter was subjected to either environmental humidity, or humidity enhanced by a water bath (open humidification), or an additional water flask connected to the medium reservoir through a ventilation filter (closed humidification). Gas exchange took place through a ventilation filter attached on the medium reservoir and on the water flask for humidification in the open and closed configuration, respectively. As a control, 25 ml medium was placed statically. Glucose concentration was calculated based on the original concentration and the volume loss of the growth medium. Using growth medium perfused at 10 ml/min for 72 h with and without humidification, rBMSC were incubated at 37°C in 5% CO_2 humidified atmosphere for a further 72 h in 12-well plates at an initial seeding density of 5,000 cells/cm^2, or on the scaffolds. Cell growth and viability on the mono-surface were assessed by the Countess 2 Automated Cell Counter (Thermo Fisher Scientifics, United States) and on the scaffolds by Live/Dead staining.

Evaluation of the Effect of Air Bubbles on Cell Growth and Osteogenic Properties

A dynamic culture system was established by connecting silicon tubes through the medium reservoir, the peristaltic pump, and the culture chamber where six scaffolds with rBMSC were placed. 25 ml of the growth medium was perfused at 0.8 ml/min (i.e., 3 rpm in the system) at 37°C in 5% CO_2 environment. The medium was refreshed every 72 h. The medium reservoir was either placed at the same level as the culture chamber or approximately 30 cm higher than the chamber, to apply an additional 20 mmHg hydrostatic pressure. After 3 days of perfusion culture, cell growth was evaluated by immunofluorescence with a proliferation marker, Ki67, and quantification of dsDNA.

Evaluation of Differential Flow Rate and Osteogenic Differentiation

To determine the optimal flow rate for cell growth and osteogenic induction, multiple flow rates were compared. Using the previously determined optimal conditions, the bioreactor was humidified by a water bath and 20 mmHg hydrostatic pressure was applied to the culture chamber. Six scaffolds with rBMSC were placed in the culture chamber, and 25 ml of the growth medium was perfused at 0.8 ml/min (i.e., 3 rpm), 1.6 ml/min (i.e., 6 rpm), or 3.2 ml/min (12 rpm) for 8 h or 24 h per day at 37°C, 5% CO_2 in a humidified environment. After 7 days of perfusion culture, cell morphology was assessed by immunofluorescence staining. Further analysis was performed on 0.8 ml/min perfusion for 8 h a day. Cell distribution in the first, third, and sixth scaffolds from the inlet was visualized by 0.5% Crystal Violet on day 7. Osteogenic differentiation was assessed by RT-qPCR, Alizarin Red S staining and ALP activity compared to the static culture conditions.

Statistics

All data are represented as mean ± standard error of mean (SEM) unless stated otherwise (sample size: $n = 5$, except for RT-qPCR $n = 3$). Statistical analysis was performed using SPSS Statistics version 25 (IBM, United States). For pairwise comparison of 2 groups, data were evaluated by Student's t-test. For multiple comparison, data were evaluated by one-way ANOVA followed by Bonferroni's multiple comparison test. A p value <0.05 was considered statistically significant.

RESULTS

Simplified yet Parameterized Geometry as a Substitute for High-Resolution Geometry Obtained From microCT

Usually, the magnitude of flow effect on cells is expressed as fluid shear stress. Fluid dynamics simulation was therefore undertaken to estimate shear stress exerted on the scaffold surfaces (i.e., the cells on the scaffold). Conventionally, a simplified geometry parameterized with porosity and permeability is adopted to reduce the computational burden. Therefore, the present study compared such a methodology and whole scaffold geometry, obtained by microCT, to validate predictive power and computational cost (**Figure 2A**). Despite the same predefined mesh resolution, minimum element size in microCT geometry was notably smaller, and the number of elements comprising the geometry reached nearly one hundred million, while the simplified geometry comprised fewer than 600,000 elements (**Figure 2B**; **Table 1**). This resulted in significantly longer free meshing time in the microCT geometry. Likewise, the enormous number of degrees of freedom solved for accounted for substantially longer computation time in the microCT geometry. Both models confirmed that fluid permeated the scaffold domains and showed comparable velocity fields (mean velocity: simplified, 0.15 mm/s; microCT, 0.12 mm/s). Highest flow velocity was estimated along with the wall of fluid column in the microCT model (**Figure 2C**). This tendency was correlated with the higher shear stress at the peripheral than at the core

parts (**Figure 2D**). In the simplified model, the magnitude of shear stress was more averaged within the scaffold domain. However, the microCT geometry tended to fluctuate more and this was assumed to be due to its geometrical specificity. The estimated values of shear stress varied between the models: the mean and maximum value of shear stress were 0.70 and 3.00 mPa in the simplified geometry and 0.87 and 10.28 mPa in the microCT geometry, respectively (**Figure 2E**). Despite the difference between the approaches, the frequent distribution of the magnitude of shear stress showed similar trend, converging into the range below 5 mPa (**Figure 2F**). This suggests that appropriately parameterized geometry may be used to calculate shear stress in an averaged manner but not be suitable for the evaluation of spatial characteristics.

Optimization of Medium Volume Required for Optimal Cell Growth in 2D and 3D Culture

The necessary and sufficient volume of culture medium allows cells to elicit their active kinetics from a paracrine effect while diluting waste products. In most studies, a medium-to-cell ratio is not well described and not standardized. To determine the optimal volume of culture medium for the bioreactor system, rBMSC were cultured for 7 days in different volumes of culture medium, on 2D mono-surfaces and on 3D porous scaffolds (**Figure 3A**). On the 2D surface, rBMSC maintained high viability of approximately 98% on days 3 and 7, regardless of medium volume (**Figure 3B**). Cell density on day 3 was slightly lower in the 0.16 μl/cell group, but there was no statistical significance (**Figure 3C**). On day 7, cell density increased as
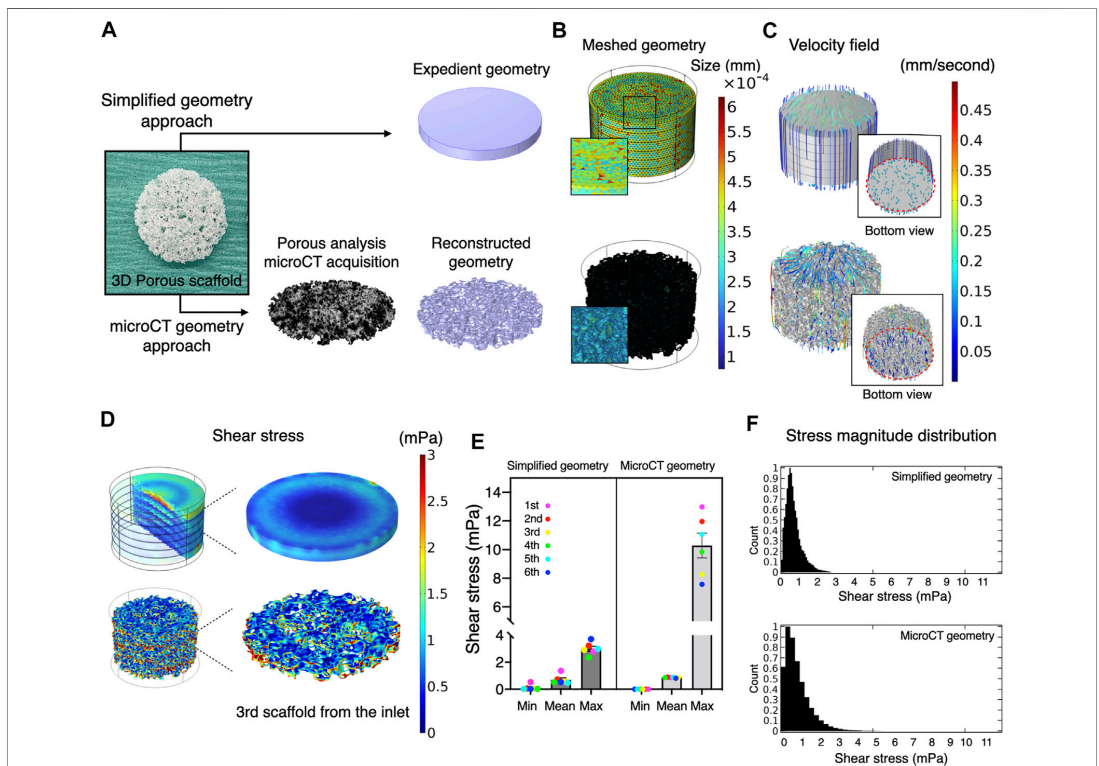
FIGURE 2 | Comparative validation of different modeling methods in fluid dynamics simulation. **(A)** A three-dimensional porous scaffold was modeled by different methods. For the simplified geometry approach, the scaffold was assigned as a porous domain parameterized with porosity and permeability. For the microCT geometry approach, an acellular scaffold was scanned by microCT, and the geometry was imported as a .stl file in CAD software. **(B)** The reconstructed geometry was then meshed for computation. The element size of simplified geometry was significantly smaller than that of the microCT geometry. **(C)** At a flow rate of 0.8 ml/minutes, medium permeated uniformly inside the scaffolds at flow velocities ranging from nearly 0 to 0.5 mm/second in both models. **(D)** Estimated magnitude of shear stress was more patterned in the expedient geometry than in the microCT geometry. The microCT geometry offered more locally specific variation. **(E)** Estimated mean and minimum but not maximum shear stress in the simplified approach was compatible with the microCT approach. **(F)** The distribution of shear stress magnitude shows monophasic peak around 0.5–1 mPa both in the simplified and microCT approaches.

TABLE 1 | Parameters for meshing and computation in the *in silico* modeling.

	Simplified geometry	microCT geometry
Meshing		
Predefined mesh resolution		Finer
Minimum element size (mm)		0.0464
Maximum element size (mm)		0.429
Maximum element growth rate		1.1
Curvature factor		0.4
Resolution of narrow regions		0.9
Actual mesh resolution		
Minimum element size (mm)	0.072428	0.013097
Maximum element size (mm)	0.4242	0.2669
Number of element	569570	83848571
Free meshing time	31 s	1 h 30 min 1 s
Computation		
Degrees of freedom solved for	203209	45218141
Computation time	1 min 52 s	28 h 15 min 54 s
RAM/Processor used	32 GB RAM 2.9 GHz 6 core Intel Core i9	

FIGURE 3 | Growth of rBMSC in culture medium at different medium-to-cell ratios. **(A)** Medium-to-cell ratios of 0.04, 0.08, and 0.16 μm/cell at the point of seeding were tested on 2D mono-surface and 3D porous scaffolds. **(B)** Cells seeded on the mono-surface maintained high viability regardless of medium-to-cell ratio. **(C)** On the mono-surface, cell growth was enhanced at a medium-to-cell ratio of 0.04 μl/cell compared to 0.08 and 0.16 μl/cell on day 3, but the tendency was reversed on day 7 when the cell density approached confluence. **(D)** On 3D porous scaffolds, quantification of double-strand DNA (dsDNA) indicated that the medium ratio of 0.04 μl/cell yielded the highest dsDNA on day 3, but medium ratios of 0.08 and 0.16 μl/cell yielded higher dsDNA on day 7. *$p < 0.05$, ***$p < 0.001$.

FIGURE 4 | Effect of culture medium loss during perfusion and humidification. **(A)** Operational configuration for the evaluation of medium loss and humidification. **(B)** Illustration of the experimental flow. Culture medium, which was perfused with and without humidification for 72 h, was collected and transferred into cell culture plates where growth of rBMSC on 2D mono-surface and 3D porous scaffolds was observed. **(C)** Evaporation of culture medium occurred in a velocity dependent manner. Humidification with a water bath and a water flask connection effectively prevented evaporation. **(D)** Medium evaporation led to the condensation of medium components (e.g., glucose), disrupting osmotic balance. **(E,F)** On the 2D mono-surface, cell viability and growth of rBMSC incubated in the perfused medium without humidification deteriorated significantly. **(G–I)** Fluorescence images of Live/Dead staining showed that rBMSC incubated in the perfused medium without humidification significantly increased the ratio of dead cells, resulting in low cell density and viability on 3D porous scaffolds. $*p < 0.05$, $**p < 0.01$, $***p < 0.001$, $****p < 0.0001$.

the medium volume increased, and accelerated cell growth was observed in the 0.08 and 0.16 µl/cell groups (0.04 µl/cell vs. 0.16 µl/cell, $p = 0.00002$; 0.08 µl/cell vs. 0.16 µl/cell, $p = 0.012$). A similar tendency, although not statistically significant, was found in the 3D porous scaffolds (**Figure 3D**). The lowest medium volume seemed advantageous for initial cell growth by day 3, but the higher medium-to-cell ratios promoted cell proliferation by day 7, when the cells were nearly confluent on the scaffold.

Minimizing Medium Evaporation During Perfusion Improved Cell Growth and Viability

For optimal cell growth, gas exchange is required. Therefore, although perfusion systems are mostly "closed" by tubing, the medium has contact with the atmosphere through ventilation filters, where evaporation takes place. Ideally, the atmosphere needs to be humidified, but most electronic devices such as pumps and sensors are incompatible with high humidity. Therefore, the impact of non-humidified conditions as well as different humidification methods on cell kinetics was evaluated during dynamic culture. Firstly, loss of medium was measured in the bioreactor system during perfusion at different flow rates, with and without humidification, and then the cellular response to perfused medium under such conditions was evaluated (**Figures 4A,B**). It was confirmed that without humidification nearly 10% of the growth medium evaporated within the first 24 h of perfusion and an amount of medium loss was positively associated with flow rate (**Figure 4C**). Humidification significantly suppressed evaporation. Notably, using a water bath as the conventional method (open humidification) and connection of water-containing flasks to the ventilation filter on the medium reservoir (closed humidification) reduced evaporation equivalently. Medium evaporation theoretically led to condensation, resulting in elevated content concentration including a glucose level as represented (static vs. open/closed humidification, $p < 0.0001$) (**Figure 4D**). rBMSC were then incubated under standard culture conditions (i.e., 95% relative humidity, 37°C, 5% CO_2) in the growth medium, which was perfused at 10 ml/min for 72 h (either with or without humidification) on the 2D surface and the 3D porous scaffolds. On the 2D surface, cell viability was significantly affected in the condensed medium, declining by approximately 20% compared to the humidified environment (without vs. with open/closed humidification, $p < 0.0001$) (**Figure 4E**). Similarly, cell growth deteriorated in medium perfused without humidification (without vs. with open humidification, $p = 0.0019$; without vs. with closed humidification, $p = 0.00086$) (**Figure 4F**). On the 3D scaffolds, Live/Dead staining showed that open as well as closed humidification effectively supported cell growth while the condensed medium led to reduced cell growth (without vs. with open humidification, $p = 0.0041$; without vs. with closed humidification, $p = 0.029$) and viability
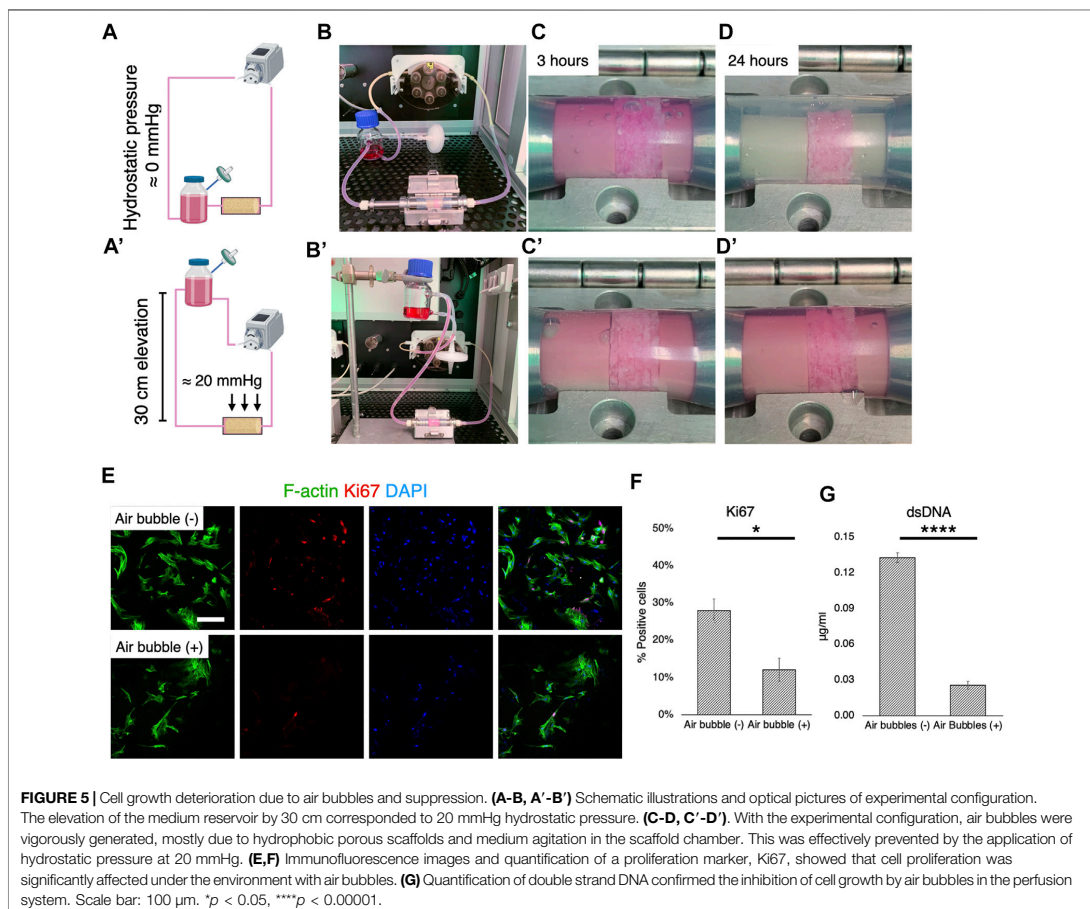
(without vs. with open humidification, $p = 0.025$; without vs. with closed humidification, $p = 0.011$) (**Figures 4G–I**).

Suppression of Air Bubbles During Perfusion is a Determinant of Cell Growth and Osteogenic Properties

The formation of air bubbles is an acknowledged problem in perfusion systems (Lochovsky et al., 2012; Kang et al., 2014), and the system used in this study was no exception. Therefore, according to Henry's law, suppression of air bubble formation was attempted by controlling static pressure (**Figures 5A,A′**). When the medium reservoir was placed at the same level as the culture chamber, air bubbles were generated rapidly within 3 h of perfusion (**Figures 5B,C**). After 24 h of perfusion, airspace dominated in the chamber, with the surfaces of fluid paths mostly dried, although the medium permeated the scaffolds with the help of capillary action (**Figure 5D**). When the reservoir was vertically positioned 30 cm higher than the culture chamber, however, the growth medium filled the chamber space (**Figures 5B′–D′**). This corresponded to a hydrostatic pressure of approximately 20 mmHg. In the environment where air bubbles were formed, the cells appeared to be less elongated and scattered and the expression of a proliferation marker, Ki67, was significantly downregulated (**Figure 5E**). Quantification revealed that approximately 30% of rBMSC were proliferative without air bubbles, while only 12% of the population expressed Ki67 (**Figure 5F**) ($p = 0.041$). The quantification of dsDNA confirmed the adverse effect of air bubble formation on cell growth, significantly suppressing cell proliferation ($p < 0.0001$) (**Figure 5G**).

Optimal Flow Rate Triggers Osteogenic Differentiation of rBMSC

MSC are exquisitely sensitive to mechano-environmental factors. The response varies, depending on the magnitude and duration of fluid stimulation (Maul et al., 2011; Lane et al., 2014). Initially, several flow rates and perfusion time were tested, to determine conditions at which cell growth was optimal: 25 ml of the growth medium was perfused under humidification by a water bath in the bioreactor, wherein 20 mmHg hydrostatic pressure was applied to the culture chamber (**Figure 6A**). Flow rates of 0.8 ml/min, 1.6 ml/min, and 3.2 ml/min were compared, corresponding to shear stress ranging from nearly 0 to 13.1 mPa (mean 0.88 mPa, mode value 0.5–1 mPa) to 26.2 mPa (mean 1.76 mPa, mode value 1.0–1.5 mPa), and to 52.6 mPa (mean 3.51 mPa, mode value 2–3 mPa), respectively, as estimated by the *in silico* modeling (**Figure 6B**). Perfusion for 8 h a day at 0.8 ml/min and 1.6 ml/min supported cell growth while 3.2 ml/min caused fragmentation of cytoskeletal structures (**Figure 6C**). However, perfusion for 24 h was found to suppress cell growth and in particular, perfusion at 1.6 ml/min induced cell damage and apoptotic response. These experiments disclosed that in the present system, perfusion for 8 h at 0.8 ml/min (mean 0.88 mPa, mode value 0.5–1 mPa) provided optimal fluidic stimulus. At the flow magnitude, no noticeable differences in cell distribution were

FIGURE 5 | Cell growth deterioration due to air bubbles and suppression. **(A-B, A′-B′)** Schematic illustrations and optical pictures of experimental configuration. The elevation of the medium reservoir by 30 cm corresponded to 20 mmHg hydrostatic pressure. **(C-D, C′-D′)**. With the experimental configuration, air bubbles were vigorously generated, mostly due to hydrophobic porous scaffolds and medium agitation in the scaffold chamber. This was effectively prevented by the application of hydrostatic pressure at 20 mmHg. **(E,F)** Immunofluorescence images and quantification of a proliferation marker, Ki67, showed that cell proliferation was significantly affected under the environment with air bubbles. **(G)** Quantification of double strand DNA confirmed the inhibition of cell growth by air bubbles in the perfusion system. Scale bar: 100 μm. *$p < 0.05$, ****$p < 0.00001$.

observed among the first, third, and sixth scaffolds from the inlet, which is consistent with the observation by the computational model (**Figure 7A**). rBMSC subjected to the fluid flow upregulated the key osteogenic transcription factors, RUNX2 and Osterix, on days 7 and 14, while under static conditions the cells gradually lost the osteogenic property (RUNX2, $p = 0.23$; Osterix, $p = 0.032$ on day 7; RUNX2, $p = 0.049$; Osterix, $p = 0.007$ on day 14) (**Figure 7B**). Alizarin Red S staining confirmed that perfusion culture of rBMSC resulted in calcium deposition, (**Figure 7C**), which became more pronounced over time ($p = 0.034$ on day 21) (**Figure D**). This was accompanied by an increase in ALP activity ($p = 0.019$ on day 3; $p = 0.032$ on day 7; $p < 0.0001$ on days 14 and 21) (**Figure 7E**).

DISCUSSION

The application of dynamic cell culture shows promise in bone tissue engineering, in which a 3D porous scaffold is a critical component of successful bone regeneration (Gaspar et al., 2012). This is mainly because medium flow homogenizes gas and nutrient concentrations within the scaffolds while removing waste products, preventing the cells in the core part of the structure from succumbing to deprivation of gases and nutrients (Bergemann et al., 2015). Moreover, previous studies on 2D systems have reported that MSC are mechanosensitive, and appropriate fluidic shear stress may direct them towards the osteogenic lineage (Holtorf et al., 2005; Yourek et al., 2010; Kim et al., 2014; Becquart et al., 2016; Stavenschi et al., 2017; Tsai et al., 2019; Dash et al., 2020). With reference to clinical translation, a number of perfusion bioreactor systems have been developed and tested using 3D porous scaffolds (Livak and Schmittgen, 2001; Yourek et al., 2010; Maul et al., 2011; Kang et al., 2014; Kim et al., 2014; Lane et al., 2014; Bergemann et al., 2015; Becquart et al., 2016; Dash et al., 2020). However, due to the complexity of the 3D culture system, each of the systems has unique features and applies original experimental configurations. The conclusions
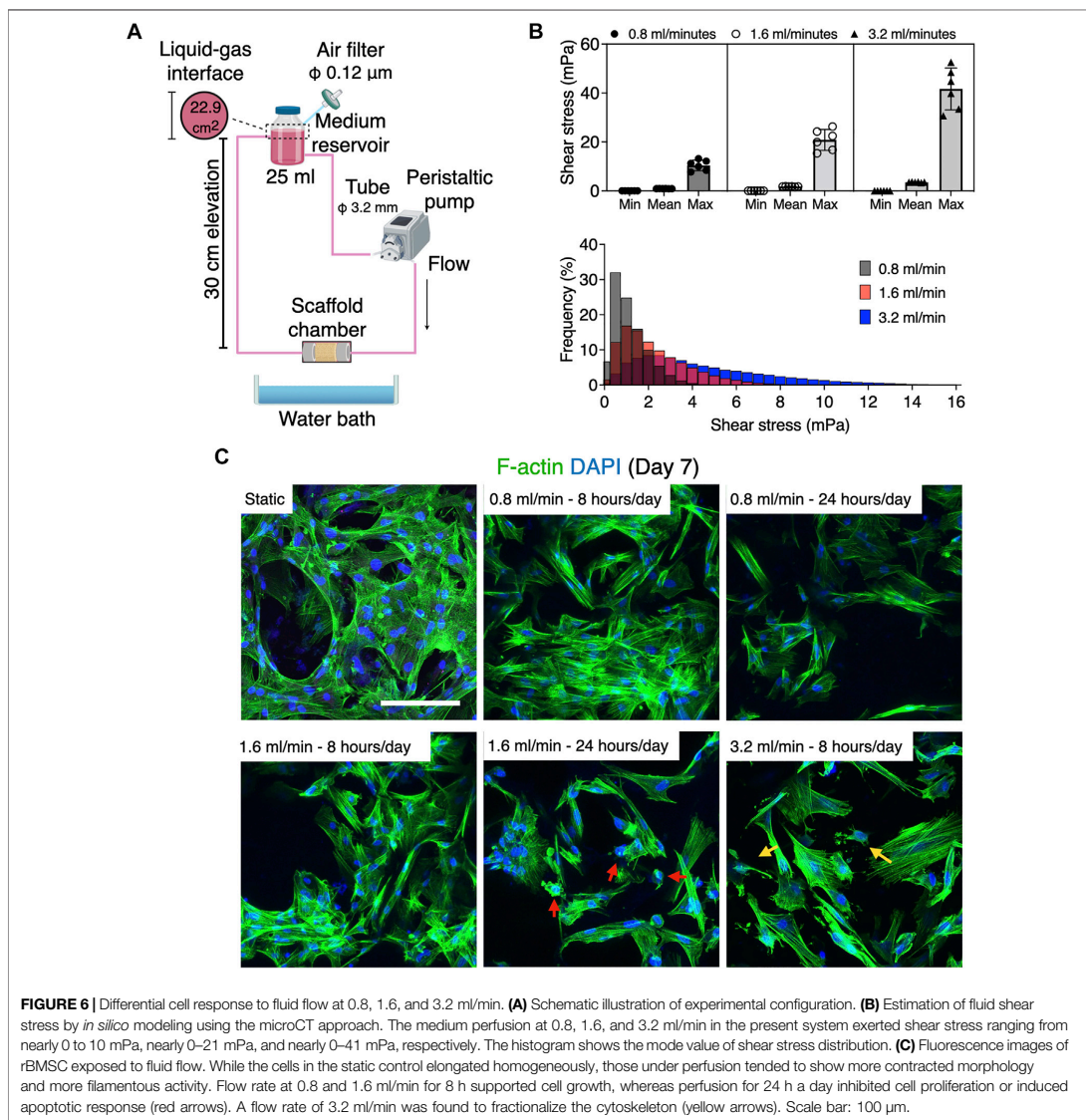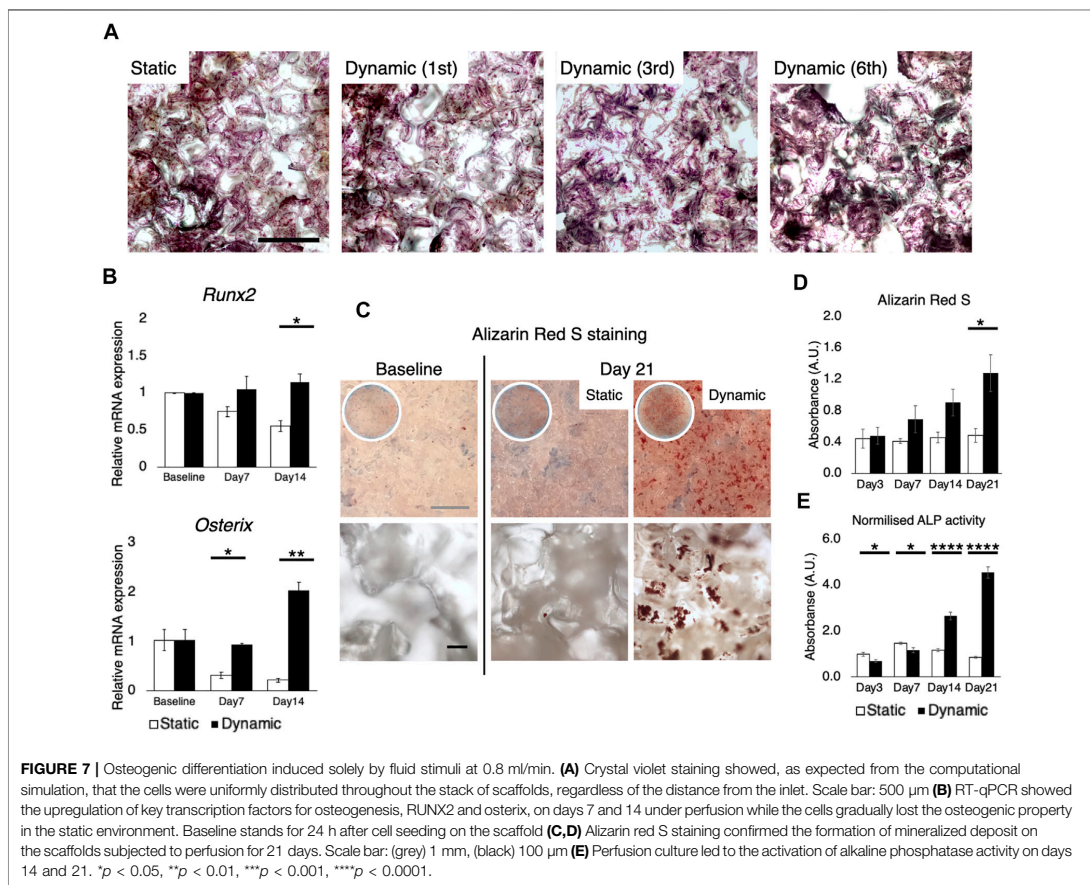
FIGURE 6 | Differential cell response to fluid flow at 0.8, 1.6, and 3.2 ml/min. **(A)** Schematic illustration of experimental configuration. **(B)** Estimation of fluid shear stress by *in silico* modeling using the microCT approach. The medium perfusion at 0.8, 1.6, and 3.2 ml/min in the present system exerted shear stress ranging from nearly 0 to 10 mPa, nearly 0–21 mPa, and nearly 0–41 mPa, respectively. The histogram shows the mode value of shear stress distribution. **(C)** Fluorescence images of rBMSC exposed to fluid flow. While the cells in the static control elongated homogeneously, those under perfusion tended to show more contracted morphology and more filamentous activity. Flow rate at 0.8 and 1.6 ml/min for 8 h supported cell growth, whereas perfusion for 24 h a day inhibited cell proliferation or induced apoptotic response (red arrows). A flow rate of 3.2 ml/min was found to fractionalize the cytoskeleton (yellow arrows). Scale bar: 100 μm.

drawn from various studies are therefore inconsistent and sometimes contradictory. This hinders cross-study comparison of different systems and the development of further optimized systems. Therefore, the aim of the present study was to identify and validate inconsistencies, mainly associated with environmental variables and then to optimize experimental configuration in the perfusion bioreactor system for bone tissue engineering.

Cell response to fluidic stimuli differs according to the magnitude of shear stress exerted by fluid in motion (Yeatts

and Fisher, 2011). Despite the wide application of flow rate (e.g., ml/minute) or pump speed (e.g., rpm) as parameters to describe the characteristics of fluid stimuli, neither represents the magnitude of flow to which the cells respond or can be used to compare the results of different bioreactor systems unless the flow rate/pump speed is correlated with the magnitude of fluid force to the cells by mathematical models or computational simulation (Sladkova and de Peppo, 2014). To reduce uncertainty when comparing study results, the accurate estimation of fluid shear stress serves as a common

FIGURE 7 | Osteogenic differentiation induced solely by fluid stimuli at 0.8 ml/min. **(A)** Crystal violet staining showed, as expected from the computational simulation, that the cells were uniformly distributed throughout the stack of scaffolds, regardless of the distance from the inlet. Scale bar: 500 μm **(B)** RT-qPCR showed the upregulation of key transcription factors for osteogenesis, RUNX2 and osterix, on days 7 and 14 under perfusion while the cells gradually lost the osteogenic property in the static environment. Baseline stands for 24 h after cell seeding on the scaffold **(C,D)** Alizarin red s staining confirmed the formation of mineralized deposit on the scaffolds subjected to perfusion for 21 days. Scale bar: (grey) 1 mm, (black) 100 μm **(E)** Perfusion culture led to the activation of alkaline phosphatase activity on days 14 and 21. $^*p < 0.05$, $^{**}p < 0.01$, $^{***}p < 0.001$, $^{****}p < 0.0001$.

reference point. The magnitude of shear stress is determined by local velocity. In contrast to 2D experimental settings, where fluid motion is limited to the X-Y direction, evaluation of fluid shear stress in 3D bioreactor systems presents a major challenge. This is attributable primarily to the geometry of porous scaffolds, in which local velocity varies from one point to another and possibly from moment to moment. Conventionally, the mathematical model applying Kozeny-Carman equation has been used to analyze shear stress within a homogeneous porous domain (Podichetty and Madihally, 2014). For the analysis of spatial shear stress distribution, an *in silico* modeling is a powerful alternative for studying microfluidics in such a complex environment. It allows fluid to be virtually traced within a given geometry and fluid dynamics to be computed. The tool has been applied in some tissue engineering studies, to examine microfluidics in bioreactor systems (Geris et al., 2016). In most cases, *in silico* modeling was performed using a simplified geometry (e.g., a cylinder), idealized by parameterization to reduce the computational burden (Zhao et al., 2019; Ramani-Mohan et al., 2018; Egger et al., 2017; Nokhbatolfoghahaei et al., 2020; Pereira et al., 2021; Melke et al., 2020). Parameterization with porosity and permeability allows the geometry to be considered as a porous domain to which Darcy flow model may be applied. This approach could be used even if a scaffold consists of several domains as long as each domain possesses a homogeneous structure. Alternatively, a CAD geometry in the case of, e.g., 3D printed scaffolds, or a geometry acquired by microCT may be used as more accurate methods where Navier-Stokes equation may be applied by assuming that a liquid property is defined as an incompressible Newtonian fluid (**Figure 8**). The present study indicates that the simplified approach may capture the averaged characteristics of fluid dynamics within the porous domains, but it does not resolve the velocity field in detail because the model does not include the geometrical information of pores. Indeed, the velocity within the porous domains is expressed as the Darcy velocity. This indicates that

FIGURE 8 | Schematic illustration of common methods for computational fluid dynamic simulation in scaffold-based perfusion cell culture. **(A)** Expedient culture chamber design. Porous scaffolds were placed in the culture chamber and perfused at 1.5 ml/min. **(B)** The computational reproduction of scaffold geometry can be undertaken using different methodologies, depending on the availability of hardware resources and feasibility. At its simplest, expedient geometry (e.g., a cylinder) may be assigned as a porous domain where porous parameters are input. The generated mesh for such a geometry tends to be coarse, being less demanding computationally. Alternatively, CAD data may be used when the scaffold is designed in CAD software (e.g., 3D printed scaffold). The mesh required for computation tends to be finer than the simplified geometry, but regular. The highest predictive power may be expected when microCT data are imported to acquire the actual geometry used in the study. Mesh generation and computation entail high computational time and costs. **(C)** The Darcy (-Brinkman) model may be applied to calculate shear stress for porous domain, whereas laminar flow may be defined by the Navier-Stokes equation by assuming that culture medium is an incompressible Newtonian fluid.

the velocity within the porous domains is expected to be uniform compared to the velocity within the pores in the detailed model, and the gradients associated with the Darcy velocity are likely to be computed smaller than the counterpart. Therefore, the simplified approach can only compute shear stress in an average sense expediently and is not suited for spatial estimation in detail. This highlights the superiority of the microCT approach where actual shear stress within the pores is explicitly resolved. The microCT-based modeling revealed great spatial variations in estimated shear stress. This suggests that cell response within the scaffold constructs is likely to be heterogeneous. In other words, it would be recommendable that biological events in a 3D perfusion system is explained by the range and frequency of shear stress distribution, but not just by the mean. For visualization of local shear stress distribution, microCT geometry is advantageous. This fact also emphasizes that the microCT approach provides possibility to correlate observed cell behavior with a magnitude of shear stress in a single cell resolution, leading to more accurate investigation on dynamic cell culture (Jungreuthmayer et al., 2009). However, the considerably greater computational burden may be a major

disadvantage in the case where a complex or large scaffold geometry is to be modeled for computation. In fact, a great amount of time was often required, not only to analyze, but also to repair and reconstruct microCT data to be compatible with CAD and *in silico* modeling software (Acosta Santamaría et al., 2013). It is acknowledged that simulation of fluid dynamics using a full-scale scaffold is not always feasible, depending on available hardware and model complexity (Acosta Santamaría et al., 2013; Zhao et al., 2019). To achieve a balance between predictive visualization and computational cost, segmentation of region of interest (ROI) from the whole scaffold geometry seems a valid procedure for demonstrating representative shear distribution (Lane et al., 2014; Sellgren and Ma, 2015; Daish et al., 2017; Pasini et al., 2019). In short, the simplified method is effective for estimating a range of shear stress with a minimal computational burden when the porous property is properly parameterized, but simulation with microCT geometry is essential to gain insight into local fluctuations of fluid dynamics. Noteworthily, in the study, the simulation was performed using an acellular scaffold, and the values may not necessarily represent later timepoints because of cell

growth and deposited extracellular matrix (Ramani-Mohan et al., 2018; Nokhbatolfoghahaei et al., 2020). Furthermore, it identified the fluid property of culture medium with water at 37°C, and therefore, further investigation is required for culture medium specific dynamics in the perfusion systems.

Next, the volume of culture medium was optimized in the present system. Perfusion bioreactors commonly consist of medium reservoirs, tubes, and culture chambers. These hold unique dimensions specifically adapted to each system and the volume of medium required needs to be modified accordingly. In general, a perfusion bioreactor requires a large volume to establish continuous flow, but the amount needs to be adjusted with reference to the vital cells on the scaffolds. Therefore, cell growth was compared in different medium-to-cell ratios, on 2D mono-surfaces and on 3D porous scaffolds. Regardless of the medium-to-cell ratio, by day 7 cell viability was maintained at nearly 98%. On both 2D and 3D cultures, 0.04 μl per cell at seeding promoted greater cell proliferation than 0.08 and 0.16 μl per cell during the initial phase of culture. This trend was reversed on day 7, when the cells approached confluence. In the present study, 25 ml medium in the bioreactor, corresponding to 0.04 μl per cell initially, was considered to be optimal because cell proliferation was expected to be suppressed by fluid shear stress (Yamada et al., 2021a). It is of interest to note that the volume of culture medium influences not only cell growth but also osteogenic differentiation. Previous studies using osteoblastic cells showed that reduction of mineralization occurred in a medium volume-dependent manner: the more medium used, the less mineralization (Yoshimura et al., 2017). Furthermore, Schreivogel et al. reported that mechanical stimuli in their bioreactor increased the secretion of bone morphogenetic protein 2 by MSC but did not induce activation of downstream signaling in their original experimental configuration. This discrepancy was solved simply by reducing the volume of culture medium and increasing the number of cells, indicating that the excessive use of culture medium dilutes secreted factors and masks phenotypical amelioration (Schreivogel et al., 2019). On 3D polymeric scaffolds, high seeding density supports the osteogenic phenotype of BMSC and enhances bone regeneration after transplantation (Yassin et al., 2015). This may be convenient for perfusion systems where a large volume of medium is required to maintain continuous flow. Together, these results confirm the importance in dynamic cell culture systems, of determining the optimal seeding density and the minimum necessary medium volume, i.e., conditions which do not cause nutrient depletion but allow the cells to condition the medium by paracrine factors.

Humidity control is a key consideration during cell culture because medium condensation disturbs the osmotic balance, and the resulting high tonicity leads to cell dehydration (Triaud et al., 2003; Chi et al., 2020). This study demonstrated that medium perfusion without humidification concentrated medium components taking glucose concentration as an example, and the concentrated medium significantly affected cell viability and growth. The concept of developing tissue engineering bioreactors is mainly classified into systems installed in conventional incubators and stand-alone bioreactor, i.e., which requires an integrated incubation unit for environmental control (Li et al., 2014). However, unlike a standard incubator, maintaining humidity above 90% is not always agreeable in bioreactors because a humidified environment may cause malfunction or possibly irreparable damage to electrical components such as sensors, pumps, electric sockets and conducting wires from a long-term perspective. Admittedly, there seems a lack of consideration with regards to humidification control in previously developed systems. Furthermore, perfusion accelerates the evaporation ratio in a velocity-dependent manner (Handa et al., 1987; Sumino and Akiyama, 1987). The present study also disclosed notable medium loss during perfusion in the non-humidified condition, and this may potentially be detrimental to cell viability and growth. The placement of a water bath, as with a standard incubator, prevented evaporation as expected. However, aqueous droplets and moisture condensation were actually found on the surface of the bioreactor. As an alternative, an additional flask containing water was connected to the filter to humidify the local atmosphere contacting the culture medium. This measure had a comparable suppressive effect on evaporation, without increasing humidity inside the bioreactor. This procedure may be applicable to most bioreactor systems, to improve the culture environment under conditions in which a water bath may not be feasible.

Air bubble formation is a long-standing issue in fluidics (Lochovsky et al., 2012; Kang et al., 2014). It impedes or blocks fluid flow, and more importantly for bone tissue engineering, air bubbles entrapped in microporous scaffolds disrupt cell growth and migration to some extent, depending on cell type and the size/number of bubbles (Podichetty and Madihally, 2014; Bergemann et al., 2015). Bubbles are a determinant of protein denaturation (Faustino et al., 2009): a gas-liquid interface in form irreversibly alters the superorganization of protein molecules by absorbing and forming aggregates, which may result in loss of biological activity. This happens particularly to proteins with high surface activity (Clarkson et al., 1999). It is reported that approximately 10% of proteins in bovine serum albumin were denatured when the proteins were absorbed to and desorbed from air bubbles (Clarkson et al., 1999). The use of perfusion bioreactors for bone tissue engineering exacerbates conditions conducive to bubble formation. Culture medium is normally supplemented with serum/proteins as nutrient sources, acting as surfactants (Faustino et al., 2009). Surfactants lower the surface tension, facilitating the formation of bubbles in the presence of agitation and stabilizing them. Microporous scaffolds of synthetic polymers, which are preferred in bone tissue engineering for their mechanical strength, formability, biocompatibility and biodegradability, exacerbate the problem because of their high porosity and hydrophobicity (Gunatillake and Adhikari, 2003). When fluid flow encounters micropores, stirring may trigger bubble formation, particularly on hydrophobic materials, which absorb gasses and form thin air layers on the surfaces (Hanwright et al., 2005; Lee et al., 2005; Yu et al., 2017b; Yao et al., 2020). It has been shown that using a bubble trap effectively removes large bubbles from the circulation and prevents them from entering the culture chambers, but the trap neither prevents

bubble formation nor removes bubbles trapped in the scaffold micropores (Li et al., 2014; Schuerlein et al., 2017). Alternatively, a complex tubing strategy is needed to control flow paths to isolate bubbles from the main stream (Bhaskar et al., 2018). Therefore, preventive measures of air bubble formation should be prioritized. In the present system, the formation of air bubbles was so extreme that rBMSC were severely affected. For total prevention, a simple yet rigorous step was taken: namely, elevation of the medium reservoir by 30 cm to apply approximately 20 mmHg (equivalent to 2.7 kPa) hydrostatic pressure onto the culture chamber. This was based on Henry's law, which governs gas solubility in liquid: at a given temperature, gas solubility is proportional to static pressure (Kang et al., 2007). It was shown that a slight increase in static pressure decreased gas release in the culture chambers, which created a bubble-free environment. The degree of pressure required may depend on experimental settings, including material selection, scaffold geometry, and flow characteristics. Previous studies have suggested that BMSC undergo osteogenic differentiation under high static pressure ranging from 10 to 100 kPa (Huang et al., 2015; Zhao et al., 2015; Stavenschi et al., 2018). In the present setting, where 2.7 kPa was sufficient to eliminate bubbles completely, its effect on osteogenesis would be negligible although the present study did not evaluate the effect solely. Nevertheless, the strategy of supressing bubbles by applying a static pressure may interact favorably with osteogenic activity given that continuity is commonly observed in biological events.

Finally, the optimization of flow rate for the purpose of bone tissue engineering was explored by testing relatively low-level shear force. The reasons were twofold: not only is cell fate fine-tuned by mechanical stimuli, but also the results should be relevant to clinical translation. In other words, cells which are maintained in a perfusion bioreactor should be also supported during integration at the recipient site in the absence of the robust perfusion provided in bioreactors. In the present study, we tested a subphysiological level of perfusion, which reportedly initiated osteogenic differentiation on 2D surfaces (Coughlin and Niebur, 2012; Gao et al., 2014; Kim et al., 2014). rBMSC were sensitive enough to distinguish 0.8 ml/min (i.e., shear stress: maximum 13.1 mPa, mean 0.88 mPa, mode value 0.5–1 mPa), 1.6 ml/min (i.e., maximum 26.2 mPa, mean 1.76 mPa, mode value 1.0–1.5 mPa), and 3.2 ml/min (i.e., maximum 52.6 mPa, mean 3.51 mPa, mode value 2–3 mPa), and the cells responded differently. Even at the low levels of fluid stimuli, cell proliferation was either delayed or suppressed. Perfusion for 8 h at 0.8 ml/min was found to be compatible with the cell growth and viability, maintaining intact the morphology of the cells and cell-to-cell integration. The finding agrees with a previous report using an osteoblastic cell line, MC3T3-E1, in which shear stress above 1 mPa suppressed cell growth on a 3D scaffold (Cartmell et al., 2003).

In 2D perfusion settings, MSC as well as osteoblasts seem tolerant of high shear stress over 3 Pa and respond to the stimuli by upregulating the expression of osteogenic markers (McAllister et al., 2000; Jiang et al., 2002; Yourek et al., 2010; Mai et al., 2013; Lim et al., 2014; Liu et al., 2015; Yu et al., 2017c). However, the cells are reportedly more vulnerable to shear stress in 3D environment, and a sub-pascal level of shear stress sufficiently stimulates the osteogenicity without deteriorating general cell health (Porter et al., 2005; Gaspar et al., 2012). Previous studies using 3D dynamic culture systems showed that extremely low shear stress ranging from 5 to 10 mPa shear stress for 16 days increased the calcium deposition by rBMSC under the presence of osteogenic supplement (Sikavitsas et al., 2003; Sikavitsas et al., 2005). The promotion of osteogenesis by a low shear stress magnitude was also reported with human BMSC on various scaffold materials (Grayson et al., 2008; Li et al., 2009).

In our experimental setting, shear stress ranging from nearly 0 to up to 15 mPa (mode value 0.5–1.0 mPa) allowed rBMSC to upregulate the key transcription factors for osteogenesis, RUNX2 and Osterix, even in the absence of osteogenic chemical supplements. Osteogenic differentiation was confirmed by enhanced calcium deposition and ALP activity. Therefore, with the scaffold geometry, material selection, and cell type in the present study, it was concluded that this level of shear stress was optimal for balancing the induction of osteogenesis and the growth of rBMSC. Nevertheless, the optimal magnitude of fluid stimuli would differ according to cell types (e.g., species, donor sites, individual variations) and scaffold properties (e.g., micro-, and macro-geometry, surface chemistry, size). Biological responses may therefore differ, even if the same flow rate is applied. This underlines the importance of flow optimization and its challenges when in future clinical translation, scaffolds are custom-designed and loaded with patient-specific cells (Roseti et al., 2017).

CONCLUSION

In bone tissue engineering, bioreactors are intended to support growth and targeted differentiation of stem/progenitor cells. There is a wide range of bioreactor systems in use, each with unique features. Moreover, dynamic cell culture inevitably involves parametric deviations from conventional static culture, which may mask or exaggerate effects of interest. As a previous study confirmed, exact comparative studies can probably be done only by using an identical "standardized" system under the same conditions (Israelowitz et al., 2012). However, some optimized parameters would be transferable to other systems and study designs. The present study explored some of basic but crucial optimization steps, namely the computational estimation of fluid force, the determination of culture medium volume, humidification, the strategy of air bubble suppression, and the identification of optimal fluid shear stress magnitude. The accurate estimation of fluid forces acts as a platform for understanding biological behaviors, while optimizing culture environmental factors contributes to stabilized and reproducible experiments. The thorough validation, optimization, and detailed description facilitate the further development of bioreactor applications in bone tissue engineering.

DATA AVAILABILITY STATEMENT

The raw data supporting the conclusion of this article will be made available by the authors, without undue reservation.

ETHICS STATEMENT

The animal study was reviewed and approved by Norwegian Animal Research Authority (local approval number 20146866).

AUTHOR CONTRIBUTIONS

SY, MY, KM, TS, and JH conceived and planned the experiments. TS and JH developed a bioreactor system. SY and MY carried out the experiments. SY, MY, KM, TS, and JH contributed to the interpretation of the results. SY and JH took the lead in writing the manuscript. All authors provided critical feedback and helped shape the research, analysis and manuscript.

SUPPLEMENTARY MATERIAL

The Supplementary Material for this article can be found online at: https://www.frontiersin.org/articles/10.3389/fbioe.2022.811942/full#supplementary-material

REFERENCES

Acosta Santamaría, V. A., Malvè, M., Duizabo, A., Mena Tobar, A., Gallego Ferrer, G., García Aznar, J. M., et al. (2013). Computational Methodology to Determine Fluid Related Parameters of Non Regular Three-Dimensional Scaffolds. *Ann. Biomed. Eng.* 41, 2367–2380. doi:10.1007/s10439-013-0849-8

Amini, A. R., Laurencin, C. T., and Nukavarapu, S. P. (2012). Bone Tissue Engineering: Recent Advances and Challenges. *Crit. Rev. Biomed. Eng.* 40, 363–408. doi:10.1615/CritRevBiomedEng.v40.i5.10

Arramon, Y. P., and Nauman, E. A. (2001). "The Intrinsic Permeability of Cancellous Bone," in *Bone Mechanics Handbook*. Second Edition.

Becquart, P., Cruel, M., Cruel, M., Hoc, T., Sudre, L., Pernelle, K., et al. (2016). Human Mesenchymal Stem Cell Responses to Hydrostatic Pressure and Shear Stress. *eCM* 31, 160–173. doi:10.22203/ecm.v031a11

Bergemann, C., Elter, P., Lange, R., Weißmann, V., Hansmann, H., Klinkenberg, E.-D., et al. (2015). Cellular Nutrition in Complex Three-Dimensional Scaffolds: A Comparison between Experiments and Computer Simulations. *Int. J. Biomater.* 2015, 1–12. doi:10.1155/2015/584362

Bhaskar, B., Owen, R., Bahmaee, H., Rao, P. S., and Reilly, G. C. (2018). Design and Assessment of a Dynamic Perfusion Bioreactor for Large Bone Tissue Engineering Scaffolds. *Appl. Biochem. Biotechnol.* 185, 555–563. doi:10.1007/s12010-017-2671-5

Blender (2021). *Blender Online Community Blender - a 3D Modelling and Rendering Package*. Available online: http://www.blender.org.

Campos Marin, A., and Lacroix, D. (2015). The Inter-sample Structural Variability of Regular Tissue-Engineered Scaffolds Significantly Affects the Micromechanical Local Cell Environment. *Interf. Focus.* 5, 20140097. doi:10.1098/rsfs.2014.0097

Cartmell, S. H., Porter, B. D., García, A. J., and Guldberg, R. E. (2003). "Effects of Medium Perfusion Rate on Cell-Seeded Three-Dimensional Bone Constructs *In Vitro*," in *Proceedings of the Tissue Engineering*. 9. doi:10.1089/10763270360728107

Chi, H.-J., Park, J.-S., Yoo, C.-S., Kwak, S.-J., Son, H.-J., Kim, S.-G., et al. (2020). Effect of Evaporation-Induced Osmotic Changes in Culture media in a Dry-type Incubator on Clinical Outcomes in *In Vitro* Fertilization-Embryo Transfer Cycles. *Clin. Exp. Reprod. Med.* 47, 284–292. doi:10.5653/cerm.2020.03552

Cignoni, P., Callieri, M., Corsini, M., Dellepiane, M., Ganovelli, F., and Ranzuglia, G. (2008). "MeshLab: An Open-Source Mesh Processing Tool," in Proceedings of the 6th Eurographics Italian Chapter Conference 2008 - Proceedings.

Clarkson, J. R., Cui, Z. F., and Darton, R. C. (1999). Protein Denaturation in Foam. *J. Colloid Interf. Sci.* 215, 333–338. doi:10.1006/jcis.1999.6256

Coughlin, T. R., and Niebur, G. L. (2012). Fluid Shear Stress in Trabecular Bone Marrow Due to Low-Magnitude High-Frequency Vibration. *J. Biomech.* 45, 2222–2229. doi:10.1016/j.jbiomech.2012.06.020

Daish, C., Blanchard, R., Gulati, K., Losic, D., Findlay, D., Harvie, D. J. E., et al. (2017). Estimation of Anisotropic Permeability in Trabecular Bone Based on microCT Imaging and Pore-Scale Fluid Dynamics Simulations. *Bone Rep.* 6, 129–139. doi:10.1016/j.bonr.2016.12.002

Dash, S. K., Sharma, V., Verma, R. S., and Das, S. K. (2020). Low Intermittent Flow Promotes Rat Mesenchymal Stem Cell Differentiation in Logarithmic Fluid Shear Device. *Biomicrofluidics* 14, 054107. doi:10.1063/5.0024437

Egger, D., Fischer, M., Clementi, A., Ribitsch, V., Hansmann, J., and Kasper, C. (2017). Development and Characterization of a Parallelizable Perfusion Bioreactor for 3D Cell Culture. *Bioengineering* 4, 51. doi:10.3390/bioengineering4020051

Faustino, C. M. C., Calado, A. R. T., and Garcia-Rio, L. (2009). Gemini Surfactant–Protein Interactions: Effect of pH, Temperature, and Surfactant Stereochemistry. *Biomacromolecules* 10, 2508–2514. doi:10.1021/bm9004723

Gao, X., Zhang, X., Xu, H., Zhou, B., Wen, W., and Qin, J. (2014). Regulation of Cell Migration and Osteogenic Differentiation in Mesenchymal Stem Cells under Extremely Low Fluidic Shear Stress. *Biomicrofluidics* 8, 052008. doi:10.1063/1.4896557

Gaspar, D. A., Gomide, V., and Monteiro, F. J. (2012). The Role of Perfusion Bioreactors in Bone Tissue Engineering. *Biomatter* 2, 167–175. doi:10.4161/biom.22170

Geris, L., Guyot, Y., Schrooten, J., and Papantoniou, I. (2016). In Silico regenerative Medicine: How Computational Tools Allow Regulatory and Financial Challenges to Be Addressed in a Volatile Market. *Interf. Focus.* 6, 20150105. doi:10.1098/rsfs.2015.0105

Grayson, W. L., Bhumiratana, S., Cannizzaro, C., Chao, P.-H. G., Lennon, D. P., Caplan, A. I., et al. (2008). Effects of Initial Seeding Density and Fluid Perfusion Rate on Formation of Tissue-Engineered Bone. *Tissue Eng. A* 14, 1809–1820. doi:10.1089/ten.tea.2007.0255

Gunatillake, P., and Adhikari, R. (2003). Biodegradable Synthetic Polymers for Tissue Engineering. *eCM* 5, 1–16. discussion 16. doi:10.22203/ecm.v005a01

Handa, A., Emery, A. N., and Spier, R. E. (1987). On the Evaluation of Gas-Liquid Interfacial Effects on Hybridoma Viability in Bubble Column Bioreactors. *Dev. Biol. Stand.* 66, 241–253.

Hanwright, J., Zhou, J., Evans, G. M., and Galvin, K. P. (2005). Influence of Surfactant on Gas Bubble Stability. *Langmuir* 21, 4912–4920. doi:10.1021/la0502894

Holtorf, H. L., Jansen, J. A., and Mikos, A. G. (2005). Flow Perfusion Culture Induces the Osteoblastic Differentiation of Marrow Stromal Cell-Scaffold

Constructs in the Absence of Dexamethasone. *J. Biomed. Mater. Res.* 72A, 326–334. doi:10.1002/jbm.a.30251

Huang, L., Cai, X., Li, H., Xie, Q., Zhang, M., and Yang, C. (2015). The Effects of Static Pressure on Chondrogenic and Osteogenic Differentiation in Condylar Chondrocytes from Temporomandibular Joint. *Arch. Oral Biol.* 60, 622–630. doi:10.1016/j.archoralbio.2015.01.003

Israelowitz, M., Weyand, B., Rizvi, S., Vogt, P., and von Schroeder, H. (2012). Development of a Laminar Flow Bioreactor by Computational Fluid Dynamics. *J. Healthc. Eng.* 3, 455–476. doi:10.1260/2040-2295.3.3.455

Jiang, G.-L., White, C. R., Stevens, H. Y., and Frangos, J. A. (2002). Temporal Gradients in Shear Stimulate Osteoblastic Proliferation via ERK1/2 and Retinoblastoma Protein. *Am. J. Physiology-Endocrinology Metab.* 283, E383–E389. doi:10.1152/ajpendo.00547.2001

Jungreuthmayer, C., Jaasma, M. J., Al-Munajjed, A. A., Zanghellini, J., Kelly, D. J., and O'Brien, F. J. (2009). Deformation Simulation of Cells Seeded on a Collagen-GAG Scaffold in a Flow Perfusion Bioreactor Using a Sequential 3D CFD-Elastostatics Model. *Med. Eng. Phys.* 31, 420–427. doi:10.1016/j.medengphy.2008.11.003

Kang, J. H., Kim, Y. C., and Park, J.-K. (2007). Analysis of Pressure-Driven Air Bubble Elimination in a Microfluidic Device. *Lab. Chip* 8, 176–178. doi:10.1039/b712672g

Kang, Y. J., Yeom, E., Seo, E., and Lee, S.-J. (2014). Bubble-free and Pulse-free Fluid Delivery into Microfluidic Devices. *Biomicrofluidics* 8, 014102. doi:10.1063/1.4863355

Kim, K. M., Choi, Y. J., Hwang, J.-H., Kim, A. R., Cho, H. J., Hwang, E. S., et al. (2014). Shear Stress Induced by an Interstitial Level of Slow Flow Increases the Osteogenic Differentiation of Mesenchymal Stem Cells through TAZ Activation. *PLoS One* 9, e92427. doi:10.1371/journal.pone.0092427

Klein, S. G., Alsolami, S. M., Steckbauer, A., Arossa, S., Parry, A. J., Ramos Mandujano, G., et al. (2021). A Prevalent Neglect of Environmental Control in Mammalian Cell Culture Calls for Best Practices. *Nat. Biomed. Eng.* 5, 787–792. doi:10.1038/s41551-021-00775-0

Lane, S. W., Williams, D. A., and Watt, F. M. (2014). Modulating the Stem Cell Niche for Tissue Regeneration. *Nat. Biotechnol.* 32, 795–803. doi:10.1038/nbt.2978

Lee, J., Kentish, S., and Ashokkumar, M. (2005). Effect of Surfactants on the Rate of Growth of an Air Bubble by Rectified Diffusion. *J. Phys. Chem. B* 109, 14595–14598. doi:10.1021/jp051758d

Li, D.-Q., Li, M., Liu, P.-L., Zhang, Y.-K., Lu, J.-X., and Li, J.-M. (2014). Improved Repair of Bone Defects with Prevascularized Tissue-Engineered Bones Constructed in a Perfusion Bioreactor. *Orthopedics* 37, 685–690. doi:10.3928/01477447-20140924-06

Li, D., Tang, T., Lu, J., and Dai, K. (2009). Effects of Flow Shear Stress and Mass Transport on the Construction of a Large-Scale Tissue-Engineered Bone in a Perfusion Bioreactor. *Tissue Eng. Part A* 15, 2773–2783. doi:10.1089/ten.tea.2008.0540

Lim, K. T., Hexiu, J., Kim, J., Seonwoo, H., Choung, P.-H., and Chung, J. H. (2014). Synergistic Effects of Orbital Shear Stress onIn VitroGrowth and Osteogenic Differentiation of Human Alveolar Bone-Derived Mesenchymal Stem Cells. *Biomed. Res. Int.* 2014, 1–18. doi:10.1155/2014/316803

Liu, Y.-S., Liu, Y.-A., Huang, C.-J., Yen, M.-H., Tseng, C.-T., Chien, S., et al. (2015). Mechanosensitive TRPM7 Mediates Shear Stress and Modulates Osteogenic Differentiation of Mesenchymal Stromal Cells through Osterix Pathway. *Sci. Rep.* 5, 16522. doi:10.1038/srep16522

Livak, K. J., and Schmittgen, T. D. (2001). Analysis of Relative Gene Expression Data Using Real-Time Quantitative PCR and the $2^{-\Delta\Delta CT}$ Method. *Methods* 25, 402–408. doi:10.1006/meth.2001.1262

Lochovsky, C., Yasotharan, S., and Günther, A. (2012). Bubbles No More: In-Plane Trapping and Removal of Bubbles in Microfluidic Devices. *Lab. Chip* 12, 595–601. doi:10.1039/C1LC20817A

Mai, Z., Peng, Z., Wu, S., Zhang, J., Chen, L., Liang, H., et al. (2013). Single Bout Short Duration Fluid Shear Stress Induces Osteogenic Differentiation of MC3T3-E1 Cells via Integrin β1 and BMP2 Signaling Cross-Talk. *PLoS One* 8, e61600. doi:10.1371/journal.pone.0061600

Mandenius, C. F. (2016). Editor C.-F. Mandenius (Weinheim, Germany: Wiley-VCH Verlag GmbH & Co. KGaA). 53; ISBN 9783527683369. *Bioreactors: Design, Operation and Novel Applications.*

Marquez-Curtis, L. A., Janowska-Wieczorek, A., McGann, L. E., and Elliott, J. A. W. (2015). Mesenchymal Stromal Cells Derived from Various Tissues: Biological, Clinical and Cryopreservation Aspects. *Cryobiology* 71, 181–197. doi:10.1016/j.cryobiol.2015.07.003

Maul, T. M., Chew, D. W., Nieponice, A., and Vorp, D. A. (2011). Mechanical Stimuli Differentially Control Stem Cell Behavior: Morphology, Proliferation, and Differentiation. *Biomech. Model. Mechanobiol.* 10, 939–953. doi:10.1007/s10237-010-0285-8

McAllister, T. N., Du, T., and Frangos, J. A. (2000). Fluid Shear Stress Stimulates Prostaglandin and Nitric Oxide Release in Bone Marrow-Derived Preosteoclast-like Cells. *Biochem. Biophysical Res. Commun.* 270, 643–648. doi:10.1006/bbrc.2000.2467

Melke, J., Zhao, F., Ito, K., and Hofmann, S. (2020). Orbital Seeding of Mesenchymal Stromal Cells Increases Osteogenic Differentiation and Bone-like Tissue Formation. *J. Orthop. Res.* 38, 1228–1237. doi:10.1002/jor.24583

Nokhbatolfoghahaei, H., Bohlouli, M., Adavi, K., Paknejad, Z., Rezai Rad, M., khani, M. M., et al. (2020). Computational Modeling of media Flow through Perfusion-Based Bioreactors for Bone Tissue Engineering. *Proc. Inst. Mech. Eng. H* 234, 1397–1408. doi:10.1177/0954411920944039

Odelius, K., Plikk, P., and Albertsson, A.-C. (2005). Elastomeric Hydrolyzable Porous Scaffolds: Copolymers of Aliphatic Polyesters and a Polyether–ester. *Biomacromolecules* 6, 2718–2725. doi:10.1021/bm050190b

Pasini, A., Lovecchio, J., Ferretti, G., and Giordano, E. (2019). Medium Perfusion Flow Improves Osteogenic Commitment of Human Stromal Cells. *Stem Cell Int.* 2019, 1–10. doi:10.1155/2019/1304194

Pereira, A. R., Lipphaus, A., Ergin, M., Salehi, S., Gehweiler, D., Rudert, M., et al. (2021). Modeling of the Human Bone Environment: Mechanical Stimuli Guide Mesenchymal Stem Cell-Extracellular Matrix Interactions. *Materials* 14, 4431. doi:10.3390/ma14164431

Piola, M., Soncini, M., Cantini, M., Sadr, N., Ferrario, G., and Fiore, G. B. (2013). Design and Functional Testing of a Multichamber Perfusion Platform for Three-Dimensional Scaffolds. *Scientific World J.* 2013, 1–9. doi:10.1155/2013/123974

Podichetty, J. T., and Madihally, S. V. (2014). Modeling of Porous Scaffold Deformation Induced by Medium Perfusion. *J. Biomed. Mater. Res.* 102, 737–748. doi:10.1002/jbm.b.33054

Porter, B., Zauel, R., Stockman, H., Guldberg, R., and Fyhrie, D. (2005). 3-D Computational Modeling of media Flow through Scaffolds in a Perfusion Bioreactor. *J. Biomech.* 38, 543–549. doi:10.1016/j.jbiomech.2004.04.011

Ramani-Mohan, R. K., Schwedhelm, I., Finne-Wistrand, A., Krug, M., Schwarz, T., Jakob, F., et al. (2018). Deformation Strain Is the Main Physical Driver for Skeletal Precursors to Undergo Osteogenesis in Earlier Stages of Osteogenic Cell Maturation. *J. Tissue Eng. Regen. Med.* 12, e1474–e1479. doi:10.1002/term.2565

Rauh, J., Milan, F., Günther, K.-P., and Stiehler, M. (2011). Bioreactor Systems for Bone Tissue Engineering. *Tissue Eng. B: Rev.* 17, 263–280. doi:10.1089/ten.TEB.2010.0612

Roddy, E., DeBaun, M. R., Daoud-Gray, A., Yang, Y. P., and Gardner, M. J. (2018). Treatment of Critical-Sized Bone Defects: Clinical and Tissue Engineering Perspectives. *Eur. J. Orthop. Surg. Traumatol.* 28, 351–362. doi:10.1007/s00590-017-2063-0

Roseti, L., Parisi, V., Petretta, M., Cavallo, C., Desando, G., Bartolotti, I., et al. (2017). Scaffolds for Bone Tissue Engineering: State of the Art and New Perspectives. *Mater. Sci. Eng. C* 78, 1246–1262. doi:10.1016/j.msec.2017.05.017

Rouwkema, J., Koopman, B. F. J. M., Blitterswijk, C. A. V., Dhert, W. J. A., and Malda, J. (2009). Supply of Nutrients to Cells in Engineered Tissues. *Biotechnol. Genet. Eng. Rev.* 26, 163–178. doi:10.5661/bger-26-163

Schindelin, J., Arganda-Carreras, I., Frise, E., Kaynig, V., Longair, M., Pietzsch, T., et al. (2012). Fiji: an Open-Source Platform for Biological-Image Analysis. *Nat. Methods* 9, 676–682. doi:10.1038/nmeth.2019.Fiji

Schreivogel, S., Kuchibhotla, V., Knaus, P., Duda, G. N., and Petersen, A. (2019). Load-induced Osteogenic Differentiation of Mesenchymal Stromal Cells Is Caused by Mechano-regulated Autocrine Signaling. *J. Tissue Eng. Regen. Med.* 13, 1992–2008. doi:10.1002/term.2948

Schuerlein, S., Schwarz, T., Krziminski, S., Gätzner, S., Hoppensack, A., Schwedhelm, I., et al. (2017). A Versatile Modular Bioreactor Platform for Tissue Engineering. *Biotechnol. J.* 12, 1600326. doi:10.1002/biot.201600326

Sellgren, K. L., and Ma, T. (2015). Effects of Flow Configuration on Bone Tissue Engineering Using Human Mesenchymal Stem Cells in 3D Chitosan Composite Scaffolds. *J. Biomed. Mater. Res.* 103, 2509–2520. doi:10.1002/jbm.a.35386

Sikavitsas, V. I., Bancroft, G. N., Lemoine, J. J., Liebschner, M. A., Dauner, M., and Mikos, A. G. (2005). Flow Perfusion Enhances the Calcified Matrix Deposition of Marrow Stromal Cells in Biodegradable Nonwoven Fiber Mesh Scaffolds. *Ann. Biomed. Eng.* 33, 63–70. doi:10.1007/s10439-005-8963-x

Sikavitsas, V. I., Bancroft, G. N., Holtorf, H. L., Jansen, J. A., and Mikos, A. G. (2003). Mineralized Matrix Deposition by Marrow Stromal Osteoblasts in 3D Perfusion Culture Increases with Increasing Fluid Shear Forces. *Proc. Natl. Acad. Sci.* 100, 14683–14688. doi:10.1073/pnas.2434367100

Sladkova, M., and de Peppo, G. (2014). Bioreactor Systems for Human Bone Tissue Engineering. *Processes* 2, 494–525. doi:10.3390/pr2020494

Sobolewski, P., Kandel, J., and Eckmann, D. M. (2012). Air Bubble Contact with Endothelial Cells Causes a Calcium-independent Loss in Mitochondrial Membrane Potential. *PLoS One* 7, e47254. doi:10.1371/journal.pone.0047254

Stavenschi, E., Corrigan, M. A., Johnson, G. P., Riffault, M., and Hoey, D. A. (2018). Physiological Cyclic Hydrostatic Pressure Induces Osteogenic Lineage Commitment of Human Bone Marrow Stem Cells: a Systematic Study. *Stem Cel Res. Ther.* 9, 276. doi:10.1186/s13287-018-1025-8

Stavenschi, E., Labour, M.-N., and Hoey, D. A. (2017). Oscillatory Fluid Flow Induces the Osteogenic Lineage Commitment of Mesenchymal Stem Cells: The Effect of Shear Stress Magnitude, Frequency, and Duration. *J. Biomech.* 55, 99–106. doi:10.1016/j.jbiomech.2017.02.002

Sumino, Y., and Akiyama, S.-i. (1987). Measurement of the Evaporation Rate of Liquid in a Shaking Flask. *J. Ferment. Technology* 65, 291–294. doi:10.1016/0385-6380(87)90090-2

Sung, J. H., and Shuler, M. L. (2009). Prevention of Air Bubble Formation in a Microfluidic Perfusion Cell Culture System Using a Microscale Bubble Trap. *Biomed. Microdevices* 11, 731–738. doi:10.1007/s10544-009-9286-8

Triaud, F., Clenet, D.-H., Cariou, Y., Le Neel, T., Morin, D., and Truchaud, A. (2003). Evaluation of Automated Cell Culture Incubators. *JALA: J. Assoc. Lab. Automation* 8, 82–86. doi:10.1016/s1535-5535(03)00018-2

Truscello, S., Kerckhofs, G., Van Bael, S., Pyka, G., Schrooten, J., and Van Oosterwyck, H. (2012). Prediction of Permeability of Regular Scaffolds for Skeletal Tissue Engineering: A Combined Computational and Experimental Study. *Acta Biomater.* 8, 1648–1658. doi:10.1016/j.actbio.2011.12.021

Tsai, H.-H., Yang, K.-C., Wu, M.-H., Chen, J.-C., and Tseng, C.-L. (2019). The Effects of Different Dynamic Culture Systems on Cell Proliferation and Osteogenic Differentiation in Human Mesenchymal Stem Cells. *Ijms* 20, 4024. doi:10.3390/ijms20164024

Walls, P. L. L., McRae, O., Natarajan, V., Johnson, C., Antoniou, C., and Bird, J. C. (2017). Quantifying the Potential for Bursting Bubbles to Damage Suspended Cells. *Sci. Rep.* 7, 15102. doi:10.1038/s41598-017-14531-5

Walsh, C., Ovenden, N., Stride, E., and Cheema, U. (2017). Quantification of Cell-Bubble Interactions in a 3D Engineered Tissue Phantom. *Sci. Rep.* 7, 6331. doi:10.1038/s41598-017-06678-y

Yamada, S., Yassin, M. A., Schwarz, T., Hansmann, J., and Mustafa, K. (2021). Induction of Osteogenic Differentiation of Bone Marrow Stromal Cells on 3D Polyester-Based Scaffolds Solely by Subphysiological Fluidic Stimulation in a Laminar Flow Bioreactor. *J. Tissue Eng.* 12, 204173142110193. doi:10.1177/20417314211019375

Yamada, S., Yassin, M. A., Weigel, T., Schmitz, T., Hansmann, J., and Mustafa, K. (2021). Surface Activation with Oxygen Plasma Promotes Osteogenesis with Enhanced Extracellular Matrix Formation in Three-dimensional Microporous Scaffolds. *J. Biomed. Mater. Res.* 109, 1560–1574. doi:10.1002/jbm.a.37151

Yao, M., Tijing, L. D., Naidu, G., Kim, S.-H., Matsuyama, H., Fane, A. G., et al. (2020). A Review of Membrane Wettability for the Treatment of saline Water Deploying Membrane Distillation. *Desalination* 479, 114312. doi:10.1016/j.desal.2020.114312

Yassin, M. A., Leknes, K. N., Pedersen, T. O., Xing, Z., Sun, Y., Lie, S. A., et al. (2015). Cell Seeding Density Is a Critical Determinant for Copolymer Scaffolds-induced Bone Regeneration. *J. Biomed. Mater. Res.* 103, 3649–3658. doi:10.1002/jbm.a.35505

Yeatts, A. B., Choquette, D. T., and Fisher, J. P. (2013). Bioreactors to Influence Stem Cell Fate: Augmentation of Mesenchymal Stem Cell Signaling Pathways via Dynamic Culture Systems. *Biochim. Biophys. Acta (Bba) - Gen. Subjects* 1830, 2470–2480. doi:10.1016/j.bbagen.2012.06.007

Yeatts, A. B., and Fisher, J. P. (2011). Bone Tissue Engineering Bioreactors: Dynamic Culture and the Influence of Shear Stress. *Bone* 48, 171–181. doi:10.1016/j.bone.2010.09.138

Yoshimura, Y., Kikuiri, T., Hasegawa, T., Matsuno, M., Minamikawa, H., Deyama, Y., et al. (2017). How Much Medium Do You Use for Cell Culture? Medium Volume Influences Mineralization and Osteoclastogenesis *In Vitro*. *Mol. Med. Rep.* 16, 429–434. doi:10.3892/mmr.2017.6611

Yourek, G., McCormick, S. M., Mao, J. J., and Reilly, G. C. (2010). Shear Stress Induces Osteogenic Differentiation of Human Mesenchymal Stem Cells. *Regenerative Med.* 5, 713–724. doi:10.2217/rme.10.60

Yu, C., Zhang, P., Wang, J., and Jiang, L. (2017). Superwettability of Gas Bubbles and its Application: From Bioinspiration to Advanced Materials. *Adv. Mater.* 29, 1703053. doi:10.1002/adma.201703053

Yu, F., Deng, R., Hao Tong, W., Huan, L., Chan Way, N., IslamBadhan, A., et al. (2017). A Perfusion Incubator Liver Chip for 3D Cell Culture with Application on Chronic Hepatotoxicity Testing. *Sci. Rep.* 7, 14528. doi:10.1038/s41598-017-13848-5

Yu, L., Ma, X., Sun, J., Tong, J., Shi, L., Sun, L., et al. (2017). Fluid Shear Stress Induces Osteoblast Differentiation and Arrests the Cell Cycle at the G0 Phase via the ERK1/2 Pathway. *Mol. Med. Rep.* 16, 8699–8708. doi:10.3892/mmr.2017.7720

Zhang, K., Fan, Y., Dunne, N., and Li, X. (2018). Effect of Microporosity on Scaffolds for Bone Tissue Engineering. *Regen. Biomater.* 5, 115–124. doi:10.1093/rb/rby001

Zhao, F., Melke, J., Ito, K., van Rietbergen, B., and Hofmann, S. (2019). A Multiscale Computational Fluid Dynamics Approach to Simulate the Micro-fluidic Environment within a Tissue Engineering Scaffold with Highly Irregular Pore Geometry. *Biomech. Model. Mechanobiol.* 18, 1965–1977. doi:10.1007/s10237-019-01188-4

Zhao, Y.-H., Lv, X., Liu, Y.-L., Zhao, Y., Li, Q., Chen, Y.-J., et al. (2015). Hydrostatic Pressure Promotes the Proliferation and Osteogenic/chondrogenic Differentiation of Mesenchymal Stem Cells: The Roles of RhoA and Rac1. *Stem Cel Res.* 14, 283–296. doi:10.1016/j.scr.2015.02.006

Publisher's Note: All claims expressed in this article are solely those of the authors and do not necessarily represent those of their affiliated organizations, or those of the publisher, the editors and the reviewers. Any product that may be evaluated in this article, or claim that may be made by its manufacturer, is not guaranteed or endorsed by the publisher.

Paper III

Induction of Osteogenic Differentiation of Bone Marrow Stromal Cells on 3D Polyester-based Scaffolds Solely by Subphysiological Fluidic Stimulation in a Laminar Flow Bioreactor

S. Yamada, MA. Yassin, T. Schwarz, J. Hansmann, K. Mustafa

III

Induction of osteogenic differentiation of bone marrow stromal cells on 3D polyester-based scaffolds solely by subphysiological fluidic stimulation in a laminar flow bioreactor

Shuntaro Yamada[1] , Mohammed Ahmed Yassin[1] ,
Thomas Schwarz[2], Jan Hansmann[2,3,4] and Kamal Mustafa[1]

Abstract

The fatal determination of bone marrow mesenchymal stem/stromal cells (BMSC) is closely associated with mechano-environmental factors in addition to biochemical clues. The aim of this study was to induce osteogenesis in the absence of chemical stimuli using a custom-designed laminar flow bioreactor. BMSC were seeded onto synthetic microporous scaffolds and subjected to the subphysiological level of fluid flow for up to 21 days. During the perfusion, cell proliferation was significantly inhibited. There were also morphological changes, with F-actin polymerisation and upregulation of ROCK1. Notably, in BMSC subjected to flow, mRNA expression of osteogenic markers was significantly upregulated and RUNX2 was localised in the nuclei. Further, under perfusion, there was greater deposition of collagen type 1 and calcium onto the scaffolds. The results confirm that an appropriate level of fluid stimuli preconditions BMSC towards the osteoblastic lineage on 3D scaffolds in the absence of chemical stimulation, which highlights the utility of flow bioreactors in bone tissue engineering.

Keywords

Bone tissue engineering, bioreactor, lamina flow, dynamic cell culture, osteogenic differentiation

Date received: 8 March 2021; accepted: 4 May 2021

Introduction

Bone has a limited capacity for spontaneous healing of critical defects caused by injury, inflammation or therapeutic resection.[1] Currently, extensive surgical intervention is required to restore the structure and function, often accompanied with considerable postoperative complications.[2] Therefore, there is an urgent need for tissue engineering strategies, based on biomaterials in combination with multipotent cells and/or growth factors as an alternative approach to regenerate bone.[3] Three-dimensional (3D) microporous scaffolds, which mimic the structure of bone matrix, are necessitated to control the spatiotemporal distribution of cells and bioactive clues. A porous structure promotes the osteogenic differentiation of multipotent cells. Specifically, highly-porous structures, with pore sizes ranging from 100 to 600 μm, appear to facilitate cell adhesion, growth and mineral formation as well as blood

vessels formation in vivo within the construct.[4] One of technical challenges to the clinical applications of cell therapy with scaffolding is its size. In a cell-based tissue engineering approach, 3D scaffolds and multipotent cells

[1]Department of Clinical Dentistry, Faculty of Medicine – Tissue engineering group, University of Bergen, Bergen, Norway
[2]Fraunhofer Institute for Silicate Research ISC, Translational Center Regenerative Therapies, Wurzburg, Bayern, Germany
[3]Chair of Tissue Engineering and Regenerative Medicine, University Hospital Würzburg, Germany
[4]Department Electrical Engineering, University of Applied Sciences Würzburg-Schweinfurt, Germany

Corresponding author:
Kamal Mustafa, Department of Clinical Dentistry, Faculty of Medicine – Tissue Engineering Group, University of Bergen, Årstadveien 19, 5009 Bergen, Norway.
Email: kamal.mustafa@uib.no

are the core of the engineered construct.[5] As the volume of the 3D scaffold increases, the cells become vulnerable to a lack of nutrient and gas supply, which leads to the deterioration of cell viability and multipotency.[6]

Perfusing culture medium through scaffolds homogenises nutritional supply while removing waste products.[7] Various types of bioreactors have been developed for this purpose, including spinner flasks bioreactors, rotating wall vessel bioreactors and laminar flow bioreactors.[8] Moreover, fluid flow influences cell behaviours, and therefore, these bioreactor systems might be used to regulate the growth and differentiation of progenitors mechanically.[9] The use of flow bioreactors has attracted particular attention in bone tissue engineering because bone remodelling is closely related to fluid micromovement due to the slight bone deformation which occurs as a result of physical activity.[10] On the other hand, it has been reported that mammalian cells are susceptible to fluid shear, and an inappropriate level of shear stress leads to cell death.[11] The shear-induced damage is further accelerated by turbulent flow, which is more likely to be generated in spinner flask and rotating wall vessel bioreactors.[11,12] Laminar flow bioreactors facilitate precise control of fluid pattern through engineered constructs, which is considered to be a less damaging and more predictable procedure.[13] Moreover, laminar flow bioreactors provide uniform gas and nutrient supply within the construct with a relatively low shear rate.[6] Therefore, the use of laminar flow bioreactors seems advantageous for controlling the fate of progenitors by fluidic stimuli.

In bone tissue engineering, several studies in 2D flow systems reported the mechanical induction of osteogenesis without the presence of osteogenic supplements, namely the combination of dexamethasone, β-glycerophosphate and ascorbic acid or bone morphogenetic protein 2 (BMP-2). For examples, as early as 1 h after perfusion, osteoblast precursors, MC3T3-E1, responded to shear stress at 2 Pa by upregulating a key transcription factor, Runt-related transcription factor 2 (RUNX2), for osteogenesis.[14] Further, the upregulation of other osteogenic markers such as collagen type 1 (COL1), osteocalcin (OCN) and alkaline phosphatase (ALP) was observed after 3 days of continuous perfusion.[15] Similarly, mesenchymal stem/stromal cells (MSC) were reported to undergo osteogenesis solely as a response to mechanical stimuli. Studies using human bone marrow-derived MSC reported that shear stress at 0.4–2.2 Pa increased the expression of BMP-2, bone sialoprotein (BSP), osteopontin (OPN) and ALP together with enhanced calcium deposition within 7 days.[16–18] Further comparable results were reported in MSC isolated from rodents at 1.09 mPa–1.03 Pa.[19] Compared with 2D models, however, there is only limited evidence on fluid flow-induced osteogenesis in the 3D environment. Human fetal osteoblasts, hFOB 1.19, subjected to cyclic fluid shear stress at 3.93 mPa for 28 days on functionalised polycaprolactone/hydroxyapatite scaffolds, exhibited increased ALP activity, extracellular matrix (ECM) formation and mineralisation.[20] A few studies of MSC in a 3D environment have reported promotion as well as suppression of osteogenesis by fluid flow. However, most of these studies were conducted in the presence of either chemical supplements or osteoinductive biomaterials such as decellularised matrix constructs, ECM-coated or hydroxyapatite-laden scaffolds.[13,21–25] The lack of concrete evidence supporting fluid flow-induced osteogenesis in 3D scaffolds may be also attributed to the complexity of 3D dynamic culture systems. A relatively complex bioreactor set-up is required to establish stable culture conditions such as systems for environmental monitoring and control. Moreover, the assessment of flow pattern in culture chambers within 3D constructs is challenging. Unlike the 2D environment, fluid effects are exerted as multidirectional shear force (i.e. a sliding force applied parallelly to the surface) and pressure (i.e. a compressive force applied perpendicularly onto the surface). Therefore, it is computationally expensive to estimate fluid effects, and a thorough parameterisation of experimental configurations is necessary to achieve high predictive power.[26]

Thus, it remains unclear whether MSC osteogenesis can be induced solely by fluid flow in 3D constructs, namely, without the presence of the osteogenic supplements. The aim of the present study was to precondition MSC for bone regeneration by developing and optimising a laminar flow bioreactor. It was hypothesised that appropriate fluid flow could direct MSC towards the osteoblastic lineage in the absence of osteoinductive supplements/materials. A further aim was to determine the optimal flow for supporting cell growth while robust osteogenesis was induced. Bone marrow-derived MSC from Lewis rats (rBMSC) were seeded onto the 3D microporous scaffolds of synthetic copolymer, poly(L-lactide-co-trimethylene carbonate) lactide (LTMC), and subjected to fluid flow at different flow rates for 21 days in a custom-designed laminar flow bioreactor. Here, we successfully provoked osteogenesis in the bioreactor without the presence of osteogenic supplements, which was confirmed by their expression patterns of osteogenic and multipotent markers, cell proliferation, morphology, ECM formation and calcium deposition. The approach will further open the possibility of clinical translation of a laminar flow bioreactor as the induction of osteogenesis without using the chemicals could reduce concern over the risk of unforeseen effects of the drugs, and it is expected to enhance bone regeneration after the transplantation of preconditioned constructs into damaged sites.

Materials and methods

rBMSC isolation and expansion

The study was approved by the Norwegian Animal Research Authority (local approval number 20146866)

and conducted according to the European Convention for the Protection of Vertebrates used for Scientific Purposes.

BMSC were isolated from the femurs of Lewis rats as described previously.[27] The cells were maintained in alpha minimum essential medium (α-MEM: 22571-020, Gibco™, USA) supplemented with 10% fatal bovine serum (FBS: 10270-106, Gibco™, USA) and 1% penicillin and streptomycin (SV30010, HyClone, USA) at 37°C in 5% CO_2 humidified atmosphere. rBMSC from the third and fourth passages were used in the experiments.

Fabrication of 3D microporous scaffolds of LTMC and cell seeding

3D microporous scaffolds of LTMC, 1.2 mm in thickness and 12 mm in diameter, were fabricated by a salt particles-leaching technique as described previously.[28] Briefly, LTMC (RESOMER® LT706 S, Evonik) was dissolved in chloroform on a magnetic stirrer and mixed in petri dished with sodium chloride particles (diameter range 90–600 μm). A lid was left on to allow gradual evaporation of the chloroform. The dried construct was then punched into 12 mm diameter pieces and washed thoroughly with distilled water to remove the sodium chloride. The scaffolds were placed in 48 well plates and sterilised using 70% ethanol and ultraviolet exposure for 2 h. The characterisation of LTCM scaffolds was described previously.[29]

Before cell seeding, the scaffolds were prewetted with α-MEM for 24 h, and 250,000 cells were then seeded per scaffold and incubated at 37°C in 5% CO_2 humidified atmosphere for 72 h, before being transferred into the bioreactor.

Characterisation of rBMSC by multilineage differentiation and flow cytometry

To confirm the multipotency of rBMSC, their capacity for differentiation into osteoblasts, adipocytes and chondrocytes was tested. For osteogenic differentiation, rBMSC were seeded and incubated in α-MEM supplemented with 1% penicillin and streptomycin, 10% FBS, 173 μM L-ascorbic acid (A8960; Sigma-Aldrich, USA), 10 nM Dexamethasone (D4902; Sigma-Aldrich, USA) and 10 mM β-Glycerophosphate (G9422; Sigma-Aldrich, USA) for 21 days. To evaluate mineral deposition, the cells were stained with 0.1% Alizarin red S for 20 min at RT, followed by washing five times with Milli-Q water. For adipogenic differentiation, rBMSC were incubated in α-MEM supplemented with 1% Penicillin-Streptomycin, 10% FBS, 100 nM Dexamethasone, 10 μg/ml Insulin (I9278-5ML; Sigma-Aldrich, USA), 0.2 mM Indomethacin (17378 -5G; Sigma-Aldrich, USA) and 0.5 mM 3-Isobutyl-1-methylxanthine (I5879-250MG; Sigma-Aldrich, USA) for 14 days. To detect lipids, the cells were stained with

0.5% Oil Red O (CAT NO) in isopropanol for 30 min at RT, followed by washing three times with PBS. The cell nuclei were counterstained with Haematoxylin solution (GHS3-50 ml, Sigma-Aldrich, USA) for 5 min and washed three times with PBS. For chondrogenic differentiation, the cells were cultured in 3D pellet and micromass culture systems. Both culture methods used chondrogenic differentiation medium (CCM000/CCM020, R&D Systems, USA) in accordance with the manufacturer's protocol. After 21 days of incubation, the chondrogenic pellets were embedded in Tissue-Tek® O.C.T.™ Compound (4583, Sakura, Netherlands) and sectioned into 7 μm thick slices at −18°C using a cryostat (MNT, SLEE, Germany). The samples were stained with 1% Alcian Blue (pH 2.5; A5268, Sigma-Aldrich, USA) dissolved in acetic acid for 30 min at RT and washed five times with Milli-Q water.

For flow cytometry, rBMSC at passage three were trypsinised and resuspended in blocking buffer which consists of staining buffer (BUF0730, Bio Rad) with 0.5% BSA (37,525, ThermoScientific) and 2% FBS. After 1 h of incubation at 4°C, approximately 15,000–20,000 cells/staining were incubated with either primary antibodies or isotype controls for 30 min at 4°C in the dark. Primary antibodies and isotype controls used were anti-CD44H IgG2aκ antibody (1:100; 203901, BioLegend, USA), anti-CD73 IgG1κ antibody (1:100; 551123, BD Pharmingen, USA), PE anti-CD90 IgG1κ antibody (1:100; 551401, BD bioscience, USA), anti-Sca1/Ly6 polyclonal antibody (1:500; AB4336, Sigma-Aldrich, USA), FITC anti-CD34 IgG2aκ antibody (1:100; 11-0341-82, eBioscience, USA), PE anti-CD45 IgG1κantibody (1:100; 202207, BioLegend, USA), PE anti-CD79 IgG1κ antibody (1:100; 12-0792-41, eBioscience, USA), anti-Stro1 antibody (1:100; 14-6688-82, Invitrogen, USA), FITC Mouse IgG2aκ Isotype Ctrl Antibody (1:100; 400207, BioLegend, USA), PE Mouse IgG1κ Isotype Ctrl Antibody (1:100; 400111, BioLegend, USA), Mouse IgM Isotype Ctrl Antibody (1:100; 14-4752, Invitrogen, USA), Mouse IgG1κ Isotype Ctrl Antibody (1:100; 554121, BD Pharmingen, USA) and Mouse IgG2a Isotype Ctrl Antibody (1:100; 401501, BioLegend, USA). After the primary antibody incubation, the cells were sequentially centrifuged at 300 rcf for 5 min and washed three times with the staining buffer with 0.5% BSA. For the samples stained with unconjugated primary antibodies, the cells were subsequently incubated with secondary antibodies followed by sequential centrifugation and wash three times. Secondary antibodies used were Alexa Fluor 488 anti-mouse IgG antibody (1:500, A-11001, Invitrogen, USA), Alexa Fluor 488 anti-rabbit IgG antibody (1:500, A-11008, Invitrogen, USA) and Alexa Fluor 647 anti-mouse IgM antibody (1:500; A-21238, Invitrogen, USA). The data of the stained cells were captured by AccuriC6 (BD Biosciences, USA) and analysed using FlowJo software version 10.6.2 (Becton, Dickinson & Company, USA)
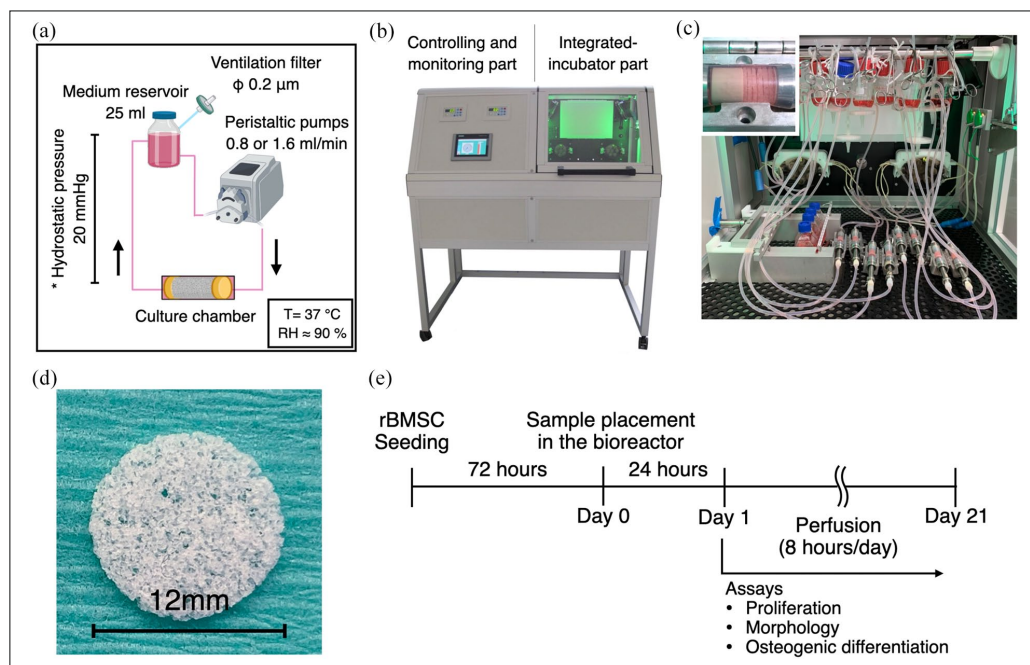
Figure 1. Experimental setup and timeline using the laminar flow bioreactor: (a) schematic illustration of environmental factors during dynamic culture. T: temperature, RH: Relative humidity, (b) the custom-made laminar flow bioreactor, which consists of controlling/monitoring part and integrated-incubation part, (c) image of inside-bioreactor during experiment. Culture chambers were connected to medium reservoirs via silicon tube, and medium was perfused by peristaltic pumps. In the culture chambers, 6 scaffolds (1.2 mm thickness and 12 mm diameter) were piled and sandwiched by rectifiers. The samples for the static control were also placed in the bioreactor so that they were subjected to the same environmental conditions except for fluid flow, (d) the optical image of the scaffold used. The scaffold was made of poly(L-lactide-cotrimethylene carbonate) and possess a microporous structure, and (e) experimental timeline. rBMSC were seeded on the scaffolds, and 3 days later, they were transferred into the bioreactor. Medium perfusion was performed for 8 h a day for 21 days.

Configuration of the lamina flow bioreactor and dynamic cell culture

The schematic experimental configuration is shown in Figure 1(a). The custom-designed laminar flow bioreactor was developed in the Fraunhofer Institute for Silicate Research. The bioreactor is equipped with 2 peristaltic pumps, monitoring sensors (temperature, gas and pressure), a CO_2 injector, electric fans, a heating pad and a control panel (Figure 1(b)). To establish continuous perfusion, medium reservoirs and culture chambers were connected by silicon tubes (inner diameter 3.2 mm). The medium reservoirs were located approximately 30 cm above the culture chamber to suppress air bubble formation in the micropores. In the culture chambers, six scaffolds were stacked to give a total thickness of 7.2 mm and sandwiched by flow rectifiers (Figure 1(c) and (d)). Culture medium was perfused at either 0.8 (FL-L) or 1.6 ml/min (FL-H) for 8 h a day for 21 days (Figure 1(e)). The static control samples were placed in T25 flasks and

incubated in the bioreactor so that both groups were subjected to the same environmental conditions (i.e. temperature, humidity, gas concentration and environmental frustration caused by opening/closing the bioreactor door). The same amount of culture medium, 25 ml, was supplied to each group for the consideration of paracrine effects, and half of the culture medium was refreshed every 3–4 days. The experiment was repeated six times to complete the planned assays.

In-silico modelling of fluid flow and characterisation

For the estimation of fluid flow pattern and its mechanical effects, in silico modelling was undertaken using COMSOL Multiphysics version 5.6 (COMSOL AB, Sweden). Briefly, the geometry of the culture chamber including the scaffolds and the rectifiers was reproduced computationally. The mechanical properties of the culture medium were assumed to be comparable with water.

The scaffolds were assigned as porous domains so that the Darcy's law was applied to avoid excessive computational burden. Porous properties were parameterised using data previously obtained by microCT analysis of the scaffold, including porosity 91.708% and permeability 5.80216e-09 m^2.[29] From the inlet to the outlet, a fully developed flow was applied at a flow rate of either 0.8 ml/min (FL-L) or 1.6 ml/min (FL-H). Non-slip wall condition was applied to the boundary condition of the fluid paths (i.e. metal parts, silicon tubes). As a representative for visualisation of shear stress within the complex 3D structure, the geometry of the scaffold was obtained by microCT (Skyscan 1172, SkyScan, Belgium) primarily and converted into an *.stl* file. A cube with a diameter of 1.2 mm was dissected from the middle of the geometry to make it possible to proceed with computation. The dissected part was assumed to be located at the front row of the scaffold pile.

Quantification of double strand DNA (dsDNA)

For the cell proliferation assay, the six samples were collected on day 3, 7, 14 and 21, in 0.1% Triton-X in Milli-Q® water, and cell lysate was obtained by three freeze-thaw cycles. The experiment was repeated twice. The amount of dsDNA was quantified using Quant-iT™ PicoGreen™ dsDNA Assay Kit (P7589; Invitrogen, USA) in accordance with the manufacturer's protocol. The intensity of fluorescence was measured at Ex/Em = 480/520 nm using a microplate reader (VLBL00D0; ThermoFisher Scientific, Finland).

Quantification of ALP activity

The cell lysate was obtained by the same method described in the section 2-6. The 50 μl of cell lysate was incubated with the same amount of P-nitrophenyl phosphate (pNPP, 20-106; Sigma-Aldrich, Germany) for 5 min at room temperature. Absorbance was measured at 405 nm using the microplate reader.

Quantitative reverse transcription polymerase chain reaction (RT-qPCR)

The samples for RT-qPCR were snap-frozen in liquid nitrogen on day 3, 7, 14 and 21 day and stored at −80°C until processed. Six scaffolds from one culture chamber were grouped into 3: 1st–2nd, 3rd–4th and 5th–6th scaffolds from the inlet, to examine variation within the group. Total RNA was extracted using a Maxwell® 16 Cell LEV Total RNA Purification Kit (AS1280; Promega, USA) in accordance with the manufacturer's protocol. Subsequently, reverse transcription was performed using a Transcription Kit (4368814; Applied Biosystems, USA). RT-qPCR was conducted with the StepOne™ real-time PCR system

(4453320, Applied Biosystems, USA). The primers used are listed in table S1. Relative expression of each mRNA was calculated with the ΔΔCt method normalised by GAPDH.[30] The data is represented as a mean value (±s.e.m) of three replicates.

Immunofluorescent staining and confocal microscopy

The samples for immunofluorescence were obtained from the middle part of the piled scaffolds (i.e. third and fourth from the inlet) and fixed in 4% PFA for 15 min at room temperature unless otherwise stated. The samples were then permeabilised in 0.1% Triton X-100 in PBS (PBSTx) for 15 min at room temperature. Nonspecific binding was blocked with 20% normal goat serum in 0.1% Tween-20 in PBS (PBSTw) followed by incubation with primary antibodies overnight at 4°C. The primary antibodies used were anti-αTubulin antibody (1:250; 62204, Invitrogen, USA), anti-ROCK1 antibody (1:250; GTX113266, GeneTex, USA), anti-PCNA antibody (1:100; sc-56, Santa Cruz Biotechnology, USA), anti-RUNX2 antibody (1:250; ab192256, Abcam, UK) and anti-collagen type 1 antibody (1:1000; ab90395, Abcam, UK). Subsequently, the samples were washed five times, for 5 min each, with PBSTw. Incubation with secondary antibodies was undertaken with Phalloidin Alexa Fluor 488 (1:250, A12379; Invitrogen, USA) and 4′,6-diamidino-2-phenylindole (DAPI; 1:5000, 62247; Thermo Fisher Scientific, USA) for 1 h at RT followed by washing five times, for 5 min each, with PBSTw. The secondary antibodies used were Alexa Fluor 568 anti-rabbit IgG antibody (1:500; A11011, Invitrogen, USA) and Alexa Fluor 635 anti-mouse IgG antibody (1:500; A31575, Invitrogen, USA). For collagen type 1 staining, ice-cold methanol was used as a fixative. For PCNA staining, antigen retrieval was performed with 10 mM sodium citrate (pH 6.0) at 95°C for 20 min prior to primary antibody incubation. For image acquisition, the samples were placed on confocal dishes and mounted in ProLong™ Gold antifade reagent (P36939; Invitrogen, USA). Z-Stack images were acquired by a confocal microscope (TCS SP8; Leica, Germany) equipped with 20x and 40x water immersion objectives. Images were processed and analysed with Fiji/ImageJ.[31] All images were represented as *z*-stack images of 150 μm thickness.

Alizarin red S staining and quantification

The six samples were fixed in 4% paraformaldehyde for 40 min and washed three times in Milli-Q® water. Calcium deposition was evaluated by Alizarin Red S staining (0.1% Alizarin Red S, A5533; Sigma-Aldrich, USA) for 20 min followed by washing six times with Milli-Q® water. For quantification, the dye was extracted with 100 mM cetylpyridium chloride overnight at room temperature.

Absorbance was measured at 540 nm using the microplate reader.

Statistics

All data are represented as mean ± standard deviation unless otherwise specified. For multiple comparison, the data were evaluated by one-way ANOVA followed by Bonferroni's multiple comparisons test by using SPSS® Statistics version 25 (IBM, USA). A p value <0.05 was considered to be statistically significant.

Results

Characterisation of rBMSC used in the study

rBMSC were characterised by their ability to adhere to plastic surfaces, multi-lineage differentiation and their expression of surface markers. The isolated cells were able to adhere to plastic surfaces, self-renew and differentiate into osteoblasts, adipocytes and chondrocytes under the inductive conditions (Figure 2(a) and (b)). Flow cytometry confirmed that the cells expressed putative rodent MSC markers including CD44H, CD73, Stem cell antigen-1 (Sca1/Ly6) and CD90, while little expression of haematopoietic markers, including CD34, CD45 and CD79, was observed. 4.1% of cells were identified as Stro-1 positive cells (Figure 2(c)–(e)).

In silico modelling for flow characterisation

To estimate the characteristics and magnitude of fluid flow through the scaffold constructs in the bioreactor system, the culture chambers were reproduced computationally. In the chambers, stacked scaffolds with a total thickness of 7.2 mm were sandwiched by flow rectifiers and placed in the culture chamber (Figure 3(a)). From the inlet, fully developed laminar flow was applied (Figure 3(b)). The estimated mean values of fluid velocity within the scaffolds were 0.21 ml/min and 0.42 ml/min in FL-L and FL-H, respectively, despite a large local variation within the groups. The velocity was larger in the middle of the scaffold than in peripherical areas (Figure 3(c)). In both groups, the Reynolds number is below 0.2 at any point (Figure 3(d)). Shear stress distribution was corresponded with the local velocity, ranging from nearly 0 to 6.75 mPa (mean: 0.20 mPa) and to 13.35 mPa (mean: 0.40 mPa) in FL-L and FL-H, respectively (Figure 3(e)). The greatest hydrodynamic pressure (i.e. pressure exerted by fluid in motion) was estimated to occur on the scaffold at the inlet side, gradually decreasing as flow goes in, with a range from 7.06 to 7.46 Pa (mean: 7.30 Pa) and 14.36 to 15.16 Pa (mean: 14.84 Pa) in FL-L and FL-H, respectively (Figure 3(f)). The representative illustration of shear stress distribution within the actual geometry of the porous scaffold was given from the closest scaffold to the inlet (Figure 4).

The magnitude of shear stress significantly varied from point to point for their complex 3D geometry, but overall, the magnitude of fluid effects from the simplified geometry with parameterisation seems comparable to the actual geometry.

Inhibitory effect on proliferation and alteration of cell morphology/distribution under fluid flow

To evaluate general cell behaviours under the fluid effects in a 3D environment, proliferation activity and cell morphology were assessed by immunofluorescence and the quantification of dsDNA. The expression of a proliferation marker, PCNA, shows that the majority of rBMSC in the static condition were highly proliferative on day 7, but PCNA positive cells decreased significantly under fluid flow, to approximately one-third compared with the static counterpart (FL-L: $p=0.007$ and FL-H: $p=0.002$) (Figure 5(a) and (b)). The percentage of PCNA positive cells was slightly higher in FL-L than in FL-H, but the difference was not statistically significant ($p=0.74$). The inhibitory effect of fluid flow on proliferation was confirmed by the quantification of dsDNA, showing that the proliferation of rBMSC in FL-L fell below the static counterpart, and in FL-H, rBMSC did not increase but decrease over the period of 21 days (Figure 5(c)). No significant difference was observed in the amount of dsDNA among the stack of scaffolds within each group. In a static condition, rBMSC maintained their spindle shape and aligned uniformly along with the porous structure of the scaffolds on day 7 (Figure 6(a) and (b)). In contrast, rBMSC subjected to fluid flow tended to show more spreading morphology. Cell distribution was not as even, and the area of cell aggregation was locally observed both in FL-L and FL-H groups as the cells formed scattered colonies. The localisation of colony-like aggregates was spotted at both peripherical and middle regions of the scaffold throughout the stacked construct. Under perfusion, rBMSC showed higher intensity of F-actin and ROCK1. RT-qPCR and image quantification showed that the cells in FL-L and FL-H upregulated ROCK1 in mRNA and protein levels significantly (Figure 6(c) and (d)). ROCK1 intensity was significantly higher in the FL-L group and FL-H groups, and statistical significance was found in the static control versus FL-H ($p=0.0011$) and FL-L versus FL-H ($p=0.0040$). The mean intensity of F-actin also increased as the flow rate increased although there was no statistical significance.

Fluid flow-induced osteogenesis of rBMSC in the absence of osteogenic supplements

During the dynamic culture, mRNA expression of osteogenic markers as well as putative MSC markers were evaluated by RT-qPCR (Figure 7(a) and (b)). A noticeable
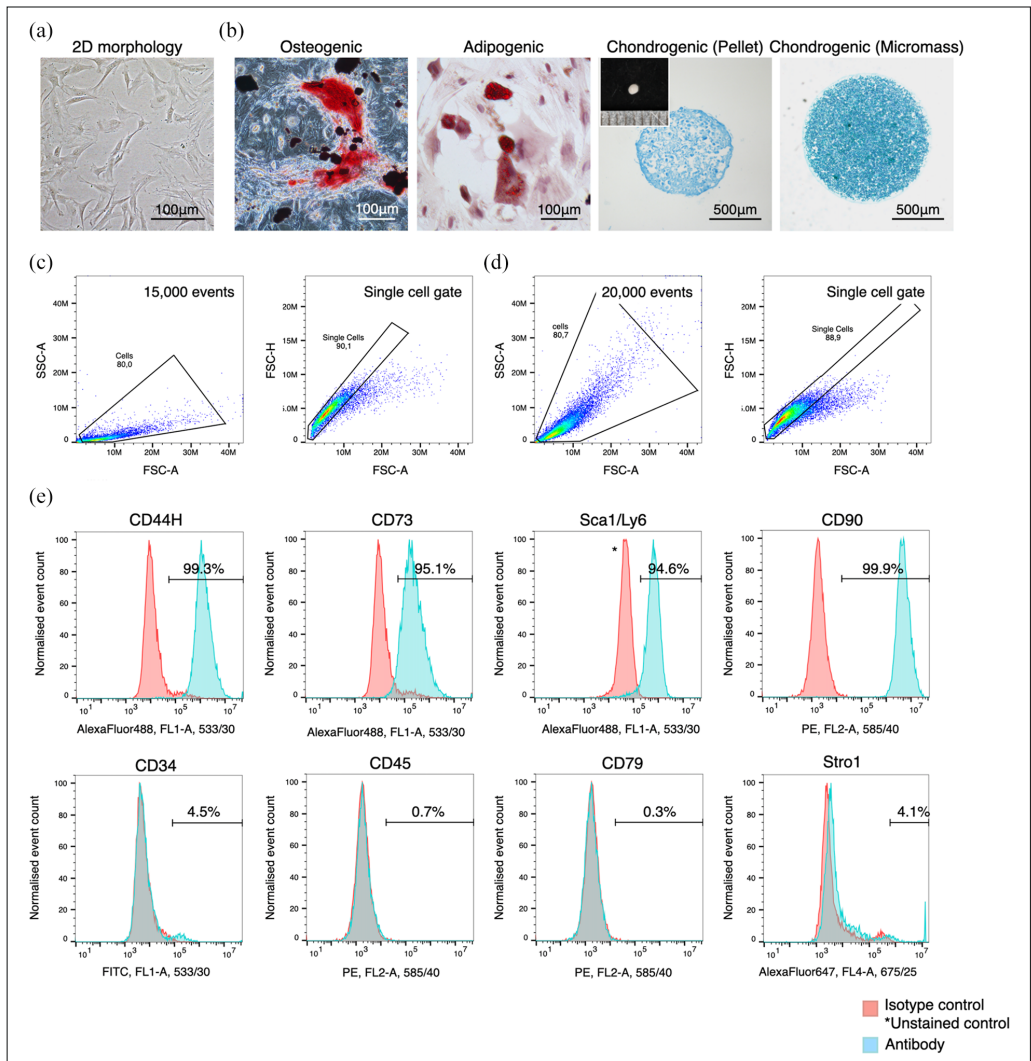
Figure 2. Characterisation of rBMSC used in the study: (a) rBMSC used in the study possessed a plastic adherent property and showed spindle morphology, (b) rBMSC were capable of differentiating into osteoblasts, adipocytes and chondrocytes under inductive culture conditions, (c) the gating strategy for the flow cytometry analysis for live cells and (d) fixed cells. Cells were distinguished from debris in the FSC-A VS SSC-A plots and then singlets were distinguished in the FSC-A VS FCS-H plot, and (e) rBMSC exclusively expressed putative rat MSC markers including CD44H, CD73, Sca-1/Ly6 and CD90 while they did not express haematopoietic markers including CD34, CD45 and CD79. Stro1 expression was only found in approximately 4% of the population.

variation in the expression patterns of the evaluated mRNA was not found between 1st–2nd, 3rd–4th and 5th to 6th scaffolds. A key transcription factor for osteogenesis, RUNX2, was consistently upregulated in the dynamic culture groups. On day 7, the expression level was 1.5 times and 2.0 times higher in FL-L ($p=0.0023$) and FL-H ($p<0.001$), respectively. While expression in the static

control decreased from day 7 to day 21, RUNX2 levels remained higher in the FL-L and FL-H groups. There was a similar tendency in the expression of another key transcription factor, SP7, which showed significant upregulation in both FL-L and FL-H groups from day 7 onwards compared with the static control. Furthermore, the upregulation of other osteogenic markers including IBSP, ALPL,
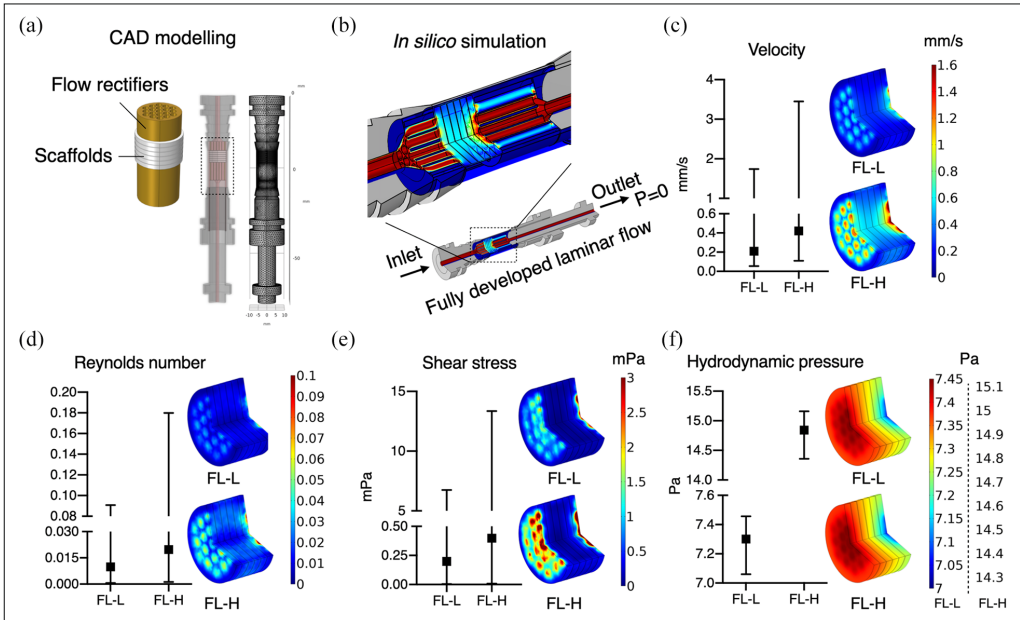
Figure 3. (a) The geometry of the culture chamber and the inlet/outlet was computationally reproduced. In the culture chambers, the scaffolds and rectifiers were placed as those in the actual experimental setting, (b) from the inlet, fully developed laminar flow of 0.8 ml/min (FL-L) or 1.6 ml/min (FL-H) was applied, and (c–f) the mean values and the range of velocity, Reynolds number, share stress, hydrodynamic pressure and their distribution within the scaffold construct were depicted.
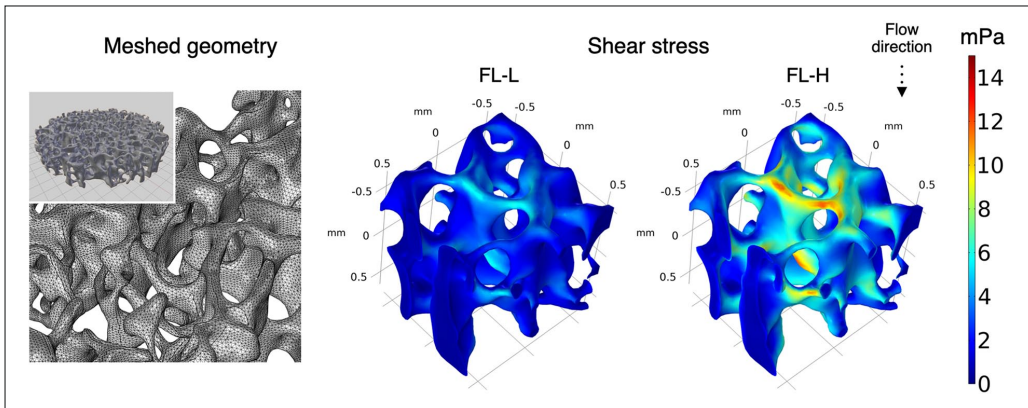

Figure 4. In silico modelling using the actual scaffold geometry obtained by microCT to illustrate the distribution of shear stress within the scaffold, the scaffold geometry was obtained by microCT and imported to the processing softwires as stl. file. To reduce computational burden, 1.2 mm cube was dissected from the middle of the scaffold and computed.

and SPP1 was observed from day 7 onwards. A late marker of osteogenesis, BGLAP, was also upregulated by approximately 7.1 and 3.9 times in FL-L ($p < 0.001$) and FL-H ($p < 0.001$) groups, respectively, on day 21. The level of expression of these osteogenic markers was consistently higher in the FL-L than in the FL-H on day 21. It was of interest to note that the putative MSC markers Nt5e (CD73) was dramatically downregulated over the period of 21 days and Thy1 (CD90) for the first 7 days during the induction of osteogenesis by fluid flow.
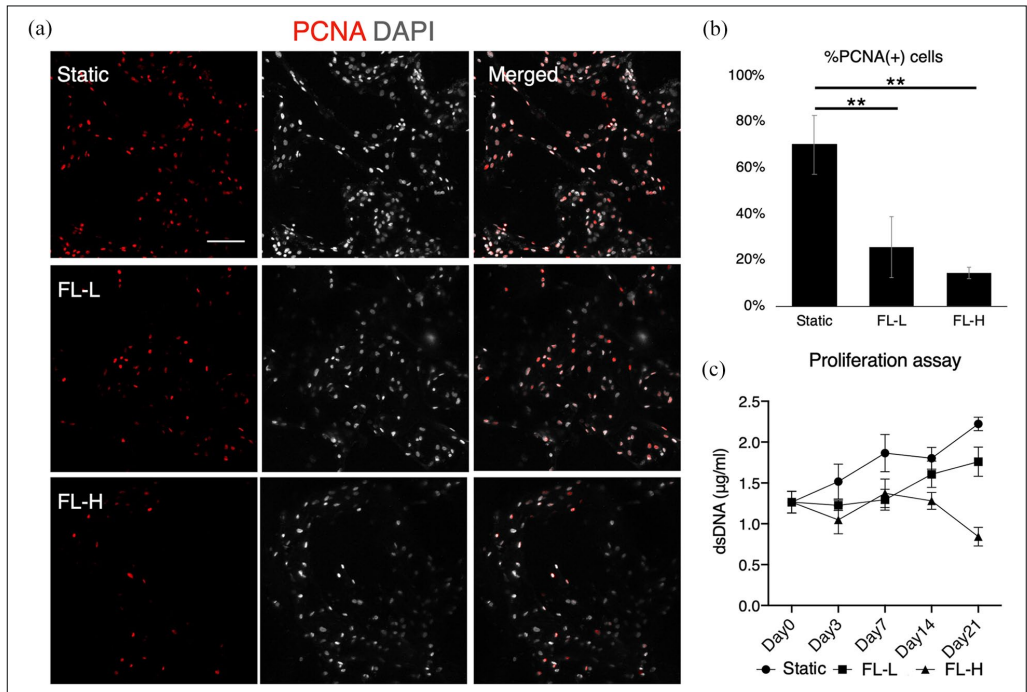
Figure 5. Proliferation of rBMSC under differential rate of fluid flow: (a) immunofluorescent images of a proliferation marker, PCNA, after 7 days of static culture and perfusion cultures at the flow rate of 0.8 ml/min (FL-L) and 1.6 ml/min (FL-H), (b) quantification of %PCNA positive cells, and (c) quantification of double-strand DNA (dsDNA) in the scaffold construct. While rBMSC highly proliferated during the period of 21 days in the static control, the cells in the FL-L and FL-H showed reduced proliferation capability. In the FL-H group, the amount of dsDNA decreased significantly on day 21.
Scale bar = 100 μm.
**p < 0.01.

To confirm the upregulation of RUNX2 by fluid flow, the samples were analysed by immunofluorescence (Figure 8(a)). In the static condition, rBMSC scarcely expressed RUNX2. However, in the dynamic culture groups, some populations of rBMSC, but not the majority, presented localised RUNX2 in the nuclei on day 7. This was confirmed by the quantification of RUNX2, revealing that 8.8% and 13.6% of cell populations increased their levels of RUNX2 expression in the FL-L ($p > 0.001$) and FL-H ($p > 0.001$), respectively, (Figure 8(b)). The ratio of RUNX2 upregulated cells was higher in the FL-L than in FL-H ($p = 0.032$). Taking representative cells whose RUNX2 intensity level was defined as the mean (shown as red lines in Figure 8(b)), it was confirmed that RUNX2 was specifically localised in the nuclei but not in the intracellular region, and its intensity was highest in the FL-H group (Figure 8(b)). Osteogenic induction was further confirmed by the formation of collagen type 1, ALP activity, and mineral deposition. On day 14, fibrous collagen structure was detected in the dynamic culture groups, whereas only sporadic collagen was secreted in the static counterpart (Figure 9(a)). The collagen structure was more evident in FL-L than in the FL-H. ALP activity, which is necessary to calcify ECM, was significantly higher in the FL-L ($p = 0.0080$) (Figure 9(b)). On day 21, mineral deposition was assessed by Alizarin Red S staining. Although the level of deposition was low in all groups, the level of calcium in the scaffolds in the FL-L were higher than in the static control ($p > 0.001$) and FL-H ($p = 0.036$) (Figure 9(c) and (d)). However, once the value was normalised by dsDNA, mineral deposition per cell was greatest in the FL-H (Figure 6(e)).

Discussion

Osteogenic preconditioning prior to transplantation was shown to enhance vascularization and bone formation at the recipient sites.[23,32] Under clinical conditions, however, the chemical induction of osteogenesis (i.e. the application of dexamethasone or growth factors) may be
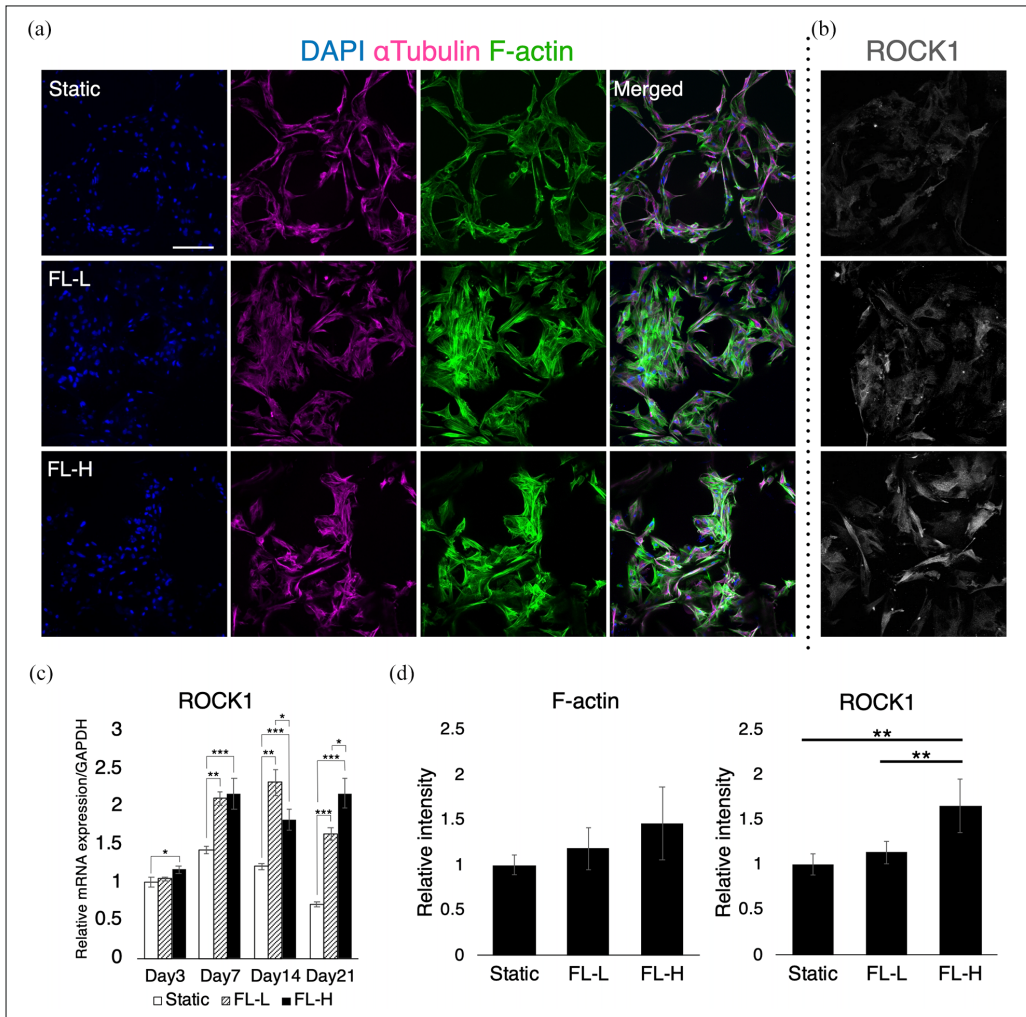
Figure 6. Morphological assessment of rBMSC subjected to differential flow rates for 7 days: (a and b) immunofluorescent images of αTubulin, F-actin and ROCK 1, (c) mRNA expression of ROCK1, and (d) image quantification of F-actin and ROCK1 intensity. Under the effect of fluid flow, rBMSC altered their morphology and alignment accompanied with the upregulation of ROCK1. FL-L: 0.8 ml/min, FL-H: 1.6 ml/min. Scale bar = 100 μm.
$*p < 0.05$. $**p < 0.01$. $***p < 0.001$.

contraindicated because of the risk of unforeseen effects. Dexamethasone is a synthetic glucocorticoid frequently supplemented both in adipogenic and in osteogenic media and determines the fate of MSC by regulating kye transcription factor for osteogenesis, RUNX2 and for adipogenesis, peroxisome proliferator-activated receptor γ2.[33] The fetal determination depends on the maturity and density of progenitor cells, its concentration and synergetic effects with other regulatory molecules.[34] Indeed, it has been suggested that the standard osteogenic medium may

induce not only osteogenic but also adipogenic differentiation of BMSC simultaneously.[35,36] Similarly, BMP-2 is an osteoinductive growth factor widely used to induce osteogenesis in vitro, and it is clinically approved by the U.S. Food and Drug Administration (FDA) for certain dental and orthoperiodic treatments to promote bone healing.[37] However, a large number of severe adverse effects have been reported, which include postoperative inflammation, infection, ectopic ossification, osteolysis, arachnoiditis, neurological deficits, retrograde ejaculation
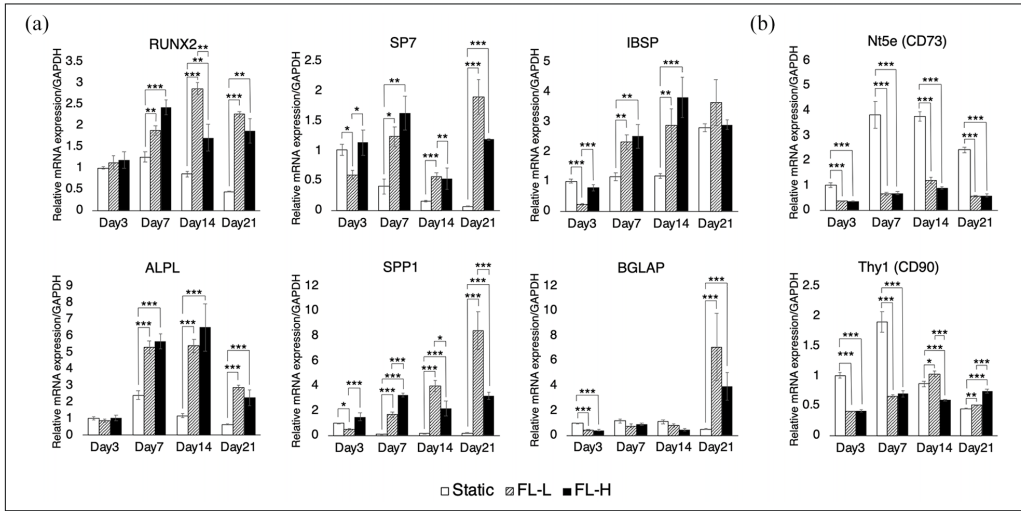
Figure 7. mRNA expression profile of osteogenic and putative MSC markers under perfusion by RT-qPCR: (a) rBMSC in the FL-L (0.8 ml/min) and FL-H (1.6 ml/min) groups significantly upregulated their early to middle osteogenic markers including RUNX2, SP7, IBSP, ALPL and SPP1 over the experimental period. A late osteogenic marker, BGLAP, was significantly upregulated in the dynamic culture groups on day 21. The upregulation was observed without the presence of osteogenic supplements and (b) putative MSC markers, CD73 and CD90, were significantly downregulated in the FL-L and FL-H.
All data are displayed as mean $\pm$ s.e.m.
*$p < 0.05$. **$p < 0.01$. ***$p < 0.001$.

and cancer.[38] Therefore, various studies have attempted to induce osteogenesis in the absence of osteogenic supplements. These include the application of osteoinductive biomaterials such as ECM-coated synthetic polymers or hydroxyapatite and co-culture systems with endothelial cells or immune cells.[25,39] Under natural conditions, bone homeostasis and remodelling are regulated by matrix strain and interstitial fluid movement caused by physical activity.[10,40] Indeed, mechanical clues including the control of microstructure, surface stiffness and roughness of scaffolds, fluid shear stress, pressure, compression and stretching, are effective in stimulating osteogenic properties.[39,41–43] In the present study, rBMSC were successfully preconditioned towards the osteoblastic lineage solely by applying low levels of fluid flow in the laminar flow bioreactor. Importantly, this was achieved without the presence of any type of osteoinductive chemicals/materials, by using medical-grade synthetic polymers, LTMC, as a scaffold material. The material offers biocompatibility and biodegradability suitable for bone regenerative therapy, but it is known to have low bioactivity and does not induce MSC osteogenesis alone.[44,45] This excludes the possibility of a synergetic effect of bioactive (i.e. osteoinductive) components and fluid flow as previously described.[24,46,47] Hence, the results provide evidence that osteogenesis of BMSC on 3D non-osteoinductive scaffolds can be induced solely by fluid flow in the absence of osteogenic supplements as reported in 2D systems where fluid effect is purely represented as shear stress.[14,15,19,20]

Various types of bioreactors have been developed for bone tissue engineering. Each of the systems has distinctive features, and therefore, the identification of experimental parameters is the first step in reconciling the experimental data. Multiple factors influence cell behaviours in addition to flow magnitude. It has been suggested that the volume of culture medium determines cell behaviour. A previous study using osteoblasts showed the reduction of mineralisation in a medium volume-dependent manner.[48] Similarly, excessive use of medium in perfusion bioreactors may dilute paracrine/autocrine factors and prevent the activation of the downstream targets.[49] Therefore, we used 25 ml culture medium, which is the minimum volume to maintain constant perfusion in our system. The initial seeding density was 250,000 cells per scaffold, and six scaffolds were placed in each culture chamber. This medium-to-cell ratio compares well with the standard static culture protocol provided by the manufacturer. In consideration of the effect of medium-to-cell ratio on cell growth, the same amount of culture medium was also applied to the static control, and the cells showed optimal growth. Another key factor taken into consideration was the prevention of air bubbles. These impede fluid flow, and bubbles entrapped within the scaffolds may adversely
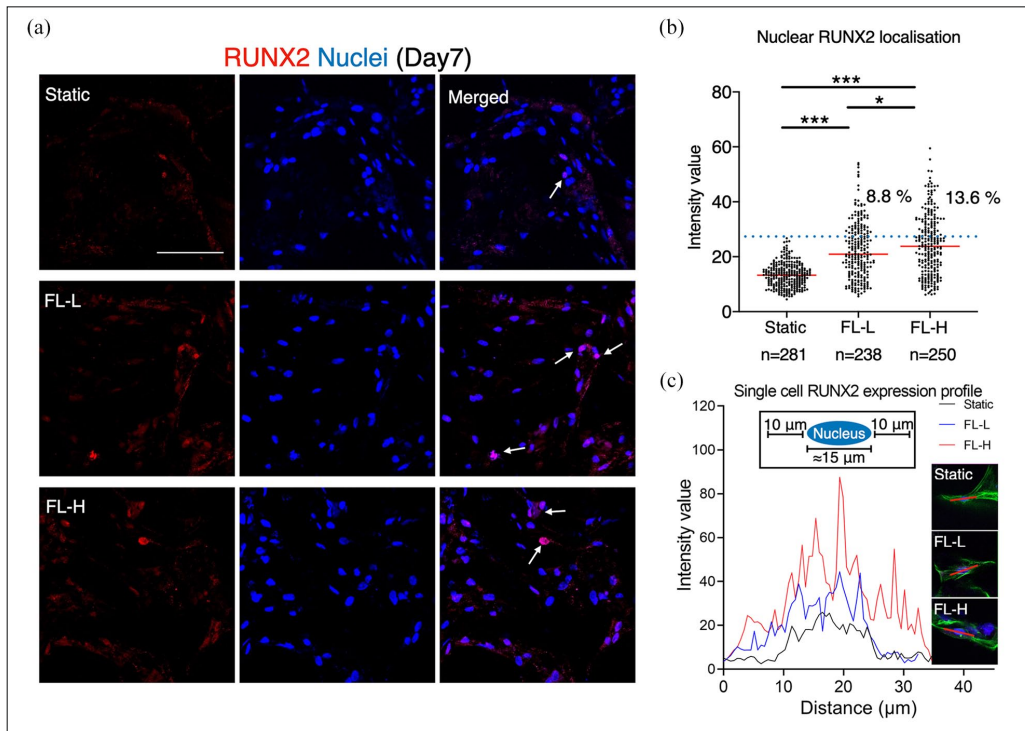
Figure 8. Upregulation and localisation of RUNX2 during the perfusion cell culture: (a) immunofluorescent images of RUNX2 showed that a small population of rBMSC in the FL-L (0.8 ml/min) and FL-H (1.6 ml/min) groups, but greater than the static counterpart, expressed RUNX2. Arrows indicate representative RUNX2 positive cells, (b) the image quantification revealed that 8.8% and 13.6% of the cells upregulated RUNX2 expression in the FL-L and FL-H, respectively, and (c) the line investigation using the representative cells confirmed that RUNX2 was localised in the nuclei but not in the intracellular areas.
Scale bar = 100 μm.
*p < 0.05. ***p < 0.001.

affect cell growth.[13,50] Indeed, air bubbles are readily generated in perfusion bioreactors used for bone tissue engineering due to continuous flow, serum proteins acting as a surfactant and the microporous structure and hydrophobic nature of 3D scaffolds.[51–54] Therefore, Henry's law was applied to supress bubble formation completely. Namely, 20 mmHg ($\approx$2.7 kPa) of hydrostatic pressure was applied simply by raising the medium reservoirs by approximately 30 cm. Previously, 100–300 kPa of hydrostatic pressure was proposed for promotion of osteogenic differentiation, but the hydrostatic pressure applied in the present study was considerably lower and therefore not considered critical. [43,55] As a key stimulus, the effect of fluid flow needs to be identified. Various studies have tested the utility of flow bioreactors, and mostly the flow rate was stated. However, flow rate itself does not represent the magnitude of fluid effects, and indeed, the magnitude varies significantly depending on the geometry of the culture chambers and the macro- and microstructures of the scaffolds.

Therefore, to allow eligible comparison with other systems, the type of flow (i.e. laminar or turbulent flow), shear stress and hydrodynamic pressure should be standardised to represent the characteristics of fluid flow. However, because real-time monitoring of these factors requires extensive equipment and is mostly impractical,[56,57] in silico finite element analysis is utilised to estimate flow characteristics computationally.[58] In silico analysis showed that the culture medium was relatively-evenly distributed within the scaffold constructs in the present study. The Reynolds numbers within the constructs were exclusively below 1, indicating laminar, but not turbulent flow.

The magnitude of fluid shear and dynamic pressure as well as the duration of perfusion are important determinants of cell growth and fate.[18] Therefore, the flow rate and duration were determined on initiation of this study. Continuous perfusion at 0.8 ml/min for 24 h did not support cell growth unlike that for 8 h, and a high magnitude flow (i.e. 3.2 ml/min) for 8 h a day caused pronounced
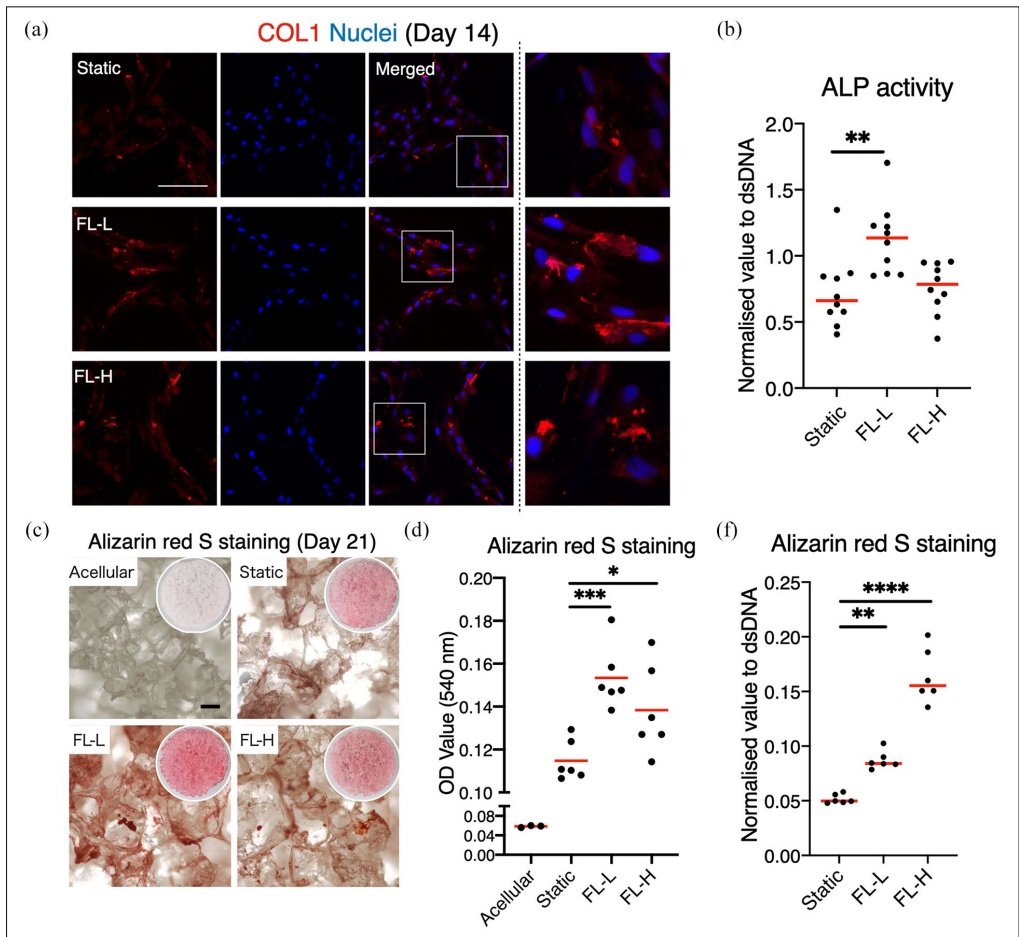
Figure 9. Promotion of rBMSC matrix production and calcium deposition by fluid flow: (a) immunofluorescent images of COL1 on day 14 showed that collagen formation was promoted in the FL-L (0.8 ml/min) and FL-H (1.6 ml/min) groups, (b) ALP activity was significantly higher on day 14 in the FL-L than the static counterpart and FL-H group, and (c–e) Alizarin red S staining on day 21 showed enhanced calcium deposition by rBMSC cultured under perfusion. Total amount of calcium deposition was the highest in the FL-L, but the ratio of the deposition per dsDNA was the highest in the FL-H.
Scale bar = 100 μm.
$*p < 0.05$. $**p < 0.01$. $***p < 0.001$.

damage (Figure S1). This is supported by a previous in silico study, demonstrating that the nutrient and gas supply become uniform within the scaffold constructs as flow rate increases, but that the high shear stress might cause cell death in vitro.[6] Even if it does not cause cell death, fluid shear reduces cell proliferation of rBMSC in a dose-dependent manner by arresting the cell cycle at G0/G1.[59] Therefore, in this study, relatively low flow rates were tested: 0.8 ml/min and 1.6 ml/min for 8 h per day up to 21 days. In the FL-L group, rBMSC were subjected to shear stress up to 6.75 mPa and hydrodynamic pressure up

to 7.46 Pa. In the FL-H group, rBMSC were subjected to shear stress up to 13.35 mPa and hydrodynamic pressure up to 14.36 Pa. These values were presumably lower than shear stress and pressure exerted by interstitial flow in bone marrow under physiological as well as loaded conditions.[60–62] As expected, even these levels of gentle fluid stimulus supressed cell growth compared with the static culture condition. Nevertheless, the data showed that FL-L allowed rBMSC to gradually increase in number while FL-H prevented cell growth. Morphological evaluation revealed that rBMSC under perfusion altered their

alignment within the scaffold construct and formed colony-like aggregates. It is known that the formation of cell aggregates facilitates paracrine signalling and activates biological events including osteogenic differentiation.[63,64] The alternation of cell morphology and alignment were accompanied with enhanced F-actin polymerisation and upregulation of ROCK1. ROCK1 plays a crucial role in cell motility, adhesion and cell contraction by activating actomyosin complex, and therefore, rBMSC presumably underwent self-reorganisation to adapt to the environment. Previous studies have shown that ROCK1 activity is associated with MSC proliferation and osteogenic differentiation.[65,66] ROCK1 activity is negatively correlated with cell proliferation, while its activation promotes RUNX2 expression, leading to osteogenesis. The present study also suggests that ROCK1 activation caused by fluid flow may link to an inhibitory effect on proliferation and the promotion of osteogenesis. However, further studies are needed to confirm the causal relationship between fluid stimuli, ROCK1 activation and the induction of osteogenesis.

Previous studies using a 2D microfluidic system showed that sub-physiological shear stress was sufficient to upregulate osteogenic markers.[17,19] Therefore, we further evaluated fluid-induced osteogenesis in a 3D environment where fluid effects were exerted not only as shear stress but also as pressure. In both FL-L and FL-H, the mRNA expression of early-to-mid phase osteogenic markers, RUNX2, SP7, IBSP, ALPL and SPP1 was consistently upregulated over the period of 21 days. Upregulation of a late osteogenic marker, BGLAP, was observed only in the FL-L and FL-H groups on day 21, clearly suggesting that fluid stimuli directed the fate of rBMSC towards the osteoblastic lineage. The immunofluorescence showed that approximately 10% of rBMSC in the dynamic culture groups upregulated their RUNX2 expression in protein level on day 7. It was localised to the nuclei, indicating that RUNX2 acted as a transcription factor. Noteworthily, although the mRNA expression of RUNX2 was upregulated as a whole construct (i.e. a stack of six scaffolds) in the dynamic culture groups from day 7 onwards, the immunofluorescence and the quantification confirmed that the expression pattern of RUNX2 in protein level was rather heterogeneous. This may be attributed to not only the heterogeneous flow pattern but also the heterogeneous population of rBMSC: some of the population seemed more prone to be directed towards the osteogenic lineage by the fluid stimuli. Furthermore, it has been reported that the mRNA and protein expression of RUNX2 does not always coordinate each other, and the localisation of RUNX2 in nuclei as a transcription factor is spatiotemporally regulated.[67] In rBMSC, the consequence of the robust mRNA expression of RUNX2 may be either cytoskeletal expression/diffusion or nuclear localisation.[29] In the present study, the quantification and line investigation confirmed that the mRNA

upregulation of RUNX2 by fluid flow was accompanied by a degree of nuclear localisation. Similarly, collagen formation, ALP activity and mineral deposition were found to be enhanced in the dynamic culture groups. It is of interest to note that the FL-H group seemed to show higher osteogenic induction than the FL-L group despite the strong inhibitory effect on cell proliferation. This may accord with the tendency to gradually lose proliferative capability as they undergo differentiation.[68] Nevertheless, the induction of osteogenesis, particularly in terms of collagen formation and mineral deposition, by fluid flow is apparently not as robust as that achieved by the osteogenic supplements as previously tested in a study of osteogenic differentiation of rBMSC on LTMC scaffolds.[29] This could be attributable to the characteristics of each component of the common osteogenic supplement (i.e. dexamethasone, β-glycerophosphate and ascorbic acid). Dexamethasone is known to boost MSC proliferation before inducing differentiation, whereas in the present study the fluid flow caused simultaneous inhibition of proliferation.[69] This resulted in a lower cell number than in the static control. β-glycerophosphate acts as a source of phosphate to produce calcium phosphate, and therefore relatively low mineral production may be attributable to a lack of phosphate. Ascorbic acid is essential for collagen synthesis. In the present study, α-MEM was used as a standard growth medium in the study. It contains 50 mg/l of ascorbic acid, and therefore collagen formation was observed in all the groups but enhanced by the fluid flow.

Apart from the mechanical stimuli from fluid flow, mass transport may have influenced cell behaviours. The previous in silico study demonstrated an increase in nutrient/gas diffusion within a 3D construct in a velocity-dependent manner.[6] Indeed, the scaffolds placed in the static condition were subjected to reduced mass transport in comparison with the dynamic condition. This may have led to increased concentration gradient within the scaffolds: the highest concentration of O_2 and nutrients at the surface and waste products at the core. Therefore, in theory, the mass transport in the static control largely depended on a passive diffusive flux driven by the concentration gradient, whereas it was predominantly by the medium movement in the dynamic condition. Nevertheless, in the present study, the highly porous scaffolds with porosity 91.708% and permeability 5.80216e-09 m^2 were designed. This presumably allowed sufficient diffusion which supported optimal cell growth even without the presence of flow, and it was microscopically confirmed that cell distribution and proliferation profile were uniform among the scaffold even in the static condition. Admittedly, the effects of mechanical stimuli and mass transport would not be separable in the 3D culture system, but the effect of variance in mass transport could be considered minimum between the groups.

BMSC from Lewis rats were used in this study in order to avoid the risk of donor-to-donor variation. Hence, the

data are not necessarily generalisable to BMSC isolated from other species including humans. Noteworthily, BMSC are more osteoblast-oriented as a nature, and fluid flow may therefore promote their spontaneous differentiation into the osteoblastic lineage.[70] It was reported that adipose tissue-derived MSC (AT-MSC) were also mechanosensitive, and AT-MSC acquired osteoblastic nature after receiving fluidic mechanical stimulation in the presence of 1,25-dihydroxyvitamin D3, but whether fluid flow solely induces the osteogenesis of AT-MSC or other types of MSC apart from BMSC remains elusive.[71] The optimal magnitude of fluid effects and the duration for the purpose of osteogenic induction may be species-specific and possibly be donor-specific. Similarly, the magnitude may vary considerably, depending on material properties such as the micro- and macro-geometry and surface chemistry of the scaffolds even when the same flow rate is applied. Further, bioreactor design must be taken into consideration. Flow rate therefore needs to be optimised for each experimental setting. Under the present study conditions, osteogenesis was successfully induced in a 3D environment in the laminar flow bioreactor in the absence of osteoinductive materials/supplements. The potential clinical implications have yet to be determined. Further in vivo study is warranted to translate the bioengineering technology into clinical application.

Acknowledgements

Declaration of conflicting interests

The author(s) declared no potential conflicts of interest with respect to the research, authorship, and/or publication of this article.

Funding

ORCID iDs

Shuntaro Yamada https://orcid.org/0000-0003-0282-5498
Mohammed Ahmed Yassin https://orcid.org/0000-0003-0030-1906

Supplemental material

Supplemental material for this article is available online.

References

1. Ho-Shui-Ling A, Bolander J, Rustom LE, et al. Bone regeneration strategies: engineered scaffolds, bioactive molecules and stem cells current stage and future perspectives. *Biomaterials* 2018; 180: 143–162.

2. Dimitriou R, Jones E, McGonagle D, et al. Bone regeneration: current concepts and future directions. *BMC Med* 2011; 9: 66.

3. Arvidson K, Abdallah BM, Applegate LA, et al. Bone regeneration and stem cells. *J Cell Mol Med* 2011; 15: 718–746.

4. Abbasi N, Hamlet S, Love RM, et al. Porous scaffolds for bone regeneration. *J Sci Adv Mater Devices* 2020; 5: 1–9.

5. Pina S, Ribeiro VP, Marques CF, et al. Scaffolding strategies for tissue engineering and regenerative medicine applications. *Materials (Basel)* 2019; 12: 1824.

6. Bergemann C, Elter P, Lange R, et al. Cellular nutrition in complex three-dimensional scaffolds: a comparison between experiments and computer simulations. *Int J Biomater* 2015; 2015: 1–12.

7. Shakeel M, Matthews PC, Graham RS, et al. A continuum model of cell proliferation and nutrient transport in a perfusion bioreactor. *Math Med Biol* 2013; 30: 21–44.

8. Rauh J, Milan F, Günther K-P, et al. Bioreactor systems for bone tissue engineering. *Tissue Eng Part B Rev* 2011; 17: 263–280.

9. Gaspar DA, Gomide V and Monteiro FJ. The role of perfusion bioreactors in bone tissue engineering. *Biomatter* 2012; 2: 167–175.

10. Wittkowske C, Reilly GC, Lacroix D, et al. In vitro bone cell models: impact of fluid shear stress on bone formation. *Front Bioeng Biotechnol* 2016; 4: 719–728.

11. Tanzeglock T, Soos M, Stephanopoulos G, et al. Induction of mammalian cell death by simple shear and extensional flows. *Biotechnol Bioeng* 2009; 104: 360–370.

12. Brindley D, Moorthy K, Lee J-H, et al. Bioprocess forces and their impact on cell behavior: implications for bone regeneration therapy. *J Tissue Eng* 2011; 2011: 620247.

13. Tsai H-H, Yang K-C, Wu M-H, et al. The effects of different dynamic culture systems on cell proliferation and osteogenic differentiation in human mesenchymal stem cells. *Int J Mol Sci* 2019; 20: 4024.

14. Song J, Liu L, Lv L, et al. Fluid shear stress induces Runx-2 expression via upregulation of PIEZO1 in MC3T3-E1 cells. *Cell Biol Int* 2020; 44: 1491–1502.

15. Yu L, Ma X, Sun J, et al. Fluid shear stress induces osteoblast differentiation and arrests the cell cycle at the G0 phase via the ERK1/2 pathway. *Mol Med Rep* 2017; 16: 8699–8708.

16. Becquart P, Cruel M, Hoc T, et al. Human mesenchymal stem cell responses to hydrostatic pressure and shear stress. *Eur Cell Mater* 2016; 31: 160–173.

17. Kim KM, Choi YJ, Hwang J-H, et al. Shear stress induced by an interstitial level of slow flow increases the osteogenic differentiation of mesenchymal stem cells through TAZ activation. *PLoS One* 2014; 9: e92427.

18. Yourek G, McCormick SM, Mao JJ, et al. Shear stress induces osteogenic differentiation of human mesenchymal stem cells. *Regen Med* 2010; 5: 713–724.

19. Dash SK, Sharma V, Verma RS, et al. Low intermittent flow promotes rat mesenchymal stem cell differentiation in logarithmic fluid shear device. *Biomicrofluidics* 2020; 14: 054107.

20. Salifu AA, Obayemi JD, Uzonwanne VO, et al. Mechanical stimulation improves osteogenesis and the mechanical

properties of osteoblast-laden RGD-functionalized poly-caprolactone/hydroxyapatite scaffolds. *J Biomed Mater Res A* 2020; 108: 2421–2434.

21. Bhaskar B, Owen R, Bahmaee H, et al. Design and assessment of a dynamic perfusion bioreactor for large bone tissue engineering scaffolds. *Appl Biochem Biotechnol* 2018; 185: 555–563.

22. Birru B, Mekala NK and Parcha SR. Improved osteogenic differentiation of umbilical cord blood MSCs using custom made perfusion bioreactor. *Biomed J* 2018; 41: 290–297.

23. Harvestine JN, Gonzalez-Fernandez T, Sebastian A, et al. Osteogenic preconditioning in perfusion bioreactors improves vascularization and bone formation by human bone marrow aspirates. *Sci Adv* 2020; 6: eaay2387.

24. Datta N, Pham QP, Sharma U, et al. In vitro generated extracellular matrix and fluid shear stress synergistically enhance 3D osteoblastic differentiation. *Proc Natl Acad Sci U S A* 2006; 103: 2488–2493.

25. Thibault RA, Scott Baggett L, Mikos AG, et al. Osteogenic differentiation of mesenchymal stem cells on pregenerated extracellular matrix scaffolds in the absence of osteogenic cell culture supplements. *Tissue Eng Part A* 2010; 16: 431–440.

26. Israelowitz M, Weyand B, Rizvi S, et al. Development of a laminar flow bioreactor by computational fluid dynamics. *J Healthc Eng* 2012; 3: 455–476.

27. Yassin MA, Leknes KN, Pedersen TO, et al. Cell seeding density is a critical determinant for copolymer scaffolds-induced bone regeneration. *J Biomed Mater Res - Part A* 2015; 103: 3649–3658.

28. Odelius K, Plikk P and Albertsson A-C. Elastomeric hydrolyzable porous scaffolds: copolymers of aliphatic polyesters and a polyether-ester. *Biomacromolecules* 2005; 6: 2718–2725.

29. Yamada H, Yassin MA, Weigel T, et al. Surface activation with oxygen plasma promotes osteogenesis with enhanced extracellular matrix formation in three-dimensional microporous scaffolds. *J Biomed Mater Res A*. Epub ahead of print 5 March 2021. DOI: 10.1002/jbm.a.37151.

30. Livak KJ and Schmittgen TD. Analysis of relative gene expression data using real-time quantitative PCR and the 2(-Delta Delta C(T)) method. *Methods* 2001; 25: 402–408.

31. Schindelin J, Arganda-Carreras I, Frise E, et al. Fiji: an open source platform for biological image analysis. *Nat Methods* 2012; 9: 676–682.

32. Ma J, Both SK, Yang F, et al. Concise review: cell-based strategies in bone tissue engineering and regenerative medicine. *Stem Cells Transl Med* 2014; 3: 98–107.

33. Zhang Y, Khan D, Delling J, et al. Mechanisms underlying the osteo- and adipo-differentiation of human mesenchymal stem cells. *Sci World J* 2012; 2012: 1–14.

34. Han L, Wang B, Wang R, et al. The shift in the balance between osteoblastogenesis and adipogenesis of mesenchymal stem cells mediated by glucocorticoid receptor. *Stem Cell Res Ther* 2019; 10: 377.

35. Ghali O, Broux O, Falgayrac G, et al. Dexamethasone in osteogenic medium strongly induces adipocyte differentiation of mouse bone marrow stromal cells and increases osteoblast differentiation. *BMC Cell Biol* 2015; 16: 9.

36. Mikami Y, Lee M, Irie S, et al. Dexamethasone modulates osteogenesis and adipogenesis with regulation of osterix expression in rat calvaria-derived cells. *J Cell Physiol* 2011; 226: 739–748.

37. Sun J, Li J, Li C, et al. Role of bone morphogenetic protein-2 in osteogenic differentiation of mesenchymal stem cells. *Mol Med Rep* 2015; 12: 4230–4237.

38. Epstein N. Complications due to the use of BMP/INFUSE in spine surgery: the evidence continues to mount. *Surg Neurol Int* 2013; 4: 343.

39. Faia-Torres AB, Charnley M, Goren T, et al. Osteogenic differentiation of human mesenchymal stem cells in the absence of osteogenic supplements: a surface-roughness gradient study. *Acta Biomater* 2015; 28: 64–75.

40. Pei G-X, Qin Y-X, Hutmacher DW, et al. Bone tissue engineering: cell motility, vascularization, micro-nano scaffolding, and remodeling. *Biomed Res Int* 2014; 2014: 286978.

41. Kim J and Ma T. Bioreactor strategy in bone tissue engineering: pre-culture and osteogenic differentiation under two flow configurations. *Tissue Eng Part A* 2012; 18: 2354–2364.

42. Zhang Q, Lin S, Zhang T, et al. Curved microstructures promote osteogenesis of mesenchymal stem cells via the RhoA/ROCK pathway. *Cell Prolif* 2017; 50: e12356.

43. Zhao Y-H, Lv X, Liu Y-L, et al. Hydrostatic pressure promotes the proliferation and osteogenic/chondrogenic differentiation of mesenchymal stem cells: the roles of RhoA and Rac1. *Stem Cell Res* 2015; 14: 283–296.

44. Yassin MA, Fuoco T, Mohamed-Ahmed S, et al. 3D and porous RGDC-functionalized polyester-based scaffolds as a niche to induce osteogenic differentiation of human bone marrow stem cells. *Macromol Biosci* 2019; 19: e1900049.

45. Donnaloja F, Jacchetti E, Soncini M, et al. Natural and synthetic polymers for bone scaffolds optimization. *Polymers (Basel)* 2020; 12: 905.

46. Lim KT, Hexiu J, Kim J, et al. Synergistic effects of orbital shear stress on in vitro growth and osteogenic differentiation of human alveolar bone-derived mesenchymal stem cells. *Biomed Res Int* 2014; 2014: 1–18.

47. Du D, Furukawa KS and Ushida T. Oscillatory perfusion culture of CaP-based tissue engineering bone with and without dexamethasone. *Ann Biomed Eng* 2009; 37: 146–155.

48. Yoshimura Y, Kikuiri T, Hasegawa T, et al. How much medium do you use for cell culture? Medium volume influences mineralization and osteoclastogenesis in vitro. *Mol Med Rep* 2017; 16: 429–434.

49. Schreivogel S, Kuchibhotla V, Knaus P, et al. Load-induced osteogenic differentiation of mesenchymal stromal cells is caused by mechano-regulated autocrine signaling. *J Tissue Eng Regen Med* 2019; 13: 1992–2008.

50. Handa A, Emery AN and Spier RE. On the evaluation of gas-liquid interfacial effects on hybridoma viability in bubble column bioreactors. *Dev Biol Stand* 1987; 66: 241–253.

51. Lee J, Kentish S and Ashokkumar M. Effect of surfactants on the rate of growth of an air bubble by rectified diffusion. *J Phys Chem B* 2005; 109: 14595–14598.

52. Hanwright J, Zhou J, Evans GM, et al. Influence of surfactant on gas bubble stability. *Langmuir* 2005; 21: 4912–4920.

53. Yu C, Zhang P, Wang J, et al. Superwettability of gas bubbles and its application: from bioinspiration to advanced materials. *Adv Mater* 2017; 29: 1703053.

54. Yao M, Tijing LD, Naidu G, et al. A review of membrane wettability for the treatment of saline water deploying membrane distillation. *Desalination* 2020; 479: 114312.

55. Stavenschi E, Corrigan MA, Johnson GP, et al. Physiological cyclic hydrostatic pressure induces osteogenic lineage commitment of human bone marrow stem cells: a systematic study. *Stem Cell Res Ther* 2018; 9: 276.

56. Paulsen J, Bajaj VS and Pines A. Compressed sensing of remotely detected MRI velocimetry in microfluidics. *J Magn Reson* 2010; 205: 196–201.

57. Kawano Y, Otsuka C, Sanzo J, et al. Expanding imaging capabilities for microfluidics: applicability of darkfield internal reflection illumination (DIRI) to observations in microfluidics. *PLoS One* 2015; 10: e0116925.

58. Geris L, Guyot Y, Schrooten J, et al. In silico regenerative medicine: how computational tools allow regulatory and financial challenges to be addressed in a volatile market. *Interface Focus* 2016; 6: 20150105.

59. Luo W, Xiong W, Zhou J, et al. Laminar shear stress delivers cell cycle arrest and anti-apoptosis to mesenchymal stem cells. *Acta Biochim Biophys Sin (Shanghai)* 2011; 43: 210–216.

60. Coughlin TR and Niebur GL. Fluid shear stress in trabecular bone marrow due to low-magnitude high-frequency vibration. *J Biomech* 2012; 45: 2222–2229.

61. Metzger TA, Schwaner SA, LaNeve AJ, et al. Pressure and shear stress in trabecular bone marrow during whole bone loading. *J Biomech* 2015; 48: 3035–3043.

62. Herzig E and Root WS. Relation of sympathetic nervous system to blood pressure of bone marrow. *Am J Physiol Content* 1959; 196: 1053–1056.

63. Sart S, Tsai A-C, Li Y, et al. Three-dimensional aggregates of mesenchymal stem cells: cellular mechanisms, biological properties, and applications. *Tissue Eng Part B Rev* 2014; 20: 365–380.

64. Chatterjea A, LaPointe V, Barradas A, et al. Cell aggregation enhances bone formation by human mesenchymal stromal cells. *Eur Cells Mater* 2017; 33: 121–129.

65. Wang T, Kang W, Du L, et al. Rho-kinase inhibitor Y-27632 facilitates the proliferation, migration and pluripotency of human periodontal ligament stem cells. *J Cell Mol Med* 2017; 21: 3100–3112.

66. Yamamoto T, Ugawa Y, Kawamura M, et al. Modulation of microenvironment for controlling the fate of periodontal ligament cells: the role of Rho/ROCK signaling and cytoskeletal dynamics. *J Cell Commun Signal* 2018; 12: 369–378.

67. Jonason JH, Xiao G, Zhang M, et al. Post-translational regulation of Runx2 in bone and cartilage. *J Dent Res* 2009; 88: 693–703.

68. Infante A and Rodríguez CI. Osteogenesis and aging: lessons from mesenchymal stem cells. *Stem Cell Res Ther* 2018; 9: 244.

69. Langenbach F and Handschel J. Effects of dexamethasone, ascorbic acid and β-glycerophosphate on the osteogenic differentiation of stem cells in vitro. *Stem Cell Res Ther* 2013; 4: 117.

70. Mohamed-Ahmed S, Fristad I, Lie SA, et al. Adipose-derived and bone marrow mesenchymal stem cells: a donor-matched comparison. *Stem Cell Res Ther* 2018; 9: 168.

71. Knippenberg M, Helder MN, Zandieh Doulabi B, et al. Adipose tissue-derived mesenchymal stem cells acquire bone cell-like responsiveness to fluid shear stress on osteogenic stimulation. *Tissue Eng* 2005; 11: 1780–1788.

Table S1. Primers used for RT-qPCR gene expression analysis

| Gene	Symbol	Cat. No.
Glyceraldehyde-3-phosphate dehydrogenase	GAPDH	Rn01749022_g1
Rho-associated kinases 1	ROCK1	Rn00681157_m1
Runt-related transcription factor 2	RUNX2	Rn01512298_m1
Sp7 transcription factor	SP7 (Osterix)	Rn01761789_m1
Bone sialoprotein	IBSP	Rn00561414_m1
Alkaline phosphatase	ALPL	Rn01516028_m1
Secreted Phosphoprotein 1 (Osteopontin)	SPP1	Rn00681031_m1
Bone gamma-carboxyglutamate protein	BGLAP	Rn00566386_g1
Ecto-5′-nucleotidase	Nt5e (CD73)	Rn00665212_m1
Thy-1	Thy1 (CD90)	Rn00562048_m1
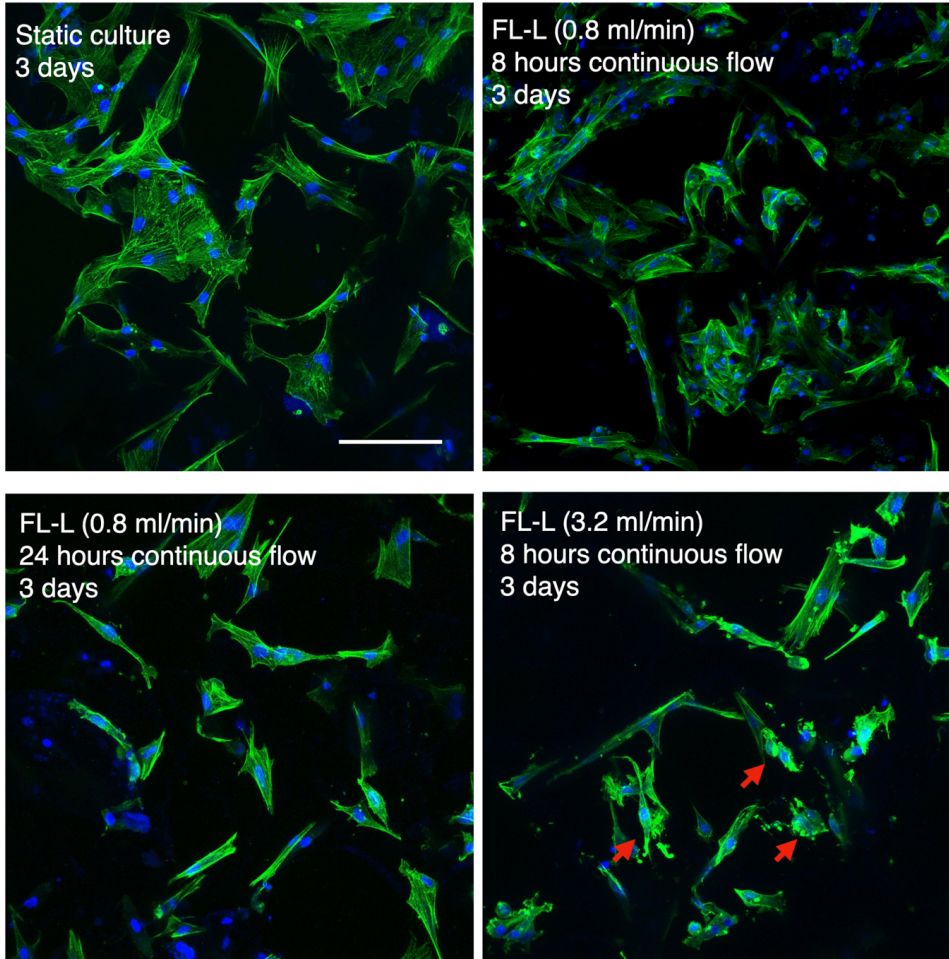
Fig. S1 Morphological change and cell damaging effect of differential flow rate and duration.

While rBMSC in the static condition as well as FL-L (i.e., 0.8 ml/min for 8 hours a day) exhibited an elongated morphology, 24 hours perfusion at 0.8 ml/min significantly suppressed cell elongation and cell-to-cell interaction. At flow rate of 3.2 ml/min, a greater number of apoptotic cells (indicated by arrows) and actin fragments due to cell collapse were observed.

Paper IV

Unique Osteogenic Profile of Bone Marrow Stem Cells Stimulated in Perfusion Bioreactor is Rho-ROCK-mediated Contractility dependent

S. Yamada, MA. Yassin, F. Torelli, J. Hansmann, JBA. Green, T. Schwarz, K. Mustafa

IV

RESEARCH ARTICLE

Unique osteogenic profile of bone marrow stem cells stimulated in perfusion bioreactor is Rho-ROCK-mediated contractility dependent

Shuntaro Yamada[1] | Mohammed A. Yassin[1] | Francesco Torelli[1] |
Jan Hansmann[2,3,4] | Jeremy B. A. Green[5] | Thomas Schwarz[2] | Kamal Mustafa[1]

[1]Center of Translational Oral Research (TOR)-Tissue Engineering Group, Department of Clinical Dentistry, Faculty of Medicine, University of Bergen, Norway

[2]Translational Center Regenerative Therapies, Fraunhofer Institute for Silicate Research ISC, Würzburg, Germany

[3]Chair of Tissue Engineering and Regenerative Medicine, University Hospital Würzburg, Würzburg, Germany

[4]Department of Electrical Engineering, University of Applied Sciences Würzburg-Schweinfurt, Schweinfurt, Germany

[5]Centre for Craniofacial & Regenerative Biology, Faculty of Dentistry, Oral & Craniofacial Sciences, King's College London, UK

Correspondence

Kamal Mustafa, Center of Translational Oral Research (TOR)-Tissue Engineering Group, Department of Clinical Dentistry, Faculty of Medicine, University of Bergen, Årstadveien 19, 5009 Bergen, Norway.
Email: kamal.mustafa@uib.no

Funding information

L. Meltzers Høyskolefond, Grant/Award Number: 103637; Trond Mohn stiftelse, Grant/Award Number: BFS2018TMT10

Abstract

The fate determination of bone marrow mesenchymal stem/stromal cells (BMSC) is tightly regulated by mechanical cues, including fluid shear stress. Knowledge of mechanobiology in 2D culture has allowed researchers in bone tissue engineering to develop 3D dynamic culture systems with the potential for clinical translation in which the fate and growth of BMSC are mechanically controlled. However, due to the complexity of 3D dynamic cell culture compared to the 2D counterpart, the mechanisms of cell regulation in the dynamic environment remain relatively undescribed. In the present study, we analyzed the cytoskeletal modulation and osteogenic profiles of BMSC under fluid stimuli in a 3D culture condition using a perfusion bioreactor. BMSC subjected to fluid shear stress (mean 1.56 mPa) showed increased actomyosin contractility, accompanied by the upregulation of mechanoreceptors, focal adhesions, and Rho GTPase-mediated signaling molecules. Osteogenic gene expression profiling revealed that fluid shear stress promoted the expression of osteogenic markers differently from chemically induced osteogenesis. Osteogenic marker mRNA expression, type 1 collagen formation, ALP activity, and mineralization were promoted in the dynamic condition, even in the absence of chemical supplementation. The inhibition of cell contractility under flow by Rhosin chloride, Y27632, MLCK inhibitor peptide-18, or Blebbistatin revealed that actomyosin contractility was required for maintaining the proliferative status and mechanically induced osteogenic differentiation in the dynamic culture. The study highlights the cytoskeletal response and unique osteogenic profile of BMSC in this type of dynamic cell culture, stepping toward the clinical translation of mechanically stimulated BMSC for bone regeneration.

KEYWORDS

actomyosin contraction, bioreactor, bone tissue engineering, fluid shear stress, osteogenic differentiation, Rho GTPase signaling

1 | INTRODUCTION

The fate and growth of bone marrow mesenchymal stem/stromal cells (BMSC) are tightly regulated by mechano-environmental factors.[1,2] The forces of load and torsion applied to bone are converted to shear forces by altered interstitial fluid flow in bone marrow, which is exerted on the resident cells, including mechanosensitive BMSC.[3] For example, hydrostatic pressure, fluid shear stress, and altered rheological properties of BMSC niche regulate their fate into osteoblast, adipocyte, chondrocyte, or stromal cell, balancing bone homeostasis and remodeling.[3,4] Physical activity increases fluid shear stress in bone marrow, which promotes bone remodeling by energizing osteoblasts and their progenitors, whereas a disbalanced mechano-environment by physiopathological conditions such as aging, diseases (i.e., osteoporosis), and disuse favors adipogenesis.[3,5–9]

The osteogenic nature of BMSC under fluid shear and its plausible mechanism have been predominantly described by conventional monolayer cell culture experiments. In osteoinductive medium (i.e., in the presence of dexamethasone, beta-glycerophosphate, and ascorbic acid), BMSC preferably respond to fluid shear stress as small as 0.01 Pa up to 2 Pa by upregulating osteogenic markers such as Runt-related transcription factor 2 (Runx2), Osteopontin (Opn), Bone morphogenetic protein 2 (Bmp2), alkaline phosphatase (ALP), collagen type 1 (Col1), and Osteocalcin (Ocn) accompanied by increased mineralization and extracellular matrix formation.[10–19] BMSC subjected to fluid flow undergo dynamic cytoskeletal rearrangement moderated by integrins, focal adhesion, MAPK/ERK signaling, Rho- and Hippo-YAP/TAZ signaling, which are tightly linked to osteogenic differentiation.[10,12,13,20–22] The evidence of flow-induced osteogenic differentiation in the absence of the osteoinductive medium is rather limited. Approximately 1 Pa shear stress was reported to increase the enzymic activity of ALP and the expression of osterix (Osx), Opn, and Col1, but whether these cellular responses can be considered as osteogenic differentiation is debatable.[21,23,24]

The knowledge gained from the field of mechanobiology has been transferred into tissue engineering for bone regeneration where three-dimensional (3D) scaffolds are combined with BMSC to create transplantable constructs. With 3D scaffolds, gas, nutrient, and waste transport to/from the loaded cells has mostly relied on passive diffusion in static culture, causing the heterogeneity of cell growth and regenerative capacity.[25,26] Therefore, high expectations have been placed on the use of perfusion bioreactor systems to improve cell production. The rationale of applying bioreactors in bone tissue engineering is threefold: to uniform nutrient and gas distribution within 3D constructs to ensure the homogeneity of cell distribution and their functionality among the constructs, to mimic the mechanical environment of bone and bone marrow to stimulate osteogenic properties of the cells, and to automate cell production process to reduce the risk of human-error and improve cost-effectiveness.[27] Similar to the 2D observations, studies using the various prototypes of bioreactors, mostly in the presence of the osteoinductive medium, reported the preferable effects of 3D perfusion culture on osteogenic differentiation.[28–35] Notably, the concept was proven by a study that

BMSC co-cultured with vascular endothelial cells in the osteoinductive medium that was preconditioned in a perfusion bioreactor improved bone formation and visualization after transplantation into calvaria bone defects.[29] We previously reported that the osteogenesis of BMSC could be induced mechanically by the sub-physiological level of flow, even in the absence of the osteoinductive medium, showing the upregulated expression of osteogenic markers and the improved functionality of the cells including matrix formation and mineralization in a perfusion bioreactor.[36] Interestingly, BMSC in a 3D environment are reportedly more perceptive to shear stress than that in a 2D environment, but the cellular mechanisms of mechanically stimulated osteogenesis in a 3D dynamic culture remain underdocumented.[37] To translate the technology into clinical application, in depth understanding of cellular response is necessary. Therefore, in the present study, we aimed at elucidating mechanically induced osteogenesis by fluid flow on 3D porous scaffolds by focusing on signaling in cytoskeletal rearrangement and osteogenic profiling in depth. The dynamic cell culture was performed using a custom-designed bioreactor with experimental parameters disclosed, and flow characteristics was computationally estimated to correlate the magnitude of shear stress with cellular behaviors.

2 | MATERIALS AND METHODS

2.1 | BMSC isolation and cell culture

The study was approved by the Norwegian Animal Research Authority (local approval number 20146866) and conducted according to the European Convention for the Protection of Vertebrates used for scientific purposes. BMSC were isolated from femurs of male Lewis rats euthanized by lethal doses of carbon dioxide and cervical dislocation. The cells were maintained for both static and dynamic culture in α-minimum essential medium (α-MEM: 22571; Gibco™, USA) supplemented with 1% penicillin and streptomycin (SV30010; HyClone, USA) and 10% fetal bovine serum (FBS: 10270-106; Gibco™, USA) at 37°C in 5% CO_2. The expression of putative stem cell markers and the capacity of multilineage differentiation were previously verified.[36] BMSC from the third to fifth passages were used in the study. Osteoinductive medium (OM) used as a positive control for osteogenic differentiation consisted of α-MEM supplemented with 1% penicillin and streptomycin, 10% FBS, 10 nM dexamethasone (D4902; Sigma, USA), 10 mM beta-glycerophosphate (G9422; Sigma, USA), and 173 μM L-ascorbic acid (A8960; Sigma, USA).

2.2 | Preparation of 3D porous scaffolds of poly (L-lactide-co-trimethylene carbonate)

3D porous scaffolds with a diameter of 12 mm and a thickness of 1.2 mm were fabricated by a solvent-casting/salt-leaching technique as described previously.[38] Briefly, synthetic polymers, poly(L-lactide-co-trimethylene carbonate) 70:30 (RESOMER® LT
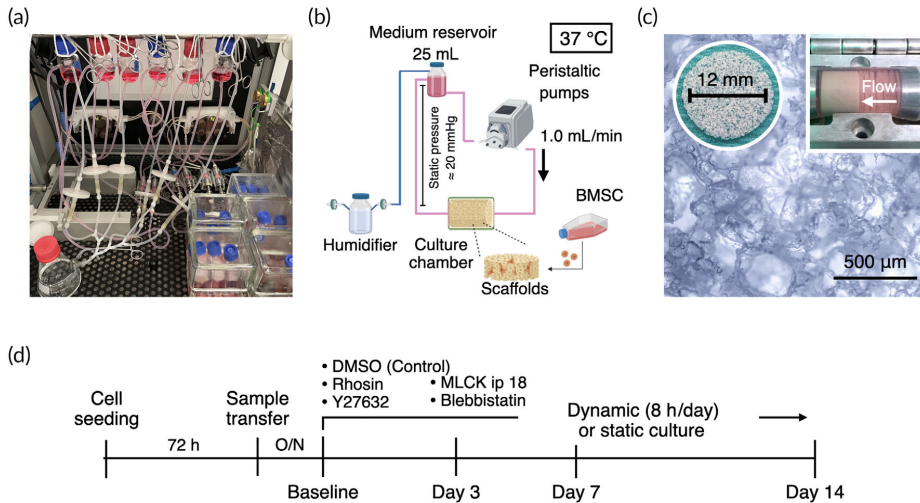
FIGURE 1 Experimental design and perfusion bioreactor. (a) The bioreactor used for 3D dynamic culture in the present study consists of integrated incubator and perfusion systems. (b) Schematic illustration of experimental setting including environmental factors in the dynamic cell culture. (c) Five cell-laden porous scaffolds of poly(L-lactide-co-trimethylene carbonate) were placed in the sample chambers where 25 mL of growth medium was perfused at 1.0 mL/min. (d) Experimental timeline.

706S; Evonik, Germany), were dissolved in chloroform and mixed with sodium chloride (NaCl) at a weight ratio of 1:10. After the slow evaporation of chloroform, the scaffolds were thoroughly washed to remove NaCl particles. Scaffolds were sterilized by 75% ethanol and UV irradiation prior to cell seeding. A total of 250,000 cells were seeded per scaffold in 48 well plates.

2.3 | Bioreactor system and 3D dynamic cell culture under perfusion

A custom-designed GMP-complied laminar flow perfusion bioreactor was utilized in the study. It consisted of an integrated incubator system with environmental sensors (i.e., temperature, gas concentration, pressure: details previously described[39]) and peristaltic pumps (Figure 1a). In the bioreactor, 25 mL of the growth medium was perfused, and the medium was refreshed twice a week unless otherwise mentioned (Figure 1b). The medium reservoirs were connected to ventilation filters via humidifiers to allow for gas exchange while minimizing medium evaporation. Approximately 20 mmHg of hydrostatic pressure was applied to sample chambers where five cell-laden scaffolds were placed in order to prevent air bubble formation during the dynamic cell culture (Figure 1c). Optimal flow rate for the cells was preliminarily determined at 1.0 mL/min.[39]

The experimental flow was given in Figure 1d. Briefly, 72 h after cell seeding on the scaffolds, five cell-laden scaffolds were transferred into the sample chamber in the bioreactor. The following day was defined as the baseline when dynamic cell culture has begun. Dynamic cell culture continued for 8 h a day for 14 days. As a control, five cell-

laden scaffolds were stacked and placed in a flask with 25 mL medium in the incubator space of the bioreactor to equalize the cell-to-medium ratio and environmental fluctuation. The samples were collected on Days 3, 7, and 14 for analyses, and the experiment was independently repeated three times unless otherwise mentioned.

2.4 | Computational fluid dynamics simulation

For flow characterization during dynamic cell culture, an in silico modeling was performed as previously described.[39] Briefly, the geometry of the scaffolds was obtained by microcomputed tomography (microCT: SkyScan 1172;Bruker-MicroCT, Kontich, Belgium) using 40 kV and 250 mA at 10 μm spatial resolution. The geometry was then imported in .stl file as a solid object using COMSOL Multiphysics version 6.0 (COMSOL AB, Sweden). Scaffold geometries were placed in a digitally reproduced sample chamber. From the inlet, fully developed flow of 1.0 mL/min was prescribed. At the outlet, pressure at 8.6 Pa was prescribed as a boundary condition, which was defined based on pressure drop over the scaffolds in a macro model as previously proposed.[39,40] Incompressible Newtonian fluid (described by Navier–Stokes equations) with a dynamic viscosity of 0.6922 mPa*s and density of 993.37 kg/m^3 was defined, which was governed by the Navier–Stokes equation and the continuity equation as follows:

$$\rho(u.\nabla)u = \nabla.[-pI + K] + F$$

$$\rho\nabla.u = 0$$

$$K = \mu \left(\nabla u + \left(\nabla u \right)^{T} \right)$$

where ρ, u, ∇, p, I, K, F, and μ are the fluid density, the fluid velocity, the divergence operator, the pressure, the identity tensor, the stress tensor, the body force per unit volume, and the dynamic viscosity of the fluid, respectively.

Nonslip boundary conditions were implemented at the solid walls.

2.5 | Pharmacological modulation of actomyosin contractility

To investigate the role of cytoskeletal rearrangement in BMSC growth and differentiation under flow, four inhibitors and two enhancers of actomyosin contractility were applied.

For the inhibition, 20 μM Rhosin chloride (Rhosin: 5003; Biotechne, UK), 10 μM Y27632 dihydrochloride (Y27632: 1254; Biotechne, UK), 1 μM MLCK inhibitor peptide 18 (MLCK ip 18: HY-P1029; MedChemExpress, USA), or 10 μM Blebbistatin (203390; Sigma-Aldrich, USA) was added to the culture medium during the dynamic cell culture to inhibit Rho GTPase, Rho-associated coiled-coil containing protein kinase (ROCK), myosin light chain kinase (MLCK), and myosin II, respectively (Figure S1A). The optimal concentrations of each inhibitor were determined preliminarily as the concentrations that mitigated actomyosin contractility without deteriorating cell viability and growth for 14 days (Figure S1). It was also confirmed that these inhibitors did not significantly influence on Runx2 expression in the static condition without the osteoinductive stimuli. Narciclasine (Narc: HY-16563; MedChemExpress, USA) and Calyculin A (CalA: sc-24000; Santa Cruz Biotechnology, USA) were used to activate Rho-ROCK signaling and to induce actomyosin contraction via the inhibition of myosin light chain phosphatase, respectively (Figure S2A,B). Dimethyl sulfoxide (DMSO) was used as a solvent and acted as a control. The culture media with inhibitors were refreshed every 2 days for 14 days.

2.6 | Reverse transcription-quantitative polymerase chain reaction and gene expression array

Samples for gene expression assay were collected on Days 7 and 14. After being immediately snap-frozen in liquid nitrogen, the samples were stored at -80°C. Total RNA was extracted using a Maxwell® 16 Cell LEV Total RNA Purification Kit (AS1280; Promega, USA) in accordance with the manufacturer's protocol. Reverse transcription was undertaken using a High-Capacity cDNA reverse Transcription Kit (4368813; Applied Biosystems, USA). RT-qPCR was performed with the StepOne™ real-time PCR system (4376357; Applied Biosystems) with TaqMan® Universal Master Mix (4352042; Applied Biosystems). The amplification was performed as follows: initial activation of polymerase at 95°C for 20 s followed by 40 cycles of PCR, at 95°C for 1 s (denature) and 60°C for 20 s (anneal and extend).

The tailored panels of gene expression assay for cytoskeletal rearrangement and osteogenesis were designed with reference to the predetermined TaqMan® gene expression arrays for focal adhesion (4413255-RPMFWWX; Applied Biosystems), cytoskeleton regulators (4413255-RPPRJ2T; Applied Biosystems), and osteogenesis (4413255-RPZTD3T; Applied Biosystems). A set of primers used in the study is listed in Tables S1–S3. Relative expression of each mRNA was calculated with the ΔΔCt method.[41]

2.7 | Gene set enrichment analysis

A list of differentially expressed genes (DEGs) identified through statistical analysis was further analyzed using the R package gprofiler2 and the STRING database version 11.5. Functional enrichment of the DEGs was evaluated using the open-source software Cytoscape version 3.9.1 by referencing the Reactome Pathways and UniProt databases.

2.8 | Cytoskeleton antibody microarray

To capture the overview of cytoskeletal rearrangement, ELISA-based antibody microarray was performed using Cytoskeleton Array kit (PCP141; Full Moon BioSystem, USA) according to the manufacturer's protocol. Briefly, samples were collected on Day 3, and protein extraction was performed by vigorous vortexing with lysis beads in the extraction buffer. Due to low protein yield, cell lysate obtained from three independent experiments was pooled. The protein samples were labeled in biotin dissolved in dimethylformamide in the labeling buffer. The biotinylated samples were then incubated with the antibody microarray slides followed by detection with Cy3-Streptavidin solution. The slides were scanned by a GenePix® Microarray Scanner (Molecular Devices, USA) and quantified using GenePix® ProMicroarray Image Analysis Software.

2.9 | ROCK enzymic activity assay

The enzymic activity of ROCK was measured on Days 3 and 7 by using ROCK Activity Assay Kit (ab211175; Abcam, USA) according to the manufacturer's protocol. Cell lysate was obtained in mammalian cell lysis buffer (ab179835; Abcam) with protease and phosphatase inhibitor cocktail (ab201119; Abcam). The cell lysate was added to wells where myosin phosphate target subunit 1 (MYPT1) was coated. Kinase reaction was initiated by adding 10 mM dithiothreitol (DTT) and 2 mM adenosine triphosphate (ATP). The wells were then incubated for 60 min at room temperature to phosphorylate MYPT1. Subsequently, the wells were incubated with anti-phospho-MYPT1 (Thr696) for 60 min at room temperature followed by secondary incubation with HRP-conjugated antibody for another 60 min at room temperature. The optical density of the HRP substrates was measured at 450 nm using a Varioskan™ LUX multimode microplate reader (VLBL00D0; Thermo Scientific, Finland).

2.10 | Immunofluorescence and confocal microscopy

For immunofluorescence, samples were fixed in 4% paraformaldehyde (PFA) for 15 min at room temperature except for collagen staining. To detect phosphorylated proteins, fixation was undertaken in the presence of protease and phosphatase inhibitor (ab201119; Abcam, UK). The samples were then permeabilized in 0.1% Triton X-100 in PBS for 15 min at room temperature. For collagen staining, samples were fixed and permeabilized in ice-cold methanol for 5 min at $-20°C$. The samples were then incubated in a blocking buffer consisting of 10% normal goat serum (NGS: ab7481; Abcam, USA) in 0.1% Tween-20 in PBS (PBSTw) for 60 min at room temperature. After blocking, the samples were incubated with the following primary antibodies in PBSTw at 4°C overnight: rabbit anti-non-muscle myosin 2A antibody (NM2A: 1:200, 909801; BioLegend, USA), mouse anti-non-muscle myosin 2B antibody (NM2B: 1:200, GTX634160; GeneTex, USA), mouse anti-phospho-MYL9 (Ser19) antibody (pMLC2: 1:250, MA5-15163; Invitrogen, USA), and mouse anti-collagen type 1 antibody (Col1: 1:500, MA1-26771; Invitrogen). Subsequently, the samples were incubated with secondary antibodies, goat anti-rabbit antibody, Alexa Fluor 546 (1:500, A11010; Invitrogen) and/or goat anti-mouse antibody, Alexa Fluor 635 (1:500, A31575; Invitrogen) for 1 h at room temperature simultaneously with 4′,6-diamidino-2-phenylindole (DAPI: 1:2500, D9542; Sigma-Aldrich, USA) and Phalloidin Alexa488 (1:500, A12379; Invitrogen) for nuclear staining and filamentous actin staining, respectively.

For image acquisition, the samples were placed on chambered coverslips (80287, ibidi, Germany) and mounted in ProLong™ Gold antifade reagent (P36939; Invitrogen). Z-Stack images were acquired by a confocal microscope (TCS SP8; Leica, Germany) equipped with a $40\times$ water immersion objective lens. The images were processed and analyzed with Fiji/ImageJ.[42] All images are presented as z-stack projection images of 100 μm thickness.

2.11 | Quantification of double-strand DNA

To assess cell proliferation, double-strand DNA (dsDNA) quantification was performed using Quant-iT PicoGreen dsDNA Assay Kit (P7589; Invitrogen) according to the manufacturer's protocol. Cell lysate was obtained by repeated freeze–thaw cycle in 0.1% Triton X-100 in Milli-Q® water. The intensity of fluorescence was measured at Ex/Em = 480/520 nm using the microplate reader.

2.12 | 5-Ethynyl-2′-deoxyuridine incorporation assay

For EdU assay, 30 μM EdU was added to the growth medium on Day 3 in the static and dynamic culture. Twenty-four hours after EdU administration, the samples were fixed in ice-cold methanol for 5 min at $-20°C$. Incorporated EdU to the nuclei was detected using Click-iT™ EdU Cell Proliferation Kit for Imaging, Alexa Fluor™ 488 dye (C10337; Invitrogen) according to the manufacturer's protocol and visualized by the Leica SP8 confocal microscope.

2.13 | ALP staining

The samples collected on Day 7 were placidly fixed in 4% PFA for 2 min at room temperature. The samples were then incubated with BCIP®/NBT solusion (B5655; Sigma-Aldrich) for 30 min at room temperature. For quantification, the substrate was extracted by incubating with 100 mM cetylpyridium chloride overnight at room temperature. Absorbance was measured at 540 nm using the microplate reader.

2.14 | Alizarin Red S staining

Samples collected on Day 14 were fixed in 4% PFA for 40 min and washed gently in Milli-Q® water. Mineralized nodes were stained by 0.1% Alizarin Red S (A5533; Sigma-Aldrich) for 20 min followed by washing six times in Milli-Q® water. For quantification, the dye was extracted with 100 mM cetylpyridium chloride overnight at room temperature. Absorbance was measured at 540 nm using the microplate reader.

2.15 | Statistics

All data are represented as mean ± s.e.m unless otherwise specified. Statistical analyses were performed by using Prism 9 (Dotmatics, USA). For comparison between the static and dynamic culture conditions, Student's t-test was performed. For multiple comparisons, the data were evaluated by ANOVA followed by Dunnett's multiple comparisons test. In the cytoskeletal inhibition experiments, the mean of the chemically treated groups was compared to the control (i.e., DMSO) group only. A p value <0.05 was considered to be statistically significant.

3 | RESULTS

3.1 | CFD assessment of fluid velocity and shear stress in the bioreactor

Prior to perfusion cell culture, in silico CFD simulation was conducted to describe the distribution and magnitude of shear stress within the stack of the porous scaffolds based on micro-CT imaging of the scaffold structure (Figure 2a). A flow rate was preliminarily determined by evaluating cell growth, and 1.0 mL/min was considered optimal for the study. With the flow rate, fluid paths were evenly distributed among the stacks through the collimators, and estimated velocity field ranged from 0.1 to 0.5 mm/second (Figure 2b). Computed shear
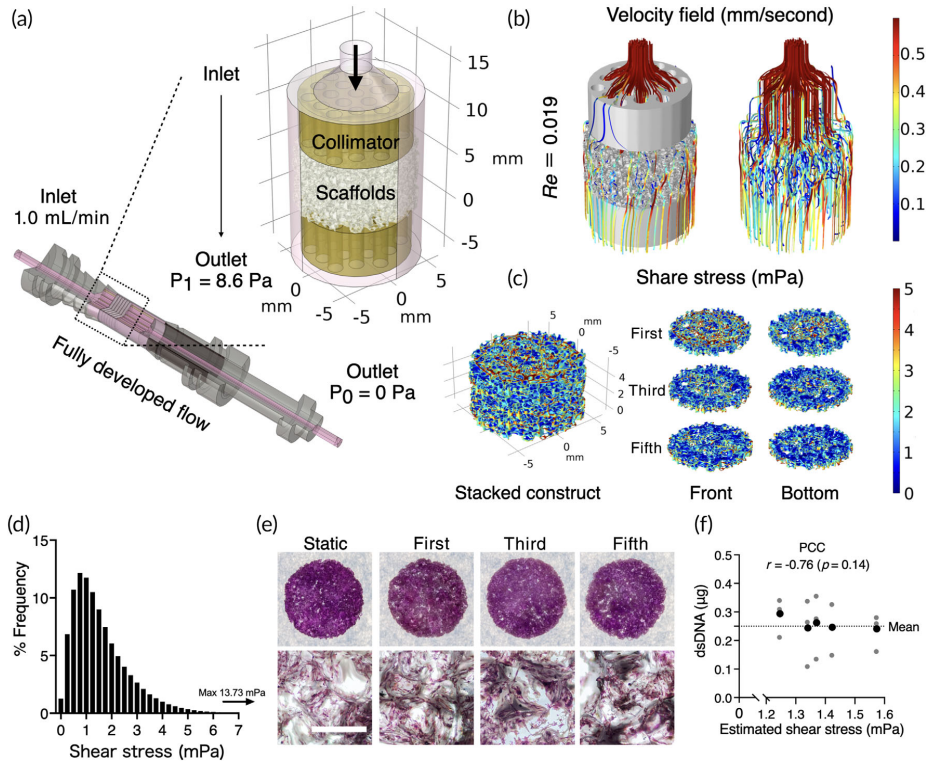
FIGURE 2 Computational fluid dynamics (CFD) for fluid shear stress estimation (a) The scaffold geometry obtained by a micro computed tomography was virtually placed in the scaffold chambers where fully developed flow at 1.0 mL/min was provided at the inlet. At the outlet of the chamber, atmospheric pressure was prescribed (P0), which determined pressure at the end of collimators on the outlet side at 8.6 Pa (P1). (b) Fluid paths were simulated evenly among the scaffolds with Reynolds number at 0.019, indicating the flow was laminar. (c) Simulation of fluid shear stress on the surfaces of first, third, and fifth scaffolds in the stack showed local shear distribution. (d) Frequent distribution of fluid shear stress ranged from 1.5e-008 to 13.73 mPa. (e) Crystal violet staining showed actual cell distribution among the scaffold stacks. (f) Pearson correlation coefficient (PCC) indicated no correlation between the estimated shear stress and harvested double-strand DNA (dsDNA) from the scaffolds at different position after 7 days of perfusion culture. Mean of harvested dsDNA (in black) were calculated from three independent samples (in gray). Scale bar = 1 mm.

stress on the surfaces showed local variation within the stack, and the highest magnitude was estimated on the surfaces the scaffold closest to the inlet (Figure 2c). Estimated shear stress ranged from 1.5e-008 to 13.73 mPa due to the heterogeneous nature of complex 3D geometry (Figure 2d). The mean and median values of estimated shear stress were 1.56 and 1.29 mPa, respectively, and over 90% of the surfaces was subjected to a range of shear stress between 0.5 and 5 mPa. DNA staining with crystal violet showed no visible difference in cell distribution between successive scaffolds in the stack (Figure 2e). Pearson correlation coefficient (PCC) did not find the correlation between the amount of dsDNA harvested and the estimated median shear stress in each scaffold, indicating that cell behaviors in the dynamic condition would be similar throughout the stack (Figure 2f).

3.2 | Fluid shear stress-induced dynamic cytoskeletal rearrangement and contractility in the 3D system

To evaluate the effect of perfusion culture on the cytoskeletal regulation, mRNA and protein expressions and enzymic activity governing cell adhesion, motility, and contractility were evaluated. Under the dynamic cell culture condition, BMSC differentially expressed genes encoding adhesion receptors (e.g., Itga2, Itga5, Itga10, and Itgb3), focal adhesion complex and actin binding proteins (e.g., Pkt2, Zyx, Pxn, Vcl, Tns2, Tns4, Vasp, and Zyx), and factors involved in Rho GTPase regulation and downstream signaling (RhoA, Rock1, Rock2, Rasgrf1, Racgap1, Rac1, Limk1, Cdc42) (Figure 3a). The gene set enrichment analysis using UniProt database identified that Ser/Thr protein kinase, cytoskeleton,
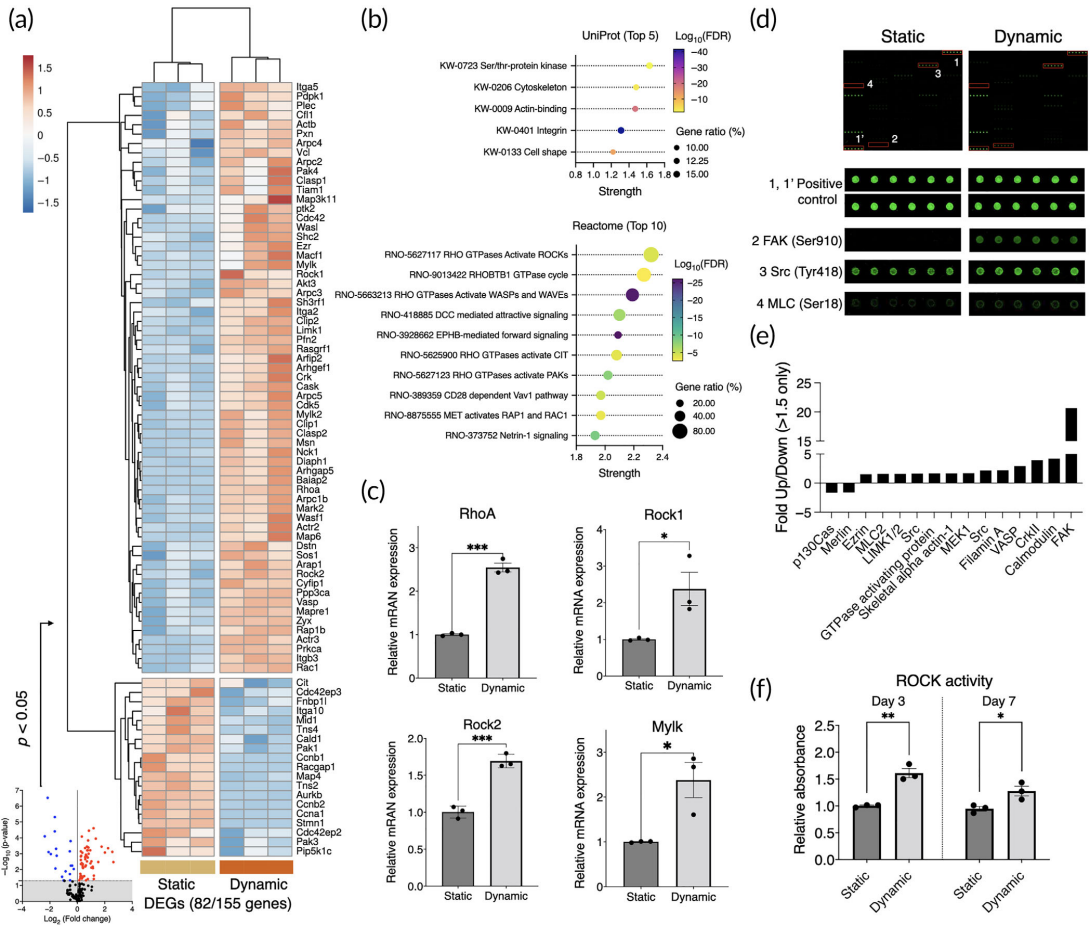
FIGURE 3 Cytoskeletal rearrangement and actomyosin contractility of BMSC in the dynamic condition. (a) Gene expression array of 155 markers encoding adhesion, migration, and cytoskeletal regulation factors. Differentially expressed genes ($p < 0.05$, DEGs) were plotted in the heatmap. Unit variance scaling was applied to $\Delta\Delta CT$ values, and rows were centered. (b) Gene set enrichment analysis using UniProt and Reactome database. Top 5 enriched keywords and top 10 enriched pathways were displayed. (c) RT-qPCR analysis of Rho-ROCK signaling down to myosin light chain kinase. (d, e) Antibody microarray of cytoskeletal regulators. (f) Enzymic activity of ROCK measured by phosphorylation of myosin phosphatase target subunit 1 (MYPT1). Statistical comparison between the static and dynamic conditions was performed by Student's t-test. *$p < 0.05$; **$p < 0.01$; ***$p < 0.001$.

actin-binding, integrin, and cell shape were the highly enriched keywords. Reactome pathway analysis indicated that Rho GTPases and downstream signaling were highly enriched (Figure 3b). Validation by RT-qPCR supported the activation of Rho-ROCK signaling in the dynamic culture where RhoA ($p = 0.00012$), Rock1 ($p = 0.039$), Rock2 ($p = 0.00061$), and Mylk ($p = 0.024$) were significantly upregulated in the dynamic culture (Figure 3c). Cytoskeleton antibody microarray showed 20.7-fold increase in the expression of focal adhesion in the dynamic culture accompanied by the minor upregulation of steroid receptor coactivator (Src: 1.64-fold increase) and myosin regulatory

light chain-2 (MLC2: 1.57-fold increase) (Figure 3d,e). The enzymic activity of ROCK significantly increased after 3 days ($p = 0.002$) and 7 days ($p = 0.031$) of perfusion culture, supporting the findings from the arrays (Figure 3f).

Immunofluorescence confirmed the dynamic cytoskeletal rearrangement and contractility under perfusion culture (Figure 4a–d). BMSC under the dynamic condition showed enhanced actin polymerization, nonmuscle myosin (NM2A/2B), and phosphorylation of myosin light chain2 (MLC2), resulting in more elongated morphology compared to the static counterpart ($p = 0.0006$).
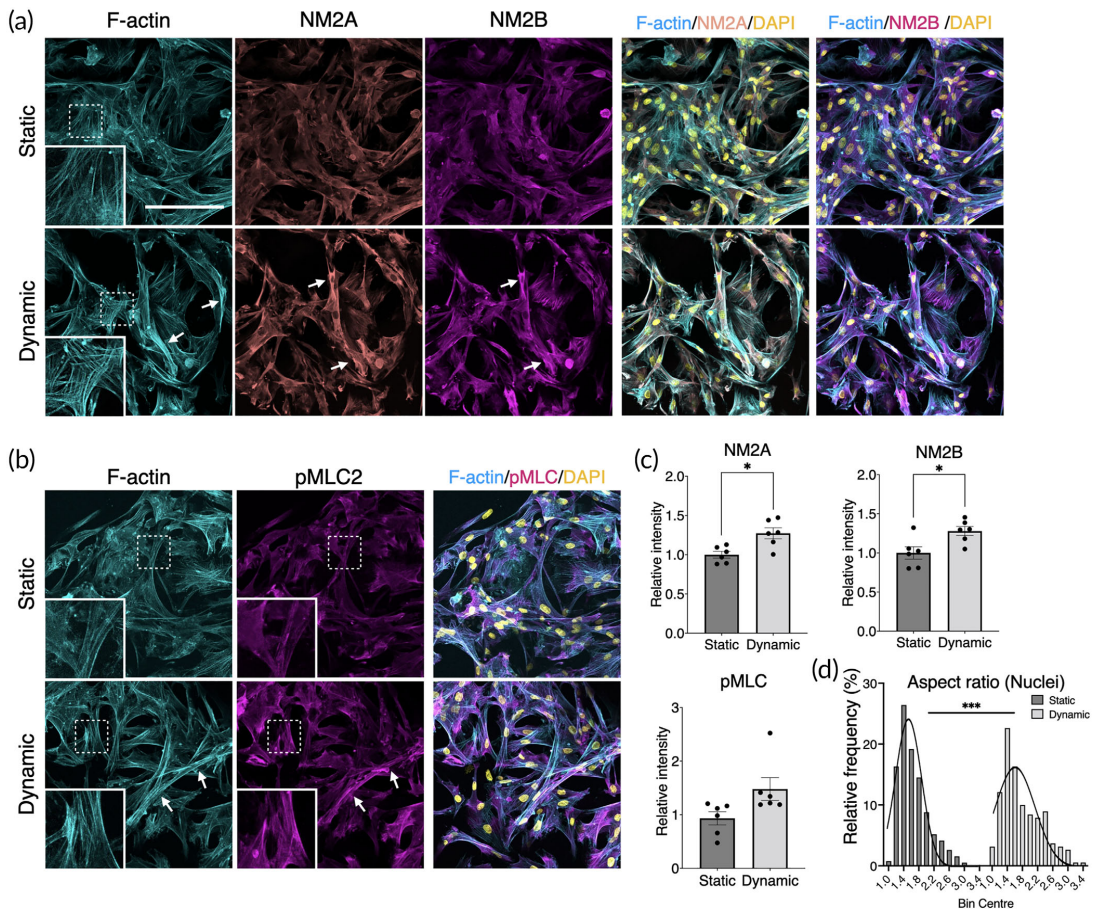
FIGURE 4 Immunofluorescence of actomyosin under static and dynamic cell culture. (a, b) In the dynamic culture condition, BMSC showed noticeable actomyosin contraction highlighted by highly polymerized filamentous actin (F-actin), nonmuscle myosin 2A (NM2A), nonmuscle myosin 2B (NM2B), and phosphorylated myosin light chain 2 (pMLC2). Arrows indicate highly contracted sites. (c) Image quantification of NM2A, NM2B, and pMLC, showing enhanced expression. (d) Cell morphometric assessment by nuclear aspect ratio supported the evidence of cell contraction ($p = 0.0006$). The fitted distribution lines were generated by Gaussian distribution equation. Statistical comparison between the static and dynamic conditions was performed by Student's t-test. *$p < 0.05$; ***$p < 0.001$.

3.3 | Cell contractility is necessary for maintaining cell growth under perfusion

To evaluate the role of cell contractility in cell growth during dynamic cell culture, four different small molecule inhibitors (i.e., Rhosin, Y27632, MLCK ip 18, and Blebbistatin) were used to drive cell relaxation (Figure 5a). In the present system, we found that perfusion culture slowed cell growth (Figure 5b,c). At concentrations that did not affect dsDNA yield in the static condition, the inhibitors did prevent cells from proliferating in the dynamic cell culture (Day 3: $p = 0.0013$, Days 7–14: $p < 0.0001$). EdU incorporation assays confirmed that the reduced dsDNA yield was due to cell cycle arrest (Figure 5d,e). With

or without inhibitors, in the static condition, approximately 60% of the cells incorporated EdU in 24 hours, but only 40% did so in the dynamic condition ($p = 0.015$). Proliferation was further diminished by the inhibitors, with < 20% of the cells found to be proliferative (DMSO VS Rhosin: $p = 0.019$; Y27632: $p = 0.0098$; MLCK ip 18: $p = 0.035$; Blebbistatin: $p = 0.0046$). When actomyosin contraction was pharmacologically induced in a static culture by dosing Narciclasine or Calyculin A for 7 days, cell proliferation also significantly decreased (Figure S3A). Together, these results suggest that excess cellular contractility slows proliferation in static culture but is necessary for maintaining their proliferative status under 3D perfusion culture.
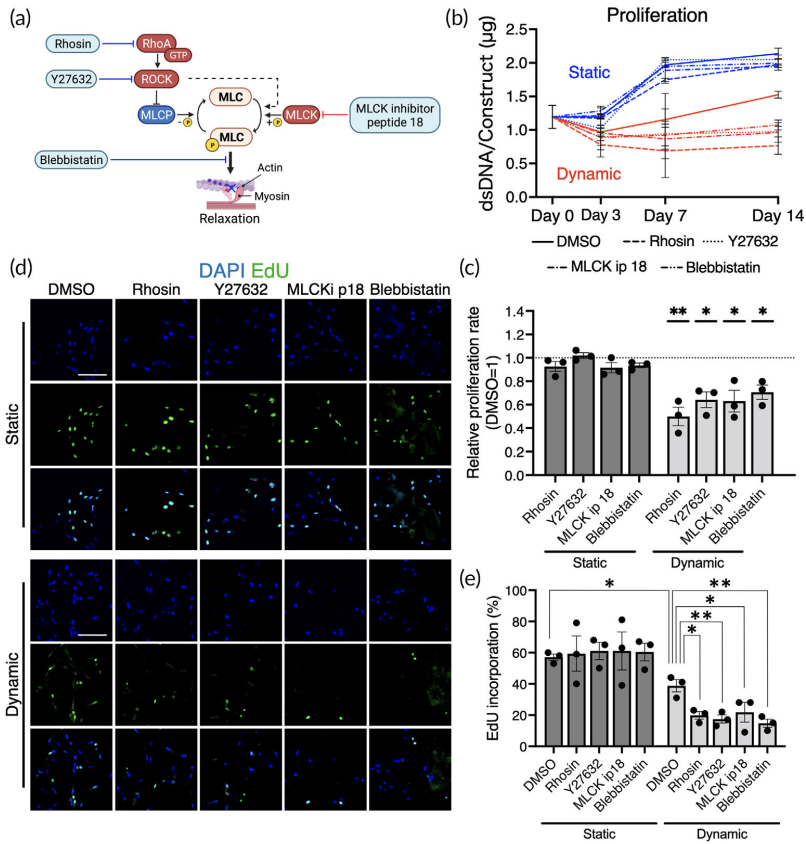
FIGURE 5 Cell growth under perfusion with/without inhibitors of actomyosin contractility. (a) Rhosin chloride (Rhosin), Y27632 dihydrochloride (Y27632), MLCK inhibitory peptide 18 (MLCK ip 18), and Blebbistatin (203390) were added to the culture medium during the dynamic cell culture, leading forcible cell relaxation. (b, c) The quantification of double strand DNA (dsDNA) demonstrated the cells in the dynamic culture were less proliferative compared to the static counterpart. The inhibition of actomyosin contractility mitigated cell proliferation in the dynamic but not static conditions. Dunnett's multiple comparison was performed by comparing to DMSO control within static and dynamic conditions. (d, e) EdU (5-ethynyl-2′-deoxyuridine) incorporation during 24 hours of cell culture, detected by confocal microscope, decreased in the dynamic condition, particularly in the presence of the inhibitors. Statistical comparison between the static and dynamic conditions without the inhibitors was performed by Student's t-test and within the groups by ANOVA followed by Dunnett's multiple comparison. *$p < 0.05$; **$p < 0.01$. Scale bar = 100 μm.

3.4 | Mechanically induced osteogenic gene expression profile differed from chemically induced osteogenesis

To elucidate the osteogenic profile of the mechanically stimulated BMSC, the expression of 84 genes associated with osteogenesis was compared between the dynamic condition, the static condition as a negative control, and the chemically osteoinductive condition (i.e., OM) as a positive control. In the dynamic condition, the BMSC upregulated 52 and 47 osteogenesis-related markers on Days 7 and 14, respectively, compared to the static counterpart (Figure 6a,b). Active metabolism of extracellular matrices during the dynamic

culture featured the expression profile on Day 7 where the upregulation of mRNA encoding the major components of bone extracellular matrices such as collagen (Col1a1, Col1a2, Col2a1, Col4a1, and Col10a1) was observed simultaneously with the robust upregulation of matrix metalloproteinases (Mmp9, 61.62-fold, $p = 0.00010$; Mmp10, 149.66-fold, $p = 0.0069$). This trend was not observed in the OM group. The upregulated genes in the dynamic condition on Day 14 included a key transcriptional factor for osteogenesis, Runx2 (2.71-fold, $p < 0.0001$), as well as common late differentiation markers such as dentin matrix acidic phosphoprotein 1 (Dmp1, 4.38-fold, $p = 0.0012$), alkaline phosphatase (Alp, 1.21-fold, $p = 0.038$), osteopontin (Spp1, 3.28-fold, $p = 0.0025$), and bone sialoprotein
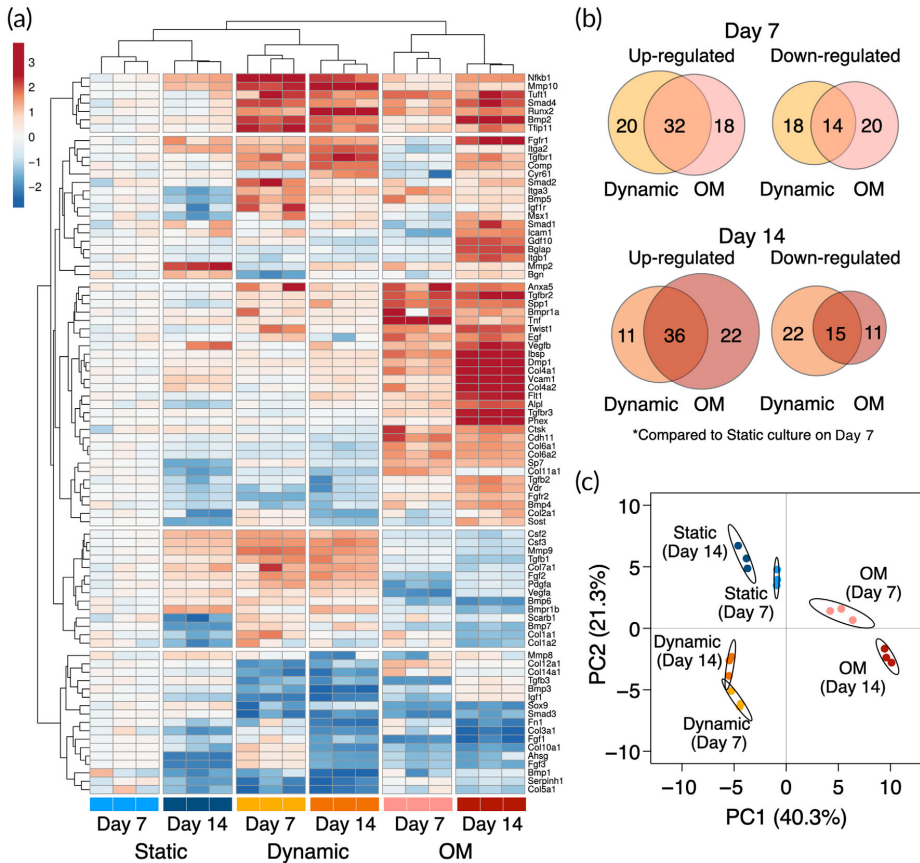
FIGURE 6 Osteogenic gene expression profile of mechanically stimulated BMSC. (a) Heatmap of mRNA expression levels showing the expression pattern of 84 osteogenesis-associated markers in the static, dynamic, and chemically stimulated conditions by osteoinductive medium (OM). Both rows and columns are clustered using Euclidean distance and complete linkage. Unit variance scaling was applied to log$_2$FC values. (b) Venn diagrams presenting number of differentially expressed gene on Days 7 and 14. (c) Principal component analysis (PCA) of osteogenic gene expression pattern. X and Y axis show principal component 1 and principal component 2 that explain 40.3% and 21.3% of the total variance, respectively. Prediction ellipses are such that with probability 0.95, a new observation from the same group will fall inside the ellipse. Samples are colored according to their conditions and timepoints.

(Ibsp, 5.15-fold, $p = 0.0021$) compared to the static counterpart. The expression of Runx2 was significantly higher in the dynamic condition than the OM group on Day 7 (1.65-fold, p-0.00077) and Day 14 (1.54-fold, $p = 0.00033$). Additionally, fibroblast growth factors (Fgfs: Fgf1, Fgf2, and Fgf3), transforming growth factor-β superfamily (Tgfs: Tgfb1, Tgfb2; Bmps: Bmp2, Bmp5, Bmp6, and Bmp7) and its transducer (Smad2, Smad4), and colony-stimulating factors (Csfs: Csf2, Csf3) were found upregulated in the dynamic condition over the period. Noteworthily, a late osteogenic marker, osteocalcin (Bglap), was downregulated in both dynamic and OM groups on Day 7 compared to the static counterpart (dynamic, 0.14-fold, $p = 0.0057$; OM, 0.58-fold, $p = 0.090$). It remained downregulated in the dynamic condition (0.26-fold, $p = 0.091$) but was

significantly upregulated in the OM group (305-fold, $p < 0.0001$) on Day 14.

Despite some quantitative differences, the overall osteogenic profile in the dynamic condition remained comparable between Days 7 and 14, whereas an increase in a number of upregulated genes (50 genes on Day 7 and 58 genes on Day 14) as well as a significant increase in the quantity of the expression was observed in the OM group. This would indicate that, although perfusion culture stimulates the expression of some osteogenesis-related genes, prolonged perfusion culture may not maturate osteogenicity, at least within the 14-days period. Principal components analysis (PCA) highlighted the unique osteogenic profile of the mechanically stimulated cells with a clear separation from the static and chemically induced groups
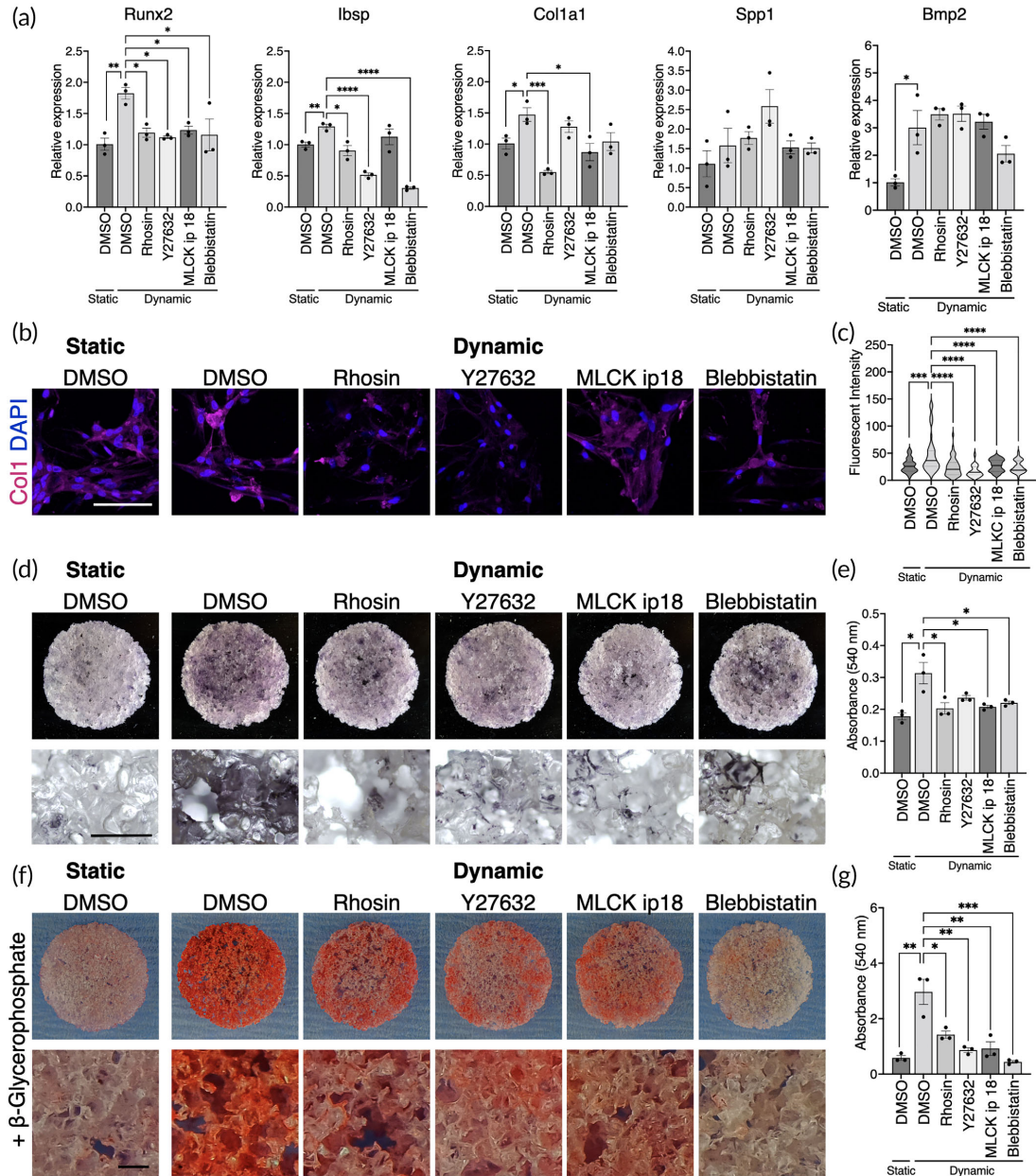
FIGURE 7 Mechanically induced osteogenesis is dependent on actomyosin contractility (a) mRNA expression levels of osteogenic markers in the static and dynamic conditions with/without the inhibitors of actomyosin contractility. (b) Immunofluorescence of type 1 collagen and (c) quantification of fluorescent intensity. (d) Alkaline phosphatase staining and (e) quantification of extracted substrate. (f) Alizarin red S staining and (g) quantification of extracted dye. The samples for the mineralization assay were cultured in the presence of β-glycerophosphate as a source of phosphate ions. Statistical comparison between the static and dynamic condition was performed by the Student's t-test and comparison among pharmacologically treated groups were by ANOVA followed by Dunnett's multiple comparison. $*p < 0.05$; $**p < 0.01$; $***p < 0.001$; $****p < 0.0001$. White scale bar = 100 μm, black scale bar = 500 μm.

(Figure 6c). The clusters of perfusion-induced osteogenesis were indeed shifted orthogonally to conventional osteogenic differentiation, but the subsequent experiments revealed the expression patterns still supported conventional osteogenic functionality.

3.5 | Mechanically induced osteoblastic functionality is governed by Rho-ROCK signaling and cell contractility

To investigate whether (1) the mechanically induced osteogenic profile was governed by cell contraction under perfusion and (2) the mechanically stimulated BMSC practically possessed the osteoblastic phenotype, osteogenic differentiation was further evaluated with and without the cell contraction inhibitors.

As the osteogenic profiling revealed, the expression of Runx2 (1.82-fold increase, $p = 0.0038$), Ibsp (1.29-fold increase, $p = 0.0053$), Cal1a1 (1.47-fold increase, $p = 0.030$), Spp1 (1.57-fold increase, $p = 0.45$), and Bmp2 (3.0-fold increase, $p = 0.035$) increased in the dynamic condition compared to the static counterpart on Day 7 (Figure 7a). The use of the inhibitors fully or partially counteracted the upregulation of Runx2, Ibsp, and Col1a1 but not Spp1. The mitigation of mechanically induced Bmp2 expression by the inhibitors was not statistically significant.

For the functionality assessment of the stimulated BMSC, collagen matrix formation, alkaline phosphatase activity, and calcium deposition were evaluated. While the cells in the static condition secreted type 1 collagen faintly, clusters of the cells significantly enriched collagen production in the dynamic condition (Figure 7b,c). This was depicted as an outstanding peak in the dynamic condition by the quantification ($p = 0.0002$). The inhibitors, particularly Y27632, disrupted the perfusion-enhanced collagen secretion. Similarly, ALP staining showed the upregulated ALP activity in the dynamic condition compared to the static counterpart ($p = 0.0019$), which was, however, negated by the inhibitors (Figure 7d,e). Calcium deposition was evaluated as an indicator of maturation of osteogenic differentiation by adding beta-glycerophosphate as a source of phosphate ions in the growth medium. Remarkably, the mechanically stimulated cells successfully deposited calcium nodes on the scaffolds while beta-glycerophosphate alone was not sufficient to induce mineralization in the static condition ($p = 0.0066$) (Figure 7f,g). Mineralization was attenuated by the inhibitors, particularly blebbistatin, completely masking the pro-osteogenic effect of dynamic cell culture. Taken together, dynamic cell culture in the perfusion bioreactor was sufficient to induce BMSC osteogenesis, which was dependent on enhanced cellular contractility.

4 | DISCUSSION

Using a bioreactor for 3D cell culture is a promising strategy to improve the efficiency of cell therapy in bone tissue engineering. Based on credible evidence identified in conventional monolayer cell culture studies that mechanical stimulation promotes BMSC osteogenesis, the concept has been brought to 3D systems for translational research. However, due to the complexity of 3D cell culture in a dynamic environment, the knowledge gained so far seems fragmented, particularly when in the absence of osteoinductive medium. This is because in different bioreactor systems developed for bone tissue engineering not only dynamic conditions but also basic cell culture factors such as volume of medium, humidification method, and static pressure may differ.[39,43,44] The chemical and physical properties of scaffolding materials may also synergistically influence cellular behaviors in a dynamic environment. Additionally, the precise evaluation of fluid dynamics with 3D scaffolds requires high computational cost, which may not always be affordable.[45] Consequently, flow is often described only by flow rate (e.g., mL/min) or pump speed (e.g., rpm), but not the magnitude of fluid force exerted on cells.[46] These factors make it difficult to interpret experimental findings from different models. In the present study by culturing BMSC in the perfusion bioreactor, the comprehensive analyses of cell behaviors under perfusion culture were performed including detailed CFD analysis, cell morphological assessment, cell growth, and mechanically induced osteogenesis in the absence of osteoinductive medium.

In the present study, the optimal flow rate was preliminarily determined as 1.0 mL/min in the system. The flow rate corresponded to estimated shear stress of approximately 0.5–5 mPa (mean 1.56 mPa) to which most of BMSC on the scaffolds were exposed. Fluid paths were estimated to be distributed uniformity throughout the constructs, which is an important aspect of the dynamic culture to improve mass transfer from/to the constructs although a magnitude of fluid shear varied spatially. BMSC and osteoblastic cells are reportedly more vulnerable to fluidic stimulation on 3D porous scaffolds compared to the 2D monolayered counterpart, and excessive shear stress can lead to apoptosis.[21,37,47–52] This could be because cell morphological adaptation and migration are restricted to the geometry of scaffolds when fluid stimuli act in multiple directions.[53] It was therefore no surprise that the shear stress used in our study, although considerably lower than that reported to promote osteogenesis in the conventional 2D systems, was sufficient to provoke dynamic cellular behaviors.

Under this level of perfusion, BMSC clearly showed a sign of morphological change with a number of upregulated factors for cell morphogenesis including surface mechanoreceptors, focal adhesion complex, and the direct inducers of actomyosin contractility. Elevated actomyosin contractility directly links to BMSC fate determination as a process and an endpoint. The angular, elongated morphology and increased rheological stiffness of BMSC is associated with high expression of actomyosin and focal adhesion and with osteoblast fate, whereas rounded morphology, low cell stiffness and lower actomyosin and focal adhesion expression is associated with adipogenic differentiation.[54–56] Therefore, it would be reasonable to mention that the cytoskeletal features exhibited by the BMSC in the present system favored osteogenic differentiation.

Our results indicated that perfusion culture delayed cell proliferation, possibly mediated by cell contraction. The reported effect of

perfusion culture on cell proliferation is inconsistent in the published literature in both 2D and 3D systems. There are studies reporting mitogenic effects,[11,12,30,33,57–60] anti-mitogenic effects,[15,16,32,36,61] and no effect,[14,34] while all promoting osteogenic phenotypes. The inconsistency could arise from differences in the magnitude of shear stress, the type of cells used, measurement methodology, and/or the efficiency of passive nutrient transport within scaffolding material since low-diffusive scaffolds would benefit from perfusion more than highly permeable materials with the respect to nutrient transport. Previous studies in a 2D cell culture model demonstrated that laminar shear stress reduces MSC proliferation in a dose-dependent manner by arresting cell cycle at G_0/G_1 phases.[51,62] In the present study, where the highly porous scaffolds with macropores were used, the reduction of cell proliferation could be attributed largely to shear stress on the cells. The cell contractility inhibitors of Rho, ROCK, MLCK, and myosin II blocked cell cycle further and hindered cell proliferation in the dynamic condition. Taken together, increased cell contraction caused by shear stress was associated with reduced cell proliferation, but contractility was indeed necessary for maintaining proliferation under flow.

Mechanically induced or promoted osteogenic differentiation is often measured by increased ALP activity and the upregulation of key osteogenic markers, such as Runx2. However, the term "osteogenic differentiation" has been used casually without sufficient definition, and the overall osteogenic profile under mechanical stimulation has not hitherto been adequately described. The present study highlighted the unique osteogenic profile of BMSC stimulated by fluid flow. Even in the absence of the osteoinductive supplements, fluid shear stress stimulated the mRNA expression of osteogenic markers, such as Runx2, Alp, and Ibsp. Interestingly, the expression of Runx2 was significantly higher in the dynamic condition than the OM group, and signaling molecules such as Bmps, Fgfs, Csfs, and Tgfs were differentially expressed. This has revealed that fluid shear stress may induce osteogenic differentiation differently from the conventionally described differentiation by the OM. Nevertheless, the functionality gained by the mechanically stimulated BMSC reconciled with typical preosteoblast-like phenotypes, featured by an increase in type 1 collagen formation and ALP activity. It is generally considered that, in the absence of the osteoinductive supplements, mechanical stimulation promotes ALP activity and the expression of early osteogenic markers, but it is not sufficient to induce osteoblastic maturation characterized by the upregulation of Bglap and mineralization.[21,23,24,57–59] Here, by adding beta-glycerophosphate as a source of inorganic phosphate ions in the growth medium, we demonstrated that the mechanically stimulated BMSC were capable of depositing calcium nodes despite a lack of Bglap expression. In fact, the initiation of mineralization precedes the significant upregulation of Bglap in vitro,[38] suggesting that the mechanically stimulated BMSC indeed possessed the phenotype of moderately mature osteoblastic cells. The inhibition of actomyosin contractility under flow significantly mitigated their osteogenic functionality, confirming that cytoskeletal rearrangement via Rho-ROCK signaling is necessary for the osteogenic responses triggered by fluidic stimuli in the absence of osteoinductive medium. Nevertheless, the

mechanically upregulated osteogenic markers were not consistently suppressed by the inhibitors. Previous studies have shown that fluid shear stress at physiological levels modulates various pathways such as ERK/MAPK signaling, P38 signaling, TGFβ signaling, Hedgehog signaling, Notch signaling, and Wnt signaling pathways in MSC as well as osteoblasts and osteocytes.[16,21,63–65] The regulation of osteogenic genes is multifactorial, and these pathway may interplay with osteogenic genes differently, which may bypass the Rho-ROCK-mediated cell contraction. Although this study does not enter the debate as to whether Rho-ROCK activation and/or cell contraction are sufficient to induce osteogenesis, we observed that the pharmacological activation of Rho by Narciclasine significantly modulated the mRNA expression level of Runx2 and Bmp2 (Figure S3B). The upregulation of Bmp2 was also induced by the inhibition of myosin phosphatase, Calyculin A. However, both drugs significantly decreased Col1a1 expression, and we did not find a rational correlation between cell contractility and ALP activity from the preliminary data (Figure S3C,D). It would be therefore reasonable to conclude that osteogenic induction by fluid stimuli is governed by, but not limited to, Rho-ROCK-mediated cytoskeletal modulation.

Translation of knowledge in mechanobiology into the field of tissue engineering has successfully paved the way for the development of prominent dynamic cell culture platforms for regenerative medicine. This will facilitate effective 3D cell culture and improve cell-based therapy for bone regeneration. To bring mechanically stimulated cells into clinical settings, it is necessary to accurately grasp cell response to dynamic environment for safety and efficacy. Each system is unique, and bioreactor designs, material selection, scaffold geometry, supplemented drugs, cell origin, and other environmental factors synergistically or reciprocally interact with resulting cell behaviors.[66,67] More to the point, biological variables attributable to donors such as age, gender, systemic conditions, and epigenetics need to be taken into consideration when it comes to clinical application.[68] In the study, male Lewis rats were used as a source of BMSC because of the abundancy of BMSC compared to female animals.[69] Admittedly, our observation needs to be verified by human cells isolated from donors with various background. Therefore, further in-depth studies using diverse experimental settings are required to fully elucidate mechanically induced osteogenesis and its potential for future clinical translation.

AUTHOR CONTRIBUTIONS

ACKNOWLEDGMENTS

CONFLICT OF INTEREST STATEMENT

The authors declare no potential conflicts of interest with respect to the authorship and/or publication of this article.

PEER REVIEW

The peer review history for this article is available at https://www.webofscience.com/api/gateway/wos/peer-review/10.1002/btm2.10509.

DATA AVAILABILITY STATEMENT

The raw data supporting the conclusion of this article will be made available by the authors, without undue reservation.

ORCID

Shuntaro Yamada https://orcid.org/0000-0003-0282-5498

REFERENCES

1. Lane SW, Williams DA, Watt FM. Modulating the stem cell niche for tissue regeneration. *Nat Biotechnol*. 2014;32:795-803.
2. Maul TM, Chew DW, Nieponice A, Vorp DA. Mechanical stimuli differentially control stem cell behavior: morphology, proliferation, and differentiation. *Biomech Model Mechanobiol*. 2011;10:939-953.
3. Gurkan UA, Akkus O. The mechanical environment of bone marrow: a review. *Ann Biomed Eng*. 2008;36:1978-1991.
4. Castillo AB, Jacobs CR. Mesenchymal stem cell mechanobiology. *Curr Osteoporos Rep*. 2010;8:98-104.
5. Metzger TA, Schwaner SA, LaNeve AJ, Kreipke TC, Niebur GL. Pressure and shear stress in trabecular bone marrow during whole bone loading. *J Biomech*. 2015;48:3035-3043.
6. Sun Y, Yuan Y, Wu W, Lei L, Zhang L. The effects of locomotion on bone marrow mesenchymal stem cell fate: insight into mechanical regulation and bone formation. *Cell Biosci*. 2021;11:88.
7. Zhong Z, Akkus O. Effects of age and shear rate on the rheological properties of human yellow bone marrow. *Biorheology*. 2011;48:89-97.
8. Bethel M, Chitteti BR, Srour EF, Kacena MA. The changing balance between osteoblastogenesis and adipogenesis in aging and its impact on hematopoiesis. *Curr Osteoporos Rep*. 2013;11:99-106.
9. Justesen J, Stenderup K, Ebbesen EN, Mosekilde L, Steiniche T, Kassem M. Adipocyte tissue volume in bone marrow is increased with aging and in patients with osteoporosis. *Biogerontology*. 2001;2:165-171.
10. Gao X, Zhang X, Xu H, Zhou B, Wen W, Qin J. Regulation of cell migration and osteogenic differentiation in mesenchymal stem cells under extremely low fluidic shear stress. *Biomicrofluidics*. 2014;8:052008.
11. Elashry MI, Gegnaw ST, Klymiuk MC, Wenisch S, Arnhold S. Influence of mechanical fluid shear stress on the osteogenic differentiation protocols for equine adipose tissue-derived mesenchymal stem cells. *Acta Histochem*. 2019;121:344-353.
12. Kapur S, Baylink DJ, William Lau K-H. Fluid flow shear stress stimulates human osteoblast proliferation and differentiation through multiple interacting and competing signal transduction pathways. *Bone*. 2003;32:241-251.
13. Liu L, Shao L, Li B, et al. Extracellular signal-regulated kinase1/2 activated by fluid shear stress promotes osteogenic differentiation of human bone marrow-derived mesenchymal stem cells through novel signaling pathways. *Int J Biochem Cell Biol*. 2011;43:1591-1601.
14. Kreke MR, Goldstein AS. Hydrodynamic shear stimulates osteocalcin expression but not proliferation of bone marrow stromal cells. *Tissue Eng*. 2004;10:780-788.
15. Kreke M, Huckle W, Goldstein A. Fluid flow stimulates expression of osteopontin and bone sialoprotein by bone marrow stromal cells in a temporally dependent manner. *Bone*. 2005;36:1047-1055.
16. Zhao Y, Richardson K, Yang R, et al. Notch signaling and fluid shear stress in regulating osteogenic differentiation. *Front Bioeng Biotechnol*. 2022;10:1-14.
17. Kim KM, Choi YJ, Hwang J-H, et al. Shear stress induced by an interstitial level of slow flow increases the osteogenic differentiation of mesenchymal stem cells through TAZ activation. *PLoS One*. 2014;9:e92427.
18. Dash SK, Sharma V, Verma RS, Das SK. Low intermittent flow promotes rat mesenchymal stem cell differentiation in logarithmic fluid shear device. *Biomicrofluidics*. 2020;14:054107.
19. Pasini A, Lovecchio J, Ferretti G, Giordano E. Medium perfusion flow improves osteogenic commitment of human stromal cells. *Stem Cells Int*. 2019;2019:1-10.
20. Sonam S, Sathe SR, Yim EKF, Sheetz MP, Lim CT. Cell contractility arising from topography and shear flow determines human mesenchymal stem cell fate. *Sci Rep*. 2016;6:20415.
21. Yourek G, McCormick SM, Mao JJ, Reilly GC. Shear stress induces osteogenic differentiation of human mesenchymal stem cells. *Regen Med*. 2010;5:713-724.
22. Li Y, Wang J, Zhong W. Regulation and mechanism of YAP/TAZ in the mechanical microenvironment of stem cells (review). *Mol Med Rep*. 2021;24:506.
23. Hu K, Sun H, Gui B, Sui C. TRPV4 functions in flow shear stress induced early osteogenic differentiation of human bone marrow mesenchymal stem cells. *Biomed Pharmacother*. 2017;91:841-848.
24. Jiao F, Xu J, Zhao Y, et al. Synergistic effects of fluid shear stress and adhesion morphology on the apoptosis and osteogenesis of mesenchymal stem cells. *J Biomed Mater Res Part A*. 2022;110:1636-1644.
25. Bergemann C, Elter P, Lange R, et al. Cellular nutrition in complex three-dimensional scaffolds: a comparison between experiments and computer simulations. *Int J Biomater*. 2015;2015:1-12.
26. Rouwkema J, Koopman BFJM, Van Blitterswijk CA, Dhert WJA, Malda J. Supply of nutrients to cells in engineered tissues. *Biotechnol Genet Eng Rev*. 2009;26:163-178.
27. Martin I, Smith T, Wendt D. Bioreactor-based roadmap for the translation of tissue engineering strategies into clinical products. *Trends Biotechnol*. 2009;27:495-502.
28. Moser C, Bardsley K, El Haj AJ, Alini M, Stoddart MJ, Bara JJ. A perfusion culture system for assessing bone marrow stromal cell differentiation on PLGA scaffolds for bone repair. *Front Bioeng Biotechnol*. 2018;6:161.

29. Harvestine JN, Gonzalez-Fernandez T, Sebastian A, et al. Osteogenic preconditioning in perfusion bioreactors improves vascularization and bone formation by human bone marrow aspirates. Sci Adv. 2020;6: eaay2387.

30. Birru B, Mekala NK, Parcha SR. Improved osteogenic differentiation of umbilical cord blood MSCs using custom made perfusion bioreactor. Biom J. 2018;41:290-297.

31. Kleinhans C, Mohan RR, Vacun G, et al. A perfusion bioreactor system efficiently generates cell-loaded bone substitute materials for addressing critical size bone defects. Biotechnol J. 2015;10:1727-1738.

32. Egger D, Spitz S, Fischer M, et al. Application of a parallelizable perfusion bioreactor for physiologic 3D cell culture. Cells Tissues Organs. 2017;203:316-326.

33. Shi F, Xiao D, Zhang C, Zhi W, Liu Y, Weng J. The effect of macropore size of hydroxyapatite scaffold on the osteogenic differentiation of bone mesenchymal stem cells under perfusion culture., Regen. Biomaterials. 2021;8:rbab050.

34. Gomes ME, Sikavitsas VI, Behravesh E, Reis RL, Mikos AG. Effect of flow perfusion on the osteogenic differentiation of bone marrow stromal cells cultured on starch-based three-dimensional scaffolds. J Biomed Mater Res. 2003;67A:87-95.

35. Pereira AR, Lipphaus A, Ergin M, et al. Modeling of the human bone environment: mechanical stimuli guide mesenchymal stem cell–extracellular matrix interactions. Materials (Basel). 2021;14:4431.

36. Yamada S, Yassin MA, Schwarz T, Hansmann J, Mustafa K. Induction of osteogenic differentiation of bone marrow stromal cells on 3D polyester-based scaffolds solely by subphysiological fluidic stimulation in a laminar flow bioreactor. J Tissue Eng. 2021;12: 20417314211019376.

37. Gaspar DA, Gomide V, Monteiro FJ. The role of perfusion bioreactors in bone tissue engineering. Biomatter. 2012;2:167-175.

38. Yamada S, Yassin MA, Weigel T, Schmitz T, Hansmann J, Mustafa K. Surface activation with oxygen plasma promotes osteogenesis with enhanced extracellular matrix formation in three-dimensional microporous scaffolds. J Biomed Mater Res A. 2021;109:1560-1574.

39. Yamada S, Yassin MA, Schwarz T, Mustafa K, Hansmann J. Optimization and validation of a custom-designed perfusion bioreactor for bone tissue engineering: flow assessment and optimal culture environmental conditions. Front Bioeng Biotechnol. 2022;10:811942.

40. Zhao F, Melke J, Ito K, van Rietbergen B, Hofmann S. A multiscale computational fluid dynamics approach to simulate the micro-fluidic environment within a tissue engineering scaffold with highly irregular pore geometry. Biomech Model Mechanobiol. 2019;18:1965-1977.

41. Livak KJ, Schmittgen TD. Analysis of relative gene expression data using real-time quantitative PCR and the 2(-Delta Delta C(T)) method. Methods. 2001;25:402-408.

42. Schindelin J, Arganda-Carreras I, Frise E, et al. An open source platform for biological image analysis. Nat Methods. 2012;9:676-682.

43. Schuerlein S, Schwarz T, Krziminski S, et al. A versatile modular bioreactor platform for tissue engineering. Biotechnol J. 2017;12:1600326.

44. Schreivogel S, Kuchibhotla V, Knaus P, Duda GN, Petersen A. Load-induced osteogenic differentiation of mesenchymal stromal cells is caused by mechano-regulated autocrine signaling. J Tissue Eng Regen Med. 2019;13:1992-2008.

45. Maes F, Claessens T, Moesen M, Van Oosterwyck H, Van Ransbeeck P, Verdonck P. Computational models for wall shear stress estimation in scaffolds: a comparative study of two complete geometries. J Biomech. 2012;45:1586-1592.

46. Sladkova M, de Peppo G. Bioreactor systems for human bone tissue engineering. Processes. 2014;2:494-525.

47. McAllister TN, Du T, Frangos JA. Fluid shear stress stimulates prostaglandin and nitric oxide release in bone marrow-derived preosteoblast-like cells. Biochem Biophys Res Commun. 2000;270: 643-648.

48. Jiang G-L, White CR, Stevens HY, Frangos JA. Temporal gradients in shear stimulate osteoblastic proliferation via ERK1/2 and retinoblastoma protein. Am J Physiol Metab. 2002;283:E383-E389.

49. Lim KT, Hexiu J, Kim J, Seonwoo H, Choung P-H, Chung JH. Synergistic effects of orbital shear stress on In vitro growth and osteogenic differentiation of human alveolar bone-derived mesenchymal stem cells. Biomed Res Int. 2014;2014:1-18.

50. Liu Y-S, Liu Y-A, Huang C-J, et al. Mechanosensitive TRPM7 mediates shear stress and modulates osteogenic differentiation of mesenchymal stromal cells through Osterix pathway. Sci Rep. 2015;5:16522.

51. Yu L, Ma X, Sun J, et al. Fluid shear stress induces osteoblast differentiation and arrests the cell cycle at the G0 phase via the ERK1/2 pathway. Mol Med Rep. 2017;16:8699-8708.

52. Porter B, Zauel R, Stockman H, Guldberg R, Fyhrie D. 3-D computational modeling of media flow through scaffolds in a perfusion bioreactor. J Biomech. 2005;38:543-549.

53. Zhao F, Xiong Y, Ito K, van Rietbergen B, Hofmann S. Porous geometry guided micro-mechanical environment within scaffolds for cell mechanobiology study in bone tissue engineering. Front Bioeng Biotechnol. 2021;9:736489.

54. Kilian KA, Bugarija B, Lahn BT, Mrksich M. Geometric cues for directing the differentiation of mesenchymal stem cells. Proc Natl Acad Sci. 2010;107:4872-4877.

55. Schillers H, Wälte M, Urbanova K, Oberleithner H. Real-time monitoring of cell elasticity reveals oscillating myosin activity. Biophys J. 2010;99:3639-3646.

56. Mathieu PS, Loboa EG. Cytoskeletal and focal adhesion influences on mesenchymal stem cell shape, mechanical properties, and differentiation down osteogenic, adipogenic, and chondrogenic pathways. Tissue Eng Part B Rev. 2012;18:436-444.

57. Bjerre L, Bünger CE, Kassem M, Mygind T. Flow perfusion culture of human mesenchymal stem cells on silicate-substituted tricalcium phosphate scaffolds. Biomaterials. 2008;29:2616-2627.

58. Sailon AM, Allori AC, Davidson EH, Reformat DD, Allen RJ, Warren SM. A novel flow-perfusion bioreactor supports 3D dynamic cell culture. J Biomed Biotechnol. 2009;2009:1-7.

59. Lembong J, Lerman MJ, Kingsbury TJ, Civin CI, Fisher JP. A fluidic culture platform for spatially patterned cell growth, differentiation, and cocultures. Tissue Eng Part A. 2018;24:1715-1732.

60. Bancroft GN, Sikavitsas VI, van den Dolder J, et al. Fluid flow increases mineralized matrix deposition in 3D perfusion culture of marrow stromal osteoblasts in a dose-dependent manner. Proc Natl Acad Sci. 2002;99:12600-12605.

61. Cartmell SH, Porter BD, García AJ, Guldberg RE. Effects of medium perfusion rate on cell-seeded three-dimensional bone constructs in vitro. Tissue Eng. 2003;9:1197-1203.

62. Luo W, Xiong W, Zhou J, et al. Laminar shear stress delivers cell cycle arrest and anti-apoptosis to mesenchymal stem cells. Acta Biochim Biophys Sin (Shanghai). 2011;43:210-216.

63. Monteiro DA, Dole NS, Campos JL, et al. Fluid shear stress generates a unique signaling response by activating multiple TGFβ family type I receptors in osteocytes. FASEB J. 2021;35:e21263.

64. Lau K-HW, Kapur S, Kesavan C, Baylink DJ. Up-regulation of the Wnt, estrogen receptor, insulin-like growth factor-I, and bone morphogenetic protein pathways in C57BL/6J osteoblasts as opposed to C3H/HeJ osteoblasts in part contributes to the differential anabolic response to fluid shear. J Biol Chem. 2006;281: 9576-9588.

65. Johnson GP, Fair S, Hoey DA. Primary cilium-mediated MSC mechanotransduction is dependent on Gpr161 regulation of hedgehog signalling. Bone. 2021;145:115846.

66. Osborne JM, O'Dea RD, Whiteley JP, Byrne HM, Waters SL. The influence of bioreactor geometry and the mechanical environment on engineered tissues. *J Biomech Eng*. 2010;132:051006.

67. Ahmed S, Chauhan VM, Ghaemmaghami AM, Aylott JW. New generation of bioreactors that advance extracellular matrix modelling and tissue engineering. *Biotechnol Lett*. 2019;41:1-25.

68. Siddappa R, Licht R, van Blitterswijk C, de Boer J. Donor variation and loss of multipotency during in vitro expansion of human mesenchymal stem cells for bone tissue engineering. *J Orthop Res*. 2007;25:1029-1041.

69. Strube P, Mehta M, Baerenwaldt A, et al. Sex-specific compromised bone healing in female rats might be associated with a decrease in mesenchymal stem cell quantity. *Bone*. 2009;45:1065-1072.

SUPPORTING INFORMATION

Additional supporting information can be found online in the Supporting Information section at the end of this article.
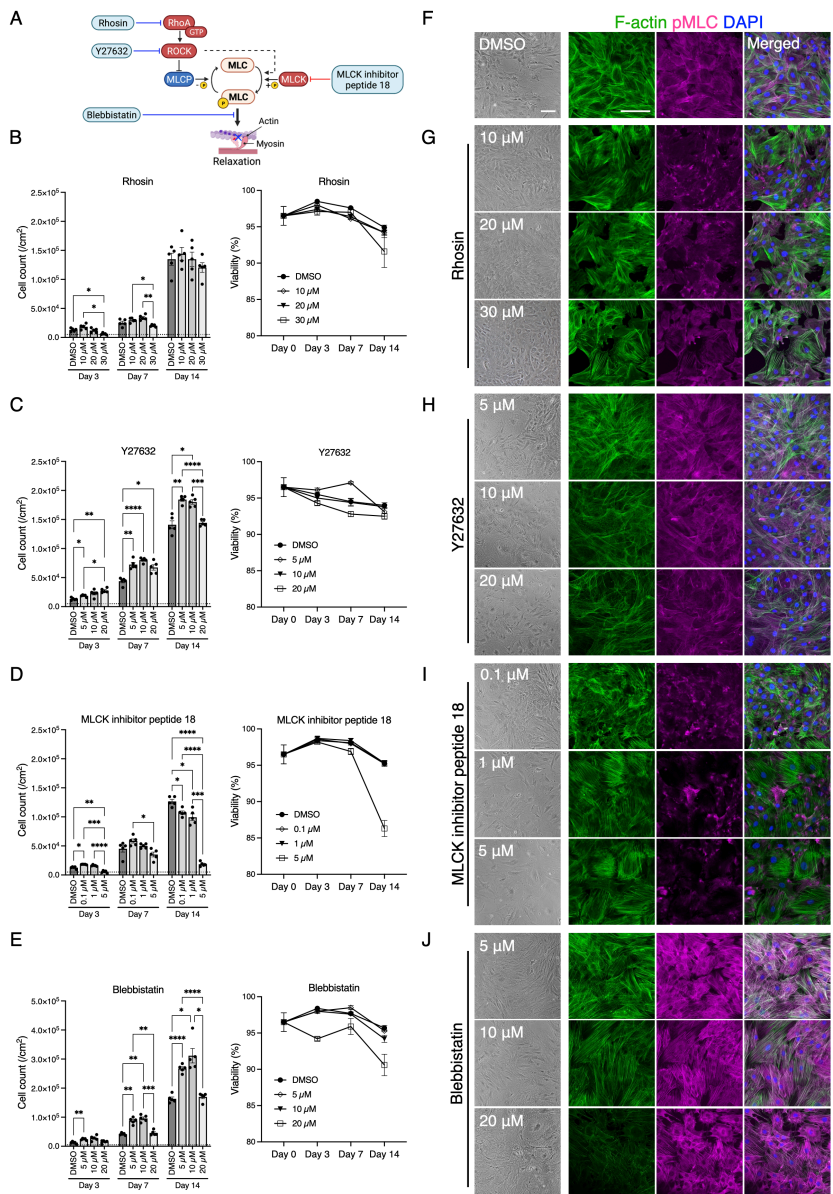
Fig. S1 Optimization of inhibitors for suppressing actomyosin contractility

(A) Rhosin chloride (Rhosin), Y27632 dihydrochloride (Y27632), MLCK inhibitory peptide 18 (MLCK ip 18), and Blebbistatin (203390) were applied to inhibit Rho, ROCK, myosin light chain kinase (MLCK), and myosin II, respectively to forcibly trigger cell relaxation. (B-J) Cell growth, viability, and actomyosin contraction were evaluated to optimize the working concentrations. * $p<0.05$, ** $p<0.01$, *** $p<0.001$, **** $p<0.0001$. Scale bar = 100 µm.
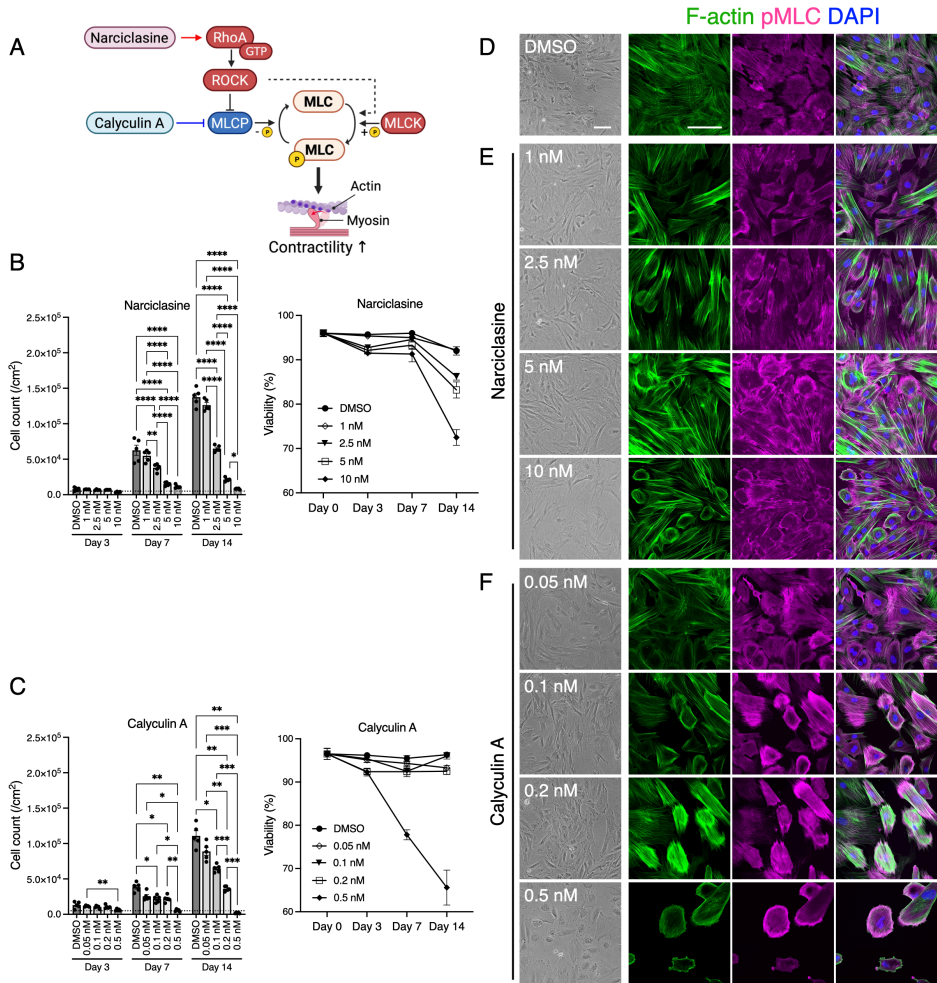
Fig. S2 Optimization of enhancers of actomyosin contractility

(A) Narciclasine and Calyculin A were applied to activate Rho and to inhibit myosin light chain phosphatase (MLCP) to forcibly trigger cell contraction.   (B-F) Cell growth, viability, and actomyosin contraction were evaluated to optimize the working concentrations. * p<0.05, ** p<0.01, *** p<0.001, **** p<0.0001. Scale bar = 100 μm.
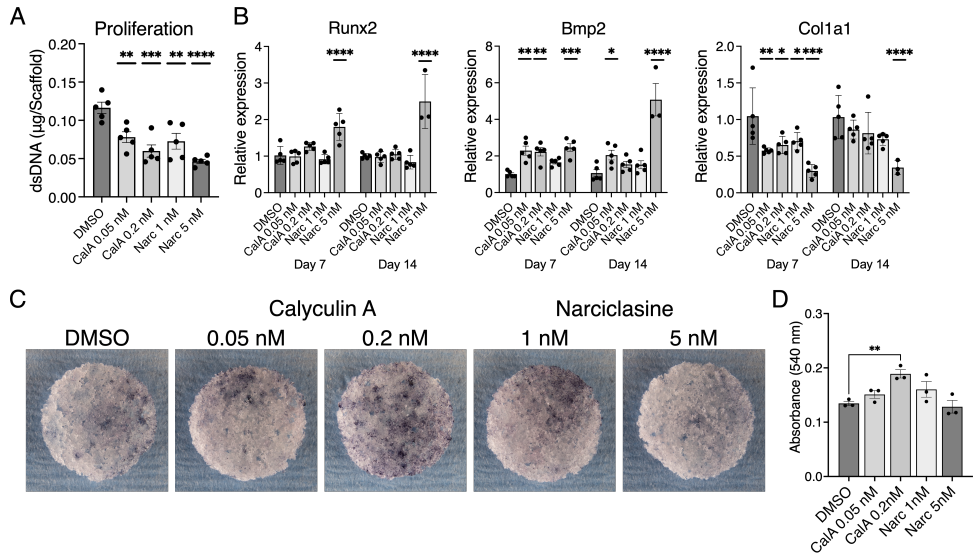
Fig. S3 BMSC Growth and osteogenic properties under pharmacologically triggered actomyosin contraction

BMSC were treated with 0.05 nM and 0.2 nM Calyculin A (CalA) and 1 nM and 5 nM Narciclasine (Narc) (A) Quantification of double-strand DNA (dsDNA) after 7 days of static culture. (B) mRNA expression of putative osteogenic markers after 7 days of static culture. (C, D) Alkaline phosphatase staining and quantification of extracted substrate after 14 days of static culture.   * $p<0.05$, ** $p<0.01$, *** $p<0.001$, **** $p<0.0001$.

Table. S1 A set of genes and primers used for the assessment of cytoskeletal rearrangement under perfusion

	Gene Symbol	Gene Name	TaqMan Assay ID	Amplicon Length (bp)
Target genes	Actn1	actinin, alpha 1	Rn00667357_m1	66
	Actn3	actinin alpha 3	Rn00591594_m1	88
	Actn4	actinin alpha 4	Rn00581554_m1	69
	Actr2	ARP2 actin-related protein 2 homolog	Rn01434079_m1	83
	Actr3	ARP3 actin-related protein 3 homolog	Rn01753774_m1	99
	Akt1	v-akt murine thymoma viral oncogene homolog 1	Rn00583646_m1	87
	Akt2	v-akt murine thymoma viral oncogene homolog 2	Rn00690900_m1	138
	Akt3	v-akt murine thymoma viral oncogene homolog 3	Rn00442194_m1	71
	Arap1	ArfGAP with RhoGAP domain, ankyrin repeat and PH domain 1	Rn01506749_m1	66
	Arfip2	ADP-ribosylation factor interacting protein 2	Rn01508475_m1	90
	Arhgap5	Rho GTPase activating protein 5	Rn03036858_s1	106
	Arhgap5	Rho GTPase activating protein 5	Rn03036858_s1	106
	Arhgdib	Rho, GDP dissociation inhibitor (GDI) beta	Rn01459333_m1	62
	Arhgef11	Rho guanine nucleotide exchange factor (GEF) 11	Rn00572505_m1	84
	Arhgef11	Rho guanine nucleotide exchange factor (GEF) 11	Rn00576857_m1	67
	Arpc1b	actin related protein 2/3 complex, subunit 1B	Rn00820959_g1	80
	Arpc2	actin related protein 2/3 complex, subunit 2	Rn01400361_m1	62
	Arpc3	actin related protein 2/3 complex, subunit 3	Rn01481651_m1	72
	Arpc4	actin related protein 2/3 complex, subunit 4	Rn01426286_m1	64
	Arpc5	actin related protein 2/3 complex, subunit 5	Rn01759260_m1	93
	Aurka	aurora kinase A	Rn00821847_g1	91
	Aurkb	aurora kinase B	Rn01460656_m1	95
	Aurkc	aurora kinase C	Rn01523742_g1	68
	Baiap2	BAI1-associated protein 2	Rn00589411_m1	99
	Bcar1	breast cancer anti-estrogen resistance 1	Rn00564003_m1	59
	Braf	B-Raf proto-oncogene, serine/threonine kinase	Rn01500563_m1	60
	Cald1	caldesmon 1	Rn00567519_m1	98
	Calm1	calmodulin 1	Rn00821407_g1	82
	Capn2	calpain 2	Rn00567422_m1	83
	Cask	calcium/calmodulin-dependent serine protein kinase	Rn00573365_m5	89
	Cav1	caveolin 1, caveolae protein	Rn00755834_m1	64
	Cav2	caveolin 2	Rn00590969_m1	72
	Cav3	caveolin 3	Rn00755343_m1	64
	Ccna1	cyclin A1	Rn01761351_m1	59
	Ccnb1	cyclin B1	Rn01494177_m1	97
	Ccnb2	cyclin B2	Rn02346769_g1	95
	Cdc42	cell division cycle 42	Rn00696671_m1	100
	Cdc42bpa	CDC42 binding protein kinase alpha	Rn00586520_m1	76
	Cdc42ep2	CDC42 effector protein (Rho GTPase binding) 2	Rn02376973_s1	63
	Cdc42ep3	CDC42 effector protein (Rho GTPase binding) 3	Rn01468719_m1	71
	Cdk5	cyclin-dependent kinase 5	Rn04219635_m1	95
	Cdk5r1	cyclin-dependent kinase 5, regulatory subunit 1 (p35)	Rn02132948_s1	134
	Cfl1	cofilin 1, non-muscle	Rn01501422_g1	77
	Cit	citron rho-interacting serine/threonine kinase	Rn00582449_m1	64
	Clasp1	cytoplasmic linker associated protein 1	Rn01408768_m1	59
	Clasp2	cytoplasmic linker associated protein 2	Rn00586859_m1	70
	Clip1	CAP-GLY domain containing linker protein 1	Rn00582048_m1	77
	Clip2	CAP-GLY domain containing linker protein 2	Rn00573248_m1	77
	Crk	v-crk avian sarcoma virus CT10 oncogene homolog	Rn00467066_m1	86
	Crkl	crk-like protein-like;v-crk avian sarcoma virus CT10 oncogene homolog-like	Rn01755203_m1	94
	Ctnnb1	catenin, beta 1	Rn00584431_s1	86
	Cttn	cortactin	Rn00573209_m1	67
	Cyfip1	cytoplasmic FMR1 interacting protein 1	Rn01409823_m1	59
	Cyfip2	cytoplasmic FMR1 interacting protein 2	Rn01471061_m1	65
	Diaph1	diaphanous-related formin 1	Rn01406955_m1	59
	Diaph1	diaphanous-related formin 1	Rn01406955_m1	59
	Dst	dystonin	Rn02110514_s1	93
	Dstn	destrin;destrin-like 1	Rn01415640_g1	89
	Ezr	ezrin	Rn01526350_m1	87
	Flna	filamin A, alpha	Rn01187530_m1	61
	Flnb	filamin B, beta	Rn01537993_m1	64
	Fnbp1l	formin binding protein 1-like	Rn01523678_m1	58
	Fscn2	fascin actin-bundling protein 2, retinal	Rn01470865_m1	61
	Fyn	FYN proto-oncogene, Src family tyrosine kinase	Rn00562616_m1	105
	Grb2	growth factor receptor bound protein 2	Rn01471333_g1	142
	Gsk3b	glycogen synthase kinase 3 beta	Rn00583429_m1	71
	Gsn	gelsolin	Rn01438922_m1	129
	Hras	Harvey rat sarcoma virus oncogene	Rn01479663_gH	72
	Ilk	integrin-linked kinase	Rn00591471_m1	70
	Iqgap1	IQ motif containing GTPase activating protein 1	Rn01478183_m1	62
	Itga1	integrin, alpha 1	Rn00578564_m1	71
	Itga10	integrin, alpha 10	Rn01533928_m1	73
	Itga11	integrin, alpha 11	Rn01421747_m1	54
	Itga2	integrin, alpha 2	Rn01489315_m1	52
	Itga2b	integrin, alpha 2B	Rn01456695_g1	108
	Itga3	integrin, alpha 3	Rn01751608_m1	61
	Itga4	integrin, alpha 4	Rn01512798_m1	97
	Itga5	integrin, alpha 5	Rn01761831_m1	91
	Itga6	integrin, alpha 6	Rn01512708_m1	53
	Itga7	integrin, alpha 7	Rn01529354_m1	56
	Itga8	integrin, alpha 8	Rn01487205_m1	78
	Itgal	integrin, alpha L	Rn01754645_m1	77
	Itgam	integrin, alpha M	Rn00709342_m1	76
	Itgav	integrin, alpha V	Rn01485633_m1	61
	Itgax	integrin, alpha X	Rn01511082_m1	64
	Itgb1	integrin, beta 1	Rn00566727_m1	81
	Itgb2	integrin, beta 2	Rn01427948_m1	142
	Itgb3	integrin, beta 3	Rn00596601_m1	66
	Itgb4	integrin, beta 4	Rn00566017_m1	66
	Itgb5	integrin, beta 5	Rn01439348_m1	63
	Itgb6	integrin, beta 6	Rn01747277_m1	82
	Limk1	LIM domain kinase 1	Rn00581900_m1	68
	Limk2	LIM domain kinase 2	Rn00577115_m1	60
	Llgl1	lethal giant larvae homolog 1	Rn00596096_m1	59
	Macf1	microtubule-actin crosslinking factor 1	Rn01516936_m1	56
	Map3k11	mitogen-activated protein kinase kinase kinase 11	Rn01502070_m1	149
	Map4	microtubule-associated protein 4	Rn01403680_m1	70
	Map6	microtubule-associated protein 6	Rn00567957_m1	95
	Mapk13	mitogen activated protein kinase 13	Rn00693138_m1	77
	Mapre1	microtubule-associated protein, RP/EB family, member 1	Rn00817431_g1	98
	Mapt	microtubule-associated protein tau	Rn01495715_m1	62
	Mark2	MAP/microtubule affinity-regulating kinase 2	Rn00433039_m1	68
	Mid1	midline 1	Rn00575975_m1	128
	Msn	moesin	Rn01424413_m1	58
	Mylk	myosin light chain kinase	Rn01439252_m1	72
	Mylk2	myosin light chain kinase 2	Rn00679009_m1	59
	Nck1	NCK adaptor protein 1	Rn01447186_m1	115
	Nck2	NCK adaptor protein 2	Rn01438228_m1	100
	Pak1	p21 protein (Cdc42/Rac)-activated kinase 1	Rn00664986_m1	98
	Pak2	p21 protein (Cdc42/Rac)-activated kinase 2	Rn00584005_m1	138
	Pak3	p21 protein (Cdc42/Rac)-activated kinase 3	Rn00693022_m1	72
	Pak4	p21 protein (Cdc42/Rac)-activated kinase 4	Rn01764387_m1	66
	Pak4	p21 protein (Cdc42/Rac)-activated kinase 4	Rn01764387_m1	66
	Parva	parvin, alpha	Rn00571958_m1	66
	Pdpk1	3-phosphoinositide dependent protein kinase-1	Rn00579366_m1	78
	Pfn2	profilin 2;profilin-2-like	Rn00450822_m1	104
	Phldb2	pleckstrin homology-like domain, family B, member 2	Rn01763372_m1	69
	Pip5k1c	phosphatidylinositol-4-phosphate 5-kinase, type I, gamma	Rn01408490_m1	61
	Plec	plectin	Rn00673737_m1	77
	Ppp1r12b	protein phosphatase 1, regulatory subunit 12B	Rn01490961_m1	67
	Ppp3ca	protein phosphatase 3, catalytic subunit, alpha isozyme	Rn00690508_m1	72
	Ppp3cb	protein phosphatase 3, catalytic subunit, beta isozyme	Rn00566864_m1	138
	Prkca	protein kinase C, alpha	Rn01496145_m1	74
	Prkcb	protein kinase C, beta	Rn00562312_m1	120
	Prkcg	protein kinase C, gamma	Rn00440861_m1	89
	Pten	phosphatase and tensin homolog	Rn00477208_m1	73
	Ptk2	protein tyrosine kinase 2	Rn01505115_m1	81
	Pxn	paxillin	Rn01499294_m1	77
	Rac1	ras-related C3 botulinum toxin substrate 1	Rn01412766_m1	86
	Rac2	ras-related C3 botulinum toxin substrate 2	Rn01504461_g1	57
	Racgap1	rac GTPase activating protein 1	Rn01761773_m1	62
	Raf1	v-raf-leukemia viral oncogene 1	Rn00466507_m1	88
	Rap1a	RAP1A, member of RAS oncogene family	Rn01533681_g1	139
	Rap1b	RAP1B, member of RAS oncogene family	Rn01509461_gH	108
	Rapgef1	Rap guanine nucleotide exchange factor (GEF) 1	Rn01438718_m1	64
	Rasgrf1	RAS protein-specific guanine nucleotide-releasing factor 1	Rn01447219_m1	54
	Rhoa	ras homolog family member A	Rn04219609_m1	100
	Rock1	Rho-associated coiled-coil containing protein kinase 1	Rn00579490_m1	75
	Rock2	Rho-associated coiled-coil containing protein kinase 2	Rn00564633_m1	73
	Sh3rf1	SH3 domain containing ring finger 1	Rn01535121_m1	78
	Shc1	SHC (Src homology 2 domain containing) transforming protein 1	Rn01458709_g1	131
	Shc2	SHC (Src homology 2 domain containing) transforming protein 2	Rn01371467_m1	63
	Sos1	Son of sevenless homolog 1	Rn01473774_m1	141
	Sos2	Son of sevenless homolog 2	Rn01468822_m1	68
	Src	SRC proto-oncogene, non-receptor tyrosine kinase	Rn00583063_m1	75
	Ssh2	slingshot protein phosphatase 2	Rn01471631_m1	77
	Stmn1	stathmin 1	Rn00691285_g1	137
	Tiam1	T-cell lymphoma invasion and metastasis 1	Rn01477317_m1	81
	Tln1	talin 1	Rn01440247_m1	64
	Tns2	tensin 2	Rn01532783_m1	130
	Tns4	tensin 4	Rn01751085_m1	69
	Vasp	vasodilator-stimulated phosphoprotein	Rn01477032_m1	146
	Vav1	vav 1 guanine nucleotide exchange factor	Rn00562712_m1	61
	Vav2	vav 2 guanine nucleotide exchange factor	Rn01436349_m1	63
	Vcl	vinculin	Rn01755894_m1	63
	Was	Wiskott-Aldrich syndrome	Rn01528309_m1	82
	Wasf1	WAS protein family, member 1	Rn01754124_m1	72
	Wasl	Wiskott-Aldrich syndrome-like	Rn01501122_m1	63
	Zyx	zyxin	Rn01501253_m1	57

Table. S2 A set of genes and primers used for the assessment of osteogenic profile under perfusion

	Gene Symbol	Gene Name	TaqMan Assay ID	Amplicon Length (bp)
Target genes	Ahsg	alpha-2-HS-glycoprotein	Rn00563700_m1	113
	Alpl	alkaline phosphatase	Rn01516028_m1	68
	Anxa5	annexin A5	Rn00565571_m1	115
	Bglap	bone gamma-carboxyglutamate (gla) protein	Rn01455285_g1	81
	Bgn	biglycan	Rn00567229_m1	76
	Bmp1	bone morphogenetic protein 1	Rn01466016_m1	75
	Bmp2	bone morphogenetic protein 2	Rn00567818_m1	126
	Bmp3	bone morphogenetic protein 3	Rn00690955_mH	60
	Bmp4	bone morphogenetic protein 4	Rn00432087_m1	61
	Bmp5	bone morphogenetic protein 5	Rn01447676_m1	78
	Bmp6	bone morphogenetic protein 6	Rn00432095_m1	122
	Bmp7	bone morphogenetic protein 7	Rn01528889_m1	65
	Bmpr1a	bone morphogenetic protein receptor, type IA	Rn01450292_g1	82
	Bmpr1b	bone morphogenetic protein receptor, type IB	Rn01748421_m1	67
	Cdh11	cadherin 11	Rn01536913_m1	61
	Col10a1	collagen, type X, alpha 1	Rn01408030_m1	80
	Col11a1	collagen, type XI, alpha 1	Rn01523309_m1	54
	Col12a1	collagen, type XII, alpha 1	Rn01521220_m1	57
	Col14a1	collagen, type XIV, alpha 1	Rn01502357_m1	57
	Col1a1	collagen, type I, alpha 1	Rn01463848_m1	115
	Col1a2	collagen, type I, alpha 2	Rn01526721_m1	96
	Col2a1	collagen, type II, alpha 1	Rn01637087_m1	97
	Col3a1	collagen, type III, alpha 1	Rn01437681_m1	71
	Col4a1	collagen, type IV, alpha 1	Rn01482927_m1	69
	Col4a2	collagen, type IV, alpha 2	Rn01482133_m1	53
	Col5a1	collagen, type V, alpha 1	Rn00593170_m1	61
	Col6a1	collagen, type VI, alpha 1	Rn01429556_m1	67
	Col6a2	collagen, type VI, alpha 2	Rn01429497_m1	77
	Col7a1	collagen, type VII, alpha 1	Rn01544829_m1	60
	Comp	cartilage oligomeric matrix protein	Rn00563255_m1	87
	Csf2	colony stimulating factor 2	Rn01456851_m1	127
	Csf3	colony stimulating factor 3	Rn00567344_m1	95
	Ctsk	cathepsin K	Rn00580723_m1	69
	Cyr61	cysteine-rich, angiogenic inducer, 61	Rn00580055_m1	113
	Dmp1	dentin matrix acidic phosphoprotein 1	Rn01450122_m1	77
	Egf	epidermal growth factor	Rn00563336_m1	93
	Fgf1	fibroblast growth factor 1	Rn00689153_m1	78
	Fgf2	fibroblast growth factor 2	Rn00570809_m1	63
	Fgf3	fibroblast growth factor 3	Rn00590754_m1	60
	Fgfr1	Fibroblast growth factor receptor 1	Rn00577234_m1	78
	Fgfr2	fibroblast growth factor receptor 2	Rn01269940_m1	87
	Flt1	FMS-related tyrosine kinase 1	Rn00570815_m1	60
	Fn1	fibronectin 1	Rn00569575_m1	97
	Gdf10	growth differentiation factor 10	Rn00666937_m1	105
	Ibsp	integrin-binding sialoprotein	Rn00561414_m1	138
	Icam1	intercellular adhesion molecule 1	Rn00564227_m1	61
	Igf1	insulin-like growth factor 1	Rn00710306_m1	69
	Igf1r	insulin-like growth factor 1 receptor	Rn00583837_m1	58
	Itga2	integrin, alpha 2	Rn01489315_m1	52
	Itga3	integrin, alpha 3	Rn01751608_m1	61
	Itgb1	integrin, beta 1	Rn00566727_m1	81
	Mmp10	matrix metallopeptidase 10	Rn00591678_m1	79
	Mmp2	matrix metallopeptidase 2	Rn01538170_m1	63
	Mmp8	matrix metallopeptidase 8	Rn00573646_m1	92
	Mmp9	matrix metallopeptidase 9	Rn00579162_m1	72
	Msx1	msh homeobox 1	Rn00667535_m1	83
	Nfkb1	nuclear Factor Kappa B Subunit 1	Rn01399583_m1	63
	Pdgfa	platelet-derived growth factor alpha polypeptide	Rn00709363_m1	62
	Phex	phosphate regulating endopeptidase homolog, X-linked	Rn00448130_m1	95
	Runx2	runt-related transcription factor 2	Rn01512298_m1	86
	Scarb1	scavenger receptor class B, member 1	Rn00580588_m1	75
	Serpinh1	Serpin Family H Member 1	Rn00567777_m1	76
	Smad1	SMAD family member 1	Rn00565555_m1	79
	Smad2	SMAD family member 2	Rn00569900_m1	67
	Smad3	SMAD family member 3	Rn00565331_m1	94
	Smad4	SMAD family member 4	Rn00570593_m1	101
	Sost	sclerostin	Rn00577971_m1	81
	Sox9	SRY (sex determining region Y)-box 9	Rn01751069_mH	60
	Sp7	Sp7 transcription factor	Rn01761789_m1	107
	Spp1	secreted phosphoprotein 1	Rn00681031_m1	73
	Tfip11	tuftelin interacting protein 11	Rn01481123_m1	125
	Tgfb1	transforming growth factor, beta 1	Rn00572010_m1	65
	Tgfb2	transforming growth factor, beta 2	Rn00579674_m1	95
	Tgfb3	transforming growth factor, beta 3	Rn00565937_m1	61
	Tgfbr1	transforming growth factor, beta receptor 1	Rn00562811_m1	86
	Tgfbr2	transforming growth factor, beta receptor 2	Rn00579682_m1	74
	Tgfbr3	transforming growth factor, beta receptor 3	Rn00568482_m1	89
	Tnf	tumor necrosis factor	Rn00562055_m1	82
	Tuft1	tuftelin 1	Rn01762781_m1	68
	Twist1	twist family bHLH transcription factor 1	Rn00585470_s1	71
	Vcam1	vascular cell adhesion molecule 1	Rn00563627_m1	90
	Vdr	vitamin D receptor	Rn00690616_m1	63
	Vegfa	vascular endothelial growth factor A	Rn01511601_m1	69
	Vegfb	vascular endothelial growth factor B	Rn01454585_g1	68

Table. S3 A set of genes and primers used as an endogeneous control

	Gene Symbol	Gene Name	TaqMan Assay ID	Amplicon Length (bp)
Endogenous control	18S	Eukaryotic 18S rRNA	Hs99999901_s1	187
	B2m	beta-2 microglobulin	Rn00560865_m1	58
	Gapdh	glyceraldehyde-3-phosphate dehydrogenase	Rn99999916_s1	87
	Gusb	glucuronidase, beta	Rn00566655_m1	63
	Hmbs	hydroxymethylbilane synthase	Rn00565886_m1	99
	Hprt1	hypoxanthine phosphoribosyltransferase 1	Rn01527840_m1	64
	Pgk1	phosphoglycerate kinase 1	Rn00821429_g1	84
	Rplp0	ribosomal protein, large, P0	Rn00821065_g1	97
	Rplp2	ribosomal protein, large P2	Rn01479927_g1	130

10. Acknowledgement

Writing this section signifies the end of my intense four-year Ph.D journey. Though it was challenging, the joy and happiness I experienced were greater than any difficulties I faced. I am grateful for the support of my friends, colleagues, and family, whose contributions have made my journey more valuable than just a degree. Despite a space limit, I would like to name a few of them to express my gratitude.

I would like to begin this section by expressing my gratitude to the Department of Clinical Dentistry, UiB, in particular, to the head of the department, **Prof. Asgeir Bårdsen**, and **all the staff members** who have supported me throughout my academic journey. The support and resources provided by the department have been instrumental in enabling me to carry out my research and achieve this significant milestone in my academic career.

I would like to express my gratitude to the **Trond Mohn Foundation** for providing principal financial support that has allowed me to pursue my PhD research.

My utmost gratitude goes to my main supervisor, **Prof. Kamal Mustafa**, for his guidance, encouragement, support, patience, and trust throughout my doctoral studies. You always listened to me, calmed me down, and gave me sound advice. Your support not only to my work but to my life as well as consideration to my family has been fundamental in the successful completion of my thesis.

I would also like to extend my appreciation to my co-supervisors, **Assoc. Prof. Mohammed Yassin**, and **Prof. Jan Hansmann** at Fraunhofer Institute for Silicate Research. Mohammed's broad insight in biomaterial research was instrumental in shaping my research questions and methodology. Thank you, Mohammed, not only as a supervisor but also for your friendship. Prof. Hansmann's valuable feedback and suggestions, as an external supervisor, greatly enriched my research and provided me with a broader perspective on the latest bioengineering technologies. I hope we continue to work on exciting projects further.

I cannot express my gratitude enough to **Prof. Jeremy Green** and **Dr. Ana Angelova** at King's College London. It was fortunate for me to be able to learn from Prof. Green, before embarking on my PhD journey, the importance of being passionate, critical, curious, and playful in research. I will never forget the smile on your face when you proposed that I collect mouse embryos at "E14.0" and "E14.25" (at 0 am and 6 am). That experience convinced me that nothing would be too tough, and I could overcome any challenge during my Ph.D. period.

Dr. Angelova, who brought me from a clinic to a lab, provided me the opportunity to learn the cutting-edge knowledge and technology in regenerative medicine/dentistry. This inspiration was the driving force behind the journey and will continue to motivate me in the future.

I cannot help but mention the Japanese mafia trio rallied in Malmö tandvårdshögskolan, **Dr. Ryo Jimbo**, **Dr. Yoshito Naito**, and **Dr. Yohei Jinno**. I would not have had the courage to take this journey without your inspiration and encouragement. Your pioneering spirit has certainly left a lasting imprint on my heart.

I am sincerely grateful to the technical staff, **Siren**, **Ying**, **Odd, Hisham**, and **Kaia**, who provided valuable assistance throughout the course of my research.

My special appreciation goes to my successive "office mates", **Jannika**, **Neha, Shubham**, **Anders**, **Kordian**, and **Niyaz**, for our productive discussion as well as for the occasional moments of lighthearted gossip that helped to make our time together enjoyable.

My colleagues in the research group, **Cecilie**, **Salwa**, **Samih**, **Ahmad**, **Tarig**, **Øyvind**, **Espen**, **Elisabeth**, **Sid**, **Nageeb**, **Hassan**, **Mariann**, **Francesco**, **Masoumeh**, **Theo**, **Mehmet**, **Åshild**, **Ragda**, **Azzurra**, **Nora**, **Natalia**, and **Eylem** have been a source of support, friendship, and thought-provoking discussions for which I am grateful.

I on behalf of my family would like to express my heartfelt appreciation to the Indrevik family, **Tom**, **June**, **Georg**, **Berit**, **Fredrik**, **Joachim**, **Vilde**, as well as the Paulsen family, **Karl**, **Anette**, **Maren**, and **Frida**, for their incredibly warm hospitality, which made us feel like we were part of your family.
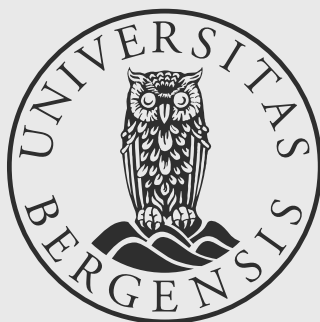
Finally, I would like to express my gratitude to my family. I am deeply thankful to **my parents** for their constant support and encouragement throughout my life. Our dear daughter, **Mia**, made my Ph.D. journey twice as challenging as it was supposed to be, but you made it as fun and memorable as I could have never imagined. I hope you will take it easy on me during my postdoc, though. To our expecting little one, I am prepared for you making my postdoc life twice as challenging. Last but not least, I want to express my heartfelt gratitude to my wife, **Kana**, for her unwavering love, support, and encouragement throughout my academic journey. Her constant belief in my abilities has been a source of strength and motivation for me.

March 2023, Bergen

Shuntaro Yamada

uib.no